Diss. ETH No. 18828; Diss. LNS No. 234

X-ray Scattering on Ordered Colloidal Assemblies

A Dissertation Submitted to the ETH Zurich
for the Degree of Doctor of Sciences

Presented by

Patrick Thomas Huber
Dipl. Phys. ETH
Born on January 11, 1980
Citizen of Gossau (ZH) and Madiswil (BE)

Accepted on the Recommendation of

Prof. Dr. Marcus Textor, Examiner
Prof. Dr. Ullrich Pietsch, Co-examiner
Prof. Dr. Walter Steurer, Co-examiner
Dr. Thomas Geue, Co-examiner

Zurich, January 2010

Abstract

Colloidal assemblies and in particular colloidal crystals are built up of colloidal particles ideally arranged in a crystalline structure. They present a promising bottom-up approach towards the fabrication of photonic materials with a complete photonic band gap. These materials have a huge potential for a wide variety of applications. The quality of the colloidal crystals is currently the main challenge of this approach. Therefore, adequate fabrication and characterization methods are imperative.

Various techniques for the self-assembly of colloidal crystals have been presented in the last two decades. In the process, convective self-assembly has been established as an approach that yields uniform assemblies over large areas while employing comparatively simple setups. The technique is able to provide close-packed colloids arranged in a fcc lattice with stacking faults. The number of layers of the final assembly can be tailored by the initial particle concentration. It has been shown that in combination with topologically structured templates, the long-range order of the opals could be increased and their crystallographic symmetry altered.

The focus of the presented work was on assessing the potential of grazing incidence small angle X-ray scattering (GISAXS) with respect to the structural characterization of colloidal crystals. For that purpose convective self-assembly has been successfully used to fabricate colloidal crystals from particles with diameters between 277 nm and 740 nm deposited on smooth glass slides. The number of layers of the investigated samples ranged from 1 to 14 layers. The best assemblies exhibited an almost constant number of layers across areas as large as 1 to 2 cm^2. Colloidal crystals have also been deposited on pDR1M surface relief gratings. This led in general to a less homogeneous coverage.

GISAXS data collected on *multilayers* with 7 and 14 layers, demonstrate that these multilayers have a similar alignment of the domains over the complete sample. The distribution describing the domain misalignment was fitted with a Gaussian function and gave for the two investigated samples an almost identical FWHM of 4.4 ± 0.9 deg (7 layers) and 4.3 ± 0.8 deg (14 layers). GISAXS, SEM and AFM investigations consistently show that the preferential orientation of the ordered domains is correlated to

the direction of the meniscus movement during the self-assembly of the multilayers. It was found that the colloidal particles align along the growth direction, i.e., the [1 0 0] direction of the hexagonal structure is parallel to the translation direction of the meniscus. The investigated *bilayer* exhibited the same preferential alignment. It was however less pronounced. The distribution describing the domain misalignment was fitted with a Lorentzian function and provided a FWHM of 7.5 ± 2.5 deg. Colloidal *monolayers* behaved distinctly different in exhibiting a random orientation.

It was concluded that the transition from a self-assembled monolayer to two layers to multilayers goes in parallel with the development of a mechanism that leads to a directed self-assembly of the particles. The increase in solvent flow in the case of multilayers may possibly play a role in the macroscopic alignment of the colloidal domains.

The presented approach for the in-plane evaluation of the scattering data shows that GISAXS is well suited to detect the precise degree of the domain alignment on samples fabricated by convective self-assembly. In case of SEM and AFM, this information can only be accessed by a laborious evaluation of large numbers of individual micrographs. Similar information on the alignment can also be accessed by laser diffraction. The laser beam has thereby to be scanned over the sample and changes in the orientation of the diffraction pattern recorded. The maximum in-plane correlation lengths achieved by GISAXS experiments in this work were $\sim 4.8\,\mu$m. The technique is accordingly not appropriate for the study of domain sizes in the case of the used particle sizes unless the resolution can be improved. SEM and AFM methods are clearly better suited for this purpose.

ED-XRR and GISAXS investigations were performed during the drying of droplets of colloidal dispersion. These investigations were intended to probe the assembly process *in situ*. The measured scattering data exhibits a rich behavior. Most of it can however be understood by effects originating from the solvent and the change in the droplet shape. No signal attributed to ordering processes was detected from the data. Subsequent AFM and SEM investigations confirmed the mostly disordered assembly of the particles. It was concluded that the chosen system is not ideal for *in situ* investigations.

A simulation tool named "3DGISAXS" was developed and implemented in the framework of this thesis for the modeling of the scattering data obtained from colloidal multilayers as no tools with the necessary capabilities have been available yet. It includes reflection and refraction effects important at grazing scattering angles. The implemented model was fitted to the scattering data of one multilayer (7 layers) to exemplify the potential of the approach. A stacking probability $a = 0.63$ has been obtained from this process indicating not complete random stacking ($a = 0.0$) but a tendency towards an fcc stacking ($a = 1.0$). The obtained stacking probability is a statistical average over the complete sampled area ($\sim 1 \times 30\,\mathrm{mm}^2$). GISAXS is the only method that can provide such information on the stacking of the hexagonally packed layers perpendicular to the substrate surface in a non-destructive manner.

The simulation tool was in a further step used for the calculation of the scattering from single crystals of just a few hexagonally close packed layers. It was found that GISAXS in combination with such calculations can in principle be used to determine the specific stacking sequences of these layers in the direction perpendicular to the surface.

Zusammenfassung

Kolloidale Kristalle bezeichnen Strukturen, in welchen Kolloide auf einem Kristallgitter angeordnet sind. Diese Strukturen stellen einen vielversprechenden “bottom-up”-Ansatz dar zur Herstellung von photonischen Kristallen. Photonische Kristalle mit einer Bandlücke in alle Richtungen (complete photonic bandgap) besitzen ein immenses Potential für eine Vielzahl an Anwendungen. Die momentan grösste Herausforderung ist dabei die Qualität der kolloidalen Kristalle. Passende Herstellungs- und Fabrikationsmethoden sind deshalb dringend gefragt.

In den letzen zwei Jahrzehnten wurden verschiedene Techniken zur Selbstanordnung von kolloidalen Kristallen vorgeschlagen. Dabei hat sich die Selbstanordnung durch Konvektion zu einem Ansatz herauskristallisiert, der auf grossen Flächen gleichmässige Strukturen erzeugen kann. Die für die Technik notwendigen Einrichtungen sind relativ einfach. Bei der Selbstanordnung durch Konvektion ordnen sich die Kolloide in einer dichtesten Kugelpackung an. Diese Packungen besitzen eine kubisch-flächenzentrierte Ordnung mit Stapelfehlern. Die Anzahl Lagen der entstehenden kolloidalen Kristalle kann anhand der Konzentration der Partikel in der ursprünglichen Dispersion festgelegt werden. Es wurde gezeigt, dass topologisch strukturierte Substrate die weiträumige Ordnung der Kristalle verbessern und deren kristalline Ordnung ändern können.

Das Augenmerk der vorliegenden Arbeit war die Ermittlung der Möglichkeit der Kleinwinkel-Röntgenstreuung unter streifendem Einfall (GISAXS) zur strukturellen Charakterisierung von kolloidalen Kristallen. Zu diesem Zweck wurden mit der Selbstanordnung durch Konvektion erfolgreich kolloidale Kristalle aus Partikeln mit Durchmessern zwischen 277 nm und 740 nm auf Mikroskopie-Objektträgern hergestellt. Die Schichtdicken der untersuchten Proben lagen im Bereich zwischen einer und 14 Lagen. Die besten kolloidalen Kristalle besassen eine beinahe konstante Anzahl Schichten auf einer Fläche von 1 bis 2 cm^2. Proben wurden auch auf topologischen Oberlächengittern aus pDR1M abgelagert. Die Beschichtung dieser Proben war jedoch im Allgemeinen weniger homogen.

Daten von GISAXS Messungen an *Multilagen* mit 7 und 14 Schichten zeigten, dass die Domänen auf der gesamten Probe ähnlich ausgerichtet sind. Die Verteilungsfunktion der Domänenorientierung konnte mit einer Gaussfunktion genähert werden. Die Halbwertsbreite war für beide Proben fast identisch: $4.4 \pm 0.9°$ für 7 Schichten und $4.3 \pm 0.8°$ für 14 Schichten. GISAXS-, SEM- und AFM-Untersuchungen zeigten übereinstimmend, dass die Orientierung der Domänen im Fall der Multilagen in einem festen Bezug zur Bewegungsrichtung des Meniskus während des Selbstordnungsprozesses steht. Es hat sich gezeigt, dass sich die Kolloide entlang der Wachstumsrichtung aufreihen. Das heisst, dass die [1 0 0] Richtung der hexagonalen Ebenen parallel ist zur Bewegungsrichtung des Meniskus. Die untersuchte Probe mit *zwei Lagen* zeigte die gleiche bevorzugte Ausrichtung der Domänen wie die Multilagen. Die Ausrichtung war jedoch weniger stark ausgeprägt und die Verteilungsfunktion konnte mit einer Lorentzfunktion genähert werden. Die Halbwertsbreite ergab $7.5 \pm 2.5°$. Auf den *Monolagen* zeigten die Domänen eine zufällige Verteilung.

Aus den aufgeführten Beobachtungen wurde gefolgert, dass sich parallel zum Übergang von der Monolage über die Doppellage zur Multilage ein Mechanismus entwickelt, der zu einem gerichteten Selbstordnungsprozess der Kolloide führt. Die Vergrösserung des Wasserflusses bei zunehmender Anzahl Lagen könnte möglicherweise eine Rolle spielen bei der makroskopischen Ausrichtung der Domänen.

Die vorgestellte Methode zur Auswertung der Ordnung in der Ebene zeigt, dass GISAXS dazu geeignet ist präzise den Grad der Orientierung der Domänen zu bestimmen bei Proben, die mit konvektiven Selbstordnungsprozessen hergestellt wurden. Im Falle von SEM und AFM kann diese Information nur mit einer mühsamen Auswertung vieler Einzelaufnahmen gewonnen werden. Ähnliche Information zur Orientierung kann man auch mit Laser-Streuung erhalten. Mithilfe eines Laserstrahls werden dabei die Wechsel in der Orientierung der Streumuster untersucht. In der vorliegenden Arbeit ist die maximal erreichte Korrelationslänge parallel zur Probenoberfläche in den GISAXS-Experimenten $\sim 4.8\,\mu$m. Daraus wurde gefolgert, dass die GISAXS-Technik nicht geeignet ist, die Domänengrössen der in dieser Arbeit verwendeten Partikelgrössen zu bestimmen. SEM- und AFM-Methoden sind klar besser geeignet für diesen Zweck.

Während des Austrocknens eines Tropfens Dispersion wurden ED-XRR- und GISAXS-Untersuchungen durchgeführt, um den Selbstordnungsprozess *in situ* zu untersuchen. Die gemessenen Streudaten zeigen vielfältige Effekte. Diese können grösstenteils dem Wasser und der Änderung der Tropfenform zugeschrieben werden. Anhand der Streusignale konnten keine Ordnungsprozesse festgestellt werden. Anschliessende AFM- und SEM-Untersuchungen bestätigten die ungeordnete Anordnung der Kolloide. Daraus wurde gefolgert, dass das Austrocknen eines Disperions-Tropfens nicht ideal ist für *in situ*-Untersuchungen.

Im Rahmen der vorliegenden Arbeit wurde das Simulationsprogramm "3DGISAXS" entwickelt und programmiert. Das Ziel war die Modellierung der Streudaten aus dem Untersuch der kolloidalen Multilagen. Bis anhin stand kein geeignetes Programm für diese

Modellierung zur Verfügung. Das Programm berücksichtigt Reflektions- und Brechungseffekte, die wichtig sind bei der Streuung unter streifendem Einfallswinkeln. Mit dem programmierten Modell wurden die Daten einer Probe mit sieben Lagen beispielhaft angenährt, um die Möglichkeiten des Programms zu demonstrieren.

Der Näherungsprozess ergab eine Schichtungswahrscheinlichkeit von $a = 0.63$. Das bedeutet, dass die Probe nicht komplett zufällig geschichtet ist ($a = 0.0$), sondern eine Tendenz zu einer kubisch-flächenzentrierten Schichtung ($a = 1.0$) besteht. Die beobachtete Schichtungswahrscheinlichkeit ist ein statistischer Mittelwert über die gesamte Probe ($\sim 1 \times 30\,\mathrm{mm}^2$). GISAXS ist die einzige Methode, die es ermöglicht, solche Informationen zur Schichtungswahrscheinlichkeit von hexagonal-gepackten Schichten senkrecht zur Oberfläche des Substrates zerstörungsfrei zu erhalten.

Das Simulationsprogramm wurde in einem weiteren Schritt dafür benutzt, die Streumuster von Ein-Kristallen mit wenigen Lagen zu berechnen. Die Untersuchungen ergaben, dass die Kombination von GISAXS und dem Simulationsprogramm die Aufklärung der konkreten Schichtabfolge ermöglicht.

Contents

CHAPTER 1

Introduction

The exploration of the micro- and nanoworld has led to many advancements in our understanding of materials and systems. It has been realized that the microstructure of a material can be crucial in understanding its macroscopic properties. This insight, paired with the desire for efficiency, have advanced our ability to manipulate matter with high precision on ever-decreasing length scales. In particular, progress has been fertilized by the development of sophisticated methods to observe and characterize structures on the micro- and nanometer length scale. Today, exploitation of such new tools affect almost all aspects of modern life ranging from the high density storage media in every computer to novel drug developments.

The focus of the presented work is on the *characterization of ordered colloidal assemblies by means of X-ray scattering* methods. The probed colloidal assemblies comprise both mono- and multilayers. The multilayers, i.e., structures with a three-dimensional order, are also referred to as *colloidal crystals.* They are the main focus of this work.

1.1 Colloidal Crystals

Colloids - the building blocks of colloidal crystals - describe small particles or droplets, in a size range from a few nanometers up to several micrometers, that are dispersed in another medium. Examples of colloidal systems are milk (fat droplets dispersed in water), smoke (airborne soot particles) or Styrofoam (air bubbles in a solid polymeric matrix). Colloidal suspensions show a very rich habitus depending on type of material, shape and interactions with the dispersant and each other. Colloids effectively play a role in a multitude of technological applications ranging from food science through dye fabrication to ore flotation [1].

Colloidal crystals are materials with a three-dimensional order of the colloidal particles. Ideally, they consist of colloids that are arranged in a crystalline lattice, i.e., neglecting the surface, the material has a periodic structure in all three dimensions and two points in the material displaced by a lattice vector from each other are congruent. In order to form such highly ordered structures, colloidal particles have to be highly monodisperse with regard to shape, size and interactions [2]. Particles that fulfill these requirements are nowadays commercially available from different suppliers.

1.1.1 Relevance of Colloidal Crystals

The broad interest in colloidal crystals can be separated into two aspects. On one hand, colloidal crystals are intensively studied as a model system of atomic crystallization. On the other hand, colloidal crystals have different fields of technological applications - the most prominent ones making use of their characteristics to act as photonic materials.

Colloidal Crystals as Model Systems of Atomic Crystals

Colloidal suspensions mimic the phase behavior of atomic or molecular systems. Unlike their molecular counterparts, suspended colloids offer experimentally directly accessible length and timescales. These systems are therefore ideal model systems to quantify the dynamics of crystal nucleation, crystal growth and melting. Additionally, control over particle interactions allows for the study of the transition kinetics between different phases. In the context of basic understanding of crystallization processes, colloidal suspensions have been extensively studied. A comprehensive overview of the field can be found in recent reviews [3, 4].

Colloidal Crystals as Photonic Materials

Photonic crystals, photonic materials or photonic bandgap materials (as this class of materials is called depending on the context) modify the propagation of light[1]. These materials exhibit a varying refractive index that is spatially periodic in one, two or three dimensions (see figure 1.1). The periodic refractive index variation creates a particular interplay of the scattered waves, as an electromagnetic wave gets scattered at every position with a change in refractive index. In some directions the intensity is extinguished through destructive interference, in others there will be constructive interference. Since this process depends on the wavelength, the outcome is iridescence - depending on the direction looked at, these materials flash in different colors when illuminated with a white light source. Naturally occurring photonic materials are for example opals [6] or

---

[1] The term “photonic” is deduced in analogy to “electronic” - the latter concerns the manipulation of electrons, the former that of photons. A comprehensive introduction into the field can be found in [5].

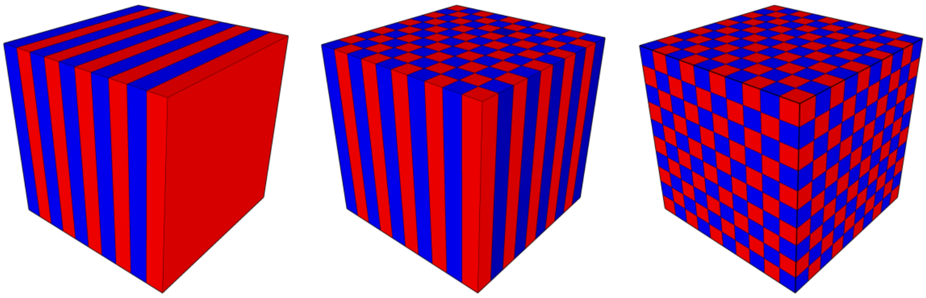

Figure 1.1: From left to right: schematics of a one- two and three-dimensional photonic crystal. The blue and red regions represent the individual units with a different refractive index.

the iridescent wings of certain butterflies [7,8] and beetles [9]. The wavelengths λ that are reflected from a material with a periodicity d can be calculated according to [10]

$$m\lambda = 2d\sqrt{n_{eff}^2 - \sin^2\epsilon}, \tag{1.1}$$

with m being an integer, n_{eff} the mean refractive index of the material and ϵ the angle between the incident light and the substrate normal.

According to equation (1.1), the largest wavelength at which the effect starts to play a role corresponds approximately to the period of the modulation in the refractive index of the material. Thus, photonic crystals for wavelengths in the visible range should be modulated in the range of one micron. A photonic material for microwave applications has a periodicity in the range of centimeters. An analogon at the angstrom scale is the Bragg diffraction (see chapter 1.2.1) of an X-ray beam from a solid state crystal. If one calculates the wavelengths that are allowed to propagate through a photonic material, the result is a dispersion relation. It describes the wavevector of the electromagnetic wave as a function of the frequency and is displayed in the band structure of a material.

The numerically calculated band structure for the case of dielectric spheres in a face centered cubic (fcc) arrangement and of its inverted structure are displayed in figure 1.2. For certain energies, there exists no wavevector. These regions correspond to the case of destructive interference described above and are called *photonic bandgaps* (PBG). If a gap persists over all directions in the crystal, it is called a complete PBG. The width and the position of the PBG are determined by the dielectric contrast between the applied materials and by the periodicity in the direction of propagation of the electromagnetic wave ([5] page 49 et seq.). A large dielectric contrast widens the PBG. The photonic band structure is closely related to the crystalline arrangement of the high and low refractive index material regions due to the influence of the periodicity.

In general, the appearance of a complete PBG is connected to materials with high dielectric contrast between the different dielectric units. This is usually air versus a

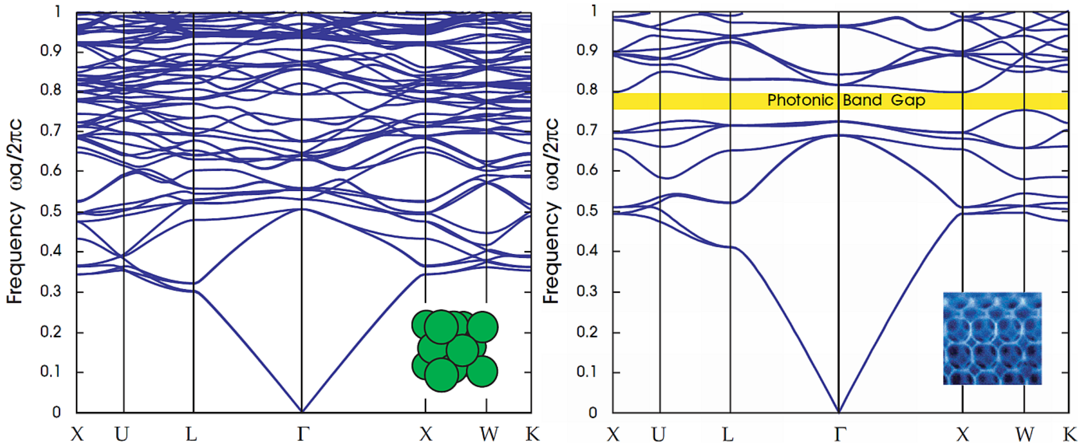

Figure 1.2: Calculated photonic band structures for (*left*) dielectric spheres and (*right*) interconnected dielectric spherical shells arranged in both cases in a face centered cubic arrangement. The refractive index of the material was set to ~3.6 for the calculations. The abscissa corresponds to the wavevectors between the high symmetry points of the first Brillouin zone (see e.g. [5], page 238). The frequency ω is given in dimensionless units where a corresponds to the lattice spacing and c is the speed of light. As can be seen, a full gap over all directions is only developed in the case on the right side. The inset in the right graph shows a structure fabricated by inverting a colloidal crystal. In order to increase the gap size, the interstices between the spheres were only partly filled up creating a network of interconnected spherical shells. Figures taken from [5].

structure built up of a material with a high refractive index. The dielectric units that build up such a material are ideally asymmetric and have a low volume filling fraction [11]. The modulation of the refractive index should additionally have a similar periodicity in all directions [11]. In three dimensions, the best suited structures to find a complete PBG known so far are the dielectric diamond and the pyrochlore crystal structures both of space group Fd3m [12].

Implementation of Photonic Materials

Various procedures for the fabrication of three-dimensional photonic structures have been developed [13–20]. Technology from the semiconductor industry has been applied in a layer by layer fashion to form structures that are periodic in three dimensions. The individual layers have thereby been structured by lithographical methods before the addition of the next layer. Different structures have already been realized, e.g., by successive etching and deposition steps [13–15] or by wafer bonding [16]. The methods allow the fabrication of almost perfect photonic crystals. Depending on the needs, defects can even be introduced at defined positions. The challenges of these approaches are the precise alignment of the individual layers, the relatively high production costs and the further miniaturization in order to arrive at materials with PBGs in the visible light region. Other so-called top-down methods towards three-dimensional photonic crystals have applied photosensitive resists, that polymerize when illuminated with a laser beam above a certain intensity threshold. After the exposure, the non-polymerized material can be dissolved, resulting in a periodic, stable structure. Three-dimensional photonic crystal structures have been made by the interference of different beams [17] and direct laser writing [21]. The combination of both techniques [22] with a successive inversion of the structure [23] presents a route towards periodic structures with defined defects.

Bottom-up schemes to fabricate nanostructured materials follow an altogether different approach. They use the concept of *self-assembly*. This describes the process that molecules or particles arrange under certain circumstances in an ordered manner without external guidance. Self-assembly can therefore offer a cost effective alternative to top-down methods. One type of bottom-up approach uses diblock copolymers [18]. Usually, simple linear copolymers consisting of two different segments are employed. These segments tend to phase separate but as they are connected, this leads to the evolution of microdomains with morphologies ranging from hexagonal-packed cylinders, lamellae structures to double gyroids. The resulting morphologies can be tuned by varying volume, molecular weight and composition of the individual blocks and their degree of immiscibility. The long-range order of the evolving microdomains can be increased by adjusting the film thicknesses, altering the substrate-polymer interaction and applying external fields [24]. A prime constraint of copolymer photonic materials is the low dielectric contrast between the two components. Possible ways to circumvent this limitation are the selective doping or removal of one component. The second major drawback is the small size of the microdomains between several and tens of nanometers. This makes the structures unsuitable for optical or telecommunication applications [25]. Comb block copolymers seem to present a way towards microdomains over 200 nm [26].

The self-assembly of colloidal particles into ordered arrangements, i.e., colloidal crystals, is another attractive route to photonic materials. They are sometimes called synthetic opals as they display the same iridescence and microscopic structure as naturally occurring opals. Plenty of techniques have been exploited to fabricate colloidal crystals and a wide variety of different colloidal particles have been used for this purpose (see chapter 1.1.2). Most of the techniques result in densely packed colloids, i.e., fcc, hexagonal close-packed (hcp) or random hcp arrangements. These structures interact with light, but theoretical calculations indicate that even for high dielectric contrast no complete PBG can be achieved, see figure 1.2 and [27]. However, the colloidal crystals can be inverted by infiltrating the interstices between the colloids with materials with a large refractive index and dissolving away the original spheres [28]. The inverted fcc and hcp structures can exhibit complete photonic band-gaps, see figure 1.2 and [27, 29]. First examples of successful realization of materials with a complete PBG in this manner proved the feasibility of this concept [19, 20]. The advantage of this approach towards three-dimensional photonic materials is its relative simplicity. As the particle assemblies act as templates only, the particles themself do not have to provide the high difference in refractive index which is necessary for the creation of a complete PBG. Therefore, one

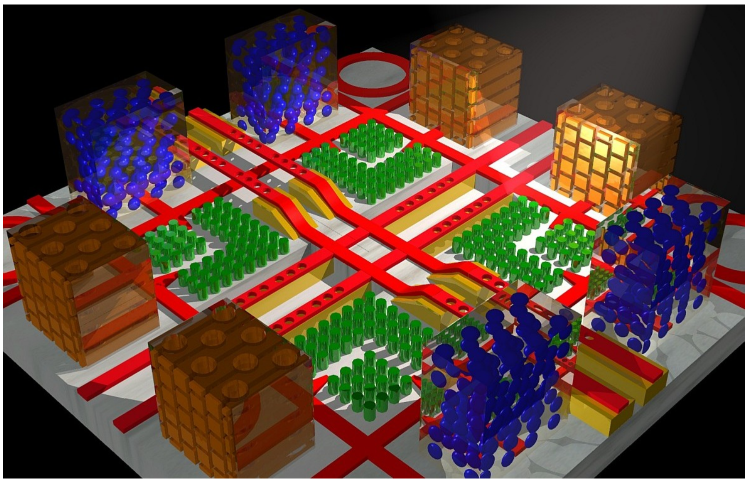

Figure 1.3: The photonic micropolis - an artistic view of an all-optical chip, according to [32]. Red “roads” with holes correspond to one dimensional photonic structures. They transport the light between the “buildings” that correspond to three-dimensional periodic structures with a complete bandgap. The green “forests” illustrate right angle waveguide bents fabricated in two-dimensional structures.

can abandon the tight restrictions concerning the materials used, and polymeric material can also be considered for the particles. By the particle size, the number of assembled particle layers and the refractive index of the infiltrating material, one can tailor the optical response of the system over a broad range. The challenge of the approach is the fabrication of large regular colloidal crystals as the self-assembly process is prone to defects. Defects such as voids, cracks, grain boundaries, deviations in the particle diameters and stacking errors will reduce the bandgap width and ultimately close it up.

There are a number of additional approaches for the preparation of photonic materials not mentioned here. Reviews on the topic can be found in [11,30].

Application of Colloidal Crystals

A large part of the effort in the field of colloidal crystals aims at their application as photonic crystals with a complete PBG in the visible or near infrared region. Such PBG materials would have many interesting technological applications. Perfect crystals could be interesting for three-dimensional mirrors and high-efficiency light-emitting diodes (LEDs). The selective introduction of defects is also of interest. By inserting line defects in an otherwise perfect crystal, one can create waveguides. Light within the frequency range of a complete bandgap propagates only along the defects as it is hindered to do so in all other directions. It can even be guided around tight corners. Defined defects in photonic crystals could also play an essential part in the development of lasers and of novel optical elements. Ultimately, photonic crystals could be a way to realize the dream of the all-optical chip of the future [31], see figure 1.3.

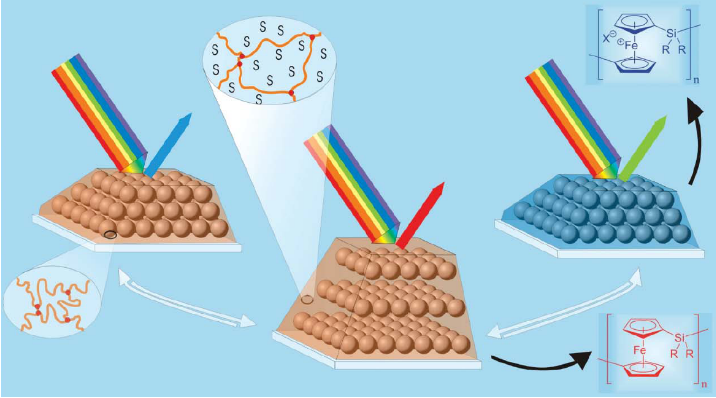

Figure 1.4: Working principle of a color display composed of a colloidal crystal. After self-assembly, the colloidal crystal is embedded in a metallopolymeric network. By absorbing solvent, the matrix swells leading to an increased lattice spacing and a concurrent red shift of the reflected light. The amount of solvent retained in the network is controlled by the oxidation states of the iron atoms in the polymer backbone. The distribution of oxidation states can be continuously adjusted by localized electrochemical stimuli, when the material is in contact with a conductive substrate [40]. Illustration taken from [41].

All applications based on the principle of a complete PBG are of course in need of highly perfect colloidal crystals. As this is a very demanding task, applications with less stringent requirements are much further developed. They mostly exploit the strong diffraction of light by regularly arranged colloidal spheres. As follows from equation (1.1), the diffracted wavelength depends critically on the distance between the colloidal layers. If this distance is made responsive to external stimuli, the corresponding material will appear in different colors depending on the environment. Sensors using this principle have been realized using self-assembled colloidal particles embedded and stabilized in polymeric matrices that change their volume depending on an environmental change. The sensing capabilities for a wide variety of responses has already been shown, e.g., for temperature [33], ions (Pb^{2+}, Ni^{2+}, Co^{2+}, Cu^{2+}) [34, 35], glucose [34, 35], deformation [36], pesticide [37], pH [38] and ethanol [38]. The same principle has been applied to fabricate a prototype of a full color display, see also figure 1.4. Self-assembled silica spheres have been embedded in a metallopolymeric network that swells upon absorbing solvent. The absorption can be controlled by localized electrochemical stimuli, leading to a change in the refracted light [39, 40].

Inverted synthetic opals have also successfully enhanced the efficiency of solar cells [42]. Furthermore, it has been suggested to use them as electrodes in batteries thereby indicating the charging state by their color [41], as macroporous materials or as dyes [43]. Colloidal assemblies of dye doped spheres have also been proposed to increase the spatial resolution of high-density storage media [44]. An increase in recording modes has been realized by microspheres including different dyes [45, 46].

1.1.2 Fabrication and Implementation of Colloidal Crystals

The main prerequisite to form highly ordered particle assemblies is the availability of colloidal spheres with tightly controlled sizes and surface properties [2]. Today, spheres with monodisperse diameters, i.e., with a polydispersity index (PDI) $\leq 3\%$, are readily prepared by emulsion polymerization in the case of polymer latexes and controlled precipitation in the case of inorganic oxides such as amorphous silica (for details see [2] and references therein). There are also commercial suppliers providing mainly latex and silica spheres with the necessary uniformity and a wide range of diameters. Various methods have been thought of to self-assemble colloidal particles into ordered structures. The following paragraphs give examples of the most prominent techniques.

Sedimentation

Colloidal particles dispersed in a liquid sediment according to the interplay between the pull from gravity and the frictional drag described by Stokes' law (see, e.g., [1] page 21). It has been recognized that the sedimented particles can form highly ordered structures. They crystallize preferentially into a fcc structure with the $\langle 111 \rangle$ direction perpendicular to the substrate when sedimented on a flat support [47]. The number of stacking faults of the hexagonally ordered planes is thereby primarily given by the growing rate of the crystal [47]. It can be controlled by the initial particle volume fraction. The sedimentation onto specially patterned templates enables both to steer the crystallographic structure and orientation of the sedimented particles and to overcome the spontaneous formation of a polycrystalline structure [48, 49]. The sedimentation of colloidal particles has been used in one of the first works that presented a photonic crystal with a three-dimensional PGB in the near infrared spectrum [19]. Nonetheless, the technique has some limitations. Depending on the size of the particles and the ratio between the densities of the colloids and the dispersant, particles may settle too fast to obtain a good quality opal, they may need several weeks to settle or they may not settle at all. Furthermore, there is no good control over the exact number of crystalline layers of the sediment. Additionally, the top layer of a crystal in solution remains fluid-like. The surface of such crystals is therefore always inhomogeneous.

Electrophoretic Deposition

Particles dispersed in a medium generally carry a surface charge. Such particles move in an electric field due to the Coulomb force exerted on the surface charges. This phenomenon is called electrophoresis. The electrophoretic deposition technique uses the electric field to deposit particles on an electrode surface [50–53]. Unstructured [50, 51], one- [52, 53], and two-dimensionally [54] patterned electrodes have already been used for this process. An increased long-range order and some control over the crystallographic order was found for templated substrates compared to templates without struc-

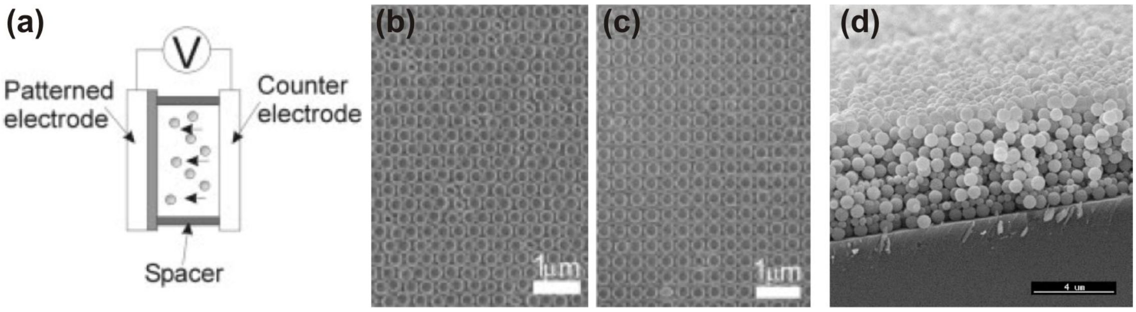

Figure 1.5: (**a**) Schematic setup used for electrophoretic deposition. Particles in the dispersion move in the electric field towards the patterned electrode. (**b**) and (**c**) correspond to SEM images of PS particle assemblies fabricated by electrophoretic deposition on hexagonally and square-patterned electrodes respectively. (**d**) Cross sectional view of colloidal crystal resulting from Langmuir-Blodgett deposition with different particle sizes. Beginning at the substrate, a sequence of one layer of 680 nm, one layer of 220 nm, two layers of 680 nm, one layer of 220 nm and five layers of 680 nm silica particles have been deposited. The scale bar corresponds to 4 μm. Figures (**a**) to (**c**) have been taken from [54], figure (**d**) from [55].

ture [52–54]. A simple schematic view of the technique and examples of resulting assemblies on structured templates are given in figure 1.5 (a)–(c).

Langmuir-Blodgett Transfer

Colloidal particles can be functionalized to obtain a hydrophilic-hydrophobic functionalization in a manner that they remain at the air-water interface. If brought into close contact, the particles form a close-packed arrangement and can be transfered in a layer-by-layer fashion onto a substrate [55, 56]. The main advantage of this approach is the fabrication of assemblies with an exact control over the number of particle layers. It is also possible to fabricate any sequence of layers consisting of different particles. However, one has neither control over the domains in the particle film at the air-water interface nor over the stacking sequence vertical to the substrate. The final crystals are therefore always polycrystalline.

Shear-induced Particle Ordering

A variety of techniques uses the effect that colloidal suspensions form hexagonally ordered layers when exposed to shear forces (see, e.g., [57] and sources therein). In [10, 58–61], the authors have injected colloidal suspensions into a fluidic cell and a constant pressure has then been applied at the inlet to force the solvent to drain through channels smaller than the colloidal diameters. The setup is schematically displayed in figure 1.6 (a). In front of the channels, the spheres have been assembled accordingly into a close-packed lattice under continuous sonication. Single crystalline domains across an area of about 1 cm^2 [58] with tunable thickness have been obtained. A similar setup has

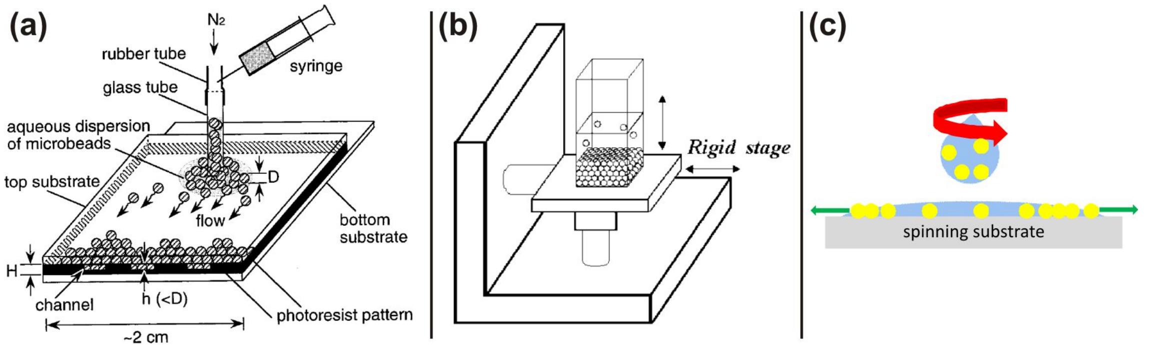

Figure 1.6: Methods applying shear forces for the particle ordering. (**a**) Scheme of the fluidic cell used by [68] for the particle assembly. Colloidal dispersion has been injected in the cell. By application of a constant pressure, the solvent has then been drained through the channels indicated in the scheme at the front of the cell. (**b**) Fluid cell with semipermeable floor exposed to oscillatory shear during the drying as used in [63]. (**c**) Spin coating of droplets of colloidal dispersion. Particles order due to shear forces during the spinning. Figures (**a**) and (**b**) have been taken from [68] and [63] respectively.

been used in [62]. Instead of sonication, pressure pulses have been used in this case to create the shear forces. The influence of oscillatory shear on the ordering in dispersions has been studied as well. An optimal oscillation regime for a drying colloidal dispersion in a fluid cell with a semipermeable floor, as shown in figure 1.6 (b), has been identified in [63]. The controlled parallel movement of two glasses comprising a colloidal dispersion with high volume fraction has led to a single domain fcc crystal with an extension of about $2\,\mathrm{cm}^2$ [64,65]. Colloidal crystals have also been fabricated by spin coating, thereby exploiting the shear forces in the liquid film during the spinning process, see figure 1.6 (c). Both non-volatile [66] and volatile [67] solvents have been employed in the process. In the former case, wafer sized assemblies with an almost uniform orientation have been created, whereas in the latter case, domains in the range of $100\,\mu$m times $100\,\mu$m with a crystalline order depending on the experimental conditions have been realized.

Convective Assembly

Most investigations have employed *convective self-assembly*. Although different variants exist, the common feature is that a meniscus of colloidal dispersion is moved over a hydrophilic surface. The assembly process is understood as a two stage process [69, 70]. Initially, an assembly of colloidal beads is formed by capillary immersion forces [71, 72] in the thin film at the drying edge of the meniscus. The menisci between the beads facilitate water evaporation and solvent starts to flow towards the particle assembly. This convective flow drags then further particles towards the three phase point. There, they are arranged both by capillary forces and the pressure of the flow. A schematic illustration of the process is given in figure 1.7 (a). In the case of colloidal multilayers,

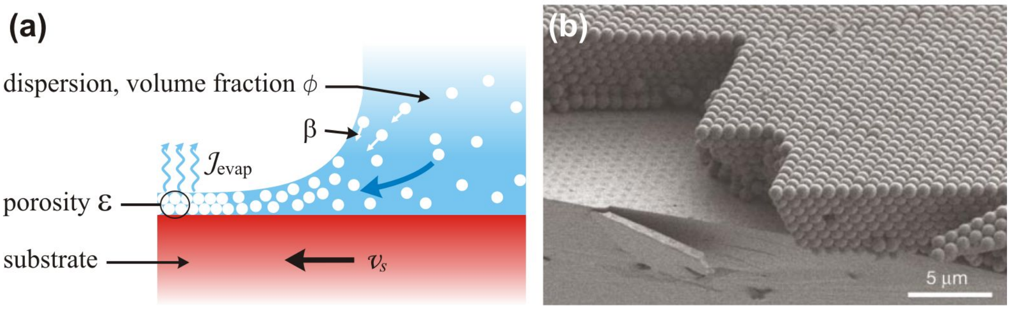

Figure 1.7: (**a**) Sketch of the convective self-assembly. The water evaporation at the three phase point induces a convective flow of colloidal dispersion towards the space between substrate and surface of the meniscus. There particles arrange due to the confinement and the flow of the solvent. If the substrate is moved according to the layer formation rate, homogeneous coatings are obtained. (**b**) Cross sectional SEM image of colloidal crystal consisting of 855 nm silica spheres fabricated by vertical deposition. The figure was taken from [20].

no detailed mechanism has been identified so far that explains how the specific three-dimensional close packed structures of colloidal spheres emerge [73]. As the particle assembly grows, the substrate is moved. A homogeneous layer gets created, if the rate of layer formation is equal to the substrate movement rate. A simple equation describing the steady-state assembly has been proposed in [74, 75]:

$$v_{g,s} = \frac{\beta \mathcal{J}_{evap} \varphi}{H(1-\mathcal{E})(1-\varphi)}. \tag{1.2}$$

The equation relates the velocity, $v_{g,s}$, of the growth and substrate respectively, the porosity, $\mathcal{E}$, and height, H, of the assembled layer, the volume fraction ratio of particles in the suspension, φ, the total water evaporation flux per unit length of the array's leading edge, $\mathcal{J}_{evap}$, and a coefficient that relates the solvent velocity to the particle velocity, β $(0 < \beta < 1)$. The fundamental relations between the different factors involved in (1.2) have been confirmed in different studies [76–80]. From equation (1.2) follows that the thickness and structure of coatings can be controlled with three major process parameters, namely the substrate velocity, v_s, the particle volume fraction φ and the evaporation flux, $\mathcal{J}_{evap}$.

Different experimental implementations making use of convective self-assembly have been put forward. *Vertical deposition* uses a substrate immersed vertically in a particle suspension that slowly evaporates. As the level of the dispersion sinks, particles assemble at the receding meniscus formed at the surface of the substrate [76]. This setup works only for particles that do not sediment noticeably during the timespan of the experiment. For the assembly of larger particles, a temperature gradient in the suspension has successfully been introduced to prevent sedimentation and assemble particles with sizes up to around 1 μm [20]. Figure 1.7 (b) displays an example of a corresponding colloidal crystal fabricated from 855 nm silica spheres. Good quality colloidal multilayers have already been formed applying different solvents, flat and structured substrates as well as elevated evaporation temperatures [52, 81–85]. The number of deposited layers can be well controlled by the particle concentration in the dispersion. However, the concentration normally increases during the experiment due to the evaporating solvent and the thickness of the assembly increases accordingly. Modified setups circumvent this drawback by slowly pumping the dispersion down [78] or by immersing the substrate into the suspension and then pulling it slowly out [75,77]. The latter approach has been called *dip coating.* It allows the independent control over the meniscus displacement velocity and the particle concentration. In a further variant, the meniscus is moved horizontally [79, 80]. The dispersion is thereby trapped between the substrate and a moving slide and only microliters are needed for the coating of square centimeters. By introducing a heater in the sample stage, the water evaporation can be varied effortlessly without influencing the humidity [80].

For convective self-assembly, close-packed crystals with identical orientation in the range of square centimeters have been reported in several works [20,75–77,83]. Different studies state that convective assembly forms fcc crystals with stacking faults [20, 77]. Even though it has originally been stated that the technique is able to precisely control the thickness of the assemblies [76], later studies propose that some amount of thickness oscillations are intrinsic to the process [86, 87].

Template Assisted Self-Assembly

In the case of sedimented crystals, it has been recognized some time ago that structured substrates influence the way colloidal particles self-assemble[2]. Template assisted self-assembly has since then been studied in combination with different techniques and employing a variety of one- or two-dimensionally structured substrates [52–54,82,83,85, 88–91]. It has been found that different crystallographic symmetries and orientations can be induced and the long range order of assemblies considerably increased. The surfaces are most frequently topologically (in contrary to chemically) structured. A variety of lithographic methods are applied for the patterning: Electron beam, photo-, soft-, nanoimprint-lithography, reactive ion etching etc.

Other well-suited substrates are surface relief gratings formed from amorphous azobenzene containing polymers [82, 88, 89]. If a thin film of such a polymer is irradiated with an interference pattern, a topological surface relief grating starts to form whose period corresponds to that of the interference pattern [92]. In contrast to lithographic methods, no additional process steps are necessary.

1.1.3 Characterization of Colloidal Crystals

The characterization of the colloidal crystals is essential as the domain sizes, the density of voids, the crystallographic order, the number of layers and the flatness of the surface

---

[2] See paragraph "Sedimentation" in this chapter.

define the optical properties of the material. The abilities and limitations of the different characterization techniques used at present are discussed in the following paragraphs.

Conventional and Confocal Microscopy

Conventional optical microscopy is well-suited for an overall optical inspection of the synthetic opals [79, 84, 87, 93]. Samples consisting of particles with diameters larger than the wavelength of visible light exhibit brilliant diffraction colors when illuminated. Regions that appear in different colors indicate an inhomogeneous crystal lattice and in the case of monolayers, equally colored regions correspond to unidirectionally aligned domains [75]. One of the restrictions is the achievable contrast for the detection of small features due to stray light. It gets increasingly difficult to extract the positions of particles with diameters below one micrometer.

Confocal microscopy in combination with fluorescent particles can reach a resolution close to the range of the theoretical resolution limit of $\sim 0.2\,\mu$m (depending on the actual wavelength and the numerical aperture of the objective). Several studies have mapped the three-dimensional positions of particles sedimented in a refractive index matched solvent. Information about the crystallographic order, defect densities and the number of layers in the crystal have been extracted from the particle coordinates [4, 47–49, 63, 77, 85, 91]. Dried colloidal crystals have to be backfilled with an index matched liquid before being investigated by confocal microscopy, see figure 1.8. The images of the inner layers are otherwise blurred due to the strong scattering of light between the spheres and air [77]. A confocal microscope that is adjusted to resolve the positions of colloids has typically a field of view in the order of $100\,\mu$m times $100\,\mu$m.

Spectroscopic Methods

Opals strongly interact with light because of the refractive index that varies with a period similar to the wavelength of visible light (see chapter 1.1.1). Accordingly, spectroscopic measurements have been used in various works to probe colloidal multilayers. The distance between Fabry-Pérot fringes has been used to assess the thickness of the crystals [56,67,76,81,84,87] and it has been stated that well-defined fringes only appear if the thickness of the sample in the optical path varies by less than ±10% [76]. The observation of Fabry-Pérot fringes is therefore a sign for thickness uniformity in the area of the probing beam. The position of the intensity minimum that appears in the transmission spectra can be calculated according to equation (1.1). Lattice parameters [10,56,66,94] and the mean refractive index [95] of the assembly have been evaluated accordingly. In-depth studies about the optical properties of colloidal crystals investigated finite size effects of the reflectivity and full width at half maximum (FWHM) of the stop band [81,96]. In references [20,93], good agreement has been found between calculated and measured transmission and reflection spectra of colloidal crystals.

Scanning Electron Microscopy

Scanning Electron Microscopy (SEM) is well-suited to map surfaces from the nanometer up to the millimeter scale. In a standard setup, samples are imaged in vacuum by scanning a high energy electron beam over the surface and measuring the electrons emitted from the sample. As isolating materials tend to charge up during scanning, a thin layer of conducting material is deposited on the sample to prevent imaging artifacts arising from static charge. The resolution of a SEM is mainly determined by the size of the electron beam. Lateral resolutions $< 10\,\mathrm{nm}$ can be achieved.

SEM is by fare the most widely used instrument for the investigation of colloidal assemblies [20, 50–56, 65–67, 76–85]. Examples can be seen in figures 1.5 (b)-(d) and 1.7 (b). As a non-conductive material, the assemblies are typically coated to obtain good quality image data. In order to assess the long-range order of synthetic opals over millimeters, different SEM micrographs have to be taken and compared. As SEM probes only the surface, colloidal crystals have to be cleaved in order to get information about the internal structure of the colloidal assembly. Such SEM pictures confirm the regular close-packed stacking of the particle layers. However, the assignment of the arrangements to a crystalline structure - fcc, hcp or a random close-packed - from SEM pictures alone is problematic [76, 77]: “This is because it is difficult to determine the exact angle of the cross-sectional view, which in turn makes it difficult to assess which crystal face is visualized in these images” [76].

Atomic Force Microscopy

Atomic Force Microscopy (AFM) provides high quality information on the three-dimensional surface structure of colloidal crystals [51,88,97]. It is used to investigate surfaces at the nanometer up to the micrometer scale. The dimension of probed areas is limited to tens of micrometers and no information about the internal structure of a sample is available.

Different modes of operation are in principle available. Colloidal crystals are typically investigated in the so called *tapping mode*[3]: A cantilever with a sharp tip at one end oscillates close to its resonant frequency in proximity of the surface and all changes in the oscillation due to the interactions between tip and specimen are registered. For imaging, the tip is scanned with piezoelectric actuators over the surface (x, y direction) and a feedback loop ensures that the interaction between sample and tip (and accordingly the oscillation) stays identical by moving the tip up and down. The resulting map $z = f(x, y)$ represents the topography of the surface.

---

[3] Equally called *intermittent contact mode*.

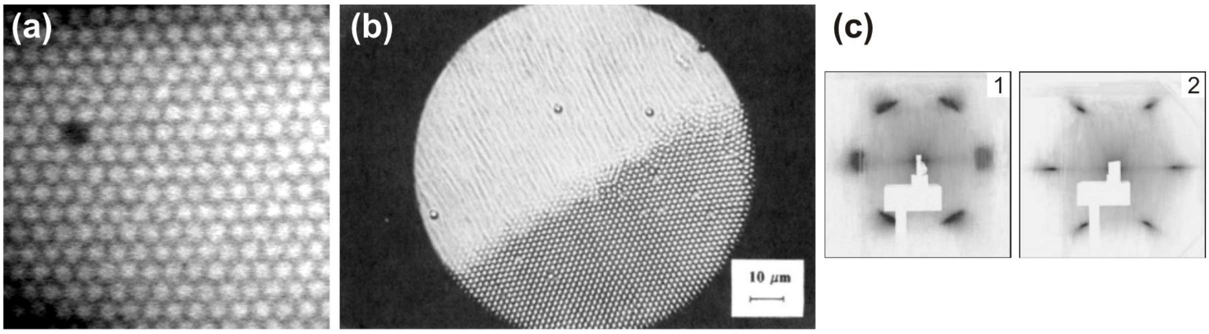

Figure 1.8: (**a**) Fluorescence microscopic image of the first layer on top of a glass substrate in case of a colloidal multilayer consisting of 737 nm spheres. For the investigation, the crystal has been infiltrated with a liquid that matches the refractive index of the spheres. (**b**) Microscopy image of the self-assembly of spheres. The particles in the upper left part of the image are wandering towards the ordered phase in the lower right part. (**c**) Laser diffraction photographs of colloidal crystals grown by convective assembly on structured ($\mathbf{c}_1$) and flat ($\mathbf{c}_2$) substrates. The diffraction pattern was observed in reflection; the sample and its holder can be seen in front of the diffraction pattern. Figure (**a**), (**b**) and (**c**) have been taken from [77], [69] and [52] respectively.

Laser Diffraction and Kossel Line Analysis

In laser diffraction, one measures the angle dependent transmission (reflection) of a monochromatic beam from the colloidal crystal. For that purpose, a laser beam is directed onto the sample and the transmitted (reflected) intensity is observed on a monitor. An example of a diffraction pattern measured at normal incidence can be seen in figure 1.8 (c). Information about the lattice symmetry, the lattice spacing, the orientation of domains and the distribution of domain orientations has been extracted from scattering patterns [52, 64, 79, 84]. These parameters are always averaged over the size of the beam. One obtains position-dependent information about the crystal parameters by scanning the beam over the sample.

For a Kossel line analysis, a laser beam is focused on a diffusor. This setup creates a monochromatic and point-like light source that is used to illuminate the colloidal crystal. Light beams propagating at angles that do not satisfy the Bragg condition penetrate the crystal. However, light beams satisfying the Bragg condition are reflected. The transmitted intensity forms the so-called Kossel pattern [20, 62, 94]. The accessible information is equal to that obtained by simple laser diffraction.

X-ray Scattering

Colloidal assemblies intended for photonic applications have also been probed by X-ray scattering. So far, such investigations have mainly been done with small angle X-ray scattering (SAXS) on sedimented assemblies [98–103]. In a SAXS experiment, an X-ray beam is transmitted through a sample and the resulting scattering pattern is recorded and evaluated. The technique is suited for particles with diameters up to a few hundred nanometers.

Compared to visible light scattering, the main advantage of X-ray scattering is the relatively weak interaction of X-rays with the photonic material. Instead of multiple scattering in the case of visible light, one can assume single scattering events for X-rays. This fact largely simplifies the evaluation of the scattering patterns and makes X-ray scattering an excellent probe for the internal three-dimensional structure and order of photonic crystals. An introduction in X-ray scattering is given in the following chapter 1.2.

Investigation of the Dynamics During Self-Assembly

Dynamics during self-assembly of colloidal particles have mainly been studied by microscopy. Confocal microscopy is an important tool for the study of crystallization in colloidal dispersions in the context of a basic understanding of these processes, see section 1.1.1. Conventional microscopy has also been applied for the investigation of the particle assembly at the drying edge of a meniscus of colloidal dispersion, see figure 1.8 (b) and [69, 75, 80]. In the case of drying multilayers, both techniques are limited because the images will blur as soon as the solvent evaporates due to the strong interaction of light with the colloidal particles. Besides, laser diffraction has been used to investigate the orientation and the symmetry of colloidal assemblies exposed to a shear force *in situ* [64]. These investigations have been done perpendicular to the hexagonal planes. In the case of a sedimented colloidal crystal, SAXS measurements revealed the loss of long-range order in the assembly as soon as the drying front reached the beam position [101].

1.2 X-ray Scattering

X-ray radiation denotes electromagnetic waves with a wavelength in the range from 10 nm to 0.01 nm corresponding to energies between 120 eV to 120 keV. These waves have been discovered by W.C. Röntgen in 1895 and since that time, they have been developed into an important tool to probe matter. The absence of intense X-ray sources limited their application at the beginning. This drawback has been overcome by the synchrotron radiation emitted from charged particles circulating in high energy storage rings. Since that time, various dedicated particle storage rings have been constructed. Nowadays, the so called third generation synchrotron sources are about 10^{12} times brighter than early lab-based sources [104]. X-ray scattering science has grown to a broad field simultaneously to the development of the sources. Today, X-rays are not only used to determine the ideal crystalline structure of materials, they have also evolved into an important tool to understand and characterize the various defects that occur in actual materials. The development of new instruments permits to probe not only crystals with lattice constants in the ångstroem region but up to the micrometer scale. X-rays are as well used to characterize surfaces and materials consisting of multilayer structures.

1.2.1 General Principles of X-ray Scattering

In a classical description, monochromatic electromagnetic waves propagating in the vacuum are described as plane waves of the form

$$\mathbf{E}(\mathbf{r}, t) = \boldsymbol{\varepsilon} \cdot A\, \mathrm{e}^{i(\mathbf{k}\cdot\mathbf{r}-\omega t)} \tag{1.3}$$

where $\boldsymbol{\varepsilon}$ corresponds to the unit vector defining the polarization of the wave and A is the amplitude. The propagation direction of the wave is defined by the wavevector $\mathbf{k}$ whose length is equal to $|\mathbf{k}| = 2\pi/\lambda$. The term ωt describes the oscillation of the electric field with time. As electromagnetic waves are transverse we have $\boldsymbol{\varepsilon} \cdot \mathbf{k} = 0$. In this description, we consider only the electric field and neglect the magnetic part for the sake of simplicity.

From a quantum mechanical perspective, an electromagnetic wave is viewed as quantized into photons with a certain energy $\hbar\omega$ and a momentum $\hbar\mathbf{k}$ with $\hbar$ being the Planck constant. The numerical relation between the wavelength λ in Å and the photon energy $\mathcal{E}$ in keV is

$$\lambda[\text{Å}] \backsimeq \frac{hc}{E} = \frac{12.398}{E\,[\text{keV}]}. \tag{1.4}$$

Both wave and particle descriptions equally characterize electromagnetic waves.

As soon as photons enter matter, they start to interact with the electrons in the material and can get scattered or absorbed. One defines the *differential cross-section*, $(d\sigma/d\Omega)$, as

$$\left(\frac{d\sigma}{d\Omega}\right) = \frac{(\text{Number of X-rays scattered per time into } \Delta\Omega)}{(I_0/F_0)\,(\Delta\Omega)}, \tag{1.5}$$

in order to describe the scattering processes and compare theoretical calculations with experimentally measured scattering intensities. The differential cross section denotes the intensity measured on the detector normalized both by the solid angle of the detector, $\Delta\Omega$, and the incident flux, I_0/F_0 with I_0 being the incident beam intensity illuminating the sample on a cross-sectional area F_0. It corresponds in other words to the scattered intensity independent of the experimental conditions and has the dimension of an area which is usually expressed in barn-units ($1\,\text{barn} = 10^{-24}\,\text{cm}^2$).

In a classical picture, the interaction between photons and electrons is described by the so called Thomson scattering. It is a purely *elastic* interaction, i.e., the initial and the scattered wave have an identical wavelength or energy[4]. Its cross section amounts to

$$\left(\frac{d\sigma}{d\Omega}\right) = \begin{cases} r_0^2 \cos^2\psi & \text{for p polarization} \\ r_0^2 & \text{for s polarization} \\ r_0^2 \frac{1}{2}\left(1+\cos^2\psi\right) & \text{for an unpolarized beam,} \end{cases} \tag{1.6}$$

where ψ is the angle between the direction of the incoming wave and the direction of observation. For scattering at shallow angles the factor $\cos\psi$ corresponds approximately to unity and can be neglected. The factor r_0 is known as the Thomson scattering length or as the classical electron radius. It corresponds to

$$r_0 = \left(\frac{e^2}{4\pi\epsilon_0 m_e c^2}\right) = 2.82 \cdot 10^{-5}\ \text{Å} \tag{1.7}$$

with e and m_e the charge and mass of the electron, ϵ_0 the dielectric permittivity of free space and c the speed of light in vacuum. In a material, the X-ray photons interact with a huge number of electrons. They are mostly located close to the atomic nuclei and one summarizes the scattering contribution of such electron clouds to the so called *atomic form factors*. In order to calculate it, one has to combine the scattering contributions of all electrons in the atomic shell. Special attention has to be payed to the phase of the waves. The phase difference $\Delta\phi$ of the waves emitted by two electrons separated by a vector $\mathbf{r}$ amounts to $\Delta\phi(\mathbf{r}) = \mathbf{k}_f \cdot \mathbf{r} - \mathbf{k}_i \cdot \mathbf{r} = \mathbf{Q} \cdot \mathbf{r}$.

$$\mathbf{Q} = \mathbf{k}_f - \mathbf{k}_i \tag{1.8}$$

is called the *wavevector transfer* or *scattering vector* where $\mathbf{k}_i$ is the wavevector of the incoming wave and the scattered intensity is measured in direction of $\mathbf{k}_f$, see figure 1.9 (a). We denote the electron density distribution around the nucleus $\rho(\mathbf{r})$. The volume element $\mathrm{d}\mathbf{r}$ at the position $\mathbf{r}$ contributes then an amount $-r_0\rho(\mathbf{r})\,\mathrm{d}\mathbf{r}$ to the scattered field. Combining the scattering strength with the appropriate phase factor one results with the total scattering length of a single atom

$$-r_0 f^0(\mathbf{Q}) = -r_0 \int \rho(\mathbf{r})\, \mathrm{e}^{i\mathbf{Q}\cdot\mathbf{r}}\ \mathrm{d}\mathbf{r} \tag{1.9}$$

with $f^0(\mathbf{Q})$ being the atomic form factor. From its derivation, it becomes clear that elements with higher atomic numbers and therefore more electrons in their shells have

---

[4] In the framework of quantum mechanics, the electron-photon interaction is always *inelastic*. The wavelength shift is described by Compton scattering formula, $\lambda'/\lambda = 1 + \frac{\hbar 2\pi}{m_e c\lambda}(1-\cos\psi)$ with λ and λ' the wavelength of the incoming and scattered wave respectively, m_e the mass of the electron, c the speed of light and ψ the scattering angle. For long wavelength (low energies) the shift in wavelength diminishes increasingly and the Thomson scattering is a valid approximation. At energies around 10 keV typically used in this work, the energy change of a backscattered photon amounts to about 4% and goes virtually to zero at grazing scattering angles.

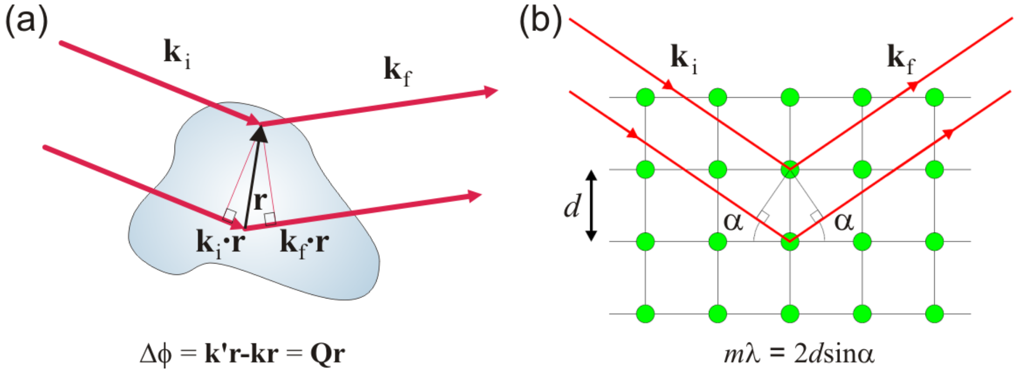

Figure 1.9: (a) Scattering from two electrons separated by $\mathbf{r}$ and (b) scattering from atomic layers separated by a distance $d = |\mathbf{r}|$. The phase difference of the two waves accounts to $(\mathbf{k}_f - \mathbf{k}_i) \cdot \mathbf{r} = \mathbf{Q} \cdot \mathbf{r}$. In the symmetric case of the scattering at atomic plains, the left hand side simplifies to $2d \sin \alpha$. Bragg scattering is observed for positive interference of the diffracted waves, i.e., whenever the phase difference is a multiple m of the wavelength λ. Figures according to [104].

superior scattering power. In the limit of $\mathbf{Q} \to 0$, the factor $f^0(\mathbf{Q})$ is equal to the number of electrons of an atom. In order to derive the differential cross section of the scattering from a single atom, one has simply to take the absolute square of the atomic form factor times the Thomson scattering length. The right side of equation (1.9) is a Fourier transform of the electron density. This is a very general result. One way to calculate the scattering length of an object is to take the Fourier transform of its electron density distribution.

In the preceding derivation of the atomic form factor, we used the scattering from a single *free* electron as the starting point. However, electrons in an atomic shell are bound and exhibit as a consequence resonant behavior and a diminished response to external driving fields. The *dispersion corrections* f' and f'' are introduced in order to account for both. The atomic form factor reads then

$$f(\mathbf{Q}, \hbar\omega) = f^0(\mathbf{Q}) + f'(\hbar\omega) + if''(\hbar\omega) \qquad (1.10)$$

where $\hbar\omega$ is the X-ray energy. The correction terms f' and if'' are related to the diminished response and absorption, respectively.

X-ray Scattering from Crystalline Structures

In the case of an X-ray beam penetrating a crystalline structure, the scattering amplitude can be calculated in a similar fashion as the atomic form factor. One sums up over the contributions of the scattering centers[5] instead of the single electrons. One

---

[5] In the case of a solid state crystal, the scattering centers are the atoms or molecules building up the material. For a colloidal crystal, the scattering centers are the colloidal particles. In the following text, “atoms” will be used without loss of generality.

imagines the crystal to be built from subunits arranged in a regular lattice that reflects the symmetry of the crystal. The subunits are called *unit cells* and contain one or more atoms depending on the actual crystalline structure. The atomic positions $\mathbf{r}$ are accordingly given by $\mathbf{r} = \mathbf{R}_m + \mathbf{r}_j$ where $\mathbf{R}_m$ describes the position of the unit cell and $\mathbf{r}_j$ is the location of the atom within the unit cell. The scattering amplitude from a crystal accounts then to

$$F_{crystal}(\mathbf{Q}) = -r_0 \sum_j f_j(\mathbf{Q})\, \mathrm{e}^{i\mathbf{Q}\cdot\mathbf{r}_j} \sum_m \mathrm{e}^{i\mathbf{Q}\cdot\mathbf{R}_m} \tag{1.11}$$

where the first sum goes over all atoms in the unit cell and the second sum goes over all unit cells in the crystal. The first term is called the *unit cell structure factor* and incorporates all contributions from the atoms in the unit cell. The second term is the *lattice sum.* It goes over all unit cells in the crystal. The sum of the phase factors is of order unity except for the cases where

$$\mathbf{Q} \cdot \mathbf{R}_m = 2\pi \times n, \text{ with } n \in \mathbb{N} \tag{1.12}$$

The positions of the unit cell $\mathbf{R}_m$ can be written in the basis vectors of the crystalline lattice $(\mathbf{a}_1, \mathbf{a}_2, \mathbf{a}_3)$

$$\mathbf{R}_m = u\mathbf{a}_1 + v\mathbf{a}_2 + w\mathbf{a}_3 \tag{1.13}$$

where (u, v, w) are integers. In order to find a unique solution for equation (1.12), we introduce the concept of the *reciprocal lattice.* The lattice is spanned by the reciprocal basis vectors

$$\mathbf{a}_1^* = 2\pi \frac{\mathbf{a}_2 \times \mathbf{a}_3}{\mathbf{a}_1 \cdot (\mathbf{a}_2 \times \mathbf{a}_3)},\ \mathbf{a}_2^* = 2\pi \frac{\mathbf{a}_3 \times \mathbf{a}_1}{\mathbf{a}_2 \cdot (\mathbf{a}_3 \times \mathbf{a}_1)},\ \mathbf{a}_3^* = 2\pi \frac{\mathbf{a}_1 \times \mathbf{a}_2}{\mathbf{a}_3 \cdot (\mathbf{a}_1 \times \mathbf{a}_2)} \tag{1.14}$$

that can then be used to describe any lattice site $\mathbf{G}$ in the reciprocal lattice according to

$$\mathbf{G} = h\mathbf{a}_1^* + k\mathbf{a}_2^* + l\mathbf{a}_3^* \tag{1.15}$$

with (h, k, l) being integers. From the product

$$\mathbf{G} \cdot \mathbf{R}_m = 2\pi(uh + vk + wl) = 2\pi \times n, \text{ with } n \in \mathbb{N} \tag{1.16}$$

it can be seen, that all lattice vectors of the reciprocal space are solutions to equation (1.12). Consequently, an ideal crystalline lattice diffracts electromagnetic waves only for specific wavevectors situated on the reciprocal lattice:

$$\mathbf{Q} = \mathbf{G}. \tag{1.17}$$

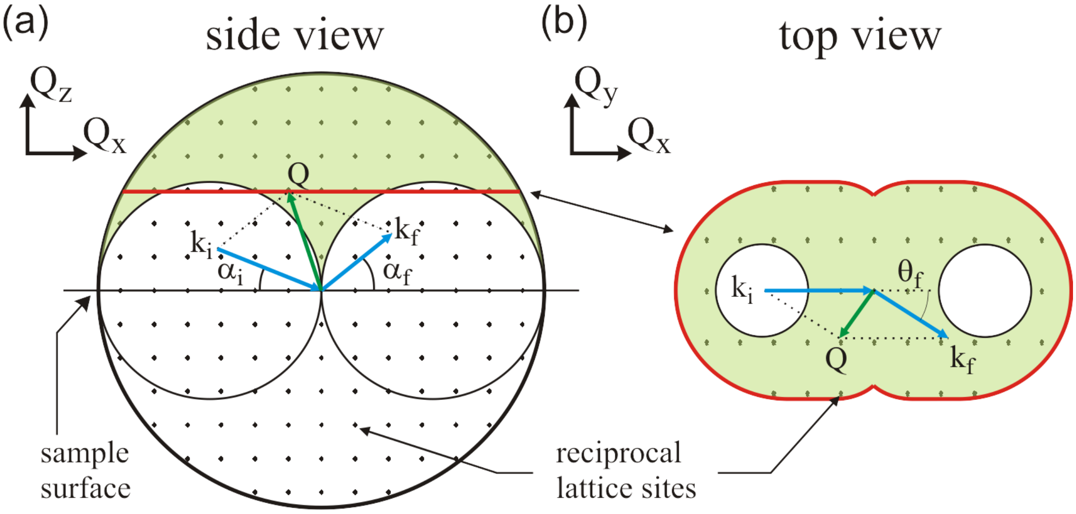

Figure 1.10: (a) Cut along the scattering plane through the three-dimensional extended Ewald sphere. The large circle has a radius of $4\pi/\lambda$. It limits the region in reciprocal space that is accessible for $\mathbf{Q}$ with a fixed wavelength λ. (b) Projection of the scattering geometry on the plane that includes the endpoint of $\mathbf{Q}$ in figure (a) and is parallel to Q_x, Q_y. The blue arrows correspond to the wavevectors of the incoming $\mathbf{k}_i$ and scattered $\mathbf{k}_f$ waves. Their direction is defined by the experimental angles α_i, α_f and θ_f. The white regions in both sketches can only be reached if either $\alpha_i < 0$, i.e., the sample is illuminated from below the sample surface or $\alpha_f < 0$ which corresponds to a transmission measurement. Only the greenish shaded region can be probed in reflection geometry and a fixed plane of incidence [105, 106]. During a scattering experiment, high intensity is measured whenever the experimental parameters, i.e., λ, α_i, α_f and θ_f are set in a manner that $\mathbf{Q}$ gets to lie on a reciprocal lattice point.

This is the so called Laue condition. It can be shown to be equivalent to Bragg's law,

$$m\lambda = 2d\sin\alpha, \tag{1.18}$$

which is derived from simple considerations, see figure 1.9 (b). λ corresponds to the wavelength, d to the spacing between atomic layers and α is the angle between the atomic layer and the direction of the incoming wave. m is a positive integer.

Motivated by the Laue condition, one often describes scattering experiments in reciprocal space. The extended Ewald construction, see figure 1.10, helps to visualize the scattering geometries and to demonstrate under which alignment the Laue condition is fulfilled. According to equation (1.16), distances in real space d and in reciprocal space q are connected by

$$q = \frac{2\pi}{d}, \tag{1.19}$$

i.e., are inversely proportional whereas angles are conserved. In order to calculate the scattering vector from an actual experimental setup, one expresses the wavevectors of the incoming and scattered wave in terms of the experimental angles.

$$\mathbf{k}_i = \frac{2\pi}{\lambda}\begin{pmatrix} \cos\alpha_i \\ 0 \\ -\sin\alpha_i \end{pmatrix}, \quad \mathbf{k}_f = \frac{2\pi}{\lambda}\begin{pmatrix} \cos\alpha_f \cos\theta_f \\ \cos\alpha_f \sin\theta_f \\ \sin\alpha_f \end{pmatrix} \tag{1.20}$$

α_i and α_f are the angles between the substrate and the incoming and scattered beam, respectively. θ_f corresponds to the angle between the plane formed by the surface normal and the scattered beam, see figure 1.10. The scattering vector is accordingly

$$\mathbf{Q} = \mathbf{k}_f - \mathbf{k}_i = \frac{2\pi}{\lambda}\begin{pmatrix} \cos\alpha_f \cos\theta_f - \cos\alpha_i \\ \cos\alpha_f \sin\theta_f \\ \sin\alpha_f + \sin\alpha_i \end{pmatrix}. \tag{1.21}$$

For the derivation of equation (1.9) and (1.11), we assumed that all the scattered waves interacting at the point of observance have parallel wavevectors. This is not generally true. However, this approximation - called the Frauenhofer approximation - is valid with a small scattering object and a sufficiently large distance between the scatterer and the detector. The validity of the Born approximation is the second assumption, that we used for the derivation of the results above. It implies that the photons interact weakly with matter so that they get only scattered once in the material.

X-ray Waves at Interfaces

So far we looked at the interplay between X-ray radiation and matter on an atomic level. For some aspects, it is however advantageous to consider a material as a continuous medium. From optics, the index of refraction of a material is familiar. The same concept is applied for X-rays where the complex index of refraction takes the form

$$n = 1 - \delta + i\beta. \tag{1.22}$$

The index of refraction is slightly smaller than one, as δ is typically of the order 10^{-6} for solid materials and only 10^{-8} for air. Some examples are given in table 1.1. The dispersive δ and absorbing part β can be connected to the atomic form factor f and the absorption coefficient μ according to

$$\delta = r_0 \frac{2\pi\rho_a}{\mathrm{k}^2}\left(f^0 + f'\right) \qquad \text{and} \qquad \beta = -r_0 \frac{2\pi\rho_a}{\mathrm{k}^2} f'' = \frac{\mu\lambda}{4\pi} \tag{1.23}$$

where ρ_a is the atomic number density. The absorption coefficient μ quantifies the attenuation of a beam $I(d)$ traveling with initial energy I_0 through a material with thickness d:

$$I(d) = I_0 \exp(-\mu d). \tag{1.24}$$

Material	δ	β	α_c
Si	$6.500{\cdot}10^{-6}$	$1.273{\cdot}10^{-7}$	0.206°
Glass	$6.903{\cdot}10^{-6}$	$1.025{\cdot}10^{-7}$	0.213°
Polystyrene (1.050 g/cm^3)	$3.104{\cdot}10^{-6}$	$3.570{\cdot}10^{-9}$	0.143°
Polystyrene (0.778 g/cm^3)	$2.300{\cdot}10^{-6}$	$2.645{\cdot}10^{-9}$	0.123°

Table 1.1: Values for δ, β and the critical angle α_c for different materials at $\lambda = 1.43$ Å ($\mathcal{E} = 8.7\,\text{keV}$). The values have been calculated with the free software tool XOP2.3 [107,108]. For Polystyrene, 1.050 g/cm^3 corresponds to the density of a colloid and 0.778 g/cm^3 is the average density for colloids in a close-packing.

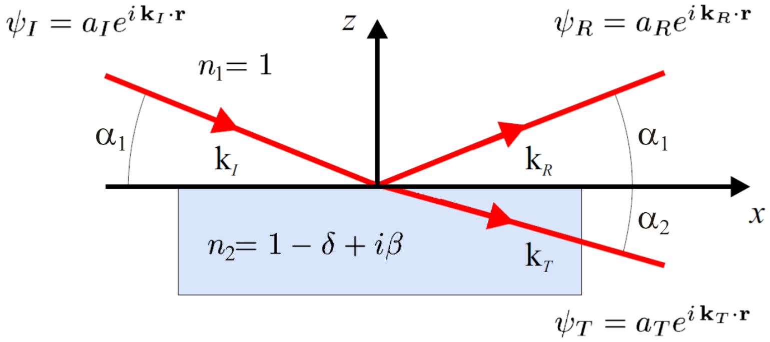

Figure 1.11: Incoming ψ_I, reflected ψ_R and transmitted ψ_T wave at an interface between vacuum (air) and material. From the continuity condition for the waves at the boundary, Snell's law and the Fresnel equations can be derived. Figure according to [104].

Now the situation of a plane wave at an interface between two media is elucidated. Without loss of generality, we choose medium one to be vaccum (air) and medium two a solid as indicated in figure 1.11. The incident wave has a wavevector $\mathbf{k}_I$ and an amplitude a_I and hits the interface at an angle α_1. $\mathbf{k}_R$, $\mathbf{k}_T$ and a_R, a_T are the wavevectors and amplitudes of the reflected and transmitted waves respectively. α_2 denotes the angle between the interface and $\mathbf{k}_T$. In vacuum, k equals $|\mathbf{k}_I|$ and in the material $n_2 k = |\mathbf{k}_R| = |\mathbf{k}_T|$. The wave field and its derivative have to be continuous at the interface. This prerequisite imposes relations between the amplitudes of the three waves. Combining these relations one results with Snell's law

$$\cos\alpha_2 = \frac{n_1}{n_2}\cos\alpha_1. \tag{1.25}$$

As $n_2 < n_1$, it immediately follows that below a certain incident angle, called the critical angle α_c, one observes total external reflection. We can relate δ to the critical angle α_c, by replacing $\alpha_1 = \alpha_c$ and $\alpha_2 = 0$, expanding the cosine and using equation (1.22) thereby neglecting the imaginary part:

$$\alpha_c = \sqrt{2\delta}. \tag{1.26}$$

The Fresnel equations follow as a further consequence of the boundary conditions at the interface. They quantify the amplitude reflectivity r and transmittivity t at the interface.

$$r := \frac{a_R}{a_I} = \frac{n_1 \sin\alpha_1 - n_2 \sin\alpha_2}{n_1 \sin\alpha_1 + n_2 \sin\alpha_2} = \frac{k_z - k_z'}{k_z + k_z'} \tag{1.27}$$

$$t := \frac{a_T}{a_I} = \frac{2n_1 \sin\alpha_1}{n_1 \sin\alpha_1 + n_2 \sin\alpha_2} = \frac{2k_z}{k_z + k_z'} = 1 + r. \tag{1.28}$$

n_1 and n_2 depict the refractive index in the medium above and below the interface. The two expressions for the Fresnel equations are equivalent because

$$n_1 k \sin\alpha_1 = k_z \qquad \text{and} \qquad n_2 k \sin\alpha_2 = k_z' \tag{1.29}$$

are the wavevectors perpendicular to the interface in vaccum (air) and the material, respectively. The reflected (transmitted) *intensity* of a wave is denoted by the capital letter R (T) and is the absolute square of r (t). Figure 1.12 (a) shows examples for R and T with different ratios between δ and β.

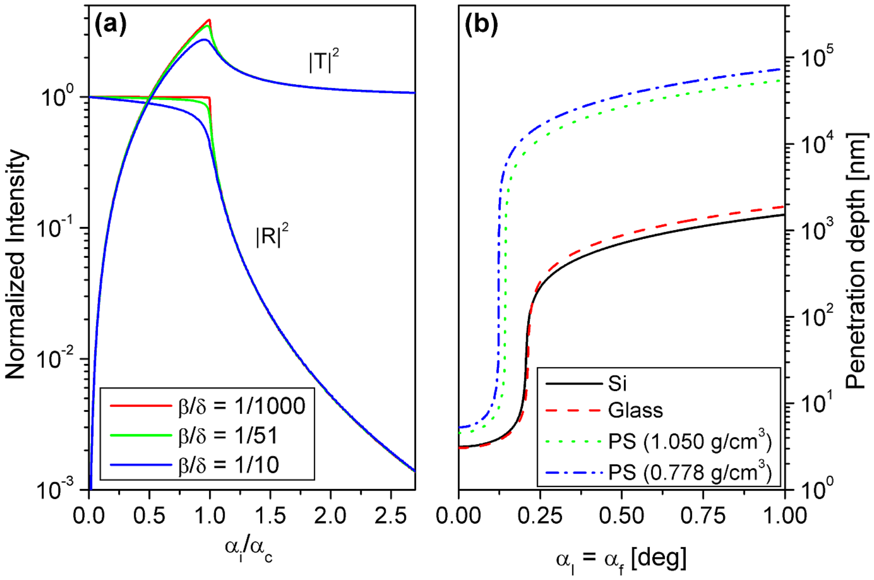

Figure 1.12: (a) Reflectivity $R = |r|^2$ and transmission $T = |t|^2$ of the intensity for different combinations of δ and β. (b) Penetration depth calculated from the values in Table 1.1.

By expanding equation (1.25) using the small angle approximation in combination with equation (1.22) and (1.26) one results with

$$\begin{aligned} \alpha_1^2 &= \alpha_2^2 + 2\delta - 2i\beta && (1.30)\\ &= \alpha_2^2 + \alpha_c^2 - 2i\beta. && (1.31) \end{aligned}$$

It can be seen that α_2 has an imaginary part and the transmitted wave is dampened with increasing depth into the material as

$$a_T\,\mathrm{e}^{ink\sin\alpha_2\cdot z} \backsimeq a_T\,\mathrm{e}^{ik\alpha_2\cdot z} = a_T\,\mathrm{e}^{ik\,\mathrm{Re}(\alpha_2)\cdot z}\,\mathrm{e}^{-k\,\mathrm{Im}(\alpha_2)\cdot z}\,. \tag{1.32}$$

It follows that the *intensity* diminishes with an 1/e *penetration depth* Λ given by

$$\Lambda = \frac{1}{2\,\mathrm{Im}(k_z')} \backsimeq \frac{1}{2k\,\mathrm{Im}(\alpha_2)}. \tag{1.33}$$

As long as the incoming angle α_1 is larger than the critical angle α_c, Λ is determined by the imaginary part of the index of refraction β. Only as $\alpha_1 \leqslant \alpha_c$ the imaginary part starts to increase rapidly as can be seen by transforming equation (1.31):

$$\alpha_2^2 = \underbrace{\left(\alpha_1^2 - \alpha_c^2\right)}_{<0} + i\beta. \tag{1.34}$$

Below the critical angle, the wave field in the material exists just as an *evanescent wave*. The damping of the evanescent wave increases for $\alpha_1 \to 0$ as Λ decreases. Examples of penetration depths at different angles can be found in figure 1.12 (b).

1.2.2 Selected X-ray Scattering Techniques

Energy Dispersive X-Ray Reflection

In a common X-ray reflection measurement (XRR), one measures the reflected intensity of a monochromatic X-ray beam as a function of the angle α between sample surface and beam, i.e., $\alpha_i = \alpha_f = \alpha$ and $\theta_f = 0$. The reflected intensity can equally be expressed as a function of the momentum transfer $\mathbf{Q}$. Since, in turn, the momentum transfer is both a function of the incident angle and the wavelength (see equation (1.21)), the same reflectivity curves can be obtained by fixing α and measuring the intensity as a function of the wavelength or equivalently the energy of the X-ray beam. This approach is denoted as an energy dispersive X-ray reflection (ED-XRR) measurement in contrast to an angular dispersive X-ray reflection or simply XRR experiment.

The experimental setup of an ED-XRR experiment and an according construction in reciprocal space can be seen in figure 1.13. ED-XRR uses a polychromatic X-ray beam (also referred to as a 'white beam') together with an energy sensitive point detector. By tuning the incident and exit angle, one defines the probed range in reciprocal space.

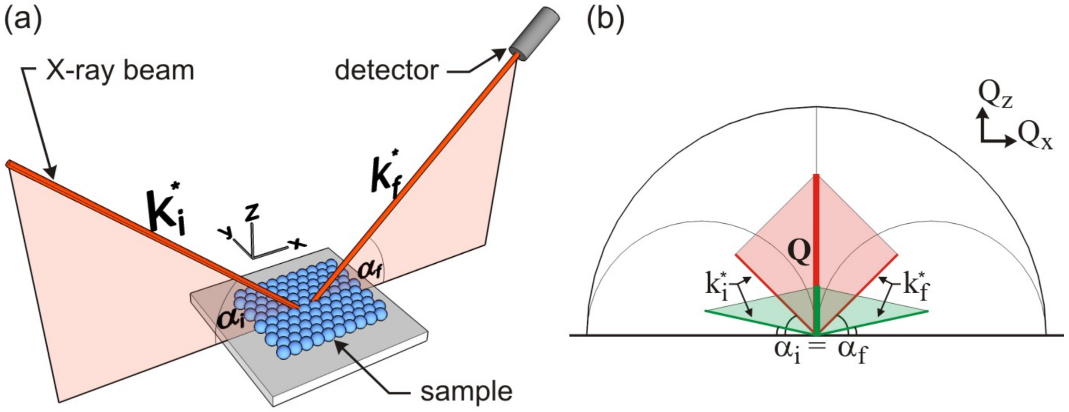

Figure 1.13: (a) Schematic setup of an energy dispersive X-ray reflection experiment. The energy dispersive detector is positioned in or very close to the reflected beam. (b) Extended Ewald construction for two experimental setups with different incident angles α. From the construction of the scattering vector $\mathbf{Q}$, one can see that one gains information in Q_z direction, i.e., perpendicular to the surface. The probed $\mathbf{Q}$-range in reciprocal space depends strongly on the chosen reflection angle α. It is small for grazing angles (green) and increases for larger angles (red). The wavevectors $\mathbf{k}$ have a *-superscript to remind that ED-XRR measurements are not performed with a unique but a continuous distribution of wavevectors meeting all the equivalent α condition but with different length. Angles and distances are strongly distorted with respect to a real experiment for the sake of clarity.

From the extended Ewald construction, it becomes clear, that an ED-XRR experiment gives information along Q_z - the direction perpendicular to the surface. Accordingly, the technique is used for the investigation of layered systems.

The main advantage of ED-XRR compared to XRR is the fixed geometric setup. Neither sample nor detector have to be moved in order to measure reflectivity curves. The acquisition time for a reflectivity curve is only limited by the time necessary to accumulate a satisfactory statistic. ED-XRR is therefore ideal for real time and *in situ* studies. Drawbacks of the technique are the resolution that is limited by the ability of the detector to resolve different photon energies, the limitation of the accessible wavevector transfers by the available energy spectrum and the necessary normalization of the measured intensity with the intensity distribution of the incident energy spectrum.

According to the advantages of the technique, ED-XRR has mostly been exploited to follow alterations in thin films *in situ* and real time. For example, effects of annealing [109, 110], the growth of oxidation layers [111], thermal expansion of polymer films [112] and the growth of films during organic molecular beam deposition [113] have been investigated. The recent development of a two dimensional energy dispersive detector [114] could in future greatly enhance the use of the technique. Combining this detector with a white beam allows to measure a three-dimensional data set in reciprocal space with a single exposure.

Grazing Incidence Small Angle X-Ray Scattering

Grazing Incidence Small Angle X-ray Scattering (GISAXS) is a versatile tool to probe electron density correlations and the shape and size of objects located at the surface, in buried interfaces or in thin films. A schematic setup of a GISAXS experiment and an according construction in reciprocal space are displayed in figure 1.14. The sample is hit by a monochromatic X-ray beam under a grazing angle α_i. Typically, α_i is between half and a few times the angle of total external reflection α_c of the sample. In a GISAXS experiment, intensities are not only measured in the specular direction but also at off-specular positions, i.e., with $\theta_f > 0$. This is usually done by an area detector.

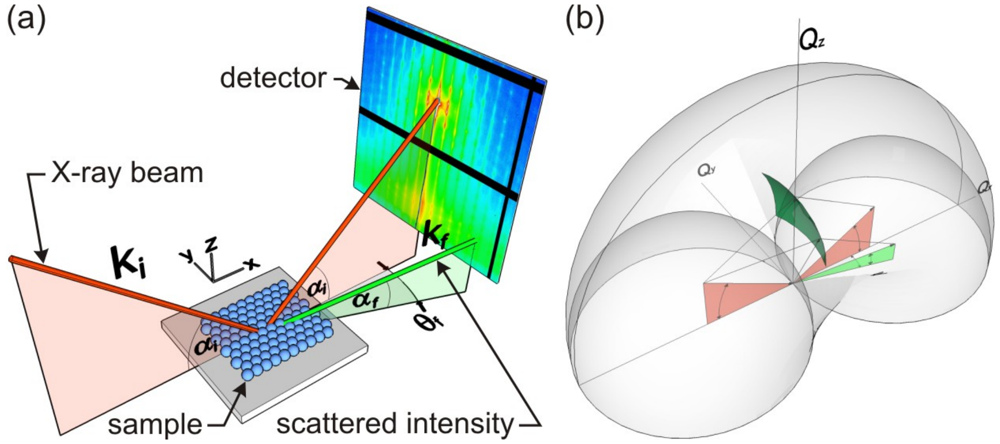

Figure 1.14: (a) Schematic setup of a GISAXS experiment. A monochromatic beam with wavevector $\mathbf{k}_i$ hits the sample with an incident angle α_i ranging between about half and a few times the angle of total external reflection of the sample. The scattered intensity, $\mathbf{k}_f$, is typically measured with a two dimensional pixel detector equally placed at a shallow angle. The distance between sample and detector varies depending on the experimental facilities and the required resolution. (b) Three-dimensional display of the extended Ewald construction according to [105, 106]. The green area corresponds to the scattering vectors $\mathbf{Q}$ probed by the detector. For two cases corresponding approximately to the cases in figure (a), the scattering vectors are explicitly constructed. It can be seen that information in both Q_z and Q_y direction can be accessed. The range of the Q_x component is typically two orders of magnitude smaller than the range along Q_y and can be neglected for small scattering angles. (For the sake of clarity, angles and distances are strongly distorted with respect to a real experiment.)

From the extended Ewald construction in figure 1.14, it can be seen that GISAXS not only probes samples perpendicular to the sample surface (along Q_z) but also parallel to the surface, i.e., in the Q_x, Q_y plane. The range of the Q_x component is thereby typically two orders of magnitude smaller than the range along Q_y and can be neglected for small scattering angles. The technique provides accordingly information on the electron density modulation on the sample in the directions parallel and perpendicular to the surface. When positioned further away from the sample, the detector collects information with an increased resolution but from a smaller slice in reciprocal space. Therefore, one probes structures with large periodicities in real space (possessing consequently small periodicities in reciprocal space) generally at large sample-detector distances.

GISAXS has originally been proposed for the investigation of growth mechanisms in thin atomic films [115] and has since then been widely used in this area [116–121]. More recently, polymeric thin films have shifted into the focus of GISAXS experimentalists and a large variety of different structures has been revealed [122–130]. Polymeric and silicon surface relief gratings have as well been characterized by GISAXS in two works [131,132]. The effortless accessibility to the nanometer scale led to different studies that probed the arrangement of self-assembled nanoparticles on substrates [133–138] and in a three-dimensional arrangement of nanoparticle-crystallites [139–141]. Additionally, the growth of nanoparticles and nanostructures has been followed *in situ* [120, 126, 134, 137, 138]. Length scales have been extended further in a work investigating the two dimensional arrangement of polymethylmethacrylat (PMMA) beads with a diameter of 350 nm [142].

CHAPTER 2

Synopsis and Motivation

Colloidal crystals have been discussed with respect to their application as photonic materials. This sort of material and in particular materials with a complete PBG have a huge potential for a wide variety of applications ranging from novel display technology to the realization of all-optical computers. The quality of the ordered colloidal assemblies is the main challenge in using them as a starting point in the fabrication of photonic materials. Every defect disrupting the perfect periodicity of the material will ultimately lead to the loss of the exciting material properties. Therefore, adequate fabrication and characterization methods are imperative.

Various techniques for the self-assembly of colloidal crystals have been presented in the last two decades. In the process, convective self-assembly has been established as a bottom-up approach that yields uniform assemblies over large areas while employing comparatively simple setups. This technique is able to provide close-packed colloids arranged in a fcc lattice with stacking faults. The number of layers of the final assembly can be tailored by the initial particle concentration. It has been shown that in combination with topologically structured templates, the long-range order of the opals could be increased and their crystallographic symmetry altered.

Currently, the quality of the three-dimensional colloidal crystals is assessed by different techniques. The surfaces are efficiently inspected by SEM and AFM. However, the internal arrangement of the particles is of paramount importance having in mind materials with a complete PBG. By breaking crystals apart, SEM can provide insight in the stacking of particles on the side wall of the crack. However, the determination of the exact crystalline structure remains problematic. The internal order has been clarified by confocal microscopy. Colloidal beads with a fluorescent core arranged in a refractive index matched solvent are prerequisites for such investigations. Both approaches provide information on a limited region only. Light spectroscopy, laser diffraction and SAXS can provide statistically averaged local and overall information by scanning the probing beam with different diameters over the sample. However, the beam hits the sample usually in the direction perpendicular to the substrate. Accordingly, no information about the stacking sequence of colloidal layers perpendicular to the substrate is obtained. In the case of visible light scattering, the strong interaction of light with the opal further complicates the evaluation due to multiple scattering interactions.

The current understanding of the processes that assemble the colloids are mainly based on the end-point examination of the resulting assemblies, and by *in situ* microscopy studies. In the case of convective self-assembly, a model has been proposed that describes the influence of the process parameters on the number of layers in the final assembly. However, the mechanism that leads to the specific three-dimensional arrangement of the particles has not been identified so far.

In summary, important open questions concerning colloidal crystals and convective self-assembly are:

- What is the exact stacking sequence of the close packed layers in a colloidal crystal fabricated by convective self-assembly?

- What are the detailed mechanisms leading to the three-dimensional arrangement of the colloidal particles in the case of convective self-assembly?

- What is the extent of order in self-assembled colloidal crystals?

X-ray scattering methods can contribute to solve these questions. The measured X-ray scattering intensity corresponds to the absolute square of the Fourier transform of the electron density distribution in the material. The technique can therefore be used to elucidate the crystalline structure of a material.

Selected scattering techniques have to be used to advance the knowledge about the posed problems. GISAXS and ED-XRR fulfill the requirements to supply non-destructive information on the microscopic structure of thin films. Both techniques provide information about the layer and surface structure. GISAXS additionally probes the lateral surface structure. The simple setup of both techniques facilitates *in situ* experiments. This allows direct probing of the self-assembly process.

While samples of colloidal multilayers are normally rather thin and consist of elements with a low scattering strength, a strong scattering signal can be obtained by taking advantage of the enhanced reflectivity close to the angle of total external reflection. The scattering signal is further enhanced by the large area of the sample that is illuminated. This purely geometrical fact arises from the projection of the beam diameter on the sample at grazing incident angles.

Specific Objectives of this Work

The specific objectives formulated at the onset of this work are listed below. They have been derived from the unsolved problems and limitations outlined in the previous chapter.

- Clarification of the potential of GISAXS with respect to the structural characterization of colloidal crystals: What parameters, important for photonic applications, i.e. crystalline structure, domain size and defect density, can be determined by GISAXS investigations.
- Fabrication of colloidal monolayers and multilayers by convective self-assembly on flat and topologically pre-structured substrates using polystyrene beads with diameters in the range between $\sim 1\,\mu$m down to $\sim 0.3\,\mu$m. The resulting colloidal mono- and multilayers are used as test objects for objective 1.
- *In situ* investigation of the self-assembly process by ED-XRR and GISAXS with the aims of (i) judging the suitability of the chosen techniques to monitor in real time the dynamics of colloidal crystal formation, and (ii) exploring these in situ techniques in terms of contributing to the mechanistic aspects of convective colloidal self-assembly.

CHAPTER 3

Theory of X-ray Scattering from Colloidal Crystals

3.1 Scattering from Real Colloidal Crystals

The scattering from a crystalline lattice as introduced in chapter 1.2.1 treats the case of a perfect and infinite crystal lattice. Although this model works well as a first approximation, it can not explain the detailed distribution of scattered intensity of a real crystal. In this chapter the scattering theory will be extended to account for different effects observed in a real crystal and in particular a colloidal crystal. The starting point of the following considerations is the scattering amplitude from a crystal as introduced in equation (1.11):

$$F_{crystal}(\mathbf{Q}) = -r_0 \underbrace{\sum_j f_j(\mathbf{Q})\,\mathrm{e}^{i\mathbf{Q}\cdot\mathbf{r}_j}}_{\text{unit cell structure factor}} \underbrace{\sum_m \mathrm{e}^{i\mathbf{Q}\cdot\mathbf{R}_m}}_{\text{lattice sum}} . \tag{1.11}$$

For the derivation of equation (1.11), it was implicitly assumed that all unit cells in the crystal are exactly identical. In a real crystal, this is not necessarily true. Scattering centers can be randomly deviated from their ideal position by a small distance and in the case of a colloidal crystal the form factor is different at every position due to the particle size distribution. In the following derivations, it is assumed without loss of generality that there is only one scattering center per unit cell. The scattering amplitude from a crystal with N scattering centers is then rewritten to

$$F_{crystal}(\mathbf{Q}) = -r_0 \sum_m^N f_m(\mathbf{Q})\,\mathrm{e}^{i\mathbf{Q}\cdot\mathbf{R}_m}. \tag{3.1}$$

Colloidal Form Factor

As was shown in the derivation of equation (1.9), the form factor of any particle corresponds to its Fourier transformed electron density. In the simpliest case, the electron distribution of a colloidal particle can be approximated by a homogeneous sphere resulting with a form factor

$$f_{Sph}(\mathbf{Q}, R, \Delta\eta) = \Delta\eta \cdot 3\frac{\sin(QR) - QR\cos(QR)}{(QR)^3} \tag{3.2}$$

where $Q = |\mathbf{Q}|$ and R corresponds to the radius of the sphere. $\Delta\eta$ is the scattering contrast with respect to the surrounding matrix. Colloidal particles with a different electron density in the shell than the core, as displayed in figure 3.1, can be viewed as a superposition of two particles:

$$f_{CsSph}(\mathbf{Q}, R, \Delta R, \Delta\eta_1, \Delta\eta_2) = f_{Sph}(\mathbf{Q}, R+\Delta R, \Delta\eta_2) - f_{Sph}(\mathbf{Q}, R, \Delta\eta_2 - \Delta\eta_1). \tag{3.3}$$

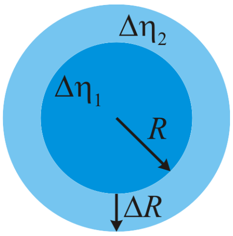

Figure 3.1: Spherical core-shell particle

Decoupling Approximation

The intensity measured in a scattering experiment corresponds to the modulus square of the scattering amplitude of a crystal $F_{crystal}(\mathbf{Q})$ as given in equation (3.1). In order to account for the finite coherence length of the beam, one takes an average over all possible microscopic states in the sample (see chapter 3.4) and results with

$$\begin{aligned} |F(\mathbf{Q})|^2 &= \left\langle \left| -r_0 \sum_m^N f_m(\mathbf{Q})\, \mathrm{e}^{i\mathbf{Q}\mathbf{R}_m} \right|^2 \right\rangle \\ &= r_0^2 \left\langle \sum_m^N \sum_n^N f_m f_n^* \, \mathrm{e}^{i\mathbf{Q}(\mathbf{R}_m - \mathbf{R}_n)} \right\rangle . \end{aligned} \tag{3.4}$$

By collecting the terms with $m = n$ in equation (3.4), one results in

$$|F(\mathbf{Q})|^2 = r_0^2 \left\langle \sum_m^N |f_m|^2 + r_0^2 \sum_{\substack{m,n \\ m \neq n}}^N f_m f_n^* \, \mathrm{e}^{i\mathbf{Q}(\mathbf{R}_m - \mathbf{R}_n)} \right\rangle . \tag{3.5}$$

A current hypothesis is to suppose that the kind of the scatterers and their position is not correlated. This assumption is also called *decoupling approximation*. It allows to extract the form factors from the second sum in equation (3.5) and one obtains

$$\begin{aligned}
|F(\mathbf{Q})|^2 &= r_0^2 \left\langle \sum_{m}^{N} |f_m|^2 \right\rangle + r_0^2 \left\langle \sum_{\substack{m,n \\ m\neq n}}^{N} f_m f_n^* \sum_{\substack{m,n \\ m\neq n}}^{N} \mathrm{e}^{i\mathbf{Q}(\mathbf{R}_m - \mathbf{R}_n)} \right\rangle \\
&= r_0^2 N \cdot \langle |f_m|^2 \rangle + r_0^2 \langle f_m \rangle \langle f_n^* \rangle \left\langle \sum_{\substack{m,n \\ m\neq n}}^{N} \mathrm{e}^{i\mathbf{Q}(\mathbf{R}_m - \mathbf{R}_n)} \right\rangle \\
&= r_0^2 N \cdot \langle |f_m|^2 \rangle + r_0^2 |\langle f_m \rangle|^2 \left\langle \sum_{\substack{m,n \\ m\neq n}}^{N} \mathrm{e}^{i\mathbf{Q}(\mathbf{R}_m - \mathbf{R}_n)} \right\rangle . \qquad (3.6)
\end{aligned}$$

Debye-Waller Factor

We assume now that the scattering centers are all slightly displaced with respect to the ideal crystalline lattice. In a conventional solid state crystal, such displacements arise through atomic vibrations. In a colloidal crystal, the particle polydispersity could trigger a similar random deviation of the spheres from the ideal lattice sites. The new particle positions $\mathbf{R}'_m$ can be written as $\mathbf{R}'_m = \mathbf{R}_m + \mathbf{u}_m$, a superposition of the ideal positions $\mathbf{R}_m$ with small deviation $\mathbf{u}_m$. Equation (3.6) is accordingly transformed to

$$|F(\mathbf{Q})|^2 = r_0^2 N \cdot \langle |f_m|^2 \rangle + r_0^2 |\langle f_m \rangle|^2 \left\langle \sum_{\substack{m,n \\ m\neq n}}^{N} \mathrm{e}^{i\mathbf{Q}(\mathbf{R}_m - \mathbf{R}_n)} \, \mathrm{e}^{i\mathbf{Q}(\mathbf{u}_m - \mathbf{u}_n)} \right\rangle . \qquad (3.7)$$

As in the case of the decoupling approximation, one assumes that the deviations $\mathbf{u}_m$ are not correlated to the exact position and one results with

$$|F(\mathbf{Q})|^2 = r_0^2 N \cdot \left\langle |f_m|^2 \right\rangle + r_0^2 \, |\langle f_m \rangle|^2 \left\langle \mathrm{e}^{i\mathbf{Q}(\mathbf{u}_m - \mathbf{u}_n)} \right\rangle_{m,n} \left\langle \sum_{\substack{m,n \\ m\neq n}}^{N} \mathrm{e}^{i\mathbf{Q}(\mathbf{R}_m - \mathbf{R}_n)} \right\rangle . \qquad (3.8)$$

If one assumes additionally that the deviations $\mathbf{u}_m$ follow a Gaussian distribution, one can simplify the average over the exponential function applying the Baker-Hausdorff theorem (see, e.g., [104], page 279)

$$\begin{aligned}
\left\langle \mathrm{e}^{i\mathbf{Q}(\mathbf{u}_m - \mathbf{u}_n)} \right\rangle_{m,n} &= \mathrm{e}^{-\frac{1}{2}\left\langle [\mathbf{Q}(\mathbf{u}_m - \mathbf{u}_n)]^2 \right\rangle_{m,n}} \\
&= \mathrm{e}^{-\frac{1}{2}\left\langle [\mathbf{Q}(\mathbf{u}_m)]^2 \right\rangle} \, \mathrm{e}^{-\frac{1}{2}\left\langle [\mathbf{Q}(\mathbf{u}_n)]^2 \right\rangle} \, \mathrm{e}^{-\frac{1}{2}\langle [\mathbf{Q}(\mathbf{u}_m)][\mathbf{Q}(\mathbf{u}_n)] \rangle_{m,n}} \\
&= \mathrm{e}^{-\left\langle [\mathbf{Q}(\mathbf{u}_m)]^2 \right\rangle} \, \mathrm{e}^{-\frac{1}{2}\langle [\mathbf{Q}(\mathbf{u}_m)][\mathbf{Q}(\mathbf{u}_n)] \rangle_{m,n}} . \qquad (3.9)
\end{aligned}$$

The first term on the right side of (3.9) is the so-called Debye-Waller factor, $exp(-W(\mathbf{Q}))$, where $W(\mathbf{Q}) = \mathbf{QBQ}$ and $\mathbf{B}$ is the tensor of the standard deviations of the particles

$$\mathbf{B} = \begin{pmatrix} \langle x^2 \rangle & \langle xy \rangle & \langle xz \rangle \\ \langle yx \rangle & \langle y^2 \rangle & \langle yz \rangle \\ \langle zx \rangle & \langle zy \rangle & \langle z^2 \rangle \end{pmatrix} .$$

The second exponential term on the right side of (3.9) is only substantially smaller than unity if the deviations $\mathbf{u}_m$, $\mathbf{u}_n$ are correlated. By assuming random deviations from the ideal particle positions, one can neglect its influence and equation (3.8) yields finally

$$\begin{aligned} |F(\mathbf{Q})|^2 &= r_0^2 N \cdot \left\langle |f_m|^2 \right\rangle + r_0^2 \left|\langle f_m \rangle\right|^2 e^{-W(\mathbf{Q})} \left\langle \sum_{\substack{m,n \\ m \neq n}}^{N} \mathrm{e}^{i\mathbf{Q}(\mathbf{R}_m - \mathbf{R}_n)} \right\rangle \\ &= \overbrace{r_0^2 N \cdot \left[\left\langle |f_m|^2 \right\rangle - \left|\langle f_m \rangle\right|^2 \mathrm{e}^{-W(\mathbf{Q})} \right]}^{I_{\mathrm{incoh}}} + \\ &\qquad \underbrace{r_0^2 \left|\langle f_m \rangle\right|^2 \mathrm{e}^{-W(\mathbf{Q})} \left\langle \overbrace{\left| \sum_{m}^{N} \mathrm{e}^{i\mathbf{Q}\mathbf{R}_m} \right|^2}^{S_L(\mathbf{Q})} \right\rangle}_{I_{coh}} \end{aligned} \tag{3.10}$$

where I_{incoh} and I_{coh} correspond to the incoherent and coherent[1] scattering contribution of the sample.

Effect of Finite Size

We focus now on the lattice structure factor $S_L(\mathbf{Q})$, i.e., the sum in the coherent scattering in equation (3.10). For an ideal crystalline lattice without boundaries, $S_L(\mathbf{Q})$ is different from zero only for sharply marked positions of the scattering vector $\mathbf{Q}$. Namely if $\mathbf{Q}$ is equal to a reciprocal lattice site $\mathbf{G}$. In a real crystal, the number of unit cells is limited which has consequences on the width of the Bragg peaks. Let N_u, N_v, N_w (with $N_u \cdot N_v \cdot N_w = N$) be the number of unit cells in the directions $\mathbf{a}_1$, $\mathbf{a}_2$, $\mathbf{a}_3$ of the crystalline lattice. Thus, by decomposing $\mathbf{Q}$ in the $\mathbf{a}_1^*$, $\mathbf{a}_2^*$, $\mathbf{a}_3^*$ basis ($\mathbf{Q} = h\mathbf{a}_1^* + k\mathbf{a}_2^* + l\mathbf{a}_3^*$ with h, k, l being *continuous variables*, i.e., h, k, $l \in \mathbb{R}$), the lattice structure reads

$$\begin{aligned} S_L(\mathbf{Q}) &= \left| \sum_{m}^{N} \mathrm{e}^{i\mathbf{Q}\mathbf{R}_m} \right|^2 \\ &= \left| \sum_{u=0}^{N_u - 1} \sum_{v=0}^{N_v - 1} \sum_{w=0}^{N_w - 1} e^{i(h\mathbf{a}_1^* + k\mathbf{a}_2^* + l\mathbf{a}_3^*) \cdot (u\mathbf{a}_1 + v\mathbf{a}_2 + w\mathbf{a}_3)} \right|^2 \end{aligned}$$

---

[1] In this context, the terms "incoherent" and "coherent" are not concerned with the quality of the beam (see cha. 3.4.1) but designate whether the scattering itself is coherent.

and as $\mathbf{a}_i^* \cdot \mathbf{a}_j = \delta_{i,j}$, with $\delta_{i,j}$ being the Kronecker delta,

$$\begin{aligned}
&= \left| \sum_{u=0}^{N_u-1} e^{i2\pi\cdot hu} \right|^2 \cdot \left| \sum_{v=0}^{N_v-1} e^{i2\pi\cdot kv} \right|^2 \cdot \left| \sum_{w=0}^{N_w-1} e^{i2\pi\cdot lw} \right|^2 \\
&= \left| \frac{\sin(\pi h N_u)}{\sin(\pi h)} \right|^2 \cdot \left| \frac{\sin(\pi k N_v)}{\sin(\pi k)} \right|^2 \cdot \left| \frac{\sin(\pi l N_w)}{\sin(\pi l)} \right|^2 . \qquad (3.11)
\end{aligned}$$

For the limits $N_i \to \infty$, one results with very sharp Bragg peaks at the positions $\mathbf{Q} = \mathbf{G}$, i.e., whenever h, k, $l \in \mathbb{N}$. However, in the case where the number of unit cells starts to decrease towards one, i.e., $N_i \to 1$, the width of the peaks starts to increase considerably until $N_i = 1$ where one is left with a single scatterer and the structure factor $S_L(\mathbf{Q})$ is equal to unity for all h, k, l.

Effect of Decreasing Correlation

Due to various kinds of defects, the correlation between two unit cells in the crystal starts to decrease with increasing distance. This is accounted for by the introduction of a correlation function $\mathcal{C}$ according to

$$S_L(\mathbf{Q}) = \sum_{m,n}^{N} \left[e^{i\mathbf{Q}(\mathbf{R}_m - \mathbf{R}_n)} \cdot \mathcal{C}(\mathbf{R}_m - \mathbf{R}_n) \right] \qquad (3.12)$$

with $\mathcal{C}(\mathbf{R}_m - \mathbf{R}_n) \to 0$ as $|\mathbf{R}_m - \mathbf{R}_n| \to \infty$. Equation (3.12) can be rewritten in the following way

$$\begin{aligned}
S_L(\mathbf{Q}) &= \sum_{\mathbf{R}_d} \left[e^{i\mathbf{Q}\mathbf{R}_d} \cdot \mathcal{C}(\mathbf{R}_d) \right] \qquad \text{with} \quad \mathbf{R}_d = \mathbf{R}_m - \mathbf{R}_n \\
&= \sum_{\mathbf{R}_d} \int \delta(\mathbf{R} - \mathbf{R}_d) \cdot \mathcal{C}(\mathbf{R}) e^{i\mathbf{Q}\mathbf{R}} \, \mathrm{d}\mathbf{R} \\
&= \sum_{\mathbf{R}_d} \int \delta(\mathbf{R} - \mathbf{R}_d) e^{i\mathbf{Q}\mathbf{R}} \, \mathrm{d}\mathbf{R} \otimes \int \mathcal{C}(\mathbf{R}) e^{i\mathbf{Q}\mathbf{R}} \, \mathrm{d}\mathbf{R} \\
&= \sum_{m,n}^{N} \left[e^{i\mathbf{Q}(\mathbf{R}_m - \mathbf{R}_n)} \otimes \mathrm{FT}\left\{ \mathcal{C}(\mathbf{R}_m - \mathbf{R}_n) \right\}(\mathbf{Q}) \right] \qquad (3.13)
\end{aligned}$$

where $\otimes$ denotes a convolution and FT$\{\ldots\}$ the Fourier transform. It follows that one can express a decreasing correlation between the lattice sites by a convolution of the structure factor with the Fourier transformed correlation function. This allows then to express the intensity in reciprocal space according to

$$S_L(\mathbf{Q}) = \sum_{h,k,l} \mathcal{S}(\mathbf{Q} - h\mathbf{a}_1^* - k\mathbf{a}_2^* - l\mathbf{a}_3^*) \qquad (3.14)$$

with $\mathcal{S}$ to be any appropriate Fourier transformed correlation function.

3.2 Scattering from Disordered Multilayers

Until now the scattering theory was treated in a rather general way. This subchapter focuses specifically on the scattering from a stack of hexagonally close packed layers as they occur in colloidal multilayers. These multilayers are well ordered along the planes, however in the direction perpendicular to the planes, the stacking can be somewhat irregular. Some of the scattering theory for layered systems with disordered stacking has already been developed around 1950. An overview can be found in [143]. The following considerations follow closely the derivation given in reference [144].

Let the system consist of a total of N scatterers arranged in L identical layers that are stacked along the z direction. The particle coordinates $\mathbf{R}_m$ can then be written in the form

$$\mathbf{R}_m = \mathbf{R}_i + \mathbf{s}_p \tag{3.15}$$

where $\mathbf{R}_i$ denotes the origin of the layer in which the particle m happens to be and $\mathbf{s}_p$ is a two-dimensional vector that indicates the location of the particle in the i-th layer. The index p goes over all particles $N_L = N/L$ in a layer. Using equation (3.15), one can split the structure factor of the multilayer in the following way

$$S_{ML}(\mathbf{Q}) = \frac{1}{L}\left\langle|\mathcal{L}(\mathbf{Q})|^2\right\rangle\left\langle\sum_{i,j=1}^{L} \mathrm{e}^{i\mathbf{Q}(\mathbf{R}_i-\mathbf{R}_j)}\right\rangle \quad \text{with} \quad \mathcal{L}(\mathbf{Q}) = \frac{1}{\sqrt{N_L}}\sum_{p}^{N_L} \mathrm{e}^{i\mathbf{Q}\mathbf{s}_p}. \tag{3.16}$$

In order to make the multilayer structure factor independent of the number of scatterers in the system, a normalization factor, $1/N = 1/(N_L \cdot L)$, has been introduced. The function $|\mathcal{L}(\mathbf{Q})|^2$ is the scattering intensity from a single layer. It is accordingly called the *layer form factor*. Equation (3.16) can be understood as the product of the layer form factor times a phase term that accounts for the phase differences between the different layers. It is important to realize that the phase term only modifies the intensity of the truncation rods predetermined by the layer form factor. It can not create peaks at positions where $|\mathcal{L}(\mathbf{Q})|^2$ is zero. One defines

$$\mathbf{R}_i - \mathbf{R}_j =: \Delta\mathbf{R}_\ell \quad \text{with} \quad i - j =: \ell. \tag{3.17}$$

Possible values for ℓ are in the range $-L+1 \leqslant \ell \leqslant L-1$ as both indices i, j, run from 1 to L. The index ℓ is $(L-|\ell|)$-fold degenerate. Inserting equation (3.17) in equation (3.16) one results with

$$S_{ML}(\mathbf{Q}) = \left\langle|\mathcal{L}(\mathbf{Q})|^2\right\rangle \sum_{\ell=-L+1}^{L-1}\left(1-\frac{|\ell|}{L}\right)\langle \mathrm{e}^{i\mathbf{Q}\cdot\Delta\mathbf{R}_\ell}\rangle. \tag{3.18}$$

For a given stacking sequence, the structure factor of the multilayer is therefore given by a weighted sum of the averaged phase factors of all the layers with respect to an arbitrary reference layer. By assuming stochastic stacking, the correlations for increasing separation will decrease rapidly, i.e., for $|\ell| \gg 1$ the averaged phase factors will be negligible. Under this condition, the equation (3.18) can be further simplified to yield

$$S_{ML}(\mathbf{Q}) = \left\langle |\mathcal{L}(\mathbf{Q})|^2 \right\rangle \sum_{\ell=-L+1}^{L-1} \langle \mathrm{e}^{i\mathbf{Q}\cdot\Delta\mathbf{R}_\ell} \rangle. \tag{3.19}$$

In order to calculate the average phase factor, we assume that all layers scatter identically and that there exist only two possible vectors, $\mathbf{r}_1$ and $\mathbf{r}_2$, describing the displacement between neighboring layers. Additionally, we introduce the *stacking probability* a that denotes the likelihood of having two consecutive $\mathbf{r}_1$ translations (or $\mathbf{r}_2$ translations) in the stacking sequence. By use of a matrix transfer method outlined in the appendix on page 122, one results then with the static structure factor

$$S_{ML}(\mathbf{Q}) = \left\langle |\mathcal{L}(\mathbf{Q})|^2 \right\rangle \cdot \frac{\mathfrak{A}}{\mathfrak{B}} \tag{3.20}$$

where

$$\begin{aligned} \mathfrak{A} &= a(1-a)\big[1 - \cos(\mathbf{Q}\cdot[\mathbf{r}_1 - \mathbf{r}_2])\big] \\ \mathfrak{B} &= 1 - 2a + 3a^2 - 2a^2\big[\cos(\mathbf{Q}\cdot\mathbf{r}_1) + \cos(\mathbf{Q}\cdot\mathbf{r}_2)\big] \\ &\qquad + a^2\cos(\mathbf{Q}\cdot[\mathbf{r}_1 - \mathbf{r}_2]) + (2a-1)\cos(\mathbf{Q}\cdot[\mathbf{r}_1 + \mathbf{r}_2]). \end{aligned}$$

Whenever

$$\mathrm{e}^{i\mathbf{Q}\cdot\mathbf{r}_1} = \mathrm{e}^{i\mathbf{Q}\cdot\mathbf{r}_2}, \tag{3.21}$$

equation (3.18) can be remarkably simplified as outlined in the appendix on page 122 and one results with

$$S_{ML}(\mathbf{Q}) = \left\langle |\mathcal{L}(\mathbf{Q})|^2 \frac{1}{L} \left| \frac{\sin(\pi l L)}{\sin(\pi l)} \right|^2 \right\rangle, \tag{3.22}$$

the case of Bragg scattering with peaks for $l = 1, 2, \ldots$ from a finite crystal as derived in equation (3.11).

The assumptions made for the derivation of equation (3.20) are fulfilled for hexagonally close packed layers stacked in a supposedly arbitrary mode on top of each other. As can be seen from figure 3.2, there are two vectors that describe the displacement between consecutive layers. For the case $a = 0$, i.e., the crystal is built by a sequence of alternating translations, one results with a perfect hcp crystal. For $a = 1$ consecutive layers are always added with the same translation and one results with a fcc crystal. For the further derivation, a coordinate system as indicated in figure 3.3 is introduced. The x- and y-axes lie parallel to the hexagonal planes whereas the z-axis is set normal to them.

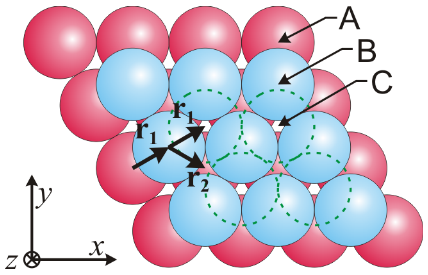

Figure 3.2: Red and blue illustrate two consecutive close packed layers stacked on top of each other. Their position is denoted by the letters **A** and **B**. One has two possibilities to add a further layer on top: either the particles are positioned again at **A** or they are placed at the positions **C** marked with the dotted circles in green. The first case emerges by a sequence of two different displacements. When further layers are added in the same manner, the lattice evolves ultimately in a hcp crystal with $a = 0$. (A definition of parameter a is given in the text.) The second case can be obtained by a sequence of equal displacements. If continued accordingly, the final structure has a fcc symmetry with $a = 1$.

The unit vectors along the axes are denoted with $\mathbf{x}$, $\mathbf{y}$, $\mathbf{z}$. A basis for the stacked hcp layers is then given by

$$\mathbf{a}_1 = d\mathbf{x}, \quad \mathbf{a}_2 = \frac{d}{2}\left(\mathbf{x} + \sqrt{3}\mathbf{y}\right), \quad \mathbf{a}_3 = d\sqrt{\frac{2}{3}}\mathbf{z} \tag{3.23}$$

where d denotes the distance between the scattering centers in the plane. In the case of an arrangement of hard spheres as in a colloidal crystal, d is equal to the diameter of these spheres. By naming the unit vectors in reciprocal space $\mathbf{x}^*$, $\mathbf{y}^*$, $\mathbf{z}^*$, one can calculate the vectors that span the reciprocal lattice according to the relation (1.14)

$$\mathbf{a}_1^* = \frac{2\pi}{d}\left(\mathbf{x}^* - \sqrt{\frac{1}{3}}\mathbf{y}^*\right), \quad \mathbf{a}_2^* = \frac{2\pi}{d}\sqrt{\frac{4}{3}}\mathbf{y}^*, \quad \mathbf{a}_3^* = \frac{2\pi}{d}\sqrt{\frac{3}{2}}\mathbf{z}^*. \tag{3.24}$$

The location of the peaks defined by the layer form factor can be constructed by a linear combination of $\mathbf{a}_1^*$ and $\mathbf{a}_2^*$:

$$\mathbf{G} = h\mathbf{a}_1^* + k\mathbf{a}_2^* \quad \text{with} \quad h, k \in \mathbb{N} \tag{3.25}$$

as sketched in figure 3.3. In order to calculate $S_{ML}(\mathbf{Q})$, the two translation vectors, $\mathbf{r}_1$ and $\mathbf{r}_2$, indicated in figures 3.2 and 3.3 have to be specified. From the geometry follows

$$\mathbf{r}_1 = d\left(\frac{1}{2}\mathbf{x} + \frac{1}{2\sqrt{3}}\mathbf{y} + \sqrt{\frac{2}{3}}\mathbf{z}\right) \quad \text{and} \quad \mathbf{r}_2 = d\left(\frac{1}{2}\mathbf{x} + \frac{1}{2\sqrt{3}}\mathbf{y} - \sqrt{\frac{2}{3}}\mathbf{z}\right) \tag{3.26}$$

and with the scattering vector $\mathbf{Q}$ expressed as a linear combination of the reciprocal lattice vectors $\mathbf{Q} = h\mathbf{a}_1^* + k\mathbf{a}_2^* + l\mathbf{a}_3^*$, equation (3.20) results in

$$S_{ML}(\mathbf{Q}) = \left\langle |\mathcal{L}(\mathbf{Q})|^2 \right\rangle \cdot \frac{\mathfrak{A}'}{\mathfrak{B}'} \tag{3.27}$$

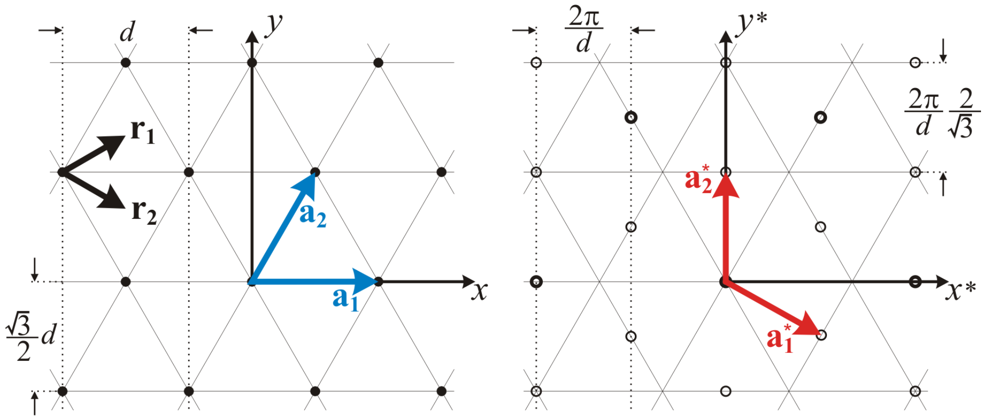

Figure 3.3: Real (*left*) and reciprocal (*right*) space representation of a two-dimensional hcp plane. The position of the scattering centers in real space are marked with black dots. The open circles in reciprocal space are the lattice sites, i.e., the location of the peaks of the layer form factor. The bold circles denote thereby the locations where the "Bragg condition" (see equation (3.28)) is fulfilled and the scattering signal is independent of the stacking probability a. All other reciprocal lattice sites are under the influence of the stacking sequence of the hexagonal layers according to equation (3.27). The lines in both graphs illustrate the crystal lattice planes. The two graphs are differently scaled.

where

$$\begin{aligned}\mathfrak{A}' &= a(1-a)\left[1-\cos\left(2\pi\,\frac{2k-h}{3}\right)\right]\\ \mathfrak{B}' &= 2(1-2a)\left[1-\cos^2(2\pi l)\right]+3a^2\\ &\qquad -4a^2(-1)^h\cos\left(2\pi\,\frac{2k-h}{6}\right)\cos(2\pi l)+a^2\cos\left(2\pi\,\frac{2k-h}{3}\right).\end{aligned}$$

By inserting the vectors $\mathbf{r}_1$ and $\mathbf{r}_2$ in (3.21), one finds that the 'Bragg condition' is fulfilled whenever

$$\left(\frac{h+k}{3}\right)\in\mathbb{N}\quad\text{and}\quad\left(\frac{2k-h}{3}\right)\in\mathbb{N}\quad\Longrightarrow\quad \mathrm{e}^{i\mathbf{Q}\cdot\mathbf{r}_1}=\mathrm{e}^{i\mathbf{Q}\cdot\mathbf{r}_2}=\mathrm{e}^{i2\pi l}\,. \tag{3.28}$$

At these positions, the structure factor $S_{ML}(\mathbf{Q})$ is independent of the stacking sequence of the hexagonal planes and Bragg peaks appear along $\mathbf{z}^*$ according to equation (3.22). For all other positions, the intensity along $\mathbf{z}^*$ ($\mathbf{a}_3^*$) depends strongly on the stacking probability a. In figure 3.4, the relative modulation of the scattered intensity along $\mathbf{z}^*$ ($\mathbf{a}_3^*$) was plotted for different values of the stacking probability a. As can be seen, peak positions, shapes and intensities strongly depend on a. A more extensive discussion can be found in [144].

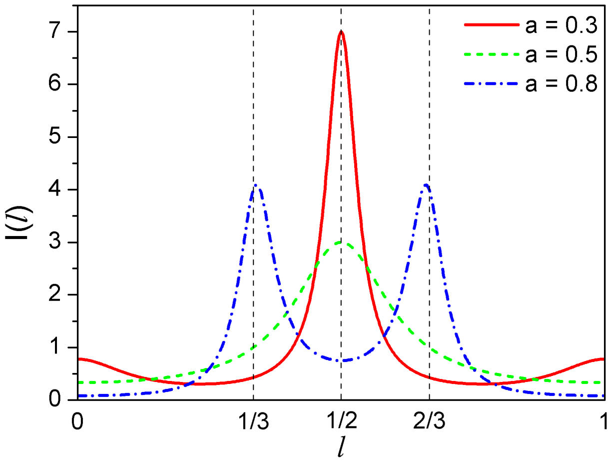

Figure 3.4: Relative dependence of scattering intensity along $\mathbf{z}^*$ ($\mathbf{a}_3^*$) on the stacking probability a. The three curves were calculated according to equation (3.27) for different stacking probabilities. $a = 0.5$ corresponds to a completely random stacking of the hexagonal layers.

3.3 Scattering at Grazing Angles: The Distorted Wave Born Approximation

In surface-sensitive experimental setups, i.e., when measurements are performed close to the angle of total external reflection, the X-ray beam starts to interact rather strong with the sample. The Born or *kinematical* approximation is then no longer valid. As the dynamic calculations are too complicated in many practical cases, one use a *semikinematical* approach to derive analytical descriptions of the scattered intensities. In this chapter, the *distorted wave Born approximation* (DWBA) is introduced and subsequently elaborated for the case of colloidal multilayers on top of a substrate[2].

Let $\mathbf{V}(\boldsymbol{r})$ be a scattering potential with two parts

$$\mathbf{V}(\boldsymbol{r}) = \mathbf{V}_A(\boldsymbol{r}) + \mathbf{V}_B(\boldsymbol{r}). \tag{3.29}$$

The first part describes the scattering from an ideal, non-disturbed system whereas the second corresponds to a small disturbance. In this context, small disturbance is meant in the sense that the potential scatters only weakly. The division is performed in such a way that the wave equation for the non-disturbed system

$$(\Delta + K^2)\boldsymbol{E}^{(A)}(\boldsymbol{r}) = \mathbf{V}_A \boldsymbol{E}^{(A)}(\boldsymbol{r}) \tag{3.30}$$

can be solved *exactly*. $|\boldsymbol{E}_i^{(A)}\rangle$ and $|\boldsymbol{E}_f^{(-A)}\rangle$ denote[3] two independent solutions of equation

---

[2] This chapter is based on [126, 145, 146].

[3] Here the Dirac notation is used.

(3.30). We choose the solution $|\boldsymbol{E}_i^{(A)}\rangle$ to correspond to the wave excited inside and outside the non-disturbed sample by the actual incident plane wave $|\boldsymbol{K}_i\rangle$. $|\boldsymbol{E}_f^{(-A)}\rangle$ is the solution of equation (3.30) for the wave $|\boldsymbol{K}_f\rangle$ that corresponds to the emitted wave. The solution $|\boldsymbol{E}_f^{(-A)}\rangle$ is therefore time inverted. This inversion is indicated by the minus sign in the superscript. The differential scattering cross section for the whole system can then be expressed as [145]

$$\left(\frac{\mathrm{d}\sigma}{\mathrm{d}\Omega}\right)_{DWBA} = \frac{1}{16\pi^2}\left|\langle\boldsymbol{E}_f^{(-A)}|\mathbf{V}_A|\boldsymbol{K}_i\rangle + \langle\boldsymbol{E}_f^{(-A)}|\mathbf{V}_B|\boldsymbol{E}_i^{(A)}\rangle\right|^2. \tag{3.31}$$

The first term on the right-hand side is the scattering from the undisturbed system. It usually results in a sharp reflection. The second term on the right hand side, is proportional to the matrix element of $\mathbf{V}_B$ expressed in the basis of the non-disturbed solutions $|\boldsymbol{E}_{i,f}^{(\pm A)}\rangle$. It represents the scattering of the exact solutions from the potential $\mathbf{V}_B$. This approximation is called *semikinematical approximation*, or *distorted wave Born approximation.*

3.3.1 Application of Distorted Wave Born Approximation on Colloidal Multilayers

In the case of a colloidal (multi-)layer with thickness d on top of a flat substrate, the model of a thin film on top of a substrate was chosen as the unperturbed system. We define the coordinate system with the z-axis perpendicular to the surface and $z = 0$ to be the upper boundary of the surface. The exact solution for a X-ray wave in the unperturbed system is then the following:

$$\langle\mathbf{r}|\boldsymbol{E}_i^{(A)}\rangle = \begin{cases} \Psi^1(\mathbf{r}) = \mathrm{e}^{i(k_x r_x + k_y r_y)} \cdot \left(\mathrm{e}^{ik_{z,1}z} + \mathcal{R}_1\,\mathrm{e}^{-ik_{z,1}z}\right) & z > 0 \\ \Psi^2(\mathbf{r}) = \mathrm{e}^{i(k_x r_x + k_y r_y)} \cdot \left(\mathcal{T}_2\,\mathrm{e}^{ik_{z,2}z} + \mathcal{R}_2\,\mathrm{e}^{-ik_{z,2}z}\right) & 0 > z > -d \\ \Psi^3(\mathbf{r}) = \mathrm{e}^{i(k_x r_x + k_y r_y)} \cdot \mathcal{T}_3\,\mathrm{e}^{ik_{z,2}(z+d)} & -d > z \end{cases} \tag{3.32}$$

where k_x, k_y are the parallel components of the wavevektor $\mathbf{k}$ of the incident wave. The perpendicular component $k_{z,i}$ can be calculated according to equation (1.29). $\mathcal{R}_i$, $\mathcal{T}_i$ are the amplitude reflectivity and transmission coefficients in the corresponding layer. They can be calculated using a transfer matrix formalism [145,147] or Parratt's recursive method [148]. The scattering potential $\mathbf{V}_B$ accounts for the scattering from the colloids. It is therefore unequal zero only for the colloidal layer, i.e., the second region in equation (3.32). Therefore, we just need to consider $\Psi^2(\mathbf{r})$ for the calculation of the scattering. $|\boldsymbol{E}_i^{(A)}\rangle$ and $|\boldsymbol{E}_f^{(A)}\rangle$ in the colloidal layer read then

$$\langle\mathbf{r}|\boldsymbol{E}_i^{(A)}\rangle = \Psi_i(\mathbf{r}) = \mathrm{e}^{i(k_{x,i}r_x + k_{y,i}r_y)} \cdot \left(\mathcal{T}_i\,\mathrm{e}^{ik_{z,i}z} + \mathcal{R}_i\,\mathrm{e}^{-ik_{z,i}z}\right) \tag{3.33}$$

$$\langle\mathbf{r}|\boldsymbol{E}_f^{(-A)}\rangle = \Psi_f(\mathbf{r}) = \mathrm{e}^{i(k^*_{x,i}r_x + k^*_{y,i}r_y)} \cdot \left(\mathcal{T}_f^*\,\mathrm{e}^{ik^*_{z,f}z} + \mathcal{R}_f^*\,\mathrm{e}^{-ik^*_{z,f}z}\right) \tag{3.34}$$

where the index for the second layer was omitted. The superscript $*$ indicates the complex conjugate for the time inversion.

Scattering Amplitude

The scattering amplitude $\Psi_{sc}(\mathbf{r})$ resulting from a small perturbation in the film, $\mathbf{V}_B(\mathbf{r}') = r_0\rho(\mathbf{r}')$ with $\rho(\mathbf{r}')$ the electron density, is then calculated according to

$$\Psi_{sc}(\mathbf{r}) = \frac{\mathrm{e}^{i\mathbf{k}_0\mathbf{r}}}{r}\int \Psi_f^*(\mathbf{r}')\mathbf{V}_B(\mathbf{r}')\Psi_i(\mathbf{r}')\,\mathrm{d}^3r'$$

and by replacing Ψ_i and Ψ_f according to (3.33) and (3.34), one results with

$$\begin{aligned} = \frac{\mathrm{e}^{i\mathbf{k}_0\mathbf{r}}}{r}\int \mathrm{e}^{-i(k_{x,f}-k_{x,i})r'_x}\,\mathrm{e}^{-i(k_{y,f}-k_{y,i})r'_y}\,\mathrm{d}r'_x\,\mathrm{d}r'_y\times& \\ \Big[\mathcal{T}_i\mathcal{T}_f\int_{-d}^{0}\mathbf{V}_B(\mathbf{r}')\,\mathrm{e}^{-i(k_{z,f}-k_{z,i})r'_z}\,\mathrm{d}r'_z+& \\ \mathcal{T}_i\mathcal{R}_f\int_{-d}^{0}\mathbf{V}_B(\mathbf{r}')\,\mathrm{e}^{-i(-k_{z,f}-k_{z,i})r'_z}\,\mathrm{d}r'_z+& \\ \mathcal{T}_i\mathcal{R}_f\int_{-d}^{0}\mathbf{V}_B(\mathbf{r}')\,\mathrm{e}^{-i(k_{z,f}+k_{z,i})r'_z}\,\mathrm{d}r'_z+& \\ \mathcal{T}_i\mathcal{R}_f\int_{-d}^{0}\mathbf{V}_B(\mathbf{r}')\,\mathrm{e}^{-i(-k_{z,f}+k_{z,i})r'_z}\,\mathrm{d}r'_z\Big].& \end{aligned} \tag{3.35}$$

By replacing

$$F(Q_x, Q_y, Q_{i,z}) = \int\int_{-d}^{0}\mathrm{e}^{-i(Q_x r'_x + Q_y r'_y)}\,\mathrm{e}^{-iQ_{i,z}r'_z}\,\mathbf{V}_B(\mathbf{r}')\,\mathrm{d}r'_z\,\mathrm{d}r'_x\,\mathrm{d}r'_y \tag{3.36}$$

and using the following notation for the scattering vector components

$$\begin{aligned} Q_x &= k_{x,f} - k_{x,i}, & Q_y &= k_{y,f} - k_{y,i}, \\ Q_{1,z} &= k_{z,f} - k_{z,i}, & Q_{2,z} &= -k_{z,f} - k_{z,i}, \\ Q_{3,z} &= k_{z,f} + k_{z,i}, & Q_{3,z} &= k_{z,f} + k_{z,i}, \end{aligned}$$

the scattering amplitude finally reads

$$\begin{aligned} \Psi_{sc}(\mathbf{r}) = -\frac{\mathrm{e}^{i\mathbf{k}_0\mathbf{r}}}{4\pi r}[&\mathcal{T}_i\mathcal{T}_f F(Q_x, Q_y, Q_{1,z}) + \mathcal{T}_i\mathcal{R}_f F(Q_x, Q_y, Q_{2,z}) \\ &+ \mathcal{R}_i\mathcal{T}_f F(Q_x, Q_y, Q_{3,z}) + \mathcal{R}_i\mathcal{R}_f F(Q_x, Q_y, Q_{4,z})]. \end{aligned} \tag{3.37}$$

Scattering Intensity

The intensity I scattered from the small perturbations in the thin film in the solid angle $\Delta\Omega r^2$ is equal to

$$I = r^2\Psi_{sc}(\mathbf{r})\cdot\Psi_{sc}^*(\mathbf{r}). \tag{3.38}$$

The scattering vectors $Q_{i,z}$ have a complex component, as they describe the wave in the colloidal layer. Consequently, the integration in equation (3.36) is not just a simple Fourier transformation of the scattering potential $\mathbf{V}_B$. By separating the imaginary part according to [126, 149], one arrives with the following expression for the intensity

$$\begin{aligned} I = & \frac{1}{16\pi^2}\frac{1-\mathrm{e}^{-2\,\mathrm{Im}(Q_z)\cdot d}}{2\,\mathrm{Im}(Q_z)}\times \\ & \Big|\mathcal{T}_i\mathcal{T}_f F(Q_x, Q_y, \mathrm{Re}(Q_{1,z})) + \mathcal{T}_i\mathcal{R}_f F(Q_x, Q_y, \mathrm{Re}(Q_{2,z})) + \\ & \quad \mathcal{R}_i\mathcal{T}_f F(Q_x, Q_y, \mathrm{Re}(Q_{3,z})) + \mathcal{R}_i\mathcal{R}_f F(Q_x, Q_y, \mathrm{Re}(Q_{4,z}))\Big|^2 \end{aligned} \tag{3.39}$$

where the $F(Q_x, Q_y, \mathrm{Re}(Q_{i,z}))$ correspond now to the Fourier transformed scattering potential $\mathbf{V}_B$ and can be calculated as introduced in section 3.1.

When calculating the absolute square of equation (3.39), one gets 16 terms. For weak scattering, the ensemble average of the *cross terms* normally either vanishes or is sufficiently small to be neglected [126]. The above equation can be further simplified:

$$\begin{aligned} I = & \frac{1}{16\pi^2}\frac{1-\mathrm{e}^{-2\,\mathrm{Im}(Q_z)\cdot d}}{2\,\mathrm{Im}(Q_z)}\times \\ & \Big[\big|\mathcal{T}_i\mathcal{T}_f F(Q_x, Q_y, \mathrm{Re}(Q_{1,z}))\big|^2 + \big|\mathcal{T}_i\mathcal{R}_f F(Q_x, Q_y, \mathrm{Re}(Q_{2,z}))\big|^2 + \\ & \big|\mathcal{R}_i\mathcal{T}_f F(Q_x, Q_y, \mathrm{Re}(Q_{3,z}))\big|^2 + \big|\mathcal{R}_i\mathcal{R}_f F(Q_x, Q_y, \mathrm{Re}(Q_{4,z}))\big|^2\Big]. \end{aligned} \tag{3.40}$$

The scattering consists then of a sum of the four *main terms*, visualized in figure 3.5, times a factor induced to account for the imaginary part of Q_z. Each summand is the absolute square of the scattering amplitude of the crystal, see equation (3.10), calculated with the appropriate scattering vector and weighted with the corresponding reflectivity and transmission coefficients.

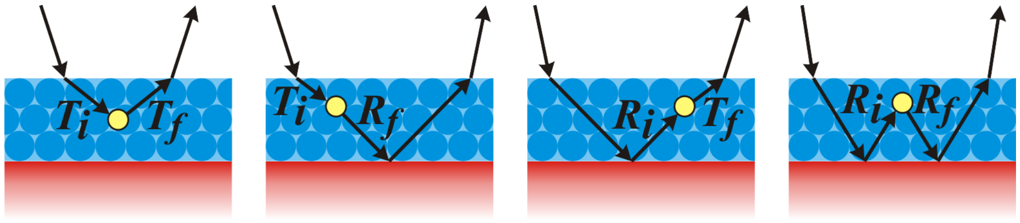

Figure 3.5: Schmenatic representation of the four terms used to calculate the intensity in (3.40). The yellow dot represents the scattering event in the colloidal layer.

3.4 Experimental Considerations

3.4.1 Beam Coherence

So far, an ideal monochromatic plane wave was assumed in the derivation of the scattering theory. However, a real beam has a finite wavelength spread and does not propagate in a perfectly well defined direction. In order to characterize these properties, one introduces the so-called *coherence length*. It is a measure of how far apart two points on a sample can be while the scattered waves from these points still interfere with each other. The coherence length has two components: The *transverse* or *lateral* coherence defines the property of the beam in its cross sectional plane whereas the the *longitudinal* or *temporal* coherence measures the degree of coherence along its propagation direction. The light source at a synchrotron beam line has an approximately Gaussian intensity distribution with σ_h and σ_v the corresponding standard deviations in the horizontal and vertical plane. The transverse coherence lengths are then given by

$$\xi_h = \frac{\lambda R}{2\pi\sigma_h} \qquad \text{in the horizontal and} \qquad \xi_v = \frac{\lambda R}{2\pi\sigma_v} \tag{3.41}$$

in the vertical direction [150] with λ the wavelength and R the distance between the source and the position where the coherence length is evaluated. The longitudinal coherence length is given by

$$\xi_l = \frac{1}{2}\frac{\lambda^2}{\Delta\lambda}. \tag{3.42}$$

It is inversely proportional to the spectral band with $\Delta\lambda/\lambda$ of the beam. The longitudinal and the two transversal coherence lengths define together a *coherence volume*.

In a X-ray scattering setup, the coherence lengths are typically much smaller than the beam size. The sample gets therefore probed by a multitude of coherence volumes and the measured intensity is averaged over the coherently sampled regions. If the probed volume is large enough to contain all possible configurations of the sample microstructure, the scattering function can be *averaged* over the statistical ensemble of all microstructure configurations (see, e.g., [145], p. 64).

3.4.2 Experimental Resolution

The parameters λ, α_i, α_f and θ_f that determine the scattering vector $\mathbf{Q}$ exhibit always a certain dispersion in an experiment. Accordingly, one defines a *resolution element* or *resolution volume* $V_{\Delta\mathbf{Q}}$ which corresponds to the volume in reciprocal space that is simultaneously illuminated by the incident beam and accepted by the detector under certain experimental conditions

$$V_{\Delta\mathbf{Q}} = \Delta Q_x \cdot \Delta Q_y \cdot \Delta Q_z. \tag{3.43}$$

By denoting the angular divergence with $\Delta\alpha_{i/f}$, neglecting the wavelength (wavevector) dispersion and using the small angle approximation, the resolution lengths ΔQ_x, ΔQ_y and ΔQ_z for GISAXS can be approximated by (see appendix on page 126)

$$\Delta Q_x = k\sqrt{\alpha_i^2\Delta\alpha_i^2 + \alpha_f^2\Delta\alpha_f^2 + \theta_i^2\Delta\theta_i^2 + \theta_f^2\Delta\theta_f^2} \tag{3.44}$$

$$\Delta Q_y = k\sqrt{\Delta\theta_i^2 + \Delta\theta_f^2} \tag{3.45}$$

$$\Delta Q_z = k\sqrt{\Delta\alpha_i^2 + \Delta\alpha_f^2}. \tag{3.46}$$

In an ED-XRR measurement, one is not interested in the resolution perpendicular to the scattering plane Q_y as one typically integrates the scattered intensity over Q_y in order to get better statistics. However, the energy resolution of the detector has to be considered. By replacing Q_i according to equation (C.1) in the small angle approximation, one results with

$$\Delta Q_x = k\sqrt{\alpha_i^2\Delta\alpha_i^2 + \alpha_f^2\Delta\alpha_f^2} \tag{3.47}$$

$$\Delta Q_z = k\sqrt{(\alpha_i + \alpha_f)^2\left(\frac{\Delta k}{k}\right)^2 + \Delta\alpha_i^2 + \Delta\alpha_f^2} \tag{3.48}$$

for the resolution in a ED-XRR experiment.

CHAPTER 4

Materials and Methods

4.1 Fabrication of Templates

The topologically structured substrates were fabricated with the azobenzene[1] containing polymer pDR1M. The abbreviation stands for polydisperse-red-1-methacrylate or rather poly(4-Nitrophenyl)[4-[[2-(methacryloyloxy)-ethyl]ethylamino]phenyl]diazene.

The formation of surface relief gratings in azobenzene-containing polymers has first been reported by [92, 151]. In this works, thin films of an azo polymer have been irradiated by the interference pattern of an argon laser beam (wavelength 514 nm). After the exposure, sinusoidal surface gratings with a spacing according to the periodicity of the interference pattern have been observed on the films. Although the grating formation involves a material transport over distances larger than the polymer chain length, the process takes place considerably below the glass transition temperature. Different models have been proposed to explain the grating formation. An overview and discussion can for example be found in [152, 153]. The key point of the grating formation is the azobenzene moiety of the polymer side chains. These subgroups undergo an isomerization process when irradiated by light with a wavelength close to the absorption maximum of the polymer at 450 nm. Thereby, they change from the straight *trans* ground state to the bent *cis* conformation upon absorbing light, see figure 4.1. The conformational change is completely reversible. The grating formation can be understood by assuming that the isomerization process induces a directed impulse on the polymer chain [153]. It arises because the *trans* and *cis* states occupy different spatial volumes [154] and the twist direction of the benzene group is defined by the electric field [155].

---

[1] Azobenezene denotes the chemical compound consisting of two phenyl rings linked by a nitrogen double bond. See also figure 4.1.

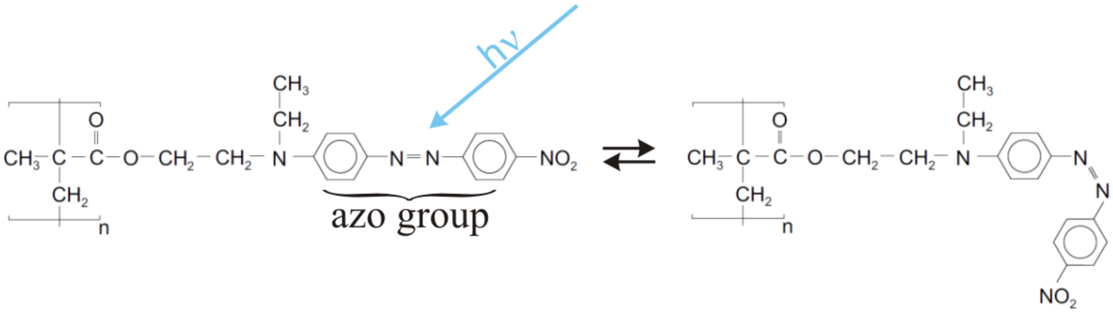

Figure 4.1: Different conformations of the azo group in the side chain of the pDR1M polymer. On the left side the straight *trans* form of the ground state that isomerizes by photon absorption to the bent *cis* form at the right side in the figure. The *cis* form occupies slightly more space.

Preparation of pDR1M Thin Films

As substrates, conventional microscopy slides (MARIENFELD or MENZEL) were cut in halves and cleaned by consecutive sonication in toluene and isopropanol for 10 minutes each and 60 minutes in acetone. All chemicals were used as provided from commercial suppliers. After rinsing the slides with deionized water (MILLIPORE), they were dried at ~70 °C.

pDR1M thin films have then been prepared by spin coating dissolved pDR1M on the cleaned glass slides. For that purpose, a 3 wt% solution of pDR1M (PDRAc27, IDM-TELTOW) in tetrahydrofurane was prepared. It was pressed through a filter (poresize $< 2\,\mu$m) to remove remaining polymer conglomerates before applying. The storage of the slides before coating and the spin coating process itself were done in an atmosphere with low relative humidity ($< 30\%$) to minimize the dewetting of the polymer solution on the microscopy slides. Until stated otherwise, the spin coater (DELTA6 RC, SUSS MICROTEC AG) was operated at 1000 rounds per minute until a solid film of pDR1M was formed. Resulting film thicknesses have typically been in the range of 200–300 nm. Remaining solvent in the film was removed by a further tempering of the coated microscopy slides at ~70 °C.

Grating Formation

The pDR1M surface relief gratings were written with a setup located in the Solid State Physics Group at the University of Siegen, Germany. The beam from either an Ar^+ laser (OMNICHROME) at 488 nm wavelength or a solid state laser at 515 nm wavelength were focused on a pinhole to create a point like source. The emanated spherical waves were collected and parallelized by a successive lens. The following spatial filter allowed only the zeroth order diffraction of the pinhole to propagate further on. A quarter-wave plate was installed in the beam path to create circularly polarized light as it has been found that this polarization leads to the highest writing efficiency [153]. The interference pattern on the pDR1M thin film was created with a mirror positioned halfway in the beam and perpendicular to the sample. A schematic setup is displayed in figure 4.2. The angle γ between the two parts of the beams that hit the sample defines the period Λ of the interference pattern and correspondingly the period of the grating:

$$\Lambda = \frac{\lambda}{2\sin(\gamma/2)} \tag{4.1}$$

where λ is the wavelength of the laser beam. As illustrated in figure 4.2, a part of each beam shone through a hole in the sample mounting stage and permitted a precise adjustment of the grating period. A red HeNe laser at 632.8 nm wavelength in combination with a photocell was used to monitor the writing process by measuring the intensity of the first order diffracted light from the evolving grating. The wavelength of the laser is in a range where the polymer does not absorb light [131, 153].

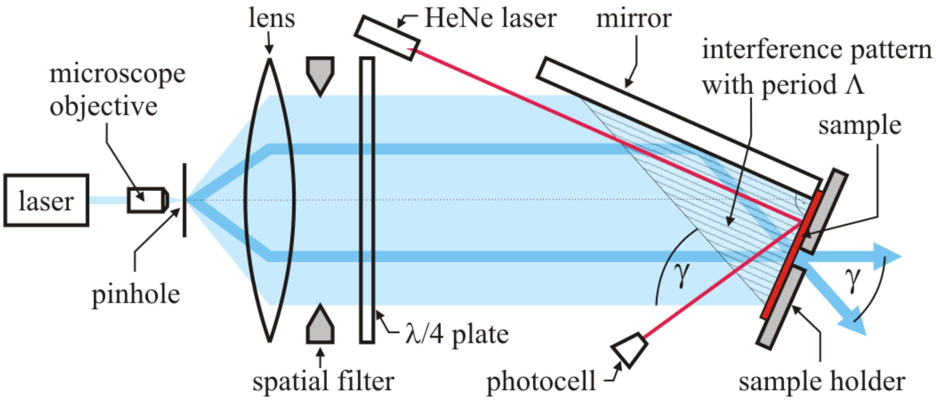

Figure 4.2: Schematic setup for the grating writing. A parallelized and a reflected laser beam create the interference pattern on the sample. The periodicity of the pattern is defined by the angle γ between the direct and the reflected beam. The quarter-wave plate fabricates a circularly polarized beam. The diffracted light from a HeNe laser is used to monitor the grating formation.

The process of grating writing produced patterned regions on the pDR1M films with a semi-circular shape due to the circular form of the spatial filter. The diameter of the regions yielded 5–8 mm depending on the actual setup. The surface relief gratings exhibited different grating heights, depending on the exact thickness of the pDR1M thin films, the power of the writing laser and the exposure time. The heights assessed by AFM ranged from a few nanometers up to about 100 nm. The influence of the different parameters on the grating formation are discussed in detail in [153] and references within. In order to arrive with cross gratings, the writing process was simply repeated with a different sample orientation.

4.2 Fabrication of Colloidal Crystals

Colloidal Particles

All colloidal particles applied in the presented work were purchased either from microParticles or Thermo Fisher Scientific[2]. The aqueous suspensions of polystyrene particles with a practically monodisperse size distribution were used as bought without further purification steps. They were diluted to the concentrations of choice using deionized water. Table 4.1 contains the list of the applied particles.

diameter [nm]	distribution CV[a] [%]	concentration [$wt\%$]	supplier
1027[b]	2.9	2	microParticles
770	≤ 3	10	Thermo Fisher Scientific
762	3.0	10	microParticles
760[b]	4.8	2	microParticles
740	≤ 3	10	Thermo Fisher Scientific
590[b]	5.4	2	microParticles
277[b]	1.4	2	microParticles
101[b]	0.7	2	microParticles

[a] CV: coefficient of variation ≡ standard deviation divided by the mean of the particle diameter. Calculated from manufacturer's data.

[b] Particles with size and distribution certified by the supplier.

Table 4.1: List of the colloidal particles used in this work. Values for the diameter, distribution and concentration as given by the supplier. Density all particles corresponded to: $1.05\,\mathrm{g/cm^3}$.

Colloidal Self-Assembly

Colloidal crystals were formed by convective self-assembly. A dedicated setup, schematically displayed in figure 4.3 (a), was constructed following the model of [156]. An extended description and technical details can be found in the appendix on page 127. The setup consists of a sample holder mounted on a translation stage. The colloidal dispersion is injected between the substrate and an inclined glass slide fixed at a constant position. By translating the sample stage, the substrate is moved under the immobile colloidal dispersion. Particles assemble at the receding contact line between substrate, air and the meniscus of the dispersion. A Peltier element stabilizes the temperature of the sample holder at a specified value. The setup allows to have good control over

---

[2] formerly Duke Scientific

the three main process parameters, namely the speed of the substrate translation, the concentration of the colloidal dispersion and the water evaporation rate.

Microscope glass slides were cleaned either as described in chapter 4.1 or with "piranha" solution - a mixture of 7 equivalents of concentrated sulfuric acid (96% H_2SO_4) and 3 equivalents of hydrogen peroxide (30% H_2O_2). In a typical assembly, the substrate was placed on the sample holder and the distance between substrate and the fixed confinement slide was set to 0.6 mm. Substrates consisted normally of bisected microscopy slides, cleaned as explained before, or pDR1M surface relief gratings. The surface gratings were treated in an air-plasma cleaner just before the start of the covering to make the surface more hydrophilic. Between 200 μl to 400 μl colloid dispersion with 0.02 wt% up to 3 wt% colloids was used for each coating. Depending on the experiment, translational velocities were chosen between 1 μm/sec to 5 μm/sec and the sample stage temperature was set in the range 15–25 °C. Ambient temperature and relative humidity were in the ranges 21.1–23.4 °C and 18–51%, accordingly.

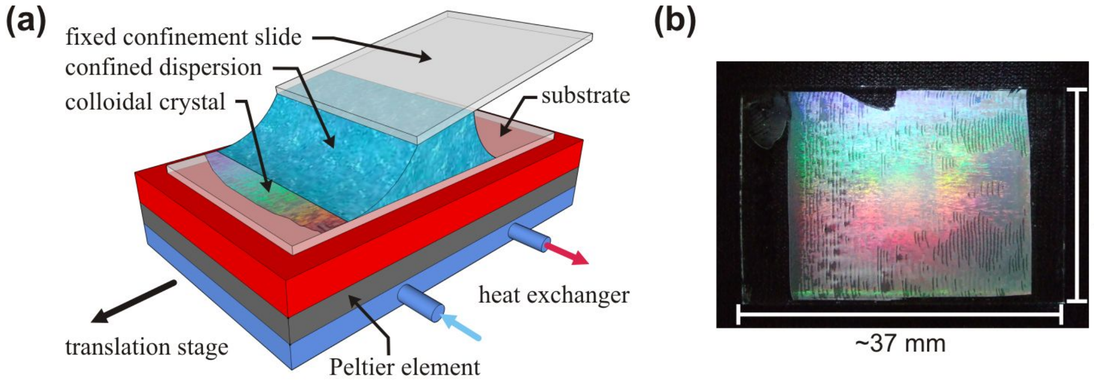

Figure 4.3: (**a**) Schematic layout of the setup dedicated for particle self-assembly. The meniscus of colloidal dispersion stays at a fixed position while the substrate is moved under it. The colloidal crystal starts to develop at the contact line between substrate, air and dispersion. The sample stage is temperature controlled by a Peltier element. (**b**) Photography of a resulting colloidal assembly on top of a bisected microscopy slide. The iridescent effect is caused by the interplay between light waves and the colloidal particles. Regions close to the edge of the substrate are irregularly covered.

A photography of a resulting colloidal assembly on top of a bisected microscopy slide can be seen in figure 4.3 (b). It corresponds to sample-740-2 discussed in chapter 5.2.3 and was fabricated with 1 wt% colloidal dispersion, a translational velocity of 4 μm/sec and a temperature of the sample stage of 25 °C. The sample was illuminated with a conventional light bulb for the picture. The iridescence is caused by the interplay between colloidal particles and the light waves as explained in chapter 1.1.1.

4.3 Characterization Techniques

Light Microscopy and Optical Profiler

A conventional light microscope (Axio Imager M1m, ZEISS) was used for an inspection of the colloidal samples. Microscopy images were taken with the included digital camera (AxioCam MRc, ZEISS). Overview images were fabricated by automatically collecting series of micrographs with a slight overlap and stitching them together. For that purpose the microscope can be controlled from a computer through a software package (AxioVision40 Version 4.5.0.0).

Individual surface profiles of colloidal crystals were assessed by an optical profiler (PLu neox, SENSOFAR) as a reference measurement. Thereby so-called 'confocal profiling' was applied. This mode of operation means that a confocal image system automatically pictures the sample at different heights. Each point in the image gets then assigned to the vertical position where it was best in focus. All investigations were done at 50 times magnification (numerical aperture 0.95).

Atomic Force Microscopy

If not mentioned otherwise, AFM investigations were performed in the Laboratory for Micro and Nanotechnology at Paul Scherrer Institute (PSI), Switzerland. A Dimension 3100 AFM (DIGITALINSTRUMENTS, VEECO) mounted on a vibration isolated table was used to image the pDR1M surface relief gratings and colloidal assemblies. All images were taken in tapping mode (cantilevers: NSC15/AIBS, ULTRASHARP). Whenever hight and distance values were evaluated in AFM images, a calibration sample (DIGITAL INSTRUMENTS, 10 μm pitch, 200 nm deep, 3D reference, P/N 498-000-026) was previously measured for normalization. Image processing and evaluation was done with the software NANOSCOPE (vs5.30r3.sr3). Processing involved usually a line fit correction or flattening but was otherwise kept at a minimum.

Scanning Electron Microscopy

The colloidal assemblies were investigated by a SEM (SUPRA 55VP, ZEISS) located in the Laboratory for Micro and Nanotechnology at PSI. Typically, an acceleration voltage of 1 kV was used and secondary electrons were detected in-lens. The colloidal samples were investigated without coating. This procedure led sometimes to charging effects decreasing the quality of the obtained images. The effect did however not impose any problem, as the focus had been on the order of the colloidal assemblies and not on high resolution images. Cross sectional images of the multilayers were done by sectioning the sample and looking at the plane of break with the SEM at a slightly inclined angle.

Dynamic Light Scattering

Dynamic light scattering, also known as photon correlation spectroscopy, investigates time dependent fluctuations in the scattered light intensity from a sample. In the case of colloidal dispersions, these fluctuations are caused by the Brownian motion of the suspended particles and it is possible to relate the autocorrelation function of the scattered light intensity with the hydrodynamic diameter and polydispersity of the colloids. A coherent introduction can for example be found in [157].

The experiments were performed at a standard setup. A 22 mW HeNe laser (UNIPHASE) was used to illuminate the colloidal dispersion. In order to minimize multiple scattering events, the colloidal dispersions were diluted to a level (10^{-4} wt%) where counting rates where around 30 kHz at 100 % laser power. A fiber-optical detection system with a static and dynamic enhancer at 632.8 nm combined with a high Q.E. APD-detector with overload protection (PERKIN ELMER) was applied to detect the scattered light. The detection module was positioned at a 90 deg angle from the beam path of the illuminating laser light. The obtained signal was processed by a multiple tau digital correlator (ALV-5000/EPP, ALV) linked to a computer. Data visualization and fitting was done in the goniometer control and analysis software (ALV-Correlator software, version 3.0.2.1).

The intensity autocorrelation function was calculated from measurements of two minutes duration. A cumulant analysis of the autocorrelation function was employed to extract the hydrodynamic diameter and the standard deviation of the diameter of the colloidal spheres. An average over three measurements was taken for the final values.

4.4 X-ray Scattering Instrumentation

cSAXS Beam Line at SLS, PSI

The cSAXS beam line is located at the Swiss Light Source (SLS) at PSI. It is dedicated to small angle scattering and coherent imaging.

The highly brilliant X-ray beam of the beam line is created by an undulator. Around 28 m from the source, a fixed exit double crystal Si(1 1 1) monochromator generates a monochromatic beam in an energy range between ~4.0 keV and ~19.0 keV. The energy resolution corresponds to about $\Delta E/E \approx 2 \cdot 10^{-4}$. The second crystal can be bend for horizontal focusing of the beam. Vertical focusing is achieved by a mirror following the monochromator in the beam path. The mirror does also reject higher harmonics from the monochromator crystal. After the mirror, the beam passes in the so called exposure box that is located in the experimental hutch. It contains a fast shutter and filters to control exposure times and the intensity of the beam. The shape of the X-ray beam can be tailored by a total of 4 slit systems. They are located before the monochromator, after the mirror and at the entrance and exit of the exposure box. No standardized sample setup is provided but an optical table allows to freely customize the experimental setup. Two evacuated flight tubes with a length of 2063 mm and 7000 mm are available. A Pilatus 2M (Dectris) detector is the standard detector at the beam line. It has 1475 × 1679 pixels with a size of 172 μm × 172 μm and is built up from 3 × 8 detector modules. The area between the modules is not sensitive to x-rays and appears as simulated "dead" pixels in the data frames. The dynamic range of the detector is 2^{20} with a counting rate per pixel $> 2 \cdot 10^6$ X-rays/sec [158]. It is mounted on a motorized stage that allows the adjustment of its position in the horizontal and vertical direction. All beam line components can be remote-controlled from outside the experimental hutch by the software SPEC (Certified Scientific Software). A detailed description of the beam line and its components can be found in [158–160].

For the experiments performed throughout this work, a hexapod (M850.11, PI) was mounted on the optical bench. It allowed to adjust the vertical rotation center at the beam position and was used to set the incident angle. A goniometer installation on top of the hexapod allowed both the alignment and rotations in the horizontal plane. The scattered intensity was recorded with the Pilatus detector after passing the 7 m long flight tube. Two beam stops were used to protect the detector from the high intensity of the direct and reflected beam. For the experiments, the flight tube had an entrance window consisting of ∼7 or ∼5 μm or mica and was either evacuated to a pressure of $3.4 \cdot 10^{-2}$ mbar or filled with helium. The exit window consisted of 350 μm Mylar in the former case and of ∼13 μm Kapton in the latter case. The X-ray beam was horizontally and vertically focused on one pixel of the detector. At the position of the sample the beam had horizontally and vertically a size of about 1 mm. Due to the grazing incident angles applied in the scattering experiments, the sample was at all angles illuminated over its whole length.

EDR Beam Line at BESSY II

The Energy Dispersive Reflectometry (EDR) beam line is located at the electron storage ring belonging to the newly formed Helmholtz Zentrum Berlin für Materialien und Energie formerly Berliner Elektronenspeicherring-Gesellschaft für Synchrotronstrahlung (BESSY II). The setup of the beam line is intentionally held simple [110,161]. It essentially consists of the bending magnet generating a white X-ray beam, three slit systems to shape the resulting beam and a system of aluminum absorbers which attenuate the intensity to the desired level. Just 50 μm unpolished Beryllium and two Kapton foils with thicknesses of 75 μm and 125 μm respectively separate the source from the experiment. They preserve and secure the ultra-high vacuum in the electron storage ring. A detailed description of the beam line and its components can be found in [162].

After the absorber box, an optical bench on the scale of 2 m × 1.5 m allows a freely variable customization of the experimental setup. For the experiments performed during this work, the sample was positioned on a goniometer. It allowed to adjust the hight, lateral position, azimuthal orientation and the pitch of the sample with respect to the beam. A second goniometer located around one meter further down the beam-path was used to position the detector. It consists of a energy dispersive Si-Drift detector

(ROENTEC) with an active area of 2 mm × 2 mm and was combined with a slit system to further constrain the detection area. Depending on the experiment, an evacuated flight tube was inserted between the sample and detector to minimize air scattering. It was capped with 75 μm thick Kapton foils on both sides. The software SPEC (CERTIFIED SCIENTIFIC SOFTWARE) was used to remote-control all goniometer and slit motors and to read out the energy spectra from the detector.

For the energy calibration of the detector, foils of different elements (Fe, Cu, Pb) were placed in the beam and the corresponding fluorescence lines appearing at well known energies were recorded with the detector. The energy resolution of the detector is $\Delta E/E \approx 10^{-2}$ keV for the range 0–40 keV used in this work[3]. Counting rates above 100'000 counts per second were carefully avoided during measurements not to cause problems with the read-out electronics [162].

Energy Spectrum

The energy resolved scattering signals measured at the EDR beam line are always weighted according to the available X-ray energy spectrum, i.e., the relative intensities of the different photon energies. The energy spectrum is primarily given by the bending magnet generating the X-ray beam. The primary spectrum is then modified by the materials that the beam travels until it reaches the detector. In particular the lower energies are strongly suppressed by the aluminum attenuators and the path of the beam in air.

The data presented in this work were normalized in a simple way[4]. After the actual investigations, spectra were collected for the identical measurement positions but without the actual sample. These spectra were smoothed by a Savitzky–Golay filter and consecutively used to normalize the scattering data collected from the sample. The influence of the incident spectrum could accordingly be ruled out.

Sedimentation Cell SMZ05 for *In situ* Scattering Experiments

A cell called "Sedimentationszelle SMZ05" [163] was used to better control the dry up process of colloidal droplets during X-ray scattering experiments. It consists of an aluminum stage with an integrated Peltier element and a removable cap. The 4 cm × 4 cm Peltier element is connected to a controller which stabilizes the temperature at the sample position in the range of ±0.3 °C. The cap of the sedimentation cell consists of Plexiglass and two Kapton foils on opposite sides which allow the X-ray beam to pass through the cell with a minimum of absorption. The enclosed volume is $\sim$125 cm^3. A humidity sensor (HTM1505, HUMIREL) with accuracy of ±5 % (in the range from 10 % to 95 %) inside the sample cell allows to log the relative humidity evolution during an experiment.

---

[3] The detector has the possibility to choose different energy ranges: 0–20 keV, 0–40 keV and 0–80 keV.

[4] A more sophisticated approach is for example discussed in [162].

CHAPTER 5

Experiments - Results and Discussion

5.1 Characterization of Colloidal Particles

The different dispersions made of polystyrene colloids were characterized by dynamic light scattering and SAXS prior to their further use as described in section 4.3. SAXS measurements were done at a photon energy of 11.2 keV at the cSAXS beamline, see section 4.4 for a description. Silver behenate was used as a diffraction standard [164]. For the scattering experiments, the colloidal dispersions were filled in glass capillaries (outer diameter 2.0 mm, wall thickness 0.01 mm, HILGENBERG GmbH) at the concentration as provided by the supplier, see table 4.1. For each sample, a minimum of five exposures were collected with the PILATUS detector, see section 4.4 for a description. Counting times were chosen for each sample so that no part of the detector was overexposured while absorbing the intense direct beam with a beam stop. All SAXS data were collected at a sample detector distance of ∼7 meters. The radial symmetrical scattering patterns have then been averaged and radially integrated. The software SASFIT [165] was used for the actual fitting of the particle parameters. A Gaussian particle size distribution was thereby successfully employed. The coefficient of variation[1] (CV) of the particles was then calculated from the standard deviation of the Gaussian distribution. The results from both dynamic light scattering and SAXS measurements are summarized in table 5.1. They are in good agreement with the values stated by the suppliers. Throughout the rest of the work, the diameter given by the supplier will always be used to refer to a specific particle size.

---

[1] The coefficient of variation corresponds to the standard deviation of the particle size divided by its mean. It is a typical value to characterize colloidal dispersions.

supplier		dynamic light scattering		SAXS	
diameter [nm]	CV[a] [%]	diameter [nm]	CV[a] [%]	diameter [nm]	CV[a] [%]
762	3.0	767 ± 23	5.4 ± 4.9	$767^{b} \pm 1$	1.4 ± 0.1
740	≤ 3	786 ± 12	4.9 ± 3.8	$768^{b} \pm 1$	< 1
590	5.4	600 ± 1	3.6 ± 3.1	$606^{c} \pm 2$	< 1
277	1.4	270 ± 1	1.3 ± 1.2	$274^{c} \pm 1$	< 1

[a] CV: coefficient of variation ≡ standard deviation of the particle diameter divided by its mean.

[b] Particles were fitted with the form factor of a homogeneous sphere.

[c] Particles were fitted with the form factor of a core shell sphere.

Table 5.1: Results for the particle diameter and coefficient of variation from characterization by light scattering and SAXS measurements. The standard deviations of the values for light scattering were calculated from the variation of the results for the three measurements. In case of the results from SAXS data, the given variation corresponds to the confidence interval returned by the fit procedure.

5.2 Investigations on Prefabricated Colloidal Assemblies

This section describes the experimental results obtained from colloidal crystals fabricated by convective self-assembly. The first section shortly exemplifies, how the number of colloidal layers on the samples was determined. The following sections are dedicated to the investigations of the colloidal assemblies by different methods with the main focus on GISAXS. It starts with samples consisting of colloidal particles with diameters of 277 nm, 590 nm and 740 nm on top of flat glass substrates and is followed by colloidal assemblies on topologically structured surface relief gratings. The experimental results are discussed at the end of this section.

5.2.1 Evaluation of the Number of Layers of the Colloidal Assemblies

An important characteristic of self-assembled colloidal crystals is the thickness of the colloidal cover and its homogeneity. Inhomogeneously covered samples consisting of colloidal particles in the diameter range used in this work display a rich structure when investigated under the light microscope. Figure 5.1 (a) and (b) each show a microscopy image of a glass substrate covered with colloidal particles with a diameter of 740 nm and 590 nm, respectively[2]. Both images were intentionally taken on the border of samples

---

[2] The samples correspond to sample-740-2 and sample-590-4 as introduced in chapter 5.2.3.

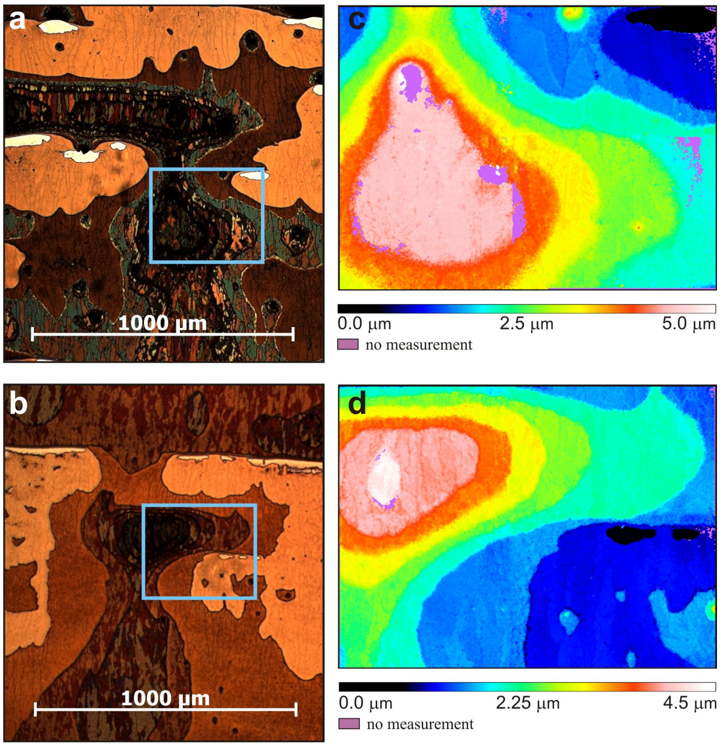

Figure 5.1: Figures (**a**) and (**b**) correspond to microscopy images of the surface of colloidal multilayers consisting of PS Particles with a diameter of 740 nm and 590 nm respectively. The regions framed with the blue rectangle mark the area investigated by a surface profiler. The corresponding results are displayed in figures (**c**) and (**d**). Regions appearing in a different brightness in the light microscope image correspond to different number of colloidal layers.

fabricated with convective self-assembly as described in chapter 4.2. The border of these samples is always inhomogeneous to a certain degree even though they can be very regularly covered in the central regions as is demonstrated in figures 5.2, 5.3 and 5.4.

As can be seen in figure 5.1 (a) and (b), large regions appear in bright or dark shadings and some of them have a speckled appearance. If the same spot on a sample is investigated both by a microscope and an optical profiler as done for the subfigures (a), (c) and (b), (d), it becomes apparent that large regions with the same shading correspond to a specific number of particle layers. This approach was used to determine the number of colloidal layers on the samples.

The speckled domains that appear in regions with the same number of layers appear only for three or more layers. The different colors can be assigned to the different possible stacking variants of hexagonal close packed layers of colloids [93]. As can be seen from figures 5.1 (a) and (b), the coloring effects are stronger for the particles with a diameter of 740 nm compared to the ones with a diameter of 590 nm. This dependence on the diameters of the particles can be understood by recalling equation (1.1). The speckled appearance is completely lost for the particles with 277 nm diameter.

5.2.2 Samples Composed of Particles with 277 nm Diameter

The three samples discussed in this section consist of ordered colloidal polystyrene particles with a diameter of 277 nm on a glass substrate. They were fabricated by convective self-assembly with the setup described in 4.2. The corresponding process parameters are given in table 5.2. The column headings in the table are the sample codes indicating particle diameter and average number of layers covering the sample. The number of layers given in the last line of the table was estimated according to the method described in chapter 5.2.1. The value corresponds to the number of layers in the central part of the sample. This region is very homogeneously covered with the same number of layers in case of sample-277-7 and sample-277-1 across an area of typically 1–2 cm^2. In the case of sample-277-14, the given value is an average over a less uniform number of layers.

sample-277	**-7**	**-14**	**-1**
substrate		flat glass slide	
particle diameter [nm]	277	277	277
concentration of dispersion [wt%]	1	1	1
translation velocity [μm/sec]	2	2	6
temperature of sample stage [°C]	15.00±0.04	20.00±0.01	15.00±0.04
ambient temperature [°C]	21.6	18.2	18.2
ambient relative humidity [%]	18.2	18.2	18.2
average number of layers	7	14	1

Table 5.2: Fabrication parameters and average number of layers of samples consisting of 277 nm colloids.

Characterization by Light Microscopy, AFM and SEM

Figures 5.2, 5.3 and 5.4 show results from AFM and microscopy investigations of the surface of the three samples. All micrographs are oriented such that the direction marked with the arrows corresponds to the direction of translation of the meniscus of colloidal dispersion over the glass substrate. In the following text, this direction will be referred to as the "growth direction" because the colloidal crystal has developed in this direction. The "growth direction" of a colloidal crystal describes therefore a concept not to be confused with the preferential growth directions of a solid state crystal.

Locally, the AFM images show an almost perfect hexagonal arrangement of the colloidal particles. For distances above 5 to 10 μm ($\sim$ 30 particle diameters) though, the order starts to slowly break down due to a multitude of defects such as missing colloids or cracks between adjacent parts of the layer. In the case of sample-277-1, the width of the cracks is in the range of a colloidal diameter, whereas the cracks extend over larger distances in the case of the samples covered with multilayers. In the case of sample-277-7 and sample-277-14, the boundaries of the cracks mirror each other. The similarity of the rims suggests that the domains did not nucleate individually but rather cracked later on in the information process. These observations are consistent with results from other studies and have been associated with capillary forces and a slight shrinkage of the colloidal particles taking place during the dry up of the assemblies [76,77,86]. Thus, the colloidal crystals were ordered over much larger distances just after the self-assembly than at the moment of observation. Only during the final evaporation of the water, the crystal has lost its long range order. In the case of a sedimented colloidal crystal, this process has been observed *in situ* by small-angle X-ray diffraction [101].

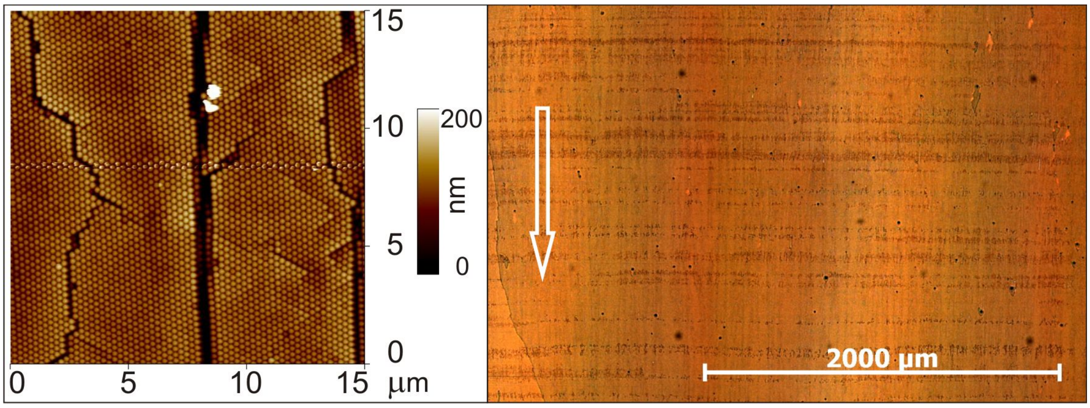

Figure 5.2: AFM (*left*) and microscopy (*right*) images of the surface of sample-277-7 covered with a multilayer of seven layers thickness. Both micrographs are oriented such that the growth direction of the colloidal multilayer is approximately parallel to the direction marked with the arrow. The microscopy image was taken with a fourfold magnification. In the bottom left-hand corner of the microscopy image, one can see a step in the number of layers. The rest of the image is homogeneously covered with seven layers.

In case of the multilayers, i.e., sample-277-7 and sample-277-14, the colloidal particles are aligned approximately in the direction of growth of the colloidal crystal, i.e., colloidal particles form chains along the growth direction. The cracks visible in the AFM micrographs follow as well more or less the direction of growth. They occur in average every 7–10 μm perpendicular to the growth direction. This is even more apparent from the microscopy image in figure 5.3 that shows the surface of sample-277-14 at a twentyfold magnification. It has been suggested [86] that the orientation of the cracks develops because the volume loss of the assembly due to particle shrinkage can be compensated in growth direction by the influx of particles at the meniscus contact line. As no such mechanism exists perpendicular to the growth direction, the volume loss leads to the formation of cracks. In the case of sample-277-1 covered with a monolayer, no alignment of the cracks can be inferred from AFM images. The hexagonally ordered regions on this sample have moreover different orientations in AFM images taken at different positions.

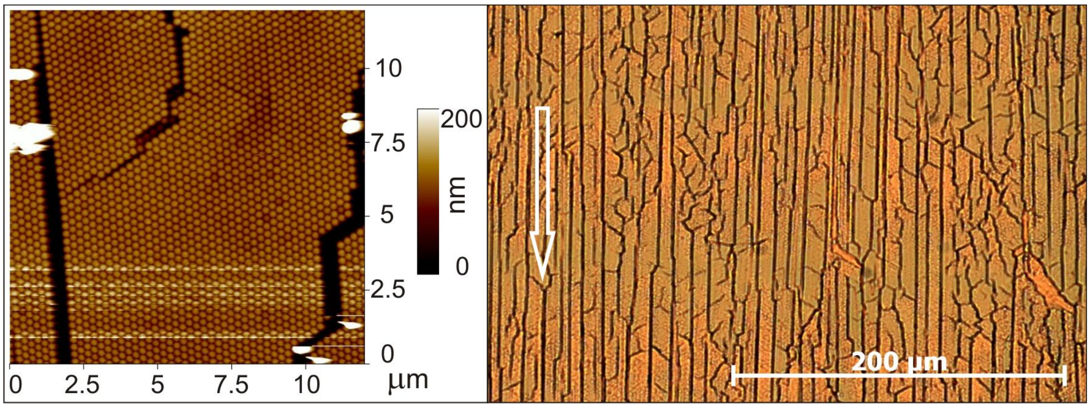

Figure 5.3: AFM (*left*) and microscopy (*right*) images of the surface of sample-277-14 covered with a colloidal multilayer of 14 layers. Both micrographs are oriented such that the growth direction of the colloidal multilayer is approximately parallel to the direction marked with the arrow. Disturbances as in the lower half of the AFM image are attributed to individual colloids that stick to the AFM tip or move freely around when touched by the tip. The microscopy image was taken with a twentyfold magnification. A very pronounced crack structure can be observed. Cracks are mostly oriented parallel to the growth direction of the colloidal assembly.

The microscopy images in figures 5.2 and 5.4 show a section of the surface of sample-277-7 and sample-277-1, respectively. Both images were done at fourfold magnification. In the case of sample-277-7, the image shows the surface of the seventh layer. Only a small part in the lower left corner has one layer less. It is not completely clear where the horizontal stripes in the image of sample-277-7 come from. AFM investigations on the stripes did not show any remarkable difference to other parts on the sample. The irregularities might just be caused by arbitrarily positioned colloids on top of the assembly. The microscopy image of sample-277-1 shows the surface of the monolayer intermitted with small islands with a double layer or no colloidal cover. Both samples are covered with the same number of layers over almost the whole picture. The whole extension of the uniformly covered area is between $1\,\mathrm{cm}^2$ to $2\,\mathrm{cm}^2$.

Figure 5.5 shows two SEM micrographs of sample-277-7. They display cross sections through the colloidal multilayer on top of the glass substrate. The cuts cross the direction of growth of the multilayer at approximately right angle. By counting the stacked layers, the number of seven found by the microscopy investigation is confirmed. The observation from AFM images that the colloidal particles are lined up along the direction of growth is validated as well. From the cross sectional view on the multilayer, the stacking was estimated by comparing the arrangement of the colloidal particles at the edge with models of fcc and hcp structures. In such a manner, fcc and hcp stacking were attributed to the crystal parts visible in figures 5.5 (a) and (b), respectively. However, such evaluations are prone to misinterpretations as the exact three-dimensional structure is not well discernible from the SEM images.

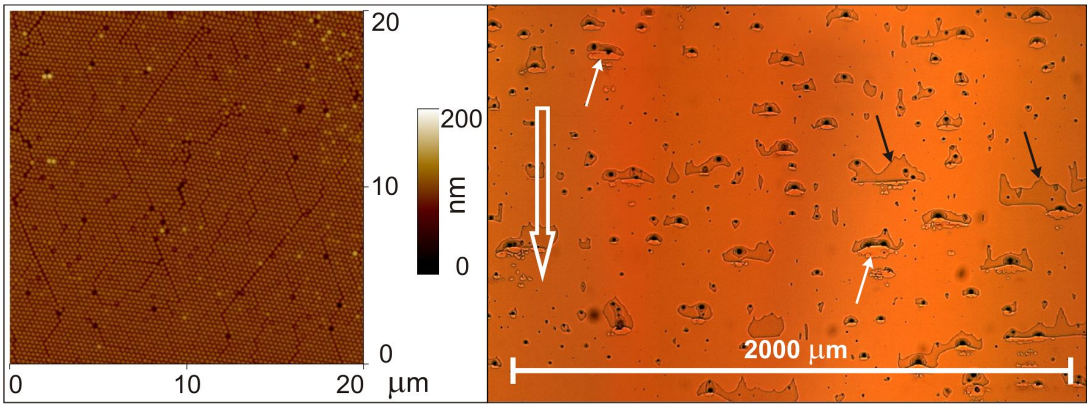

Figure 5.4: AFM (*left*) and microscopy (*right*) images of the surface of sample-277-1 mainly covered with a monolayer. Both micrographs are oriented such that the growth direction of the colloidal multilayer is approximately parallel to the direction marked with the large arrow. The black arrows in the microscopy image indicate regions covered with a double layer. The small white arrows indicate uncovered areas. The microscopy image was taken with a fourfold magnification.

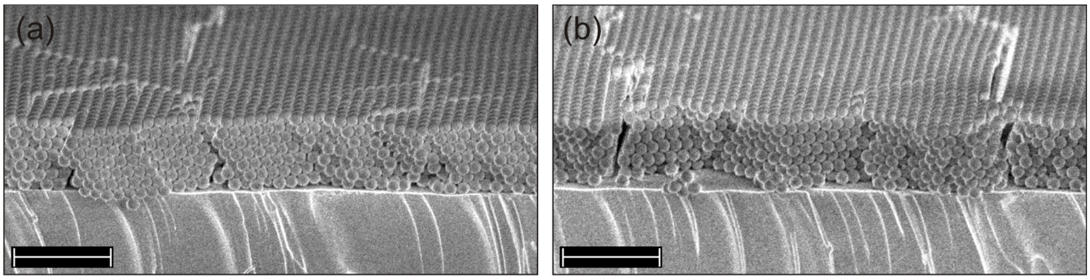

Figure 5.5: SEM images of sample-277-7. Both micrographs show a cross section of the colloidal multilayer on top of a glass substrate that was cleaved approximately perpendicular to the direction of growth. The assembly consists of seven layers. The stacking of the layers in the center of the image is attributed to fcc and hcp in (a) and (b) respectively. The scales correspond in both images to 2 μm.

GISAXS Experiments

GISAXS investigations on sample-277-7, sample-277-14 and sample-277-1 were performed at the cSAXS beam line at the SLS. A detailed description of the beam line and its components can be found in chapter 4.4 and [159]. A photon energy of 8.7 keV was used for the experiments. The beam was focused on approximately one pixel on the detector. The beam diameter at the sample position was accordingly $\sim 1 \times 1\,\mathrm{mm}^2$. The 7 m long flight tube was inserted after the sample. It had an entrance window of $\sim$7 μm of Mica, an exit window of $\sim$13 μm Kapton and was filled with Helium. A Pilatus 2M detector was used to record the scattered X-ray intensity. It was positioned right after the exit window of the flight tube.

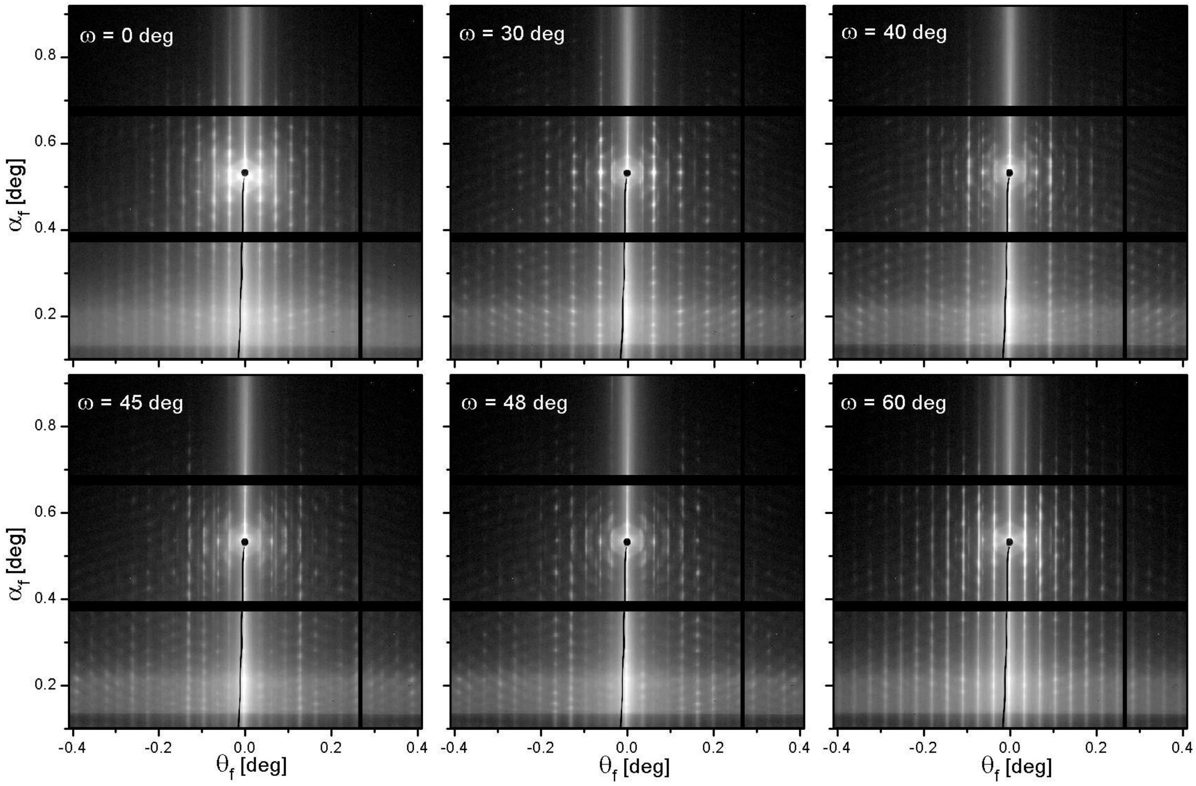

Figure 5.6: Scattering pattern collected from sample-277-7. All scattering patterns were measured at the same incident angle $\alpha_i = 0.53$ deg but at varying sample orientations ω. The displayed scattering patterns are an average over eleven exposures, covering an ω-range of 1 deg. The intensity scale is logarithmic and equal for all scattering patterns.

For an actual measurement, the colloidal crystals were mounted on the goniometer with their growth direction approximately parallel to the beam direction. After setting the desired incident angle α_i between sample and beam, the sample was turned around its surface normal and a scattering pattern was collected at every 0.1 deg over a total of 100 deg. In the further text, ω will be used to denote the sample orientation for the rotation of the sample around the surface normal. The angle $\omega = 0$ deg is defined as the orientation where the growth direction is parallel to the beam.

Figures 5.6 to 5.7 show examples of resulting scattering patterns for sample-277-7, sample-277-14 and sample-277-1. They are each a result of an average over 11 frames taken over an ω-range of 1 degree and an average over 31 frames taken over an ω-range of 3 deg in the case of figure 5.9. The averaging was done uniquely for the purpose of a distinct representation of the scattering patterns. The scattering patterns corresponding to the exact experimental position of figure 5.6 but without any averaging is displayed in the appendix on page 129 as a comparison. For the subsequent evaluations, no averaging was done if not explicitly mentioned otherwise.

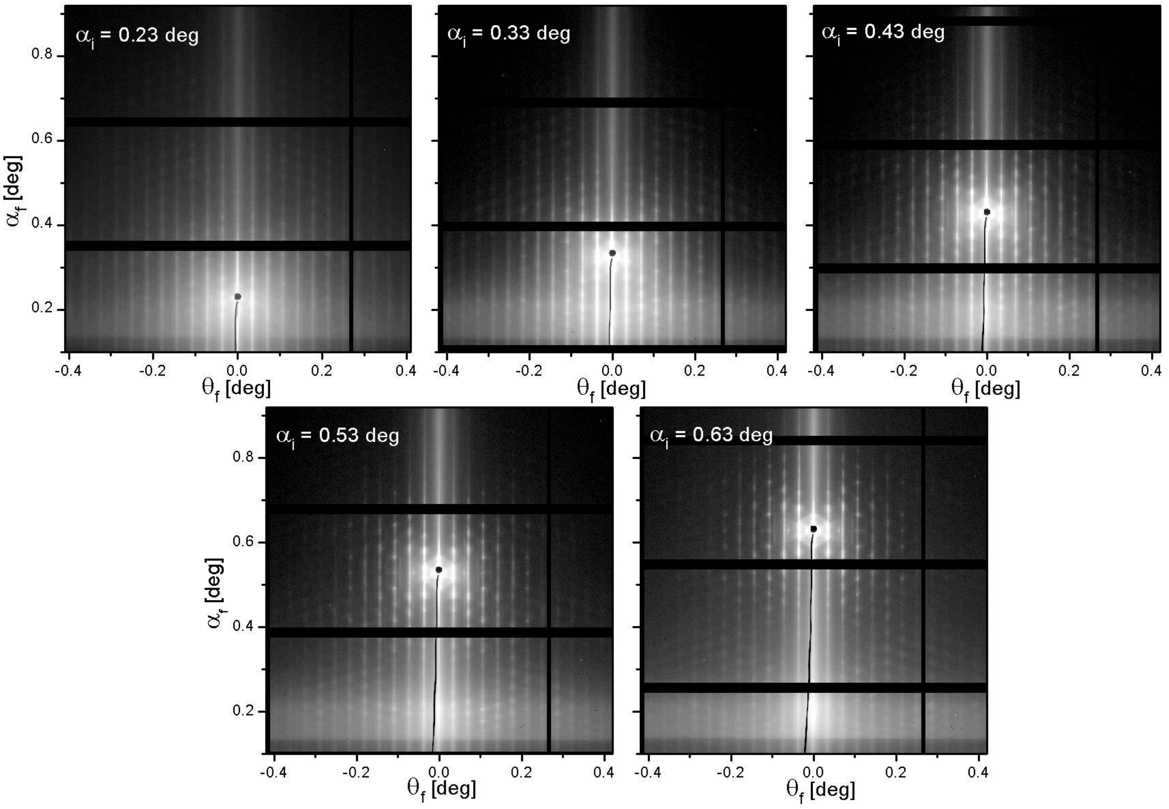

Figure 5.7: Scattering patterns from sample-277-7 collected at $\omega = 0$ deg but increasing incident angles α_i. The displayed angles range from $\alpha_i = 0.23$ deg, just above the angle of total reflection of the substrate, up to $\alpha_i = 0.63$ deg. The displayed scattering patterns are an average over eleven exposures, covering an ω-range of 1 deg. The intensity is logarithmically scaled and the range was chosen for each figure individually to make the structure of the peaks optimally visible.

The black "bars" appearing in all the scattering patterns originate from the PILATUS detector. This detector is built up of individual modules. The bars without intensity correspond to the interspace between the individual modules. In the data, these regions appear as simulated "dead" pixels. The high intensity of the reflected beam was absorbed by a beam stop in the presented scattering patterns. It was inserted from below. The small line without intensity coming from the lower edge to the position of the reflected beam corresponds to the shade of the wire holding the beam stop. The intensity band visible in all GISAXS patterns in the range between $\alpha_f \approx 0.14$ deg up to $\alpha_f \approx 0.22$ deg is caused by the dynamical effects at the angle of total external reflection. In the further text, this intensity is also referred to as the Yoneda band in reference to the corresponding feature in reflectivity measurements. The position of the upper limit of the band is defined by the glass substrate of the sample. The position of the lower limit is given by the colloidal particles. The rest of the streaks and peaks on the scattering

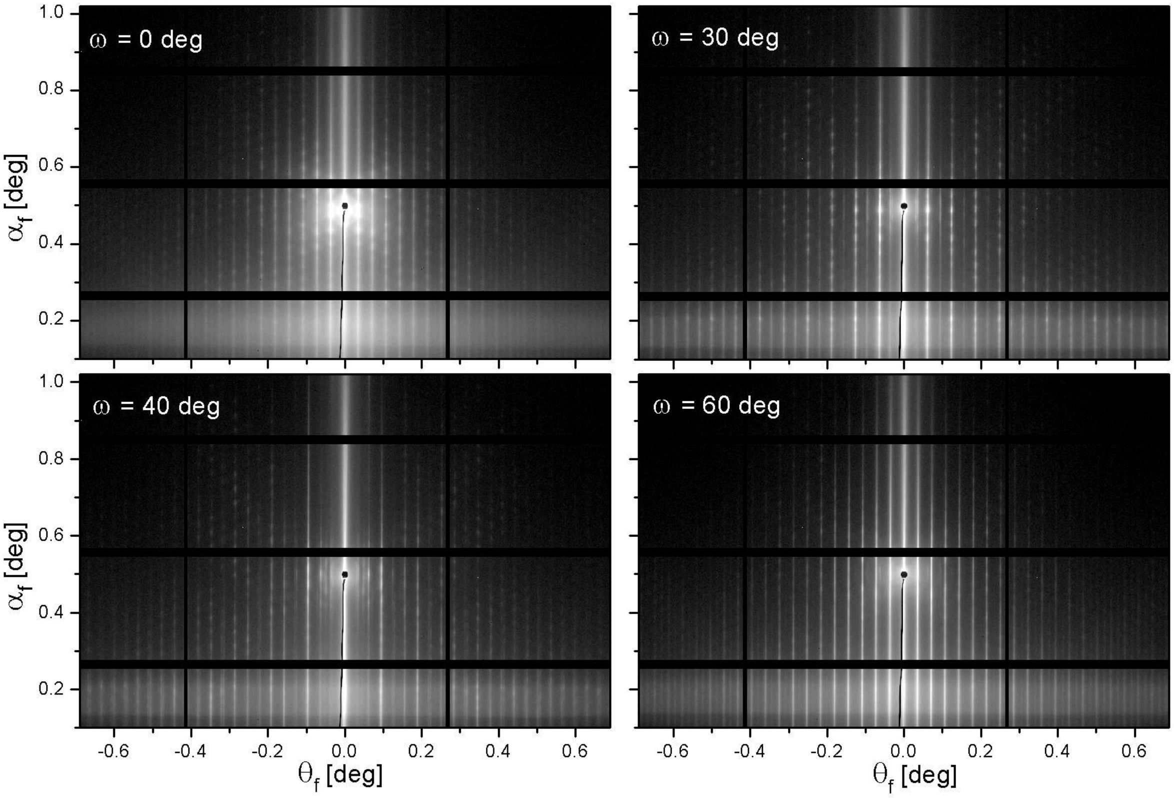

Figure 5.8: Scattering pattern of sample-277-14. All scattering patterns were measured at the same incident angle $\alpha_i = 0.49$ deg but at varying sample orientations ω. The displayed scattering patterns are an average over eleven exposures, covering an ω-range of 1 deg. The intensity scale is logarithmic and equal for all scattering patterns.

patterns originate from the arrangement of the colloidal particles. The corresponding information will be evaluated in the following sub-chapters.

The axes α_f and θ_f in the graphs denote the two angles that define the direction of the scattered intensity as shown in the schematic setup of the GISAXS technique in figure 1.14 (a). Introducing these angles in the equation for the scattering vector (1.21), it becomes apparent that the scattering patterns correspond to cuts through reciprocal space that can be approximated by planes parallel to the Q_z component of the scattering vector and perpendicular to the Q_x, Q_y plane. The α_f axis in the scattering patterns is therefore in first approximation parallel to the Q_z component and the θ_f axis denotes a direction in the Q_x, Q_y plane. If one considers the geometrical setup of the experiment, it follows that the reciprocal space segments measured with the scattering patterns stand perpendicular to the hexagonal planes of the colloidal crystal. Along the θ_f or Q_x, Q_y direction one obtains therefore information about the ordering within the hexagonal planes and along the α_f or Q_z direction, the stacking of the hexagonal planes gets probed.

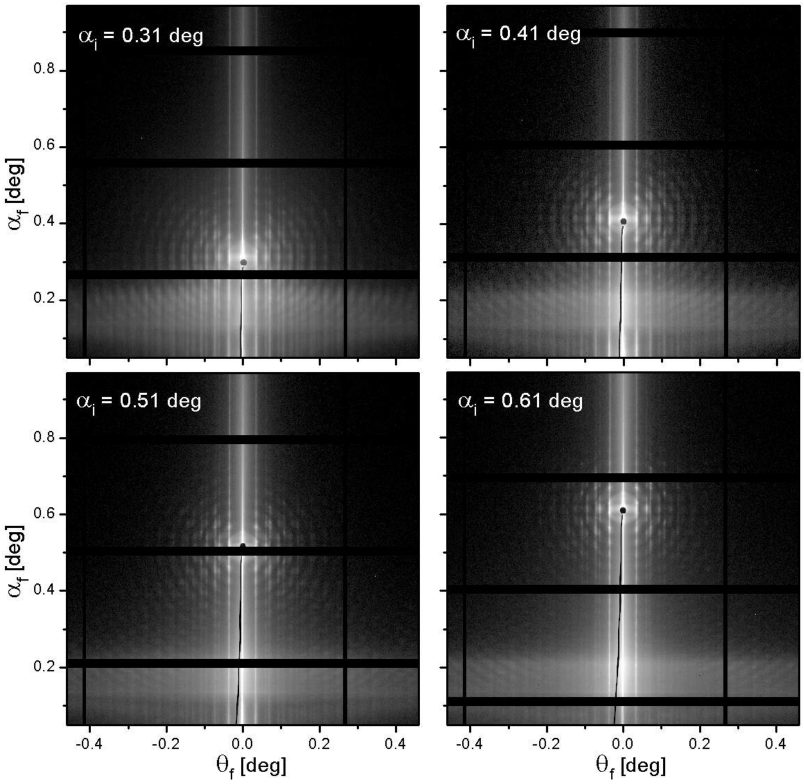

Figure 5.9: Scattering patterns from sample-277-1 covered with a monolayer. All patterns were collected at an identical sample orientation (equal ω) but different incident angles α_i. The displayed scattering patterns are an average over 31 exposures, covering an ω-range of 3 deg. The intensity is logarithmically scaled and the range was chosen for each figure individually to make the structure of the peaks optimally visible.

Figures 5.6 and 5.8 show the scattering patterns for sample-277-7 and sample-277-14 for a constant incident angle but a varying sample orientation ω. Sample-277-7 was measured at $\alpha_i = 0.53$ deg and sample-277-14 at $\alpha_i = 0.49$ deg. The difference in the sample orientation ω between the first and last scattering pattern in figures 5.6 and 5.8 corresponds to 60 deg. The direction of the θ_f axes of these two scattering patterns can be attributed to the $(0\,1\,0)$ (at $\omega = 0$ deg) and the $(1\,1\,0)$ (at $\omega = 60$ deg) directions defined in the reciprocal lattice of the hexagonal plane as introduced in equation (3.24) and illustrated in figure 3.3. The other scattering patterns correspond then to directions along $(1\,2\,0)$ at $\omega = 30$ deg, $(2\,3\,0)$ at $\omega = 40$ deg, $(3\,4\,0)$ at $\omega = 45$ deg and $(4\,5\,0)$ at $\omega = 48$ deg.

Figures 5.7 and 5.9 show the evolution of the scattering pattern for sample-277-7 and sample-277-1 at a constant sample orientation but an increasing incident angle α_i. It can be seen from the two figures that the number of visible scattering peaks increases as α_i approaches the critical angles of the substrate and the colloids. This is due to the increased reflectivity close to the angles of total external reflection. If one inspects the scattering patterns of sample-277-1 at different sample orientations, no marked changes in the scattered intensity can be observed but the pattern stays approximately the same.

In-Plane Evaluation of GISAXS Data

The scattering data collected as described in the previous section was used to assess the colloidal arrangement parallel to the plane of the sample surface. This arrangement is referred to as the "in-plane" order of the colloids.

For that purpose, all scattering patterns collected at a specific incident angle α_i were integrated over α_f between the lower limit of the Yoneda band and the position of the reflected beam. Thereby, incident angles α_i close to the angle of total external reflection were chosen. The actual angles for α_i were 0.329 ± 0.005 deg, 0.297 ± 0.005 deg and 0.314 ± 0.005 deg for sample-277-7, sample-277-14 and sample-277-1, respectively. The small variations are caused by a slight curvature of the sample surface or imperfect alignment. The arrays of intensities resulting from the integration were plotted in a polar graph where the angle and radial position of each array element was defined by the orientation of the sample, ω, and the distance to the specular direction, θ_f, respectively. The corresponding graphs for sample-277-7, sample-277-14 and sample-277-1 can be seen in figures 5.10 (a), 5.11 (a) and 5.12 (a), respectively. In these graphs, only the intensity for the positive θ_f values is displayed. For the negative θ_f, the graphs look symmetric. The coordinates were transformed to correspond to the components of the scattering vector Q_x and Q_y. Thereby, it was assumed that the basis vectors of reciprocal space are fixed to the sample, i.e., Q_x is always oriented approximately parallel to the growth direction of the colloidal crystal and Q_y perpendicular to it. The equation to calculate the scattering vector from the experiemental angles, (1.21), has then to by modified to account for the sample orientation, ω, and yields

$$\mathbf{Q} = \begin{bmatrix} \cos\omega & -\sin\omega & 0 \\ \sin\omega & \cos\omega & 0 \\ 0 & 0 & 1 \end{bmatrix} \cdot \frac{2\pi}{\lambda} \begin{pmatrix} \cos\alpha_f \cos\theta_f - \cos\alpha_i \\ \cos\alpha_f \sin\theta_f \\ \sin\alpha_f + \sin\alpha_i \end{pmatrix} . \tag{5.1}$$

The graphs 5.10 (a) and 5.11 (a) corresponding to sample-277-7 and sample-277-14 give clear evidence of a hexagonal arrangement of the colloids on the sample. Considering the grazing incidence angles ($\alpha_i \approx 0.3$ deg) used in the experiment and the vertical beam size of almost 1 mm at the position of the sample, one gets a beam footprint of more than 10 cm. The sample is therefore illuminated over its complete length. It can therefore be inferred from the two graphs that the ordered domains on the whole self-assembled sample are equally oriented. Additionally, the orientation of the domains seems to be equal for both multilayers. This is in good agreement with the observation from AFM images that the colloidal particles seem to be stringed in the direction of growth of the colloidal multilayer.

Graphs 5.10 (b) and 5.11 (b) show different cuts along ω extracted from the corresponding graph in (a) while holding the absolute value of the in-plane components of

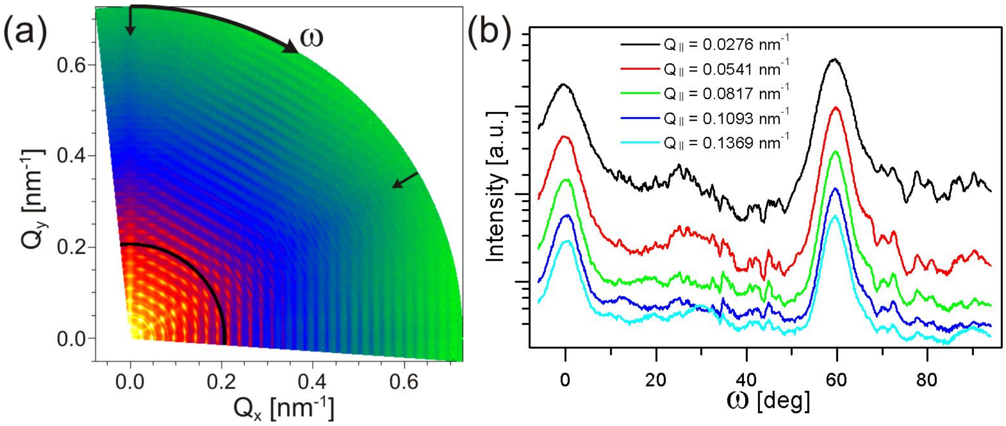

Figure 5.10: Data of sample-277-7: (**a**) Visualization of the scattered intensity parallel to the substrate. The graph gives clear evidence of a hexagonal ordering of the colloidal particles. The black segment in the graph is caused by the gap between two detector modules. (**b**) Cuts along ω extracted from graph in (**a**) with $\mathbf{Q}_{||}$ held constant. The $\mathbf{Q}_{||}$ values were chosen in a manner that the cuts come to rest on a peak when crossing the directions at $\omega = 0$ deg and $\omega = 60$ deg marked with an arrow. The averaged FWHM of the peaks amounts to 4.4 ± 0.9 deg.

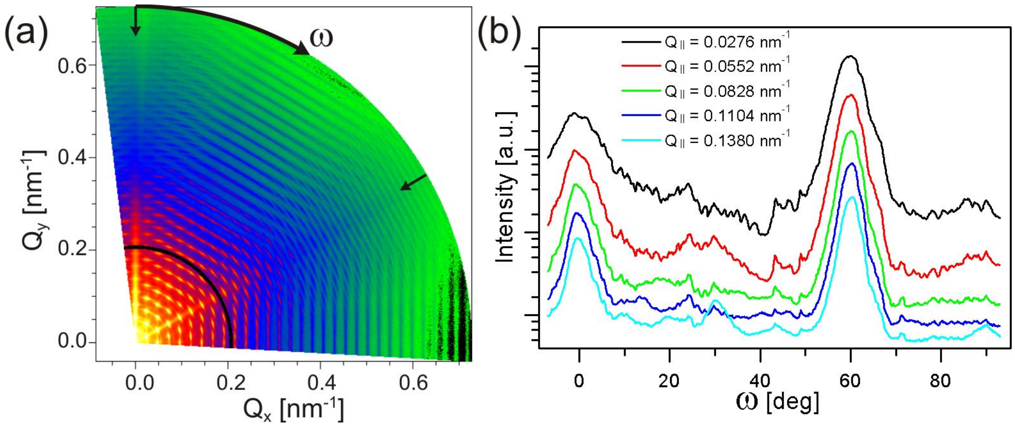

Figure 5.11: Data of sample-277-14: (**a**) Visualization of the scattered intensity parallel to the substrate. As can be seen, the colloidal spheres are arranged in a hexagonal arrangement. The black segment in the graph is caused by the gap between two detector modules. (**b**) Cuts along ω extracted from graph in (**a**) while holding $\mathbf{Q}_{||}$ constant. The $\mathbf{Q}_{||}$ values were chosen in a manner that the cuts come to rest on a peak when crossing the directions at $\omega = 0$ deg and $\omega = 60$ deg marked with an arrow. The averaged FWHM of the peaks amounts to 4.3 ± 0.8 deg.

the scattering vector, $\mathbf{Q}_{||} = (\mathrm{Q}_x^2 + \mathrm{Q}_y^2)^{1/2}$, constant. The $\mathbf{Q}_{||}$ values were chosen in a manner that the cuts come to rest on a peak when crossing the directions at $\omega = 0$ deg and $\omega = 60$ deg marked with arrows in the graphs. By fitting the individual peaks with a Gaussian curve, one obtains for both samples a peak distance of almost exactly 60 deg. The averaged FWHM of the peaks provides an estimation of how well aligned the domains are. For sample-277-7 the FWHM corresponded to 4.4 ± 0.9 deg and for sample-277-14 to 4.3 ± 0.8 deg. The intensity modulations in between the peaks can be attributed to the fact that the beam probing the sample does "see" different parts of the sample depending on ω. The sample orientation changes also the length of the illuminated sample and influences accordingly the percentage of the beam that gets reflected.

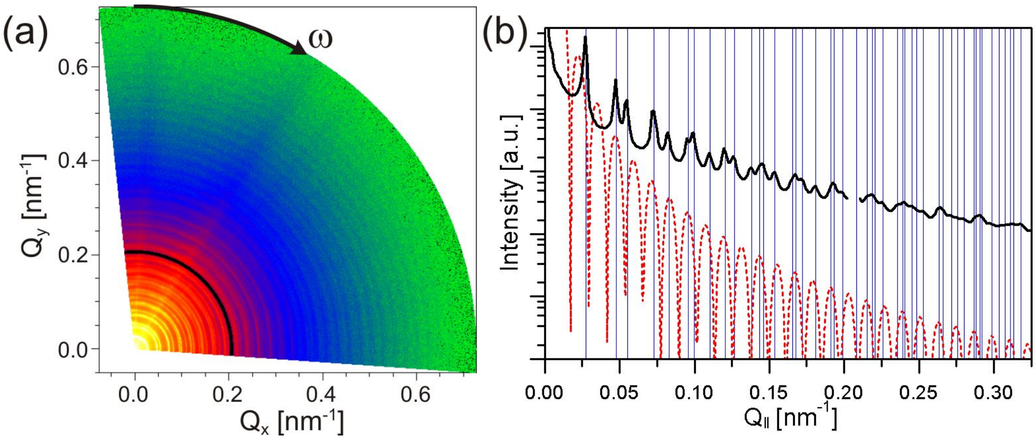

Figure 5.12: Data of sample-277-1: (**a**) Visualization of the scattered intensity parallel to the substrate. The concentric circles indicate that the ordered regions on the substrate have a random orientation and show a powder-like scattering behavior. (**b**) The *solid black* line corresponds to the intensity of graph (**a**) averaged over ω and plotted versus $\mathbf{Q}_{||}$. The $\mathbf{Q}_{||}$-values of the blue lines denote the position of the powder lines. They were calculated assuming a hexagonal arrangement of the scattering centers in the grains of the powder and a center to center distance of 263 nm. The *red dashed* curve is the calculated form factor of a sphere with a diameter of 263 nm shown as a comparison.

Graph 5.12 (a) corresponds to the in-plane evaluation of the scattering for sample-277-1. The concentric circles indicate a random orientation of the ordered regions in the plane parallel to the surface. Cuts similar to those in figures 5.10 (b) and 5.11 (b) (not shown here) do exhibit some modulation in intensity but no pronounced ω dependence. For graph 5.12 (b) the intensities in graph (a) were averaged over ω and plotted versus in-plane component of the scattering vector $\mathbf{Q}_{||}$. The form factor of a sphere with a diameter of 263 nm was plotted in the same graph for comparison. It can be seen that it can not account for the various peaks in the scattering data. The blue lines mark the calculated $\mathbf{Q}_{||}$-positions of peaks that appear under the assumption of a powder like orientation of the hexagonally packed colloidal regions parallel to the surface. The center to center distance of the colloidal particles used for the calculations was 263 nm. The blue lines perfectly match the position of the peaks in the data. The agreement of the calculated position of the powder peaks with the scattering data supports the observation made from AFM images that the ordered regions on sample-277-1 are randomly oriented.

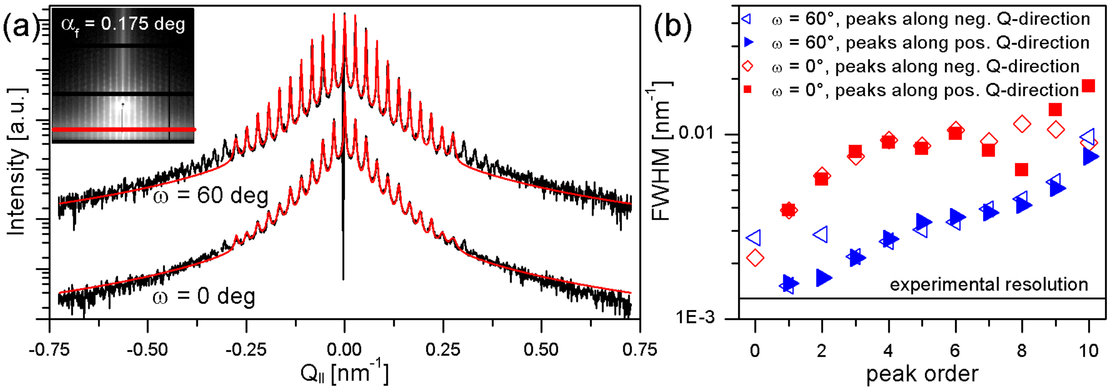

Figure 5.13: Data of sample-277-7: (**a**) Scattering data and fit along θ_f for fixed α_f = 0.175 deg at two sample orientations $\omega = 0$ deg and $\omega = 60$ deg. The position of the extracted cut is schematically illustrated in the inset of figure (a). The incident angle was equal to 0.33 deg. Fits were done with a sum of Lorentzian peaks. (**b**) FWHM of the peaks fitted in (**a**).

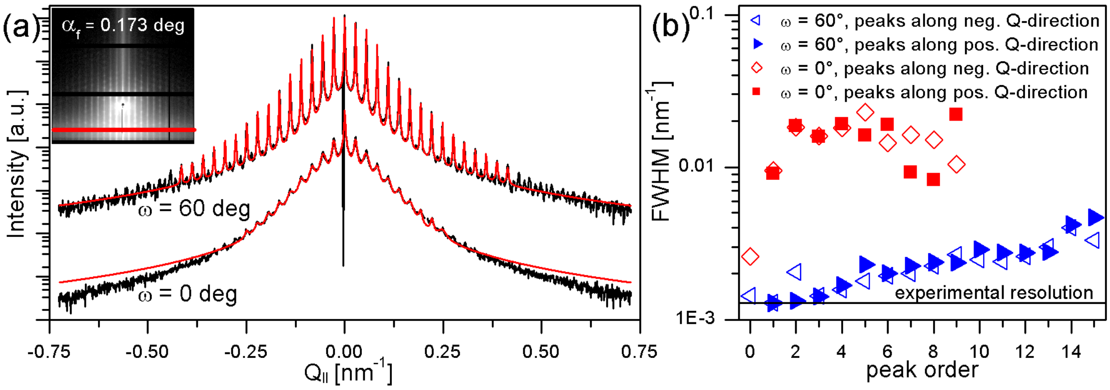

Figure 5.14: Data of sample-277-14: (**a**) Scattering data and fit along θ_f for fixed α_f = 0.173 deg at two sample orientations $\omega = 0$ deg and $\omega = 60$ deg. The position of the extracted cut is schematically illustrated in the inset of figure (a). The incident angle was equal to 0.29 deg. Fits were done with a sum of Lorentzian peaks. (**b**) FWHM of peaks fitted in (**a**).

Graphs 5.13 (a) and 5.14 (a) show line cuts extracted from scattering patterns along θ_f at constant α_f. In the plot, the coordinates were transformed to the absolute value of the in-plane components of the scattering vector $\mathbf{Q}_{||}$. The exit angle α_f of the cuts corresponded to a value in the center of the Yoneda band. The position of the cut through the GISAXS patterns is illustrated by the red bars in the insets. The incident angles α_i were 0.33 deg for sample-277-7 and 0.29 deg for sample-277-14. The sharp dip in the scattering intensity close to $\mathbf{Q}_{||} = 0$ is caused by the holder of the beam stop. The two curves in the graphs were taken from scattering patterns measured at $\omega = 0$ deg and at $\omega = 60$ deg. These orientations correspond to the directions marked with arrows in figures 5.10 (a) and 5.11 (a). As can be seen, there is a prominent difference in the width of the peaks along the two directions while the peak position is identical.

From the distance between the peaks in the curves of the two samples one can recalculate grating constants resulting with 228 ± 1 nm for both samples. The resulting colloidal center to center distance in the hexagonal layer is then for both samples 263 ± 1 nm.

In order to quantify the difference in the peak width, the line cuts were fitted by a sum of Lorentzians peaks. In case of sample-277-7, peaks up to the tenth order were included. In case of sample-277-14, peaks up to the fifteenth and up to the ninth order were included in the directions $\omega = 60$ deg and $\omega = 0$ deg, respectively. An additional Lorentzian peak centered at $\mathbf{Q}_{||} = 0$ was used take account of the broad background. It arises due to the surface roughness of the sample. The fits including all the individual components are given in the appendix on page 130. The red curves correspond to the final fit.

The graphs in 5.13 (b) and 5.14 (b) show the resulting peak widths as a function of the peak order. For both samples, one finds a similar behavior. The peak widths of the two orientations do differ significantly. For $\omega = 0$ deg, the peaks are clearly wider than for $\omega = 60$ deg. This result indicates that the ordered regions extend over shorter distances in the former case than in the latter, i.e., the order on the sample perpendicular to the growth direction extends over shorter distances than in a direction 30 deg away from the growth direction. This concurs with the observations made by AFM and microscopy where a system of cracks was found along the direction of growth splitting the colloidal domains in the direction perpendicular to it. Additionally, the peaks exhibit a clear tendency to get broader for higher orders in all cases but for sample-277-14 at $\omega = 0$ deg. In this case, the large variance in the peak widths resulting from the fit can be attributed to the low peak intensity with respect to the background. The broadening of the peaks is an indication of a so called paracrystalline ordering. That means that the scattering centers have larger and larger deviations from an ideal crystalline grating as one increases the distance to an arbitrary reference point.

Out of Plane Evaluation of the GISAXS Data

The scattering data collected in the previous section is not only useful to investigate the in-plane order. Information about the stacking of the colloidal layers can also be extracted from the data. This order is referred to as the “out of plane” ordering

Figure 5.15 (a) shows the scattering of sample-277-7 at $\alpha_i = 0.53$ and $\omega = 0$ deg as described earlier in this section. At the positions marked with the arrows in figure (a), line cuts were extracted and displayed in figure 5.15 (b). Remarkably, the cuts do have different peak shapes as well as different peak positions. The curves at θ_f equal -0.035 deg, -0.071 deg, -0.143 deg and -0.179 deg seem to have broad double peaks at a position in between the ones for θ_f equal -0.107 deg and -0.215 deg. The curves at the latter position have rather sharp and clearly defined peaks.

These differences can be understood consulting the theory on disordered multilayers introduced in section 3.2. The scattering pattern displayed in figure 5.15 (a) corresponds to a section in reciprocal space that cuts the hexagonal plane along a direction given

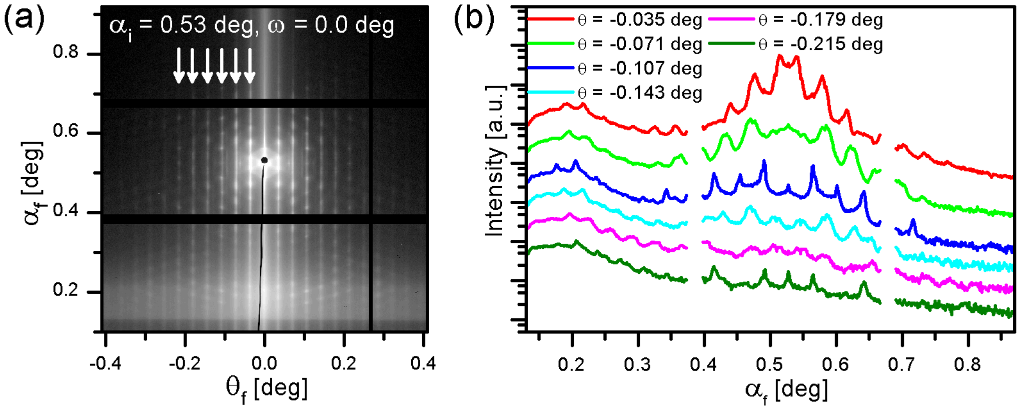

Figure 5.15: (**a**) Scattering pattern of sample-277-7 collected at $\alpha_i = 0.53$ deg and $\omega = 0$ deg). (**b**) Line cuts extracted from the scattering pattern along the truncation rods marked with the arrows in (**a**). The curves are vertically displaced for better visibility. The different peak positions and shapes of the truncation rods can be understood by the assumption of a irregular stacking of the hexagonal planes of the colloidal crystal. See the text for details.

by the reciprocal basis vector $\mathbf{a}_1^*$ or equally $\mathbf{a}_2^*$ as defined in figure 3.3. The curves in figure 5.15 (b) describe accordingly the intensity modulation of the truncation rods at the location of the reciprocal lattice points defined by the form factor of the hexagonal lattice. In the directions defined by $\mathbf{a}_1^*$ or $\mathbf{a}_2^*$, one finds a sequence of two lattice points that are sensitive to the stacking sequence of the hexagonal layers followed by one that exhibits simple Bragg reflections from the planes independent of the stacking. This can be deduced from equation (3.28).

The different peaks in the curves can be understood accordingly. The clearly defined peaks at θ_f equal -0.107 deg and -0.215 deg correspond to Bragg reflections whereas the peak shape and width of the other peaks is given by the stacking probability of the colloidal arrangement. From the extracted line cuts, it is difficult to directly extract a value for the stacking probability due to the interplay of the different scattering components such as the particle form factor of the colloids, the scattering from the grating and the refraction and reflection effects. To fit the data, a model has to be used that includes all these components. This is done in chapter 6 for sample-277-7 and sample-277-14.

5.2.3 Samples Composed of Particles with 590 nm and 740 nm Diameter

The three colloidal assemblies treated in the following consist of polystyrene particles with diameters of 590 nm and 740 nm arranged on a bisected microscopy slide. They were fabricated with convective self-assembly as described in chapter 4.2. The corresponding process parameters are summed up in table 5.3. The column headings in the table are the sample codes indicating particle diameter and average number of layers covering

sample	**-590-1**	**-740-1**	**-740-2**
substrate		flat glass slide	
particle diameter [nm]	590	740	740
concentration of dispersion [wt%]	1	1	1
translation velocity [μm/sec]	4	4	4
temperature of sample stage [°C]	15.00±0.04	20.00±0.01	25.00±0.04
ambient temperature [°C]	22.8	22.8	23.4
ambient relative humidity [%]	22.9	49.7	50.8
average number of layers	1	1	2

Table 5.3: Fabrication parameters and average number of layers of the samples consisting of 590 nm and 740 nm colloids.

the sample. The number of layers corresponds thereby to the most prominent coverage encountered in the central part of the sample. In the case of sample-590-1, there is also a small contribution of uncovered spots and regions with a bilayer. Sample-740-1 does exhibit parts covered with an additional layer on the first one. The bilayer in case of sample-740-2 is almost perfect. The number of layers was evaluated by microscopy as described in chapter 5.2.1.

Characterization by Light Microscopy, AFM and SEM

Figure 5.16 displays a SEM image of the surface of sample-740-1. The micrograph was taken such that the growth direction of the crystal was along the direction marked with the arrow. Individual regions display almost perfect hexagonal order. This order is deranged on larger distances by vacancies, small cracks barely visible at this magnification and ultimately by the changes in the orientation of the hexagonal grating. No preferential orientation of the ordered regions was found from the SEM and AFM images done for the three samples examined in this section.

From the image, it can be seen that the equally oriented regions extend over the whole image in the direction of growth. This elongation of the ordered regions is a typical observation for monolayers fabricated by convective self-assembly [166] and was observed at all particle diameters used in this work. It can be understood considering that particles arriving at the assembly zone in the meniscus will most probably adopt the order given by the already ordered colloids.

If one compares the dimensions of the ordered regions for the different particle sizes, they have different sizes. However, one arrives with a similar range of extensions, by comparing the number of ordered particles. In general, investigations with AFM, microscopy and SEM from samples consisting of colloids with diameters of 277 nm, 590 nm and 740 nm yield results that differ by scale but are otherwise comparable.

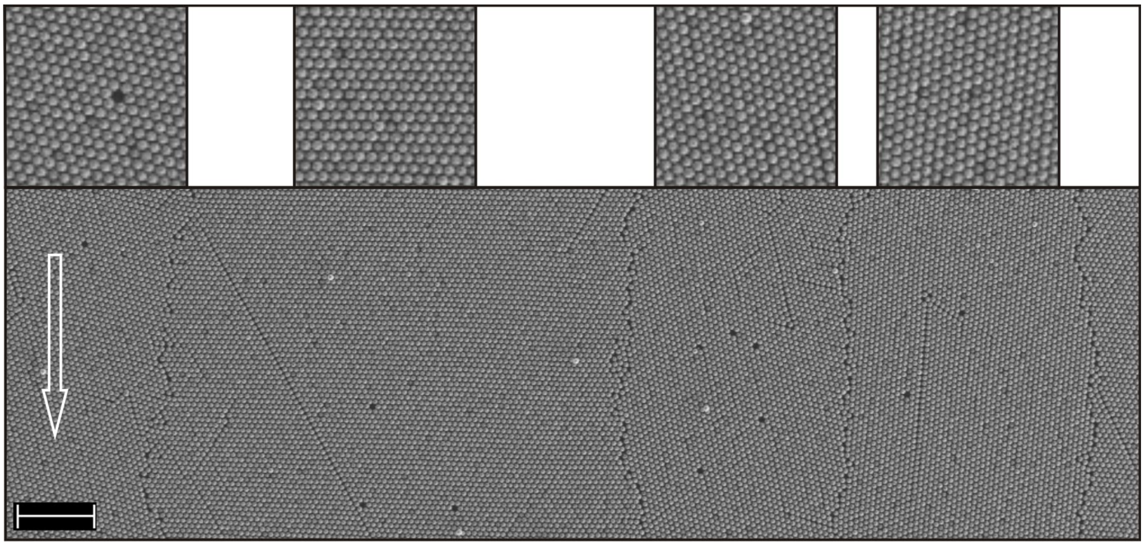

Figure 5.16: SEM image of sample-740-1: The growth direction of the colloidal monolayer is marked with the arrow on the left hand side. The scale corresponds to 10 μm. The smaller figures in the upper row are zoomed in areas of the domain below. They illustrate the different orientation of the individual regions.

GISAXS Experiments

The GISAXS experiments on sample-590-1, sample-740-1 and sample-740-2 were performed at the cSAXS beam line, see chapter 4.4 or [159] for a description. An X-ray beam with an energy of 11.2 keV was used. It was focused on the detector leading to a beam diameter at the sample position of $\sim 1 \times 1\,\mathrm{mm}^2$. The Pilatus 2M detector and the 7 m long flight tube were used. The flight tube had an entrance window of Mica, ~5 μm thick and an exit window consisting of a ~350 μm thick Mylar foil. The Pilatus 2M detector was positioned right behind the exit window of the flight tube.

The experiments were done as described in the previous section. Samples were positioned on the goniometer and the scattered intensities were then measured at various sample orientations and different incident angles α_i. The sample orientation is indicated by the angle ω. As before, $\omega = 0$ deg denotes the position where the growth direction is parallel to the scattering plane. Sample-590-1 and sample-740-1 have both been scanned in a range from -90.5 deg to 90.5 deg at every 0.2 deg. The ω-interval for sample-740-2 covers a range of 70 deg starting at $\omega = 25$ deg and ending at $\omega = 95$ deg. A scattering pattern was measured every 0.1 deg.

Figure 5.17 shows examples of the collected GISAXS intensity maps for sample-590-1, ($a_{1/2}$), sample-740-1 ($b_{1/2}$) and sample-740-2 ($c_{1/2}$). The displayed intensity maps correspond to an average over 11 individual maps covering an ω interval of 2 deg in the case of sample-590-1 and sample-740-1 and an interval of 1 deg for sample-740-2. The average has only been done for the sake of a distinct representation of the scattering

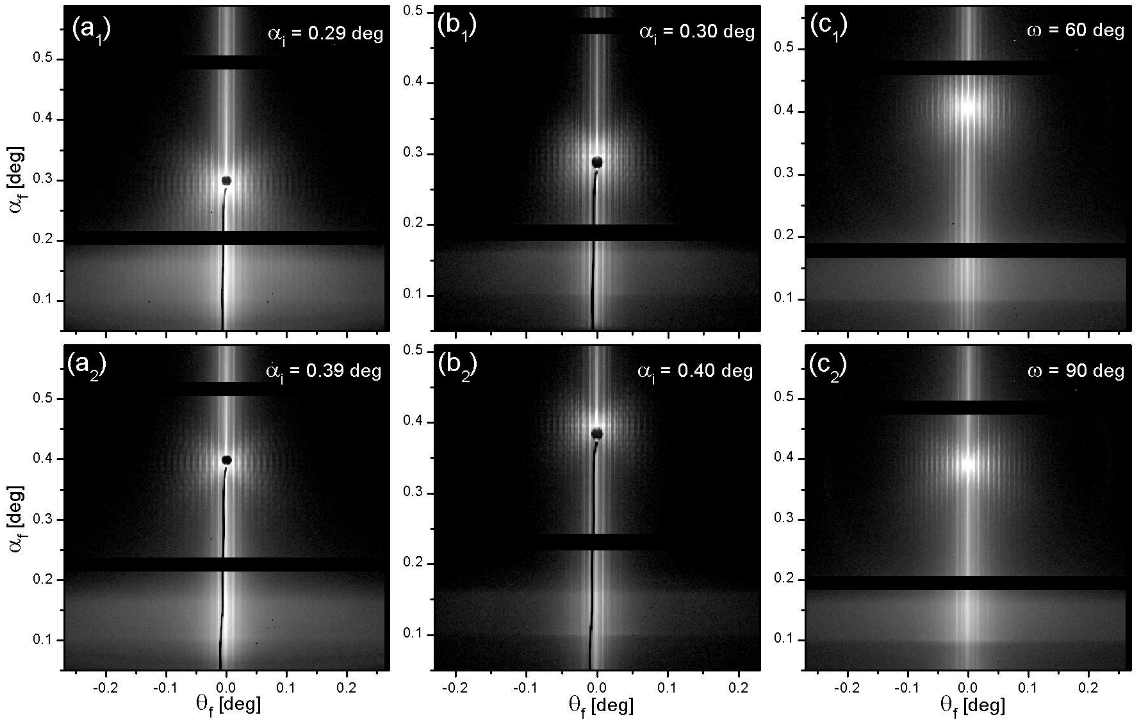

Figure 5.17: GISAXS patterns measured from (**a**) sample-590-1, (**b**) sample-740-1 and (**c**) sample-740-2. In the case of the first two samples, scattering patterns with a different incident angle are displayed: α_i = 0.29 deg for ($\mathbf{a}_1$), α_i = 0.39 deg for ($\mathbf{a}_2$), α_i = 0.30 deg for ($\mathbf{b}_1$) and α_i = 0.40 deg for ($\mathbf{b}_2$). The scattering patterns for sample-740-2 have both an incident angle of 0.44 deg but the sample orientation is different. The intensity is differently scaled in all scattering patterns for the sake of better visibility.

patterns. As previously described, the bars without intensity originate from the detector. The reflected beam is shadowed by a beam stop only in case of sample-590-1 and sample-740-1. No beam stop was inserted for sample-590-2.

When examined, it becomes apparent that the GISAXS patterns stay basically unchanged for all sample orientations in the case of the two samples covered with a monolayer. Only sample-740-2 exhibits some difference between different sample orientations. Figure 5.17 (c_1) and (c_2) display the cases for a sample orientation at ω = 60 deg and ω = 90 deg, respectively. A slight change in the positions of the main peaks is detectable.

In-Plane Evaluation of GISAXS Data

An evaluation on the scattering data equal to the one detailed in chapter 5.2.2 was used to asses the in-plane order of the colloids, i.e. the arrangement of the particles parallel to the glass substrate. The corresponding graphs for sample-590-1, sample-740-1 and sample-740-2 are shown in figure 5.18 (a), (b) and (c), respectively. In case of (a) and (b), the graphs display the integrated intensities from positive and negative θ_f sides of the original intensity maps. The point where $Q_x = Q_y = 0$ is in the center of the plots. Graph (c) shows the intensities only for the positive θ_f values. $\mathbf{Q}_{||} = (Q_x^2 + Q_y^2)^{1/2} = 0$ corresponds accordingly to the apex of the segment. The ω scans to create the figures were measured at incident angles $\alpha_i = 0.294 \pm 0.005$ deg for sample-590-1, $\alpha_i = 0.293 \pm 0.005$ deg for sample-740-1 and $\alpha_i = 0.30 \pm 0.01$ deg for sample-740-2.

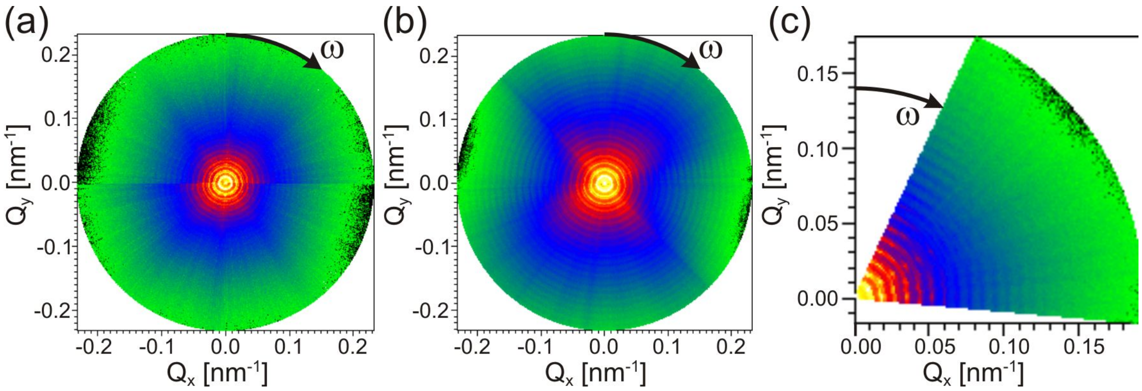

Figure 5.18: Visualization of the scattering intensity modulation parallel to the substrate. The concentric circles in the case of (**a**) sample-590-1 and (**b**) sample-740-1 indicate a random orientation of the hexagonally packed regions on the sample. The intensity modulations in the according structures of (**c**) sample-740-2 are a sign of a preferential orientation.

The concentric circles in the case of the monolayers indicate that the hexagonally ordered grains on the sample have a random orientation. Cuts along ω similar to those done in 5.10 (b) and 5.11 (b) display a certain ω dependence but no clear peaks. The center to center distance of the colloidal particles found for sample-590-1 is 604 ± 20 nm and 760 ± 20 nm for sample-740-1. The large error with respect to earlier results is caused by the fact that the position of the peaks is not that well located due to the lower experimental resolution. An example of a cut through the data can be seen in figure 5.19 (b). Figure 5.19 (a) shows cuts along ω for two different $\mathbf{Q}_{||}$ values in the case of sample-740-2. As can be seen, one curve has maxima at 30 deg and 90 deg and the other one has a single maximum at 60 deg. The peaks do not have such a clearly defined shape as the ones observed in figures 5.10 (b) and 5.11 (b) but they demonstrate a preferential orientation of the ordered grains on the sample. The peak at 60 deg was fitted with a Lorentzian function. The resulting FWHM amounted to 7.5 ± 2.5 deg.

Figure 5.19 (b) displays the intensities taken from the data displayed in 5.18 (c) at $\omega = 60$ deg and $\omega = 90$ deg plotted versus $\mathbf{Q}_{||}$. The $\mathbf{Q}_{||}$ positions where the cuts in 5.19 (a) were extracted from are indicated by an arrow. By calculating the grating parameters resulting from the main peaks along the two dimensions, one can identify the direction at $\omega = 60$ deg with the (1 1 0) and the direction at $\omega = 90$ deg with the (2 1 0) direction on the hexagonal plane in reciprocal space. The resulting distance between the colloidal particles yields 754 ± 20 nm.

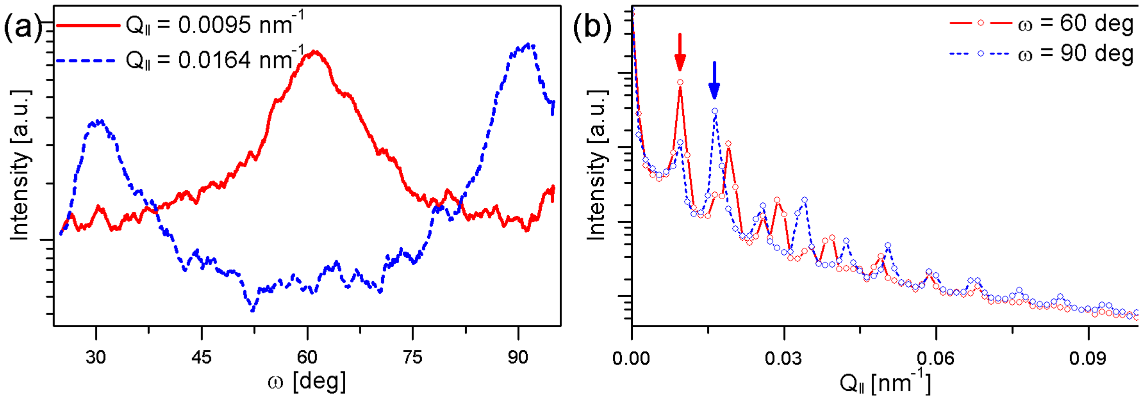

Figure 5.19: Data of sample-740-2: (**a**) Cuts along ω extracted from graph 5.18 (c) at different $\mathbf{Q}_{||}$ values. The corresponding positions are marked in graph (**b**) with arrows of the corresponding color. The two line cuts are data extracted along increasing $\mathbf{Q}_{||}$ and constant sample orientation from 5.18 (c).

Therefore, one finds a preferential orientation of the ordered grains with respect to the growth direction that is the same for sample-740-2 than for sample-277-7 and sample-277-14. While the order is not as well expressed as in the case of the samples with more than two layers, it is still appreciable. By fitting the peak at $\omega = 60$ deg in figure 5.19 (a) and further peaks at higher $\mathbf{Q}_{||}$ values with a Lorentzian line shape, one results with a FWHM of 7.5 ± 2.5 deg.

5.2.4 Colloidal Assemblies on Surface Relief Gratings

Apart from smooth glass slides, pDR1M surface relief gratings were also applied as substrates in the self-assembly process of the colloidal assemblies. These substrates introduce a patterned surface in the self-assembly process. Such templates have been found to influence the long range order and the crystallographic symmetry of the final self-assembled colloidal structures, see chapter 1.1.2. The surface relief gratings were prepared as described in chapter 4.1 and covered by dip-coating, a convective self-assembly technique described in chapter 1.1.2.

Each of the two samples that are discussed in this section consist of two gratings written on top of each other. In one case, an angle of 60 deg was set between the two gratings. On the other sample, the two gratings were written with a 90 deg angle between them. The parameter that characterize the gratings and the self-assembly process for the two samples are summarized in table 5.4. The sample codes in the column headings indicate the gratings and the average number of particle layers. Throughout the remaining text the two samples will be termed correspondingly sample-60-2 and sample-90-2. Both samples are mainly covered with two layers of polystyrene colloids but almost a third of the area on both cross gratings are covered by three or more layers. In the case of sample-60-2, the multilayers are in addition relatively irregular.

sample	**-60-2**	**-90-2**
substrate	pDR1M surface relief grating	
grating period [nm]	648±16	752±89
grating height [nm]	96±5	80±3
angle between gratings [deg]	60	90
particle diameter [nm]	740	740
concentration of dispersion [wt%]	3	3
translation velocity [μm/sec]	2.5	2.5
temperature of sample stage [°C]	ambient temperature	
ambient temperature [°C]	23.0	23.2
ambient relative humidity [%]	54.5	53.5
average number of layers	2	2

Table 5.4: Fabrication parameters and average number of layers characterizing the pDR1M surface relief gratings covered with 740 nm colloids.

The values for the grating period and height were assessed by AFM measurements before actually covering the sample with colloids. Results of such measurements for both samples can be seen in the left part of figure 5.20. By the angle between the structures, the two images can be assigned to the corresponding sample. The grating height describes the difference between the lowest and the topmost parts of the surface structure. AFM measurements on cross gratings gave a large variation of obtained grating periodicities. This is because an averaged correction factor was used to calibrate both scan axes of the AFM. The grating period was chosen to match diameter of the colloids as close as possible. A hexagonal colloidal assembly was aimed for the 60 deg grating. Accordingly, the period is around $3^{1/2}/2$ times smaller than the particle diameter. In case of the 90 deg grating, a cubic arrangement was intended and the grating periodicity matches approximately the colloidal diameter. The difference between the ideal diameter that perfectly matches the measured periodicity of the grating and the actual particle diameters evaluated with different methods, see table 5.1, is less than 6 % for all cases. This is well below the 10 % missmatch that has been found to lead to an uncontrolled assembly in other studies [52, 53].

Characterization by Light Microscopy, AFM and SEM

The inspection by light microscopy gave for both samples the impression that they are covered more inhomogeneous than the samples on the glass substrates. AFM and SEM investigations on sample-60-2 and sample-90-2 do in general display results very similar to the ones found for colloidal assemblies on flat glass substrates. It appears that the template does not increase the order. For both samples, one can spot ordered regions that seem to be oriented along the grooves of a grating. Such domains seem not to occur with an increased probability with respect to other orientations. However, it is quite hard to detect the exact orientation of the surface grating on a covered sample with the two techniques in order to get a reference direction.

On the right hand side of figure 5.20, one can see a SEM micrograph of the colloidal assembly on top of sample-90-2. The image shows a change in the number of layers. The domains have various orientations and a hexagonal symmetry although the underlying template has a cubic symmetry. Only at the start of the second layer one observes a cubic arrangement. These are transitional states observed at the change over different number of layers [79, 167] and can also be seen on glass substrates.

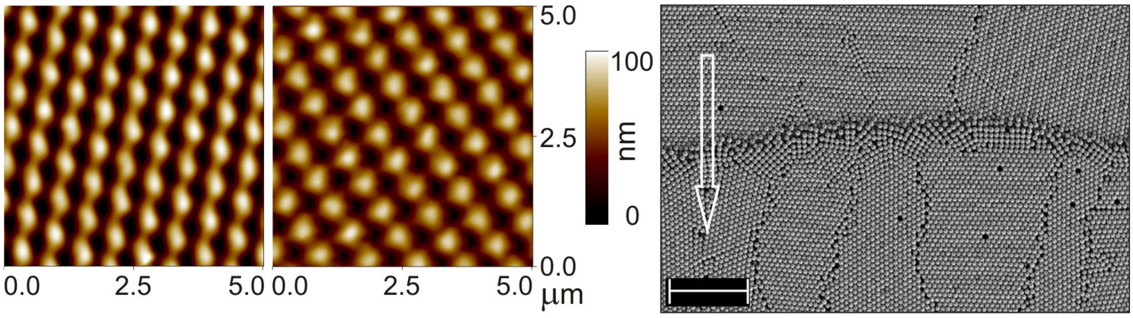

Figure 5.20: *left*: AFM data of the surface structure of sample-60-2 and sample-90-2. *right*: SEM image of the colloidal assembly on sample-90-2 templated with a 90 deg square lattice. The image shows a change in the number of layers. The domains have various orientations and a hexagonal symmetry. The growth direction is marked with the arrow. The scale corresponds to 10 μm.

GISAXS Experiments

The GISAXS experiment on sample-60-2 and sample-90-2 were done at the cSAXS beam line with a setup identical to the one described in the previous section 5.2.3. For comparison, data of bare surface relief gratings are also displayed.

Sample-60-2 was scanned in an ω range between -90.5 deg to 90.5 deg and a step size of 0.2 deg. $\omega = 0$ deg marks the sample orientation where the beam was parallel to the growth direction of the colloidal crystal. The scan for sample-90-2 covered a range between 2.0 deg to 102.0 deg with a step size of 0.1 deg.

Figure 5.21 shows measured GISAXS intensity maps for different sample orientations. The upper row, i.e., images (a_i) correspond to results obtained from a bare surface relief grating while the images (b_i) show intensity maps of sample-60-2. The bare grating corresponded to a simple grating with a period of 675 ± 1 nm and a height of 14 ± 1 nm both values obtained by AFM. The scattering patterns are well understood [168] and were measured with the identical parameters as for sample-60-2. The images with the index 1 were taken at an orientation where a gratings was aligned parallel to the beam.

The patterns to the right display the dramatic change in the scattered intensity as the grating is turned away from the parallel direction. This effect can be understood by the intersection of the Ewald sphere with the surface truncation rods of the grating and is described in detail in [132, 163]. If one compares the corresponding scattering patterns from the bare and the covered grating, one notices that there is mainly a change of intensity around the reflected beam and at the position of the Yoneda band. This intensity can be attributed to the scattering signal from the colloidal assembly by recalling earlier scattering patterns obtained from assemblies on flat glass substrates.

From the distance of the grating peaks in figures 5.21 (a_1) and (b_1), one can calculate the grating period of the two samples. A period of 667 ± 20 nm was found for the bare surface grating and 658 ± 20 nm for sample-60-2. This agrees with the values obtained by AFM measurements.

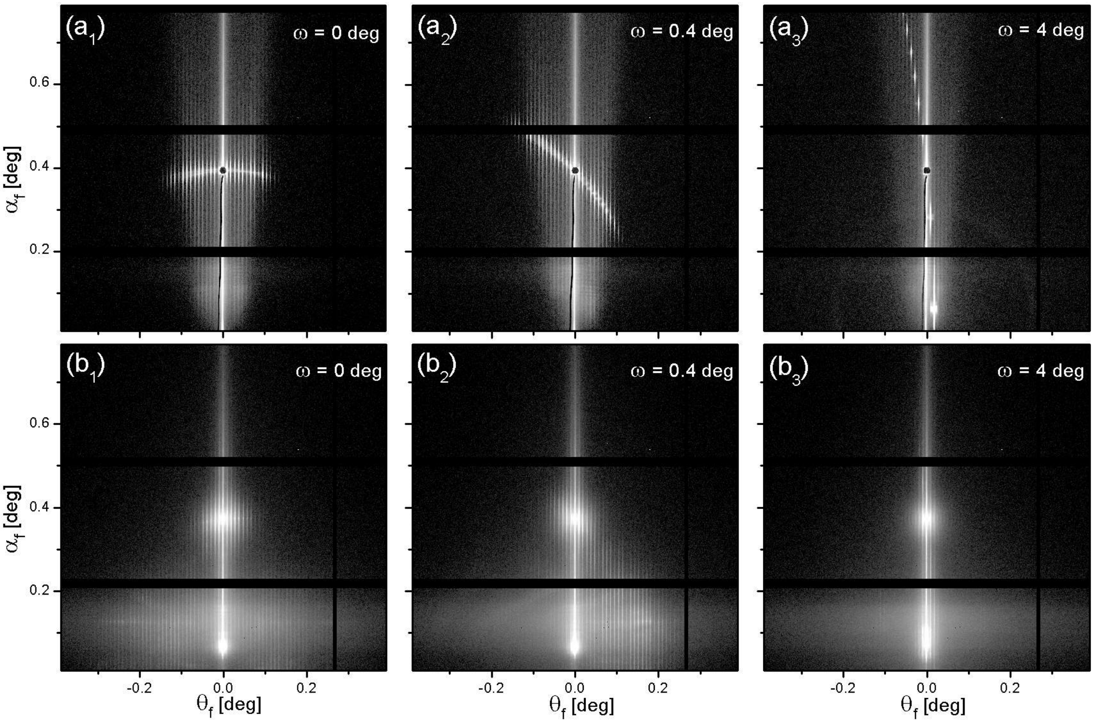

Figure 5.21: GISAXS intensity maps at different sample orientations: (**a**) a bare surface grating and (**b**) sample-60-2 consisting of a surface grating covered with a double layer of colloids. The scattering patterns (**a**$_1$) and (**b**$_1$) correspond to the situation where one of the gratings on the sample is parallel to the beam. The patterns to the right display the dramatic change in the scattered intensity as the grating is turned away from the parallel direction. This effect is well understood and described in [132,163]. The intensity is differently scaled for each sample but the same each row.

In-Plane Evaluation of GISAXS Data

The in-plane order of sample-60-2 and sample-90-2 was examined by the same method as described in chapter 5.2.2. As a comparison, the same approach has also been used on the scattering data of a bare 60 deg cross grating. The corresponding plots can be seen in figures 5.22 (a), (b) and (c) for the bare grating, sample-60-2 and sample-90-2, respectively. In case of (a) and (c), the graphs only displays the intensities for the positive θ_f values of the original scattering pattern. Graph (b) shows the integrated intensities from positive and negative θ_f sides. The corresponding ω scans were done at incident angles α_i of 0.41 ± 0.01 deg for the bare grating, 0.260 ± 0.01 deg in case of sample-60-2 and 0.30 ± 0.01 deg for sample-90-2.

The highly periodic structure of the bare surface relief grating leads to a very regular arrangement of the peaks in figure 5.22 (a). The hexagonal symmetry is well identifiable. In the case of sample-60-2, similar peaks are still present but not as clearly visible. There appear also weak hexagonally shaped rings around the center of the corresponding graph. It can be inferred that the underlying sample structure does induce a certain if only weak ordering in the arrangement of the colloidal particles. The graph corresponding to sample-90-2 does exhibit a cubic arrangement of peaks reflecting the symmetry of the surface grating. In addition, weak powder rings are detectable that have a circular shape as far as discernible. Ordered regions on the sample seem therefor to have an arbitrary orientation.

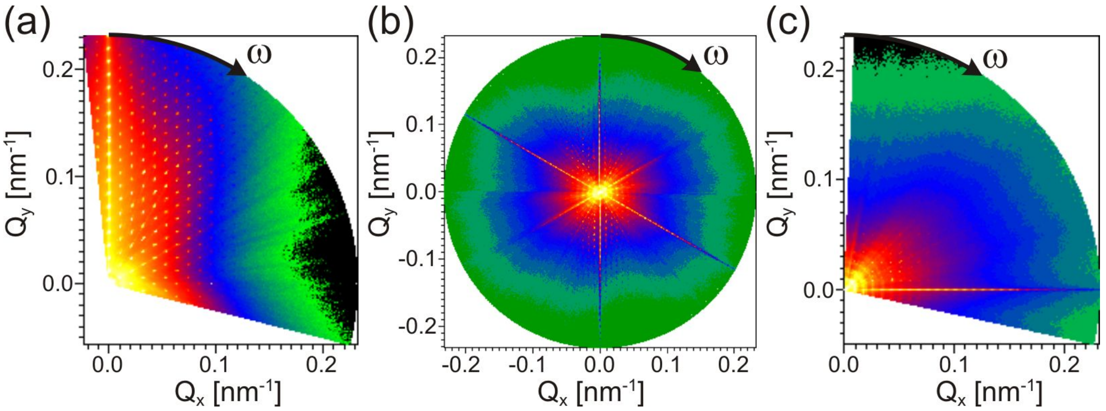

Figure 5.22: Display of the scattering intensity modulation parallel to the substrate. (**a**) The highly regular structure of the uncovered cross grating leads to a multitude of regularly arranged peaks. Similar peaks are still perceptible in the case of (**b**) sample-60-2. The main peaks in the case of (**c**) sample-90-2 indicate a cubic symmetry.

5.2.5 Discussion

Colloidal Assemblies on Glass Substrates

Colloidal assemblies of different particle sizes were fabricated by convective self-assembly on smooth glass substrates. They have then been characterized by GISAXS and "classical"[3] methods such as light microscopy, AFM, SEM. In combination, a detailed picture of the samples was obtained.

Domain Size from Microscopy, AFM and SEM

Concerning the domain size, no appreciable dependence on the particle size was found from the samples investigated throughout this work. All investigated samples exhibit locally an almost perfect hexagonal close packed arrangement of the colloids. This order breaks down as one increases the distance to a reference point. Missing colloids, cracks or differently oriented regions corrupt the perfect order. The estimated size of the perfectly ordered domains from AFM and SEM pictures was for all samples in the range of about 20–40 particle diameters perpendicular to the direction of growth and 40–60 along the growth direction. This difference is a consequence of the directed growth of the colloidal crystals in case of convective self-assembly. While regions with the same orientation of the particle arrangement can extend over much larger distances, >300 particle diameters perpendicular and parallel to the growth direction, the given values account for small cracks and irregularities within these zones. Overview images taken with a SEM give the impression of a perfect structure in these domains. However, AFM investigations clearly show small imperfections. As X-ray scattering methods are already sensitive to small deviations, these imperfections have been defined as the domain boundaries in this work. AFM and SEM data were not collected to provide statistical relevant information on the individual samples. In the following discussion samples will only be distinguished by the number of layers due to the comparable results for the different particle diameters.

Domain Size from GISAXS Measurements

X-ray scattering methods access the correlation length of a crystalline structure through the width of the Bragg reflections in reciprocal space, see chapter 3.1. Relatively disordered materials exhibit smeared out diffraction peaks while a correlation over large distances leads to sharp reflections. In a real experiment, the resolvable peak width is limited by the experimental resolution that arises from the beam divergence, the distance between sample and detector and the pixel size of the detector. The experimental resolution defines accordingly the longest correlation length that is accessible.

In case of the cSAXS beam line, the calculated in-plane resolution, i.e., the resolution along Q_y amounted to $\Delta Q_y = 1.3 \cdot 10^{-3}\,\mathrm{nm}^{-1}$. The maximal measurable correlation length corresponded therefore to $\sim 4.8\,\mu$m. This corresponds to about 17 particle diameters in the case of the 277 nm colloids, about 8 in the case of the 590 nm particles and

---

[3] In the following discussion, this term subsumes the the three methods, microscopy, AFM and SEM, that are well established for the investigation of the colloidal samples.

about 7 diameters for the 740 nm colloids. From these values, it can be concluded that the technique is not appropriate for the study of domain sizes in the case of these large particles unless the resolution can be improved by an order of magnitude.

In case of the multilayers consisting of 277 nm particles, the evaluation of the in-plane peak width did nevertheless provide insight in the crystal structure. It was found that the peak width broadens for increasing peak orders along the (1 0 0) and (1 1 0) directions in reciprocal space, i.e., $\omega = 0$ deg and $\omega = 60$ deg, respectively. This corresponds to a so-called paracrystalline ordering meaning that the scattering centers have larger and larger deviations from the ideal crystalline grating as one increases the distance to an arbitrary reference point. For both multilayers, the broadening of the peaks occurs clearly faster for $\omega = 0$ deg, i.e., for the case where the GISAXS pattern was sensitive to the order perpendicular to the growth direction, than for $\omega = 60$ deg. This observation concurs with the results from microscopy, SEM and AFM that show a decreased order perpendicular to the growth direction.

Multilayers

In the case of the samples consisting of 7 and 14 layers, the domains were found to exhibit a similar alignment on all investigated regions, i.e., different sample regions, millimeters apart from each other, did exhibit an almost identical alignment. This agrees with results of other authors that found identically oriented regions across ranges of 1 cm on colloidal multilayers fabricated with convective self-assembly [20, 75–77, 83]. These results have been obtained by SEM.

GISAXS data collected on our multilayers, demonstrates that the investigated samples have a similar alignment of the domains over the complete sample. This is ascertained by the fact that the beam footprint ($\sim$1 mm lateral and $>$ 60 mm along the beam path) has probed the complete length of the sample due to the grazing incident angles. The distribution describing the domain misalignment was fitted with a Gaussian function and gave for the two investigated samples an almost identical FWHM of 4.4 ± 0.9 deg and 4.3 ± 0.8 deg, respectively. Furthermore, all characterization methods indicate that the preferential orientation of the ordered domains depends on the growth direction of the multilayers. It was found that the colloidal particles align along the growth direction, i.e., the [1 0 0] direction of the hexagonal planes are parallel to the growth direction. A correlation between the growth front and the orientation of the domains has also been observed in an earlier investigations [83, 96] where the alignment was probed by comparing the orientation of SAXS scattering patterns obtained from positions all over the sample.

Monolayers

In the case of the monolayers, no alignment of the individual domains could be detected by AFM and SEM measurements. This observation is confirmed by the in-plane evaluation of the GISAXS data that proofs the arbitrary orientation of the domains in the plane parallel to the sample surface.

Bilayer

Sample-740-2 seems to be a transitional state between the two cases described so far. GISAXS data shows clear evidence of a preferential alignment of the ordered regions. As in the case of the multilayers, the data gives evidence that the colloidal particles align along the growth direction. The orientation is not as expressed as in the case of the multilayers. The distribution describing the domain misalignment was fitted with a Lorentzian function and provided a FWHM of 7.5 ± 2.5 deg.

Summary

From the presented data, one can conclude that the transition from a self-assembled monolayer to two layers and further towards multilayer goes in parallel with the development of a mechanism that leads to the directed self-assembly of the particles. In the case of monolayers, the assembly mechanism is well studied [69–72]. It is understood that the particles aggregate because of capillary immersion forces. These forces start to act as colloidal particles protrude from a thin water film as sketched in figure 5.23. In the case of multilayers, the process is understood qualitatively only. A detailed mechanism that explains how three-dimensional close packed structures of colloidal spheres emerge has not been clearly identified so far [73]. First theoretical considerations have been done that concentrate on the reasons for the specific three-dimensional stacking of the colloidal assemblies [73]. Two mechanisms have thereby been considered. The solvent flow through the pore space between the already packed colloids could on the one hand cause a preferential positioning of further particles. On the other hand, a flow parallel to the surface of a hexagonal packed layer could cause a preferential deposition due to the surface topography.

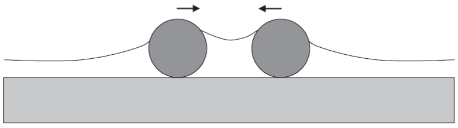

Figure 5.23: Capillary immersion forces [71, 72] acting on colloidal spheres protruding from a thin layer of water. Figure taken from [73].

It can only be hypothesized that the strength of the solvent flow also plays a role in the macroscopic alignment of the ordered colloidal regions. This hypothesis could be checked by colloidal multilayers with an identical thickness that have been fabricated at different evaporation rates, i.e., different solvent flow rates. If the sample with the better alignment was produced at higher flow rates, this would indicate an influence of the solvent flow on the alignment. In reference [83], the authors observed also a dependence of the degree of orientation on the particle size. Assemblies consisting of smaller particles (250 - 400 nm) have been found to exhibit in general a better orientation than colloidal crystals built up of larger particles (450 - 750 nm).

As shown with the presented investigations, GISAXS is an ideal tool to detect the exact degree of the domain alignment on samples. The technique could therefore assess the influence of different factors influencing the alignment of the ordered domains. This evaluation could then lead to a deeper understanding of the detailed mechanisms that lead to the three-dimensional particle assembly. A profound control over the particle assembly would be gained.

Colloidal Assemblies on pDR1M Surface Relief Gratings

Colloidal multilayers have also been assembled on templated supports. The two presented samples were fabricated on pDR1M thin films with a hexagonal and a cubic cross grating inscribed. The samples were characterized with GISAXS and classical methods in the same manner as the samples with an unstructured glass substrate.

Results Obtained by Microscopy, AFM and SEM

Investigations with the classical methods did not reveal perceptible differences to the samples assembled on flat glass. The inspection by light microscopy yielded the result that the samples on the structured supports exhibited a more inhomogeneous coverage than the samples on glass substrates. The influence of the topologically templated substrate on the colloidal arrangement could neither be ascertained by SEM nor by AFM. No evidence of cubic arrangement induced by the substrate was found on the corresponding sample.

Results Obtained by GISAXS

The GISAXS data confirmed the findings by the classical methods. The hexagonally structured surface grating induced only weak alignment. In the case of the cubically structured support, the in-plane evaluation revealed even an arbitrary alignment of the ordered domains. This is in contrast to the generally accepted and experimentally confirmed view, that template assisted self-assembly leads to an increased long-range order and can be used to influence the crystal orientation and crystal symmetry, see chapter 1.1.2.

Summary

The differing results can with a high probability be attributed to problems during the assembly of the colloidal particles. The structure of the templates could brake the free mobility of the colloidal particles on the surface. They could then be hindered to assemble in an ordered fashion. Other studies using topologically structured surfaces in combination with convective self-assembly did however not report on similar problems [83]. A too large mismatch between the colloidal diameter and the corresponding grating periodicity could also be a reason for a decreased ordering. With AFM measurements before the covering, it was however ascertained that the mismatch is $< 6\,\%$ for the two presented samples. In earlier studies, a pronounced decrease in the quality of the assembly has only been found for a missmatch $\gtrsim 10\,\%$.

Much more probable seem problems induced during the fabrication of the thin pDR1M polymer films and the writing process of the grating. The films were prepared in a normal laboratory and are therefore prone to contamination by dust particles. Particles sitting on top of the polymer surface or included in the surface of the polymer films can easily derange the self-assembly process. Moreover, it was observed that even small misalignments in the optical setup upon writing the surface structure lead to the formation of bleached ring patterns on the polymer. These regions exhibited very irregular colloidal coverage after convective self-assembly. Prior to further self-assembly experiments on pDR1M surface gratings, these factors will have to be investigated in more detail.

5.3 Investigations During the Formation of Colloidal Assemblies

X-ray scattering methods were used to probe the self-assembly process of colloidal particles *in situ*. As a simple and readily available system for such investigations, the drying up of droplets of colloidal dispersion was chosen. It is known since a long time that the residual particles of a dried droplet exhibit ordered close packed structures [169]. Later investigations revealed that the assembly process can be understood by convective self-assembly [69, 70] as introduced in chapter 1.1.2.

In the current work, the drying was probed by ED-XRR and GISAXS. The drying of the colloidal droplets was done on top of pDR1M surface relief gratings. The period of the gratings was matched with the distance between rows of hexagonal close packed colloids. The templated surfaces were used to direct the ordering process. The results of the experiments are presented and discussed in the following.

5.3.1 ED-XRR Results

All ED-XRR experiments were performed at the EDR beam line at BESSY II in Berlin. A detailed description can be found in chapter 4.4 and [110,161]. The sample cell SMZ05 described in chapter 4.4 was mounted on a goniometer and the surface grating positioned in it. For the *in situ* investigations, the cell was capped in order to reduce the water evaporation rate from the colloidal droplet. The desired temperature of the sample stage was set on a controller that actuated the Peltier element integrated in the stage of the cell. Temperatures of the sample stage were in the range between ∼ 17–26 °C. The distance between the sample and the slits in front of the energy dispersive Si-drift detector (RÖNTEC) amounted to ∼ 1.2 m.

In an actual *in situ* experiment, the surface grating was illuminated at a certain incident angle α_i and the detector was position slightly above and beside the reflected beam, i.e., in a slightly off-specular position. This position was tuned to optimally detect the grating peaks. The surface grating was oriented such that the beam crosses the grating at an acute angle. The grating period "seen" by the X-ray beam, Λ_B, has accordingly been much larger than the effective period measured perpendicular to the grating grooves, Λ. The period measured by the beam can be calculated according to

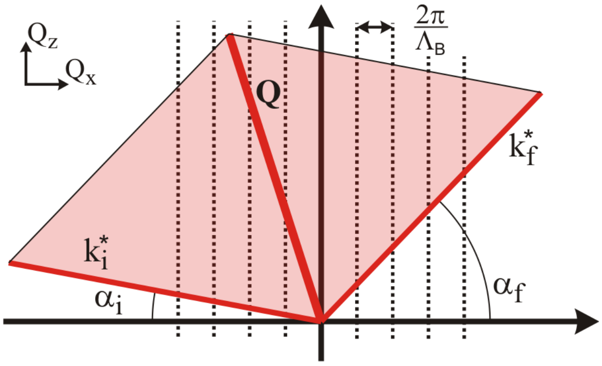

Figure 5.24: Schematic of the reciprocal space corresponding to the *in situ* experiments performed at the ED-XRR beam line. Experimentally, one measures an increased intensity wherever the scattering vectors (red line) cross a surface truncation rod of the grating.

$\Lambda_B = \Lambda / \sin\omega$ where $\omega = 0$ denotes the angle at which the grating is aligned parallel to the beam. A simple schematic of the experiment in reciprocal space can be seen in figure 5.24. The figure is a projection on the Q_x, Q_z plane where Q_z denotes the direction perpendicular to the sample surface and Q_x is parallel to the surface in the plane spanned by the incident and reflected beam.

Before putting the droplet of colloidal dispersion on top of the pDR1M surface relief grating, the pDR1M surface was shortly (∼ 10–20 sec) treated by diluted sulfuric acid (40 μl, 1 %) to make it more hydrophilic. The acid was carefully removed by a wipe before applying the droplet of colloidal dispersion. It generally consisted of 40 μm dispersion with 0.02–1.00 wt% colloidal particles. The cap of the sample cell was then put on and the scattering experiment started. Counting times of the detector where set to 25.75 sec. Together with the read out time, this resulted in about one measurement every 30 sec. The humidity in the sample cell was continuously read out by the controller for the Peltier element and was manually noted in the logbook during the experiments.

Figure 5.25 shows a summary of an *in situ* experiment done on a drying droplet of colloidal dispersion. This experiment was done with a temperature of the sample stage at 19.2±0.4 °C. The colloidal dispersion contained 0.08 wt% polystyrene colloidal particles. The upper graph shows the evolution of the integral intensity measured by the detector (red solid line) and the humidity in the sample cell (blue dashed line) during the minutes before and shortly after the complete dry-out of the colloidal droplet. The inset depicts the evolution of these two parameters during the complete measurement. The time scale is given in minutes and exemplifies a typical duration of such an experiment between 2 to 5 hours. The instant when all water has evaporated from the droplet is marked by the abrupt change in steepness of the humidity evolution. After this instant, there is no longer a source of water that maintains the elevated relative humidity with respect to the surrounding of the sedimentation cell. As can be seen, the integral intensity starts to increase shortly before the complete dry-out and reaches an elevated level around the dry-out. In between, there is a sharp peak in the integral intensity. The lower graph of figure 5.25 shows the detector signal for the identical period as the graph above in the range between 5.2 - 14.5 keV. The intensities were corrected for the incident spectrum as described in chapter 4.4. Very few photons reach the detector before the last minutes of the experiment. Only then, the signal intensity increases starting at higher energies, peaks and reaches an elevated level with two maxima. They correspond to the grating peaks visible in the scattering signal already before the *in situ* experiment and do not show a difference in their position before and after the experiment.

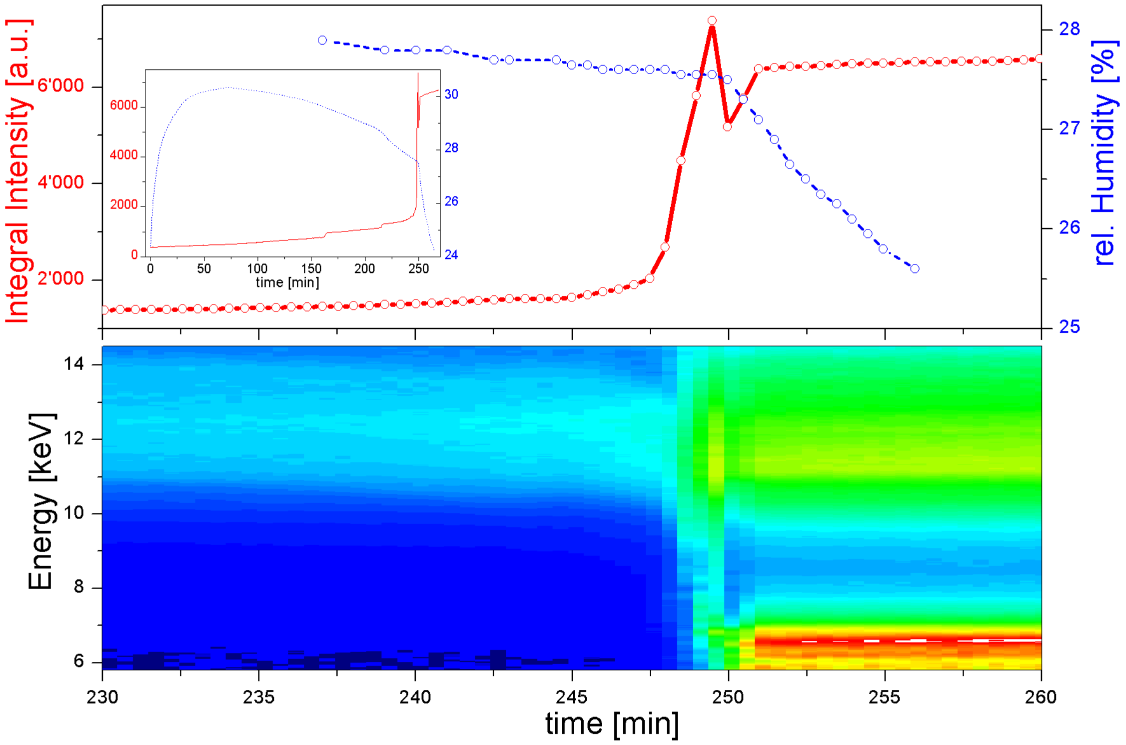

Figure 5.25: (*above*) Evolution of the integral detector intensity and the relative humidity in the sample cell during the last minutes of the experiment. The inset shows the corresponding parameters for the complete experiment. (*below*) Detector signal for the identical period as the graph above. See text for details.

No clear evidence of ordering process of the colloidal particles can be detected from the presented scattering data. Up to the last few minutes the scattering intensity is too low to measure any discriminable signal. The low intensity is attributed to the absorption of the water. This explains why the intensity of the higher energies starts to increase first as the beam penetrates less and less water. The higher energies are less absorbed by mater than lower ones. The interval until the complete dry-out is only between 5 to 10 minutes which gives not enough measurements with the applied scattering method to result with a conclusive interpretation of the data. About the origin of the intense maximum just before the drop in the relative humidity can only be speculated.

5.3.2 GISAXS Results

The *in situ* GISAXS experiments were done at the cSAXS beam line with a setup identical to the one already described in section 5.2.3. Only for these experiments, the sedimentation cell SMZ05 was fixed on the goniometer and the surface grating was placed in it. The cell was only introduced to diminish the evaporation rate of the water in the colloidal droplet. The Peltier element was not used to control the temperature of the sample stage but all GISAXS experiments were performed at ambient temperature of about 24 °C.

For the actual experiments, surface gratings were positioned in a manner that the scattering from the grating can be clearly detected. The droplet of colloidal dispersion was given on the surface of the grating as described above, the cell covered and the experiment started. In the first part of the experiment, the detector was set to take an exposure of 1 second every 29 seconds. This scheme was switched to one frame each second as soon as the first distinct changes in the scattering pattern were observable. The humidity in the sedimentation cell was logged simultaneously to the exposures. For that purpose the sensor had previously been connected to the beam line electronics and could be read out automatically during the experiment.

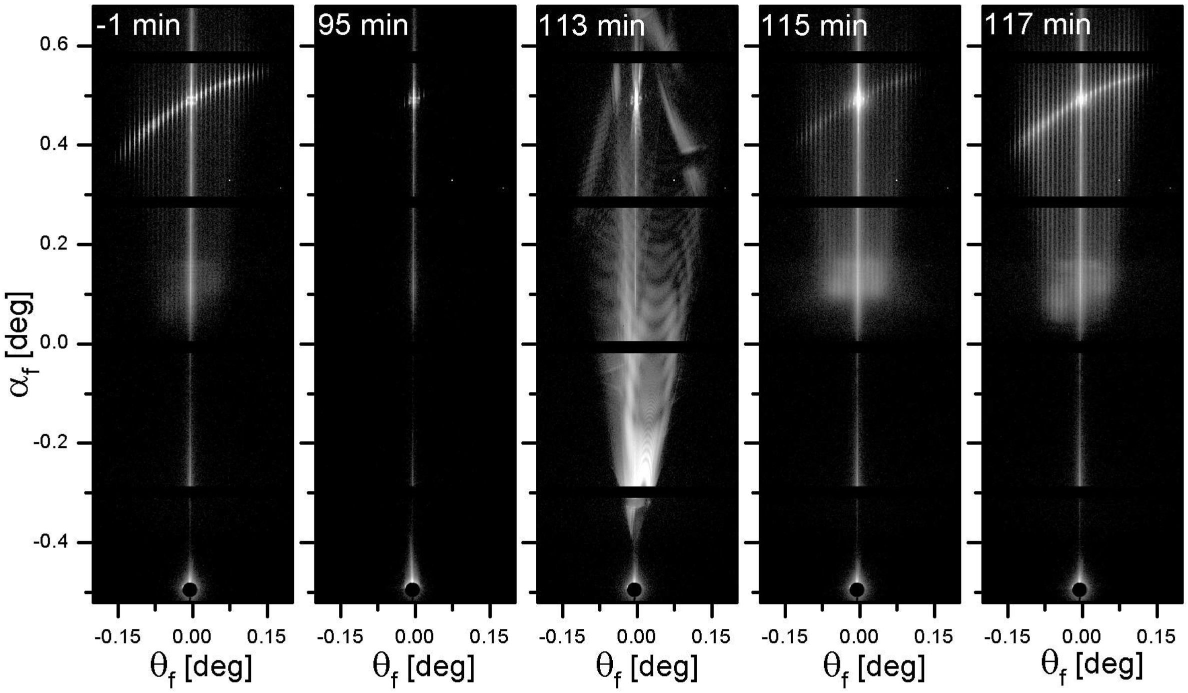

Figure 5.26: Example of the evolution of the GISAXS signal during an *in situ* experiment on a drying droplet of colloidal dispersion. The displayed part of the detector ranges from the direct beam up over the reflected beam. The direct beam at $\alpha_i = -0.49$ deg is shadowed with a beam stop. The counting time and the intensity scale is identical for all graphs.

Figures 5.26 and 5.27 show data and evaluation of a representative GISAXS *in situ* experiment. It was performed at an ambient temperature of 23.8 °C with a droplet of colloidal dispersion that contained 0.08 wt% polystyrene colloids. α_i was set to 0.49 deg. The grating was turned to $\omega = 0.25$ deg where $\omega = 0$ corresponds to the position where the grating is parallel to the beam. A grating period of 667 ± 20 nm was obtained from the evaluation of the scattering data. This is in good agreement with the period of 675 nm measured with AFM.

The scattering pattern in figure 5.26 correspond to different stages of the experiment. The instant they were collected is marked on the scattering patterns. The displayed part of the detector ranges from the direct beam up over the reflected beam. The direct beam at $\alpha_i = -0.49$ deg is shadowed with a beam stop. The first intensity map at -1 minutes was measured before the droplet was brought on the sample. It corresponds to the scattering from the bare surface grating. After applying the droplet the intensity is much lower. Only the reflected beam and a few reflexes from the grating can be seen. This situation is still observable in the same way 95 minutes after the start of the experiment. Shortly after that, intensity streaks begin to appear which form complex and sometimes rapidly changing patterns. An example of a such a pattern is displayed in the figure at 113 minutes. The intensity streaks concentrate in the following on the specular direction and right after that, the scattering of the grating is again visible (115 minutes). In just a few seconds, the intensity of the scattering from the grating increases and stays than constant for the remainder of the experiment (117 minutes).

Figure 5.27 shows a summary of the scattering data collected in the *in situ* experiment. For the lower graph, the individual scattering patterns were averaged over $0.046 \text{ deg} < \alpha_f < 0.855$ deg. This corresponds to a range from the Yoneda band up to an exit angle with practically no more intensity on the detector. The resulting intensity arrays have then been plotted versus time. The instants marked with an arrow correspond to the times at which the scattering patterns of figure 5.26 were taken. The y-axis gives the corresponding component of the scattering vector parallel to the substrate $\mathbf{Q}_{||}$. That means that $\mathbf{Q}_{||} = 0$ corresponds to the position $\theta_f = 0$ or equally to the specular direction in the scattering patterns. A second integration over the components of each array yielded the red curve in the upper part. The data displayed in blue corresponds to the measured relative humidity in the sample cell. The noisier appearance of the curve compared to the one in figure 5.25 comes from the automatic read out every second. Data points for figure 5.25 were in contrast collected by hand every 30 seconds at maximum. The inset in the upper figure shows the evolution of both parameters during the complete experiment.

The results found in the *in situ* GISAXS experiments are comparable to the ones found in the ED-XRR experiments. No change in the distance between the grating peaks from the bare and the covered grating could be detected. The scattering intensity is also low at the beginning of the experiment and reaches a constant value as soon as the droplet has completely evaporated. As can be seen from figure 5.26, the intensity of the scattering pattern before the application of the droplet and after the complete dry-out

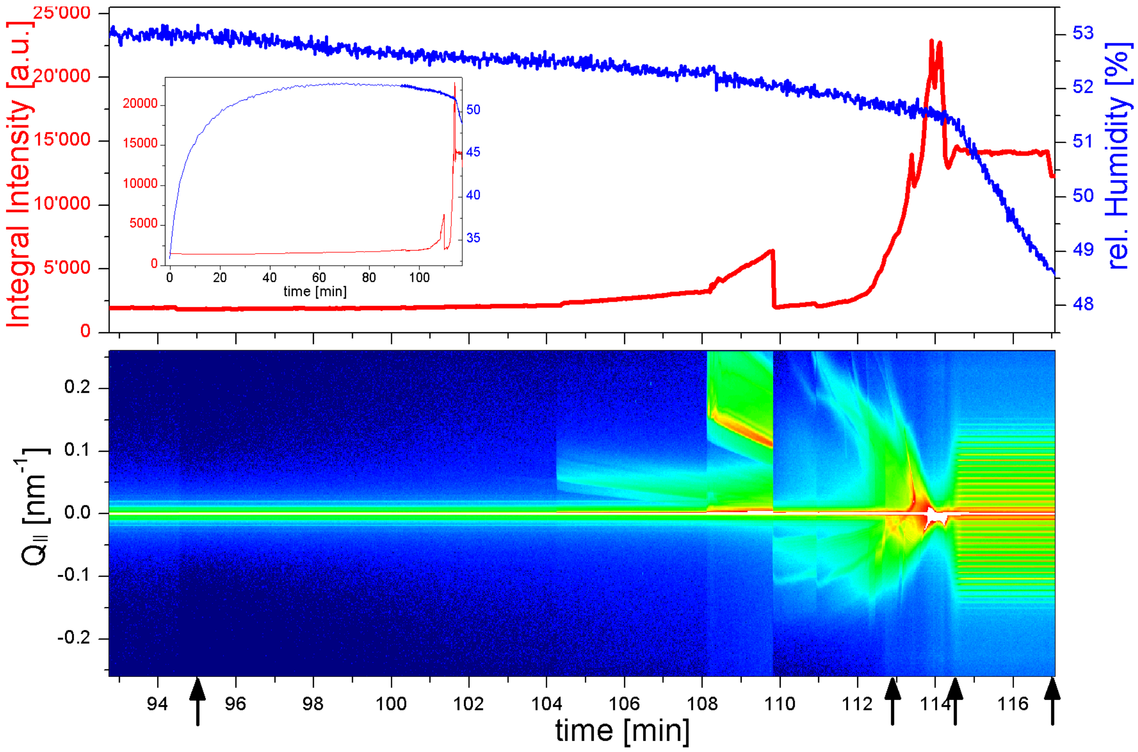

Figure 5.27: (*above*) Evolution of the detector intensity integrated in a certain area over α_f and θ_f and the relative humidity in the sample cell during the last minutes of the experiment. The inset shows the corresponding parameters for the complete experiment. (*below*) Identical detector area as in the upper graph integrated solely over α_f and plotted versus time. The arrows mark the times at witch the GISAXS patterns of figure 5.26 were collected.

are comparable. This behavior is accordingly attributed to the absorption from water. The intense maxima and the sudden changes in the integrated intensity just before the final increase can now also be interpreted. From the comparison with the scattering data at the corresponding instants, see, e.g., the scattering pattern at 113 minutes in figure 5.26, one understands that the intensity varies because of the intensity streaks. The streaks are attributed to the flattening of the droplets. Following this interpretation, they correspond to parts of the direct beam that get somehow redirected as the drop thins out more and more. The sudden drops in the integral intensity in figure 5.27 can be caused by sudden changes in the drop shape as observed sometimes during the *in situ* experiments with a camera.

Even though the presented GISAXS data give a much clearer picture of the events during the experiment as the data from the ED-XRR measurements, the influence of the colloids can only be seen in a broadening of the diffuse background. No signal of an ordering process could be detected.

5.3.3 AFM and SEM Characterization

Figure 5.28 depicts representative results of AFM and SEM investigations on samples coated in *in situ* experiments as described in the previous two sections. Figure (a) is taken from a different sample than figures (b), (c) and (d). On graphs (a) and (d) and partly on (b), it can be seen that the colloidal particles formed only rather small agglomerates on the surface. No large hexagonally ordered regions can be found. The influence of the grating is recognizable in these graphs but not very pronounced. The observed number of colloids on the surface is clearly below expectations, if one calculates the theoretical coverage from the concentration of the dispersion and an estimated droplet contact area on the substrate. This discrepancy becomes understandable when looking at figure 5.28 (c) that shows the inner part of a former border of the droplet. A large part of the particles has obviously agglomerated there. Such borders could be observed by the naked eye on almost all samples. They gave the impression that the droplet contracted not in a continuous but in a discrete manner forming a thick accumulation of particles at every pinning position.

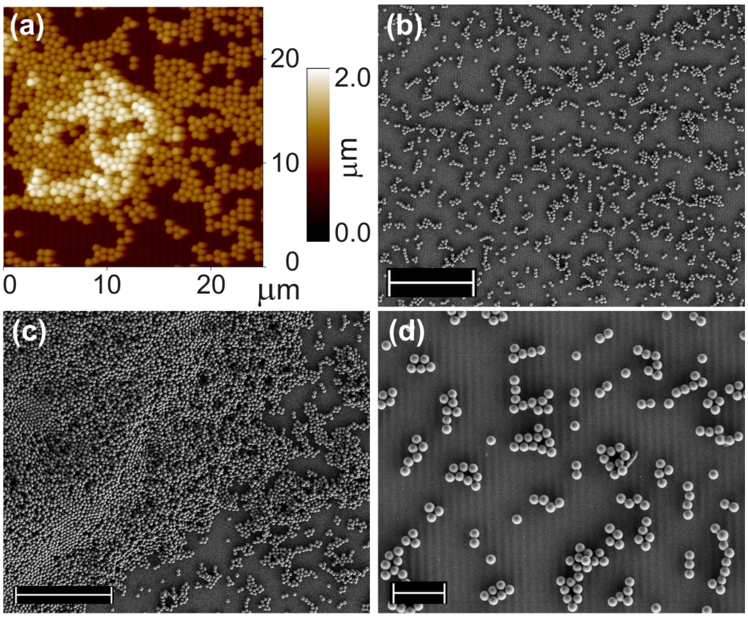

Figure 5.28: (**a**) AFM and (**b**), (**c**) SEM images of the surface of samples that were covered by a droplet of colloidal dispersion during the *in situ* X-ray scattering experiments. (**d**) SEM image of a border of the former droplet. (**a**) was taken from a different sample than (**b**), (**c**) and (**d**). The scales correspond to 20 µm in case of (**b**) and (**c**) and to 4 µm in case of (**d**).

5.3.4 Discussion

The *in situ* ED-XRR and GISAXS experiment performed on drying colloidal droplets show a rich behavior. Most of it can however be understood by effects originating from the solvent and the change in the droplet shape. From the presented data, no signal of ordering processes could be discerned.

In particular, no evidence of a change in the peak distance of the grating peaks was observed during the *in situ* experiments. Such a change has been seen in earlier studies [170] and had been interpreted as the signal from assembled colloidal particles. Different reasons could account for this difference. In the presented experiments, the diameter of the colloidal particles is well matched to the period of the substrate. A weak signal of an ordered particle assembly could therefore be subsumed in the scattering from the grating. The particles used in the earlier study [170] had on the other hand a clearly different particle diameter from the grating period. Besides, the experimental resolution is about three times higher in [170] than in the investigations presented in the previous sections. By considering figure 5.28 and similar investigations on other samples not shown here, there is though the strong suspicion that the colloidal particles did not develop ordered structures large enough to cause a coherent scattering signal.

It remains the question on the reasons for the low ordering of the particles with respect to earlier observations on dried out droplets of colloidal dispersion [69, 70, 169]. There are two marked distinctions of these studies compared to the presented one wich could also account for the low order on the obtained samples. On the one hand, a X-ray beam passed through the droplet during the drying process. On the other hand, the support for the assembly has not been a flat substrate but a structured polymer.

The influence of the beam is twofold. As long as the beam gets almost completely absorbed in the droplet, the corresponding beam energy heats the water and leads to an increased evaporation rate with respect to a droplet without irradiation. The increased evaporation could then lead to an assembly speed that is too fast for a regular arrangement. Particles would not have enough time to arrange on a close packed lattice and would just get thrown together. The temperature of the sample stage was varied in a range of about 10 °C in the ED-XRR experiments. This variation increased the duration of the experiment for typically one to two hours. No influence on the results could be inferred. X-ray beams are also known to cause damage through the intense radiation and a few samples contained colloidal particles that seemed “melted”. However, these cases were exceptions. Almost all particles seen in AFM and SEM seemed not to be damaged in any way.

The topologically structured pDR1M surface gratings seem to be the more likely reason to hinder the assembly. Some possible reasons have already been given in the discussion of the results from prefabricated colloidal assemblies, see section 5.2.5. Another reason that seems to play an important role in this experiment is the fact that the surface of pDR1M has a receding contact angle of about 40 deg with water. It is however known that convective self-assembly works only up to an angle of ~ 20 deg [80]. This effect was tried to account for by the use of sulfuric acid on the polymer surface just before the application of the droplet of colloidal dispersion. While this treatment clearly decreased the contact angle, it might still have been a problem. The retreating contact line between water, air and the substrate does then not lead to an assembly but the particles get dragged along inside the droplet volume [80] as illustrated in figure 5.29. The observed rings as displayed in figure 5.28 (c) correspond in this picture to locations where the contact line got pinned for some reason and a large mass of colloidal particles was deposited. The loosely dispersed colloids in the other three subfigures can be understood as the small fraction of particles that have arrived by sedimentation at the bottom of the droplet. This is only a small fraction as the sedimentation velocities for the used polystyrene particles are in the range of $50\,\mu$m/hour[4] compared to a typical length of an experiment of about three hours.

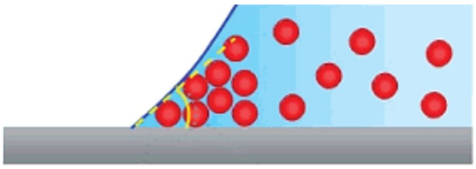

Figure 5.29: Convective self-assembly prevented because of a too large contact angle. Figure taken from [80]

As a reference, an experiment was also performed on an untreated microscopy slide. While the observable order after the experiment was increased with respect to the pDR1M surface gratings, the ordered regions were still small and no clear coherent scattering signal was detected. In summary, it was concluded that the chosen system is not ideal for *in situ* investigations.

---

[4] Calculated according to Stokes' law, see, e.g. [1] page 22, with a particle density of $1.05\,\text{g/cm}^3$.

CHAPTER 6

Numerical Calculation of Scattering Data - Results and Discussion

This chapter discusses the tool implemented in the framework of this project to simulate and fit scattering data from three dimensionally arranged scatterers in the GISAXS geometry.

Scattering data collected in a GISAXS experiment can usually not be satisfactorily described with a model including just the simple Born approximation as this leads to inadequate agreement with the measured intensity distributions. A theory that appropriately describes the scattering at grazing incidence angles has to account for refraction and reflection effects because one works very close to the angle of total external reflection. The appropriate theory is presented in chapter 3.3. To our best knowledge, two tools have so far been implemented for the interpretation, simulation and the fitting of GISAXS data.

IsGISAXS [171] is specialized on the simulation of scattering data of islands supported on surfaces. It is very well suited for that purpose but has no extension to simulate the scattering from a three-dimensional arrangement of particles on a surface. The tools NANOCELL [146] and NANODIFT [172] have been developed to clarify the structure of polymeric thin films. The former calculates expected peak positions in the scattering pattern depending on the crystallographic symmetry. The latter computes the intensity distribution on the detector by a Fourier transform of an electron density distribution written in a three-dimensional matrix. For a given extension of the electron density distribution in real space, the accessible range in reciprocal space is limited by the number of matrix elements. This number gets quickly unmanageable if simulating the scattering from periodicities in the range of hundreds of nanometers.

As a result of the evaluation of the two programs above, it was decided to implement a tool of our own that was called 3DGISAXS. Upon request, the tool is available from the author. IDL (ITT VIS) was chosen as the programming language. It is an array based language specialized on the analysis and visualization of data. In the following section, the specific implementation of the theory of chapter 3 will get discussed. The main focus is thereby on the possibilities and the limits of the implemented solution[1]. In the following sections, the routines are used for fitting and simulation of GISAXS data. In the appendix on page 131, the program itself is explained in more detail.

6.1 Implementation of the Model

3DGISAXS is based on the theory discussed in chapter 3. The points for which the intensity is calculated in the model are defined by the experimental angles α_i, α_f and θ_f and a given wavelength λ. For each point, these parameters get transformed to the components of the scattering vector which is used by 3DGISAXS to compute the scattered intensity. Additional parameters specify the specific system for which the scattering is calculated. Such parameters include for example the particle diameter, the thickness of the colloidal layer or material constants.

The core of the tool consists in the implementation of the two formulas below replicated from chapter 3. The main formula is the following equation

$$\begin{aligned} I = & \frac{1}{16\pi^2} \frac{1 - \mathrm{e}^{-2\,\mathrm{Im}(Q_z)\cdot d}}{2\,\mathrm{Im}(Q_z)} \times \\ & \Big[\left| \mathcal{T}_i \mathcal{T}_f F(Q_x, Q_y, \mathrm{Re}(Q_{1,z})) \right|^2 + \left| \mathcal{T}_i \mathcal{R}_f F(Q_x, Q_y, \mathrm{Re}(Q_{2,z})) \right|^2 + \\ & \left| \mathcal{R}_i \mathcal{T}_f F(Q_x, Q_y, \mathrm{Re}(Q_{3,z})) \right|^2 + \left| \mathcal{R}_i \mathcal{R}_f F(Q_x, Q_y, \mathrm{Re}(Q_{4,z})) \right|^2 \Big]. \end{aligned} \tag{3.40}$$

These are the four main terms resulting from the DWBA approach. The absolute square of the scattering amplitudes $|F(Q_x, Q_y, Q_z)|^2$ appearing in all four terms of the sum above are calculated according to

$$\begin{aligned} |F(\mathbf{Q})|^2 = & \overbrace{r_0^2 N \cdot \left[\left\langle |f_m|^2 \right\rangle - |\langle f_m \rangle|^2 \,\mathrm{e}^{-W(\mathbf{Q})} \right]}^{I_{\mathrm{incoh}}} + \\ & \underbrace{r_0^2 \, |\langle f_m \rangle|^2 \, \mathrm{e}^{-W(\mathbf{Q})} \overbrace{\left\langle \left| \sum_m^N \mathrm{e}^{i\mathbf{Q}\mathbf{R}_m} \right|^2 \right\rangle}^{S_L(\mathbf{Q})}}_{I_{coh}} \end{aligned} \tag{3.10}$$

where f_m is given by the particle form factor of a homogeneous sphere as introduced in equation (3.2). Scattering contributions not treated in chapter 3 are so far not included

---

[1] A word of warning for the future 3DGISAXS user: The tool does **NOT** have a nice graphical user interface where you can just click to activate the desired feature. However, most of the described possibilities need manipulations directly in the code!

in the model. Such contributions are for example scattering effects due to interface roughness and incoherent scattering from grating defects. The precise solution chosen for the implementation of different parts of the previous formulas is discussed in the following. The selected solution was always chosen with regard to the aim of calculating the GISAXS intensity of a thin colloidal multilayer on top of a substrate.

Particle Size Distribution

The SAXS data collected for the characterization of the the colloidal dispersions, see chapter 5.1, could be well fitted with a Gaussian particle size distribution. Therefore, the averages over $\langle f_m \rangle$ and $\langle |f_m|^2 \rangle$ are also computed under the assumption of a Gaussian particle size distribution. For the averaging over the particle diameters, the numerical integration includes diameters from the average radius minus three times to plus three times the standard deviation of the Gaussian distribution. Larger or smaller particles do accordingly not contribute to the average but they amount only to a fraction of 0.3 % of all particles.

Implementation of Lattice Sum

Two ways were implemented to calculate the lattice sum $S_L(\mathbf{Q})$. In the first approach, one defines an array of particle coordinates $\mathbf{R}_m$ and the lattice sum is then computed explicitly from the given particle arrangement. This approach has the advantage that the scattering can in principle be simulated for any kind of particle arrangement including defective structures. The challenge consists in the generation of the corresponding particle coordinates. Special procedures have do be implemented to do this task. So far, this has only been done for hexagonal close packed and body centered cubic structures in 3DGISAXS. The main drawback of this approach is yet the computation time. This increases remarkably for larger particle sets[2].

The second approach to calculate the lattice sum $S_L(\mathbf{Q})$ is specially dedicated to the scattering from the irregularly stacked hexagonal planes as described in chapter 3.2. The approach described in equation (3.14) was applied for the computation of the layer form factor $|\mathcal{L}(\mathbf{Q})|^2$ in equation (3.27). An exponential decrease in the particle correlation was assumed leading to a Lorentzian function for $\mathcal{S}(\mathbf{Q})$. The same assumption was used to describe the scattering perpendicular to the hexagonal planes at the locations fulfilling the 'Bragg condition' given in equation (3.28). For the positions of the hexagonal plane that feel the stacking disorder, the analytical function given in equation (3.27) was implemented. The approach using analytical functions was always used for the fitting of the scattering data. It is of course not as versatile as the first approach but computation

---

[2] As an example, 10'000 detector points were calculated for a set of 8000 particles, i.e., 20 x 20 x 20 particles. This calculation took about 100 seconds on a notebook with a 2 GHz Intel chip. No averaging over different domain orientations was included.

times are massively shorter than in the first one[3].

There is the possibility in 3DGISAXS to account for differently oriented domains on the sample. Numerically, this possibility is realized by the calculation of the lattice sum for each direction and a subsequent averaging process. At the moment, a Gaussian distribution of the domain orientations is the only implemented distribution function.

Distributions over domain sizes are not implemented in the program. This is only accounted through the type of function used for the convolution with the lattice sites in case of the approach using analytical functions.

Experimental Resolution

Parameters such as the incident and exit angles and the wave length correspond never to a singular value in a real experiment. Instead, they exhibit a certain distribution caused by the divergence or the focus of the beam, the sample size and the finite bandwidth of the monochromator. The resulting resolution element was derived in chapter 3.4.2. For the experimental setup used during this work at the cSAXS beam line, the resolution lengths amounted to $\Delta \mathrm{Q}_x = 1 \cdot 10^{-5}\,\mathrm{nm}^{-1}$, $\Delta \mathrm{Q}_y = 1.3 \cdot 10^{-3}\,\mathrm{nm}^{-1}$ and $\Delta \mathrm{Q}_z = 1.1 \cdot 10^{-3}\,\mathrm{nm}^{-1}$ compared to a distance between two pixels in reciprocal space along $\mathrm{Q}_z \approx \mathrm{Q}_y \approx 1.1 \cdot 10^{-3}\,\mathrm{nm}^{-1}$. As these values do not differ significantly, no spread in the experimental angles and the wavelength were incorporated in 3DGISAXS so far.

6.2 Fitting of the Model to Scattering Data

The implemented model can in principle be used to fit scattering data collected at any point on the detector. The main purpose of the following investigations is however to elucidate the stacking probability of the colloidal multilayers. Therefore, the evaluation concentrates on line cuts extracted from the measured scattering intensities along the truncation rods as described in figure 5.15 and the corresponding text.

6.2.1 Investigation of Finite Size Effects

In chapter 3.2, the scattering function of irregularly stacked hexagonal planes was developed under the assumption that finite size effects do not play a role. It was supposed that the correlation of two hexagonal planes decreases rapidly with increasing separation so that the corresponding phase factor can be neglected at large distances, see equations (3.18) and (3.19). As the colloidal layers investigated in this work have all less than twenty layers, it is important to assess the validity of the analytical scattering function (3.27) for very few layers.

---

[3] As an example, 10’000 detector points were calculated applying analytical functions. This calculation took less than 2.4 seconds on the identical notebook as used before, i.e., 2 GHz Intel chip. Again no averaging over different domain orientations was included in the calculation.

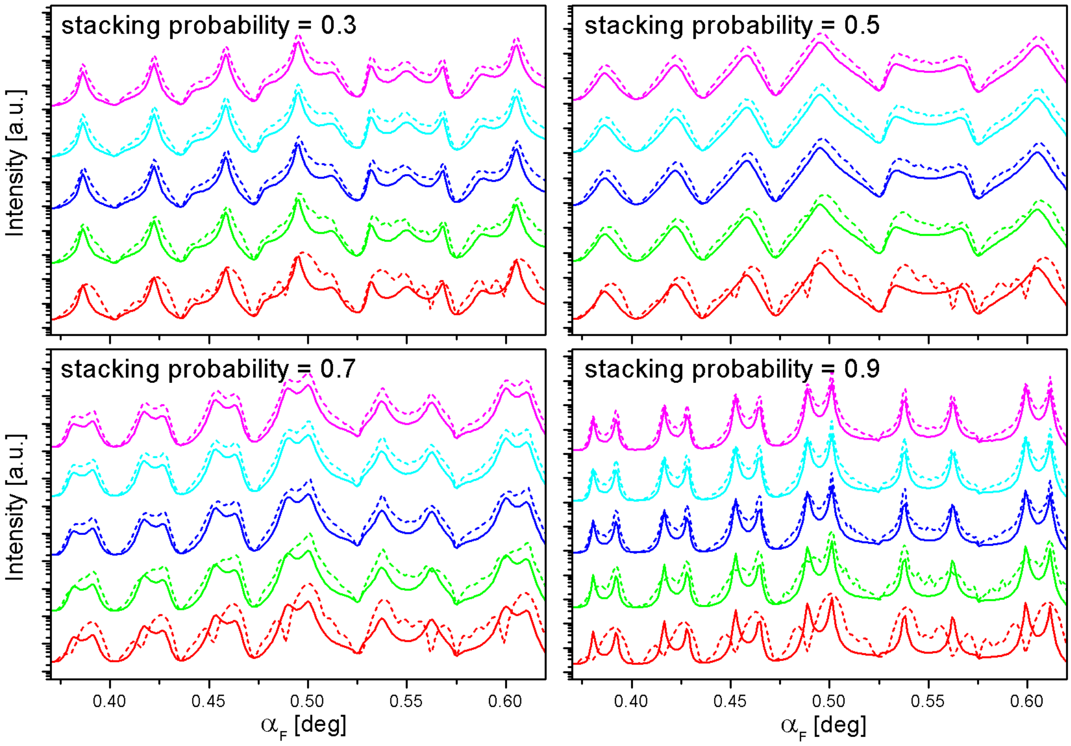

Figure 6.1: Comparison of the scattering from multilayers with finite size and a certain stacking probability (dashed curves) to the corresponding analytical scattering function (solid lines). The differently colored curves in each graph correspond to $3, 7, 14, 21$ and 28 layers starting from the bottom. The calculations were done with $\alpha_i = 0.55$ deg and a θ_f corresponding to a position on truncation rod. The curves are vertically displaced for better visibility.

This evaluation was done by using the possibility of 3DGISAXS to calculate the scattering from the coordinates of defined particle assemblies. For a certain number of layers, coordinates of hexagonal multilayer were created with a certain stacking probability and the corresponding scattering pattern have subsequently been calculated. In oder to get a valid average, this process was repeatedly done for each investigated layer thickness and stacking probability until no further change was deduced in the resulting scattering pattern. The result of this investigation is shown in figure 6.1. All curves were calculated at an incident angle of $\alpha_i = 0.55$ deg and correspond to the scattering along a truncation rod sensitive to the stacking probability. The dashed curves denote the scattering intensities calculated as described before. The solid curves are computed with the analytical scattering function given in equation (3.27). The four different graphs show the result at different stacking probabilities in the range between 0.3 up to 0.9. In each individual graph, the number of investigated layers increases as on goes from the lowest curves in red to the topmost curves in violet. The corresponding number of layers are 3, 7, 14, 21 and 28. The curves are vertically displaced for better visibility.

From the graph, it can be seen that effects due to the finite size decrease very rapidly. Above 21 layers, the line shape is practically identical to the analytical function. But already at seven layers the main features of the analytical scattering curve are well expressed. It was therefore considered a valid approximation to fit sample-277-7 with the analytical function (3.27).

6.2.2 Fitting of Scattering Data

Figures 6.2, 6.3 and 6.4 depict results from the actual fitting of the model to data obtained from the samples covered with seven and fourteen layers of colloids with a diameter of 277 nm as described in chapter 5.2.2. The first two figures correspond to data from sample-277-7 whereas the third figure shows line cuts of sample-277-14. The data used for the fitting is an averag over 30 individual scattering patterns collected in an ω range of 3 deg. This range is smaller than the FWHM of the peaks in the ω cuts

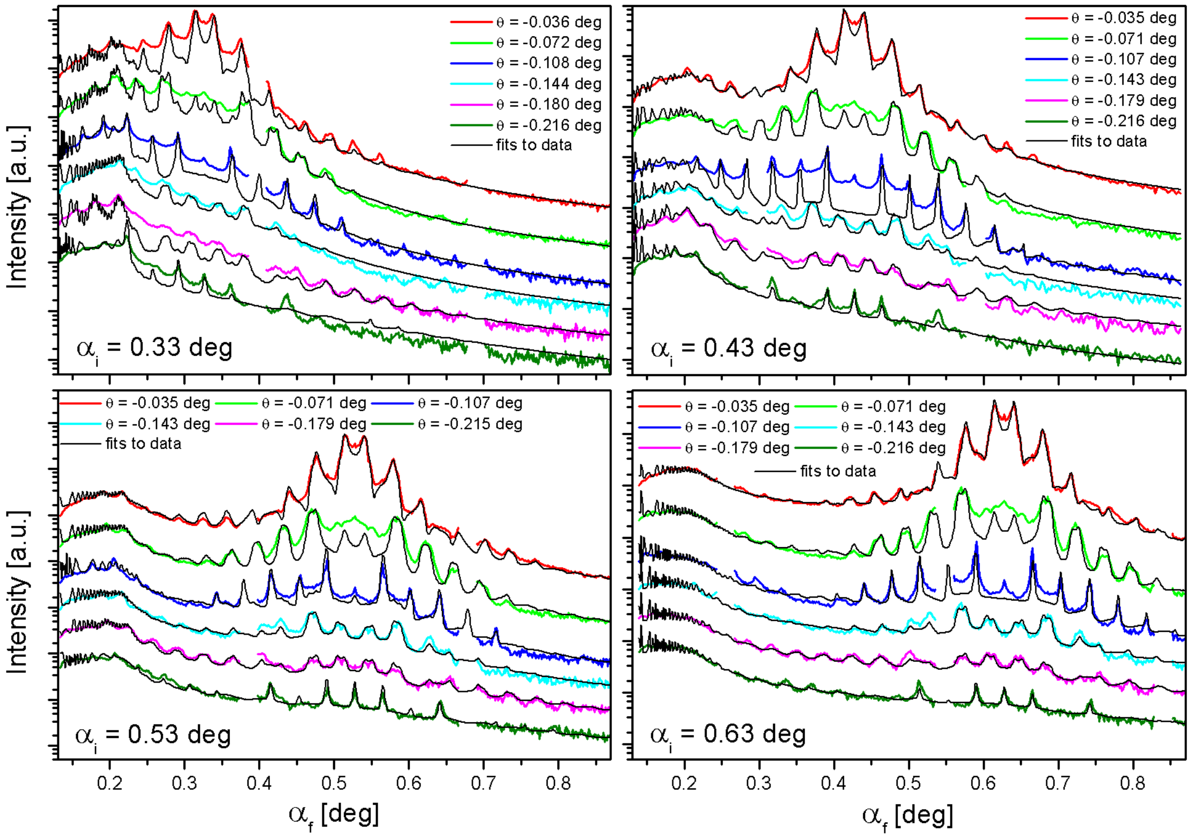

Figure 6.2: Fits to data of sample-277-7 for different α_i and $\omega = 0$ deg. The colored curves correspond to the line cuts extracted from the scattering patterns at the position of the truncation rods as illustrated in figure 5.15. The fits are displayed in black. Curves have been vertically displaced for better visibility.

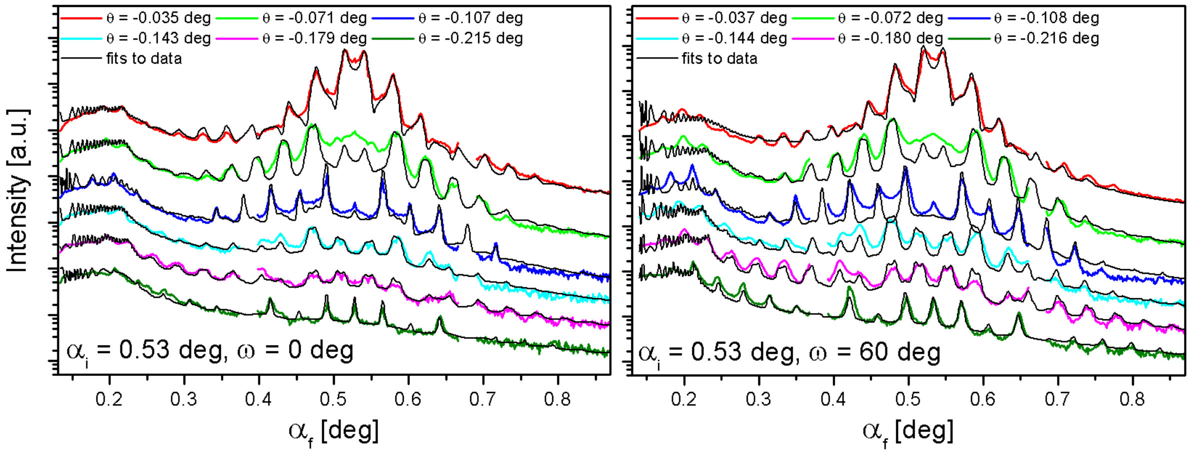

Figure 6.3: Fits to data of sample-277-7. The colored line cuts were extracted from scattering patterns corresponding to a sample alignment of (*left*) $\omega = 0$ deg and (*right*) $\omega = 60$ deg. The fits are displayed in black. Curves have been vertically displaced for better visibility.

of figures 5.10 and 5.11 and practically no change can be detected in the corresponding scattering patterns. The central ω value of the averaging process was in each case at a sample orientation that exhibited a maximum number of truncation rods, i.e., $\omega = 0$ deg or $\omega = 60$ deg. The displayed line cuts were extracted from the averaged data at the positions of the truncation rods as illustrated in figure 5.15. These curves are in each plot denoted by the colored curves. The topmost, red curve corresponds to the position closest to the specular direction. The distance increases for the lower curves. The corresponding θ_f positions are given in the plots. The black lines are the respective fits of the model to the data. All curves have been vertically displaced for better visibility.

Generally it can be stated that the model fits the scattering data better at larger incident angles. This can be understood by the fact that multiple scattering events get increasingly important as one approaches the critical angle of the substrate. In order to take these events into account, higher order terms of the DWBA would have to be included in the model.

Figure 6.2 depicts scattering data and fits for different incident angles, α_i, in the case of sample-277-7. The corresponding scattering patterns were measured at a sample alignment where the growth direction was parallel to the beam, i.e., $\omega = 0$ deg. As a comparison, the data has also been fitted for a specific α_i in the case of $\omega = 60$ deg, see figure 6.3. Neither the visual comparison of the data and fits of the two displayed directions nor the parameters obtained from the fit do show any significant difference.

The scattering intensities along the truncation rods of sample-277-14, shown in figure 6.4, look at first glance very similar to the ones of sample-277-7. A closer inspection of the scattering at $\omega = 0$ deg revealed however a set of double peaks on the truncation rods located at $\theta_f = -0.108$ deg and $\theta_f = -0.216$ deg. Only simple Bragg scattering is expected at these positions. The double peaks can be understood assuming a slight tilt

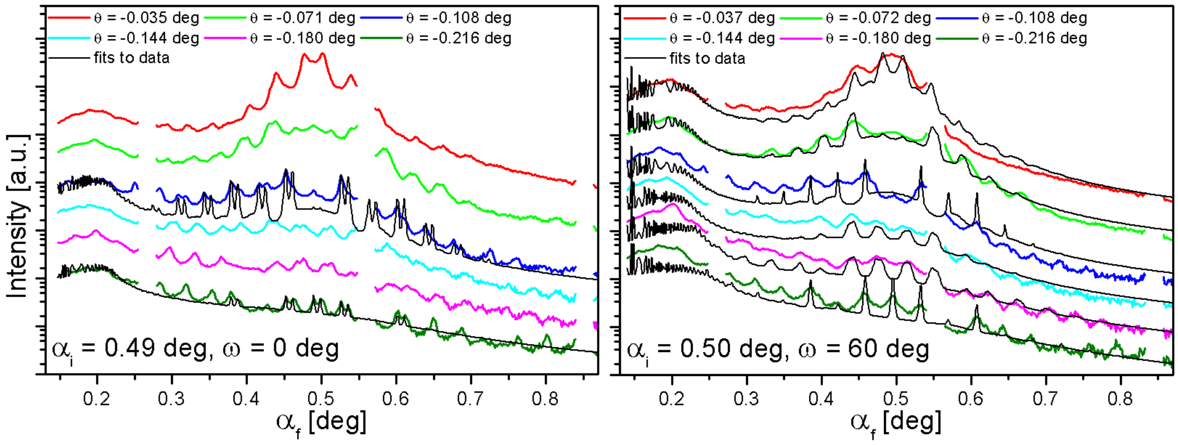

Figure 6.4: Data of sample-277-14 for sample orientations (*left*) $\omega = 0$ deg and (*right*) $\omega = 60$ deg. The double peaks for θ_f equal -0.108 deg and -0.216 deg and the smeared out appearance of the maxima of the other curves can be understood by a slight tilt of different parts of the crystal versus each other.

between two parts of the crystal of ~0.005 deg[4] with respect to the incident angle. The black lines correspond to simulations calculated under this assumption. The line cuts at $\omega = 60$ deg do not exhibit the double peaks. However, the smeared out appearance of the maxima and the low quality of the fits indicate a similar although smaller misalignment of crystallites in the colloidal assembly as seen for $\omega = 0$ deg. Due to the low quality of fits, parameters resulting from sample-277-14 are not considered in the following.

The parameter values resulting from the fits to the data of sample-277-7 are given in table 6.1. Each value corresponds to an average over all individually fitted truncation rods at a specific α_i, ω position. Good agreement is found between the values.

sample orientation ω	0 deg				60 deg
incident angle α_i	0.33 deg	0.43 deg	0.53 deg	0.63 deg	0.53 deg
stacking probability a	0.64	0.62	0.62	0.64	0.62
sphere diameter (form factor) [nm]	265	265	265	264	265
standard deviation of diameter [%]	5	4	3	3	4
diameter (grating constant) [nm]	259	258	258	258	258

Table 6.1: Parameter values obtained from fitting the model to the GISAXS data measured on sample-277-7; sample covered with an average of 7 layers of colloidal particles with a diameter of 277 nm.

---

[4] An effect from the averaging process can be excluded as all individual scattering patterns exhibit the same double peak.

Stacking probability The scattering patterns measured in a X-ray scattering experiment provide information on the sample that is an average over the area illuminated by the beam. As the beam footprint in the GISAXS experiments extended over macroscopic areas ($\sim 1\,\mathrm{mm}$ lateral and $> 60\,\mathrm{mm}$ along the beam path), it can be assumed that the obtained scattering patterns correspond to an average over a very large number of domains of the colloidal crystal.

For a colloidal multilayer consisting of seven layers, there exist 32 different possible stacking sequences. All variants and their associated stacking probabilities are listed in the appendix on page 132. The stacking probability takes only the discrete values $a = 0.0, 0.2, 0.4, 0.6, 0.8$ and 1.0. Assuming complete random stacking of a colloidal crystal with 7 layers, one would find an equal amount of all the 32 possible stacking variants in the area illuminated by the beam[5]. The measured stacking probability would then be the average over all the individual stacking variants resulting in $a = 0.5$.

The stacking probability, $a \sim 0.63$, extracted through the fitting process from the scattering data of sample-277-7 indicates a tendency towards a fcc ordering of the stacked planes. Though the stacking probability is still fairly close to $a = 0.5$, the fitted value clearly indicates a tendency versus a fcc ordering as the double peaks on the truncation rods sensitive to the stacking sequence appear only from a value $a > 0.61$ on.

Sphere diameter The sphere diameter was evaluated in two ways. The first value is directly obtained as the mean value of the colloidal size distribution used to calculated the form factor. The second value was recalculated from the grating constant derived from the distance of the Bragg peaks lying on the rods that are not sensitive to the stacking probability. Thereby, hexagonal close-packed layers stacked on top each other were assumed for the calculation of the particle diameter. The fitted intensities respond sensitively on both parameters by alterations in peak positions and changes in the relative intensity of different peaks. An error in the range of $\pm 2\,\mathrm{nm}$ can be attributed to these values.

Standard deviation of diameter The averaged standard deviation of the particle diameter is approximately the same for all incident angles as well as the two sample orientations even though the variation of the standard deviations of the individual fits was large. Compared to the standard deviations of the particle diameter found for the particles in solution in chapter 5.1, see table 5.1, there is clearly an increase in the otained value for the particles in the dry colloidal crystal.

6.2.3 Discussion

The X-ray scattering intensities from two colloidal multilayers fabricated by convective self-assembly on glass substrates were fitted to a model. The applied model includes both

---

[5] It is assumed that the stacking of neighboring domains is independent.

reflection and refraction effects occurring at gracing incident angles and the possibility to calculate the scattering depending on the stacking probability of the hexagonal layers.

The scattering intensities of sample-277-14 exhibited evidence of a large mosaicity of the colloidal multilayer, i.e., parts of the crystal that are illuminated with a slightly different incident angle. A extensive evaluation of the scattering data along the truncation rods has accordingly been omitted.

The fitting of the model to the scattering data of sample-277-7 resulted with the parameter values in table 6.1. Neither a dependency on the sample orientation nor the incident angle can be inferred from these values. If one calculates the penetration depth of the X-ray beam into the colloidal layer as done for figure 1.12 (b), it can be seen that the complete thickness of the colloidal layer is probed at all presented incident angles. Accordingly, the information on the colloidal layer is comparable for these incident angles.

The sphere diameter obtained from the form factor agrees with the value of 263 nm obtained from the evaluation of the in plane scattering. Surprisingly, the value calculated from the stacking of the hexagonal planes is slightly smaller. As the calculated intensities respond very sensitively to changes in the grating constant, it is reckoned that this discrepancy is real. It might be caused by the capillary forces acting during the dry-out. These forces are believed to cause the pronounced system of cracks interrupting the self-assembled colloidal multilayers in the plane parallel to the substrate. The same forces act also in the direction perpendicular to the surface and could lead to a slight compression of the individual colloids along this orientation.

The stacking probability extracted from the scattering data of sample-277-7 amounts to ~ 0.63. This indicates a stacking of the close-packed layers with a tendency towards an fcc symmetry. Compared to earlier studies that found fcc stacking with just a few stacking faults [20, 77] in samples fabricated with convective self-assembly, this value is surprisingly low. The different techniques used for the characterization of the colloidal assemblies may provide a reason for this difference. In [20] the stacking was assessed by SEM and transmission spectra that have been collected on a limited field of view ($\sim 2 \times 90\,\mu\text{m}^2$ corresponding to $\sim 3 \times 100$ colloidal diameters) and consecutively compared with a calculated transmission spectrum of a colloidal multilayer with a fcc stacking. From the matching features of both spectra it has then been concluded that the assembly has an FCC structure with stacking faults. In the second study [77], the stacking sequence has been inspected with a confocal microscopy on a region of about $11 \times 11\,\mu\text{m}^2$ (corresponding to $\sim 15 \times 15$ colloidal diameters). While the cited studies probed most likely a single domain for the assessment of the stacking of the sample, the stacking probability obtained from GISAXS provides a value that is a statistical average over the complete sample. The number of layers of self-assembled colloidal multilayers or the convective flow during the assembly as proposed in [73] could be parameters that also have an influence on the resulting stacking probability. Such a dependencies could also be the reason for the different stacking probabilities found previously. In summary, the stacking sequence of the close-packed layers in colloidal crystals have only been investigated in detail by a couple of studies [20, 77, 93]. These studies probed the crystalline structure on a local scale in contrast to an overall view of the presented investigation.

The presented work explicates at one example that GISAXS in combination with the tool 3DGISAXS is well suited to characterize the stacking sequence of colloidal multilayers over a complete sample. It is the only technique that can provide this information from self-assembled colloidal multilayers on top of a substrate with a reasonable effort. Similar measurements have only been done with SAXS on a colloidal crystallite that has been sedimented in a capillary [99–102]. A random stacking has been found in the investigated area of $100 \times 100\,\mu\mathrm{m}^2$. The assembly mechanism is however different from convective self-assembly [73].

GISAXS with an appropriate simulation tool can therefore provide a valuable contribution to the further exploration of colloidal crystals as a basis material in the fabrication of photonic crystals. GISAXS in combination with 3DGISAXS offers for the first time the possibility to study the averaged stacking sequence of colloidal multilayers. This possibility opens new ways to systematically investigate the relation between the averaged stacking sequence and the process parameters of the convective self-assembly. Such a study could lead to the identification of the microscopic processes governing the arrangement of the colloids. This knowledge would be useful to optimize the process parameters of the self-assembly towards the desired crystalline structure.

6.3 Simulation of Scattering Data

6.3.1 Scattering Patterns as Measured with an Area Detector

After fitting the model to the scattering data, 3DGISAXS was used to simulate the complete scattering intensity as measured with an area detector in a GISAXS experiment.

Figure 6.5 shows experimental GISAXS data of sample-277-7 measured at a sample orientation $\omega = 0$ deg (**a**) and $\omega = 30$ deg (**b**) as described in chapter 5.2.2. The corresponding simulations calculated by 3DGISAXS are displayed in figures (b) and (d). The results obtained from the in-plane and out of plane evaluation were used as input parameters for the simulation. The calculated positions and intensity modulations of the peaks around the reflected beam are in very good agreement with the experimental scattering pattern. However, the intensities closer to the Yoneda band are apparently not well reproduced in the simulation. This discrepancy is attributed to two facts. On the one hand, the increased intensity close to the Yoneda band in the experimental scattering patterns was attributed to surface roughness of the substrate. No such component was included in the simulation tool so far. On the other hand, multiple scattering effects might also become increasingly important close to and on top of the Yoneda band. However, the DWBA as implemented in 3DGISAXS does not include higher order terms that could account for these scattering events, see equation (3.40) and figure 3.5.

The experimental data displayed in figure 6.6 (a) was measured on sample-277-1, i.e., the colloidal monolayer as described in chapter 5.2.2. Figures (b) and (c) show simulations calculated with IsGISAXS and 3Dgisaxs respectively. For both simulations, the position of the truncation rods and the rings from the colloidal form factor are in good agreement with the scattering data. The Yoneda band is more clearly reproduced in the simulation done by 3Dgisaxs than the one by IsGISAXS. This difference arises from the fact, that a different system was assumed as a basis for the DWBA in the calculations of the two programs. A layer on top of a substrate was used in the case of 3Dgisaxs, see equation (3.32) and figure 3.5, whereas a simple interface is assumed in the calculations of IsGISAXS, see figure 6.7. Reflection and refraction effects at the interface between the colloidal layer and air are therefor not included in the latter case. Only the effects of total reflection from the substrate can be seen.

The intensity modulation along α_f observed in the scattering data and correctly reproduced by IsGISAXS could not be simulated by 3Dgisaxs. Further investigations

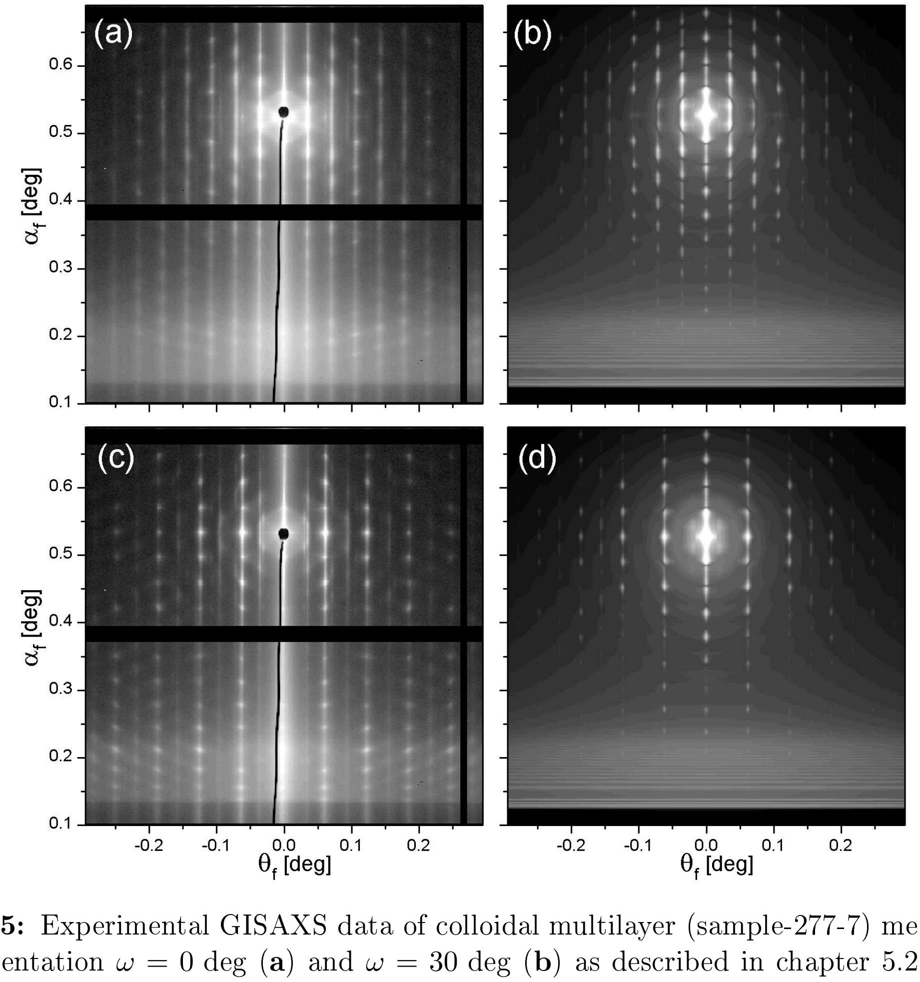

Figure 6.5: Experimental GISAXS data of colloidal multilayer (sample-277-7) measured at a sample orientation $\omega = 0$ deg (**a**) and $\omega = 30$ deg (**b**) as described in chapter 5.2.2. Figures (**b**) and (**c**) are the corresponding simulations calculated with 3Dgisaxs.

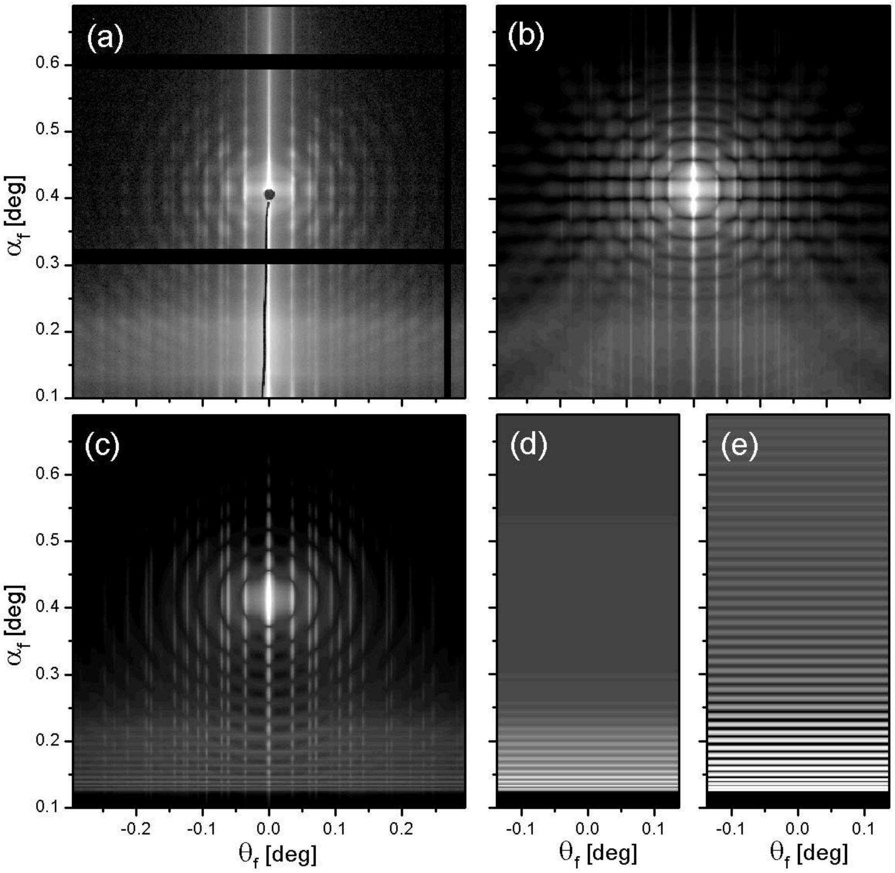

Figure 6.6: (**a**) Experimental GISAXS data measured on a colloidal monolayer (sample-277-1) as described in chapter 5.2.2. Corresponding simulations were done with (**b**) IsGISAXS [171] and (**c**) 3DGISAXS . (**d**) and (**e**) illustrate the GISAXS intensity simulated with 3DGISAXS for the case where the form factor in the numerical calculation of equations (3.40) and (3.5) was set to unity, respectively. Explanations are given in the text.

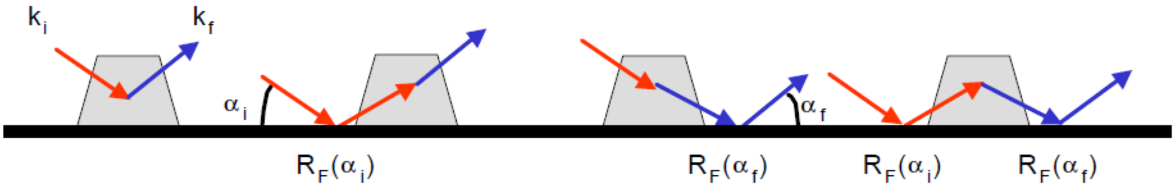

Figure 6.7: Illustration of the system and the terms of the DWBA approach used for particles on top of a simple substrate. This approach was used for the calculation of the simulation in figure 6.6 (b) done by IsGISAXS. Figure taken from [171].

revealed that the cross terms in the DWBA approximation are responsible for this modulation. Figures 6.6 (d) and (e) show the scattering calculated according to equations (3.40) and (3.5), respectively. The form factor was thereby set to unity. It can be seen, that in case of figure (e) an intensity modulation along the exit angle does appear. This modulation corresponds to the case where all the cross terms in the DWBA approach were considered. In figure (d), a modulation is present close to the Yoneda band but it disappears at larger exit angles. Only the four main terms were used for this calculation. The cross terms become important in the case of the monolayer because the beam penetrates much less material. The contribution of multiple scattering events becomes therefor more important. The intensity modulation along α_f is not any longer apparent in the scattering patterns of sample-740-2, i.e., in the case of a double layer of colloids with a diameter of 740 nm.

6.3.2 Scattering Intensities from Selected Stacking Sequences

GISAXS in combination with 3DGISAXS is in principle extremely sensitive to specific stacking sequences. It is possible to differentiate between all possible stacking sequences of *perfect* multilayers consisting of only a few layers of hexagonally close packed spheres.

As an example, figure 6.8 displays the calculated scattering intensities for all possible combinations of stacking sequences of three (a), four (b), and five (c) layers. The intensities were calculated with $\alpha_i = 0.55$ deg on a truncation rod sensitive to changes in the stacking. The sequence of the letters “A”, “B”, “C” denotes the stacking of the hexagonal layers that was used for the calculation of the corresponding scattering curve. The letters correspond to the possible stacking positions in a close-packed assembly of spheres as illustrated in figure 3.2. Sequences marked with bold letters correspond to the cases with a stacking probability $a = 0$ or $a = 1$. Sequences that can be transformed into one another by an inversion have in general only been displayed once as they can not be distinguished. The two cases marked with a star in figure 6.8 (c) are given as an example.

6.3.3 Discussion

The calculations done in the previous sections exemplify the potential and limits of 3DGISAXS. From the comparison of measured scattering intensities of a complete two-dimensional detector with simulated ones, it became clear that 3DGISAXS reproduces the intensity modulation in the scattering patterns due to the three-dimensional order of the colloidal particles very accurately. The tool reaches its limitation in situations where the cross terms in the DWBA approach can no longer be neglected. The two discussed examples corresponded to the case of scattering close to the critical angle and to the case of a colloidal monolayer. In the current implementation of the tool, it is not possible to include the cross terms into the calculation because the form factor, given

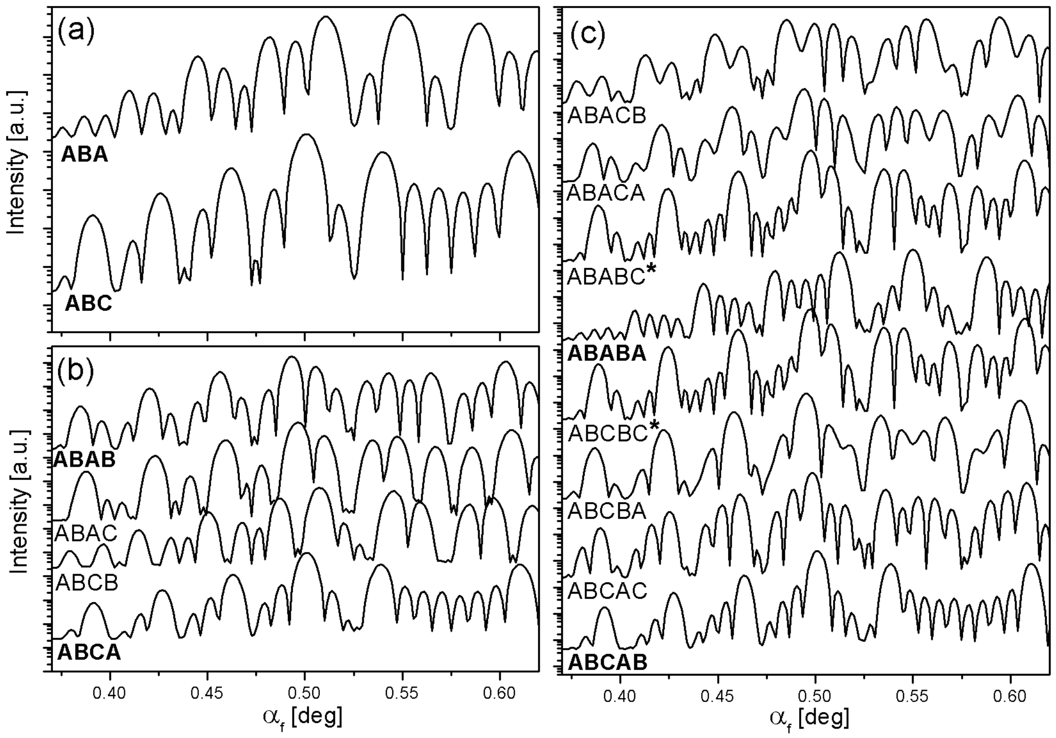

Figure 6.8: Simulated scattering curves (with 3DGISAXS) from hexagonally close-packed multilayers with different stacking sequences and different number of layers - three layers in the case of (**a**), four for (**b**) and five in the case of (**c**). The corresponding stacking of the layers is indicated by the sequence of the letters “A”, “B”, “C” under each calculated curve. Sequences marked with bold letters correspond to the cases with a stacking probability $a = 0$ or $a = 1$. The calculations were done with $\alpha_i = 0.55$ deg and a θ_f value corresponding to a position on a truncation rod sensitive to changes in the stacking. The curves are vertically displaced for better visibility.

in equation (3.10), and all its components are already calculated as an absolute square. For an enhanced tool, one would have to think about how to overcome this limitation.

The calculated scattering curves obtained from hexagonally packed layers with a specific stacking sequences indicate the potential of the combination of GISAXS with a simulation tool such as 3DGISAXS. It was demonstrated that for just a few layers an unambiguous assignment of the scattered intensity to a specific stacking sequence is in principle possible. In an actual experiment, such investigations require of course access to perfect single crystals or have to be done on a single domain of an otherwise disordered colloidal crystal. The further development of the convective self-assembly method and GISAXS combined with a micro-focus[6] could make such investigations possible in the future.

---

[6] Such a setup has for example been realized at the beam line BW4 at HASYLAB, DESY with a focus of $65\times35\mu\text{m}^2$ [173].

CHAPTER 7

Conclusions and Outlook

7.1 Conclusions

7.1.1 Investigations on Prefabricated Colloidal Assemblies

The primary aim of this thesis has been to clarify the potential of GISAXS for the investigation of colloidal assemblies and in particular colloidal crystals. For that purpose, convective self-assembly was successfully used to fabricate colloidal assemblies from particles with diameters between 277 nm up to 740 nm deposited on unstructured glass slides. Samples used for further investigations consisted of monolayers and multilayers up to 14 layers. The resulting assemblies exhibited an almost homogeneous number of layers over large areas. For the best samples, the dimension of such zones ranged from $1\,\mathrm{cm}^2$ to $2\,\mathrm{cm}^2$. Colloidal crystals were also deposited on pDR1M surface relief gratings. This led in general to a less homogeneous coverage.

In-Plane Domain Sizes

Concerning the domain size, no appreciable dependence on the particle size was found from the samples investigated throughout this work. All investigated samples exhibit locally an almost perfect hexagonal close packed arrangement of the colloids. This order breaks down as one increases the distance to a reference point. The estimated size of the perfectly ordered domains from AFM and SEM pictures was for all samples in the range of about 20–40 particle diameters perpendicular to the direction of growth and 40–60 along the growth direction. This difference is a consequence of the directed growth of convective self-assembly. While regions with the same orientation of the particle arrangement can extend over much larger distances, >300 particle diameters perpendicular and parallel to the growth direction, the given domain sizes account for small cracks and irregularities within these zones well visible in AFM images. This definition was chosen as X-ray scattering methods are already sensitive to small deviations from the perfect order.

The maximum correlation lengths achieved by GISAXS experiments in this work were $\sim 4.8\,\mu$m. From these values, it can be concluded that the technique is not appropriate for the study of domain sizes in the case of the used particles unless the resolution can be improved by an order of magnitude. In case of the multilayers consisting of 277 nm particles, the evaluation of the in-plane peak widths revealed paracristalline ordering. For both samples, the broadening of the peaks occurs clearly faster for $\omega = 0$ deg, i.e., for the case where the GISAXS pattern was sensitive to the order perpendicular to the growth direction, than for $\omega = 60$ deg. This observation concurs with the results from microscopy, SEM and AFM that show a lower order perpendicular to the growth direction ($\omega = 0$ deg).

In-Plane Domain Alignment

In the case of the *multilayers* on flat glass substrates, AFM and SEM measurements revealed a similar orientation of the domains on the complete sample. This observation agrees with findings of other investigations performed by SEM on samples fabricated by convective self-assembly. GISAXS data collected on the multilayers with 7 and 14 layers, demonstrate that the investigated samples have a similar alignment of the domains over the complete sample. This is ascertained by the fact that the beam footprint (~ 1 mm lateral and > 60 mm along the beam path) has probed the complete length of the sample. The distribution describing the domain misalignment was fitted with a Gaussian function and gave for the two investigated samples an almost identical FWHM of 4.4 ± 0.9 deg (7 layers) and 4.3 ± 0.8 deg (14 layers), respectively. All characterization methods show that the preferential orientation of the ordered domains is correlated to the direction of the meniscus movement during the self-assembly of the multilayers. This has also been observed in an earlier study. Additionally, it was found that the colloidal particles align along the growth direction, i.e., the [1 0 0] direction of the hexagonal plane is parallel to the growth direction.

In the case of the *monolayers* deposited on the unstructured support, no alignment of the individual domains could be detected by AFM and SEM measurements. This observation is confirmed by the in-plane evaluation of the GISAXS data.

The investigated *bilayers* covering glass slides seem to be a transitional state between the two cases described so far. GISAXS data shows clear evidence of a preferential alignment of the domains over the complete sample. As in the case of the multilayers, the particles are aligned along the growth direction. The orientation is however relaxed with respect to the multilayers. The distribution describing the domain misalignment was fitted with a Lorentzian function and provided a FWHM of 7.5 ± 2.5 deg.

From the presented data, one can conclude that the transition from a self-assembled monolayer to two layers and further towards a multilayer goes in parallel with the development of a mechanism that leads to the directed self-assembly of the particles. In the case of monolayers, the assembly mechanism is well studied. It is presumed that the particles aggregate in a first step because of capillary immersion forces and in a second step due to the induced convective flow. In the case of multilayers, the process is understood qualitatively only. A detailed mechanism that explains how three-dimensional close packed structures of colloidal spheres emerge has not been clearly identified so far. The increase solvent flow in the case of multilayers could possibly play a role in the macroscopic alignment of the colloidal domains.

The here presented approach in methodology for the in-plane evaluation of the scattering data shows that GISAXS is an ideal tool to detect the exact degree of the domain alignment on samples. In case of SEM and AFM, this information can only be accessed by a laborious evaluation of large numbers of individual micrographs. The introduced method to asses the in-plane order from GISAXS data can therefore be used to efficiently assess the influence of different factors influencing the alignment of the ordered domains. This evaluation could eventually contribute to a deeper understanding of the detailed mechanisms that lead to the three-dimensional particle assembly.

GISAXS has limitations concerning the evaluation of the domain sizes. These dimensions have not been accessed by GISAXS in this work because the maximum correlation lengths achieved by GISAXS experiments corresponded to less than 20 particle diameters for all investigated particles. SEM and AFM methods are clearly better suited for this purpose.

Colloidal Assemblies on Surface Gratings

The two presented *samples assembled on pDR1M surface relief gratings* did not reveal perceptible differences to the samples assembled on flat glass when investigated with microscopy, AFM and SEM. The influence of the topologically templated substrate on the colloidal arrangement could neither be ascertained by SEM nor by AFM. No evidence of cubic arrangement was found on the sample with a cubically structured substrate. The GISAXS data confirmed the findings of the classical methods. Only weak or no alignment of the domains was observed. This is in contrast to the generally accepted and experimentally confirmed view, that template assisted self-assembly leads to an increased long-range order and can be used to influence the crystal orientation and crystal symmetry, see chapter 1.1.2. The deviant results can be attributed to an inhomogeneous wetting behavior of the polymer with a high probability (arguably due to problems during the polymer film formation and the writing process of the grating).

7.1.2 Investigations During the Formation of Colloidal Assemblies

ED-XRR and GISAXS investigations were performed during the drying of droplets of colloidal dispersion. These investigations were intended to probe the assembly process *in situ*. The measured scattering data exhibits a rich behavior. Most of it can however be understood by effects originating from the solvent and the change in the droplet shape. No signal attributed to ordering processes was detected from the data. Subsequent AFM and SEM investigations confirmed the mostly disordered assembly of the particles. It was concluded that the chosen system is not ideal for *in situ* investigations.

7.1.3 Numerical Calculation of Scattering Data

A tool named "3DGISAXS " has been developed and implemented in the framework of this thesis for the modeling of the scattering data obtained from colloidal multilayers. It includes reflection and refraction effects important at grazing scattering angles. The scattering intensities can be calculated from actual particle coordinates or from an analytical function incorporating the stacking probability of the hexagonal close packed layers.

Stacking of the Hexagonal Layers

The implemented model was fitted to the scattering data of one multilayer (7 layers) to exemplify the potential of the approach. The analytical function incorporating the stacking probability has thereby been used to fit the data. The extracted stacking probability amounts to $a = 0.63$[1]. Compared to earlier studies that found fcc stacking this value is relatively low. It can be understood by the fact, that the previous studies investigated the colloidal assembly on a very local basis, i.e., on the micrometer scale, while the information obtained by GISAXS is a statistical average over the *complete* sample, i.e., over a centimeter scale.

The advantage of GISAXS with respect to currently used characterization methods derives from the possibility of the technique to probe microscopic properties on a macroscopic scale. While classical methods such as SEM or confocal microscopy have been used for the local determination of the stacking order in colloidal crystals fabricated by convective self-assembly, GISAXS is the only method that can provide statistical relevant information on the *stacking of the hexagonally packed layers perpendicular to the substrate surface* for these samples. Additionally, this information is gained in a destruction free manner. In contrary to SEM and confocal microscopy, samples can therefore be used in further processing steps. These characteristics make GISAXS combined with a simulation tool to a valuable addition to the toolbox of techniques for the characterization and the further advancement of the convective self-assembly technique.

Simulations

The tool 3DGISAXS was in a further step used for the simulation of complete scattering patterns as measured with area detectors. These simulations have been compared with actual scattering data. In general, an accurate agreement of the calculated and experimental intensity patterns was found. The comparison led also to the identification of the limitations of the simulation tool.

---

[1] $a = 0.0$ corresponds to hcp, $a = 0.5$ to complete random and $a = 1.0$ to fcc stacking

Simulations were done for single crystals of just a few hexagonally ordered layers exhibiting a specific stacking sequences in the direction perpendicular to the surface. It was demonstrated that GISAXS in combination with 3DGISAXS is able to discriminate between these differently stacked multilayers. An unambiguous assignment to a specific stacking is possible for these thin layered structures, see figure 6.8.

7.2 Outlook

Based on the presented study, there are several interesting aspects worth future investigations:

GISAXS with the presented simulation tool permits now a *systematic investigation of the order in colloidal assemblies* parallel and perpendicular to the surface. A detailed understanding of the mechanisms leading to the three-dimensional assembly could be gained by studying the properties of the colloidal crystals related to original process parameters of the assembly. Such knowledge could then be used for a further advancement of the convective self-assembly technique.

The method is not limited to the investigation of colloidal assemblies fabricated by convective self-assembly. In principle, the method developed in this work can *probe every kind of three-dimensionally structured film* deposited on a substrate that reflects X-rays. This opens a broad field of investigations on very different structures - colloidal crystals produced by other methods, copolymer thin-films or nanoparticle arrangements. Such structures have already been characterized by GISAXS but these investigations concentrated in general on the determination of the crystalline symmetry of the films. Only peak positions are needed for such investigations. The information in the intensity distribution between the peaks has mostly been ignored in previous studies. However, the further investigation of the intensity distributions between the peaks with the simulation tool developed in this work could provide information about correlations and disorder in these systems.

Investigations as proposed in the previous paragraph will of course need a *further development of the simulation tool*. The extension on other crystalline symmetries, the inclusion of effects of surface roughness and the cross terms in the DWBA approach are just a few enhancements that would be interesting for future GISAXS investigations. These developments could ultimately lead to a tool that provides detailed information about three-dimensionally structured thin films.

By tuning the incident angle of the experiment, a *depth dependent investigation of the properties of colloidal crystals* is in principle possible. In the presented study the penetration depth of the X-ray beam extended always over the complete thickness of the colloidal crystal due to the angles relatively far away from the critical angle of the colloidal particles. In order to realize a depth dependent study, the substrate should ideally have a critical angle at a lower value than the polymer particles. Otherwise, the analysis of the data will get demanding due to multiple scattering effects that get increasingly important as one approaches the critical angle of the colloidal particles.

A very exciting prospect is given by the *CAPA tool* constructed in the framework of this thesis. It was specifically built in a way that it is possible to *investigate the convective self-assembly in situ by X-ray scattering*. This provides a system that is much better defined for such investigations than the dry-out of a droplet of dispersion. Additionally, the dry-out process could be very precisely investigated. All the stages between the particle assembly in the solvent and the dry colloidal assembly can be probed by setting the relative distance to the meniscus that itself stays at a fixed position. An adjustable “time resolution” of the assembly and dry-up process could be achieved following this approach. This would again increase the knowledge about the specific processes occurring during self-assembly.

Appendix

A Abbreviations

AFM	atomic force microscope
CV	coefficient of variation
DWBA	distorted wave Born approximation
ED-XRR	energy dispersive X-ray reflection
fcc	face centred cubic
FWHM	full width at half maximum
GISAXS	grazing incidence small angle X-ray scattering
hcp	hexagonal close-packed
PBG	photonic bandgap
PDI	polydispersity index
pDR1M	polydisperse-red-1-methacrylate
PMMA	polymethylmethacrylat
PS	polystyrene
PSI	Paul Scherrer Institute
SAXS	small angle x-ray scattering
SEM	scanning electron microscope
SLS	Swiss Light Source
XRR	X-ray reflection

B Transfer Matrix Method

In this appendix, the matrix transfer method used to calculate (3.20) is presented for the sake of completeness. Apart from changes in the nomenclature, this text was taken without modifications from reference [144].

A three-dimensional structure is constructed by stacking the identical layers along the z direction according to a stochastic stacking sequence. For our purposes it is sufficient to assume two different possible connecting vectors, $\mathbf{r}_1$ and $\mathbf{r}_2$, between the origins of neighboring layers. For $\ell > 0$, let a denote the probability that the $\updownarrow$th stacking operation is an $\mathbf{r}_1$ translation, i.e., $\Delta\mathbf{R}_\ell = \Delta\mathbf{R}_{\updownarrow-1} + \mathbf{r}_1$, if the preceding stacking step was also $\mathbf{r}_1$. In other words, a is the probability of having two consecutive $\mathbf{r}_1$ translations in the stacking sequence. If this probability is symbolized by $\mathscr{P}(\mathbf{r}_1 \rightarrow \mathbf{r}_1)$, the probabilities for all possible two-step sequences are defined by

$$\begin{aligned} a &:= \mathscr{P}(\mathbf{r}_1 \rightarrow \mathbf{r}_1) \qquad & b &:= \mathscr{P}(\mathbf{r}_1 \rightarrow \mathbf{r}_2) \\ c &:= \mathscr{P}(\mathbf{r}_2 \rightarrow \mathbf{r}_1) \qquad & d &:= \mathscr{P}(\mathbf{r}_2 \rightarrow \mathbf{r}_2) \end{aligned} \tag{B.1}$$

Note, $a + b = c + d = 1$. For the initial translation no predecessor is specified and an equal probability of $l/2$ is assumed for the two possibilities. Hence, on average the phase factor of two immediately neighboring layers is

$$\langle \mathrm{e}^{\mathbf{Q}\cdot\Delta\mathbf{R}_\ell} \rangle = \tfrac{1}{2}a\,\mathrm{e}^{i\mathbf{Q}\cdot\mathbf{r}_1} + \tfrac{1}{2}b\,\mathrm{e}^{i\mathbf{Q}\cdot\mathbf{r}_2} + \tfrac{1}{2}c\,\mathrm{e}^{i\mathbf{Q}\cdot\mathbf{r}_1} + \tfrac{1}{2}d\,\mathrm{e}^{i\mathbf{Q}\cdot\mathbf{r}_2} \tag{B.2}$$

summing up the four different possible stacking sequences with their respective probabilities. This can equivalently be written in matrix form: Let the matrix A be defined by

$$A := \begin{pmatrix} a\,\mathrm{e}^{i\mathbf{Q}\cdot\mathbf{r}_1} & b\,\mathrm{e}^{i\mathbf{Q}\cdot\mathbf{r}_2} \\ c\,\mathrm{e}^{i\mathbf{Q}\cdot\mathbf{r}_1} & d\,\mathrm{e}^{i\mathbf{Q}\cdot\mathbf{r}_2} \end{pmatrix},$$

i.e.,

$$A_{\mu,\nu} := \mathscr{P}(\mathbf{r}_\mu \rightarrow \mathbf{r}_\nu)\,\mathrm{e}^{i\mathbf{Q}\cdot\mathbf{r}_\nu}, \tag{B.3}$$

then

$$\langle \mathrm{e}^{\mathbf{Q}\cdot\Delta\mathbf{R}_\ell} \rangle = \frac{1}{2}(1\ 1) \begin{pmatrix} A_{11} & A_{12} \\ A_{21} & A_{22} \end{pmatrix} \begin{pmatrix} 1 \\ 1 \end{pmatrix}. \tag{B.4}$$

The matrix elements $A_{\mu,\nu}$ are the weighted phase differences between two *neighboring Layers* for the case that the first layer was generated by an $\mathbf{r}_\mu$ translation and the second by an $\mathbf{r}_\nu$ translation (μ, $\nu = 1, 2$), thus comprising all four possibilities. The average phase difference is then obtained by simply summing all elements of A, formally $(1\ 1)A$ $(1\ 1)^T$.

Let $A^{(2)}$ be the matrix corresponding to the weighted phase difference between two layers which are *separated by one intermediate layer*. Again, the matrix elements $A^{(2)}_{\mu,\nu}$ shall denote the weighted phase differences between these two layers for the four possible cases that the first layer was generated by an $\mathbf{r}_\mu$ translation and the final layer by an $\mathbf{r}_\nu$ translation. $A^{(2)}_{\mu,\nu}$ is then determined by summing the phase differences along all possible paths between these two layers which begin with $\mathbf{r}_\mu$ and end with $\mathbf{r}_\nu$ weighted with the probabilities for their occurrence. Clearly, this sum extends over the two possible configurations of the intermediate layer:

$$\begin{aligned} A^{(2)}_{\mu,\nu} &= \sum_{\alpha=1}^{2} \mathscr{P}(\mathbf{r}_\mu \to \mathbf{r}_\alpha)\mathscr{P}(\mathbf{r}_\alpha \to \mathbf{r}_\nu)\,\mathrm{e}^{i\mathbf{Q}\cdot(\mathbf{r}_\alpha+\mathbf{r})} \\ &= \sum_{\alpha=1}^{2} A_{\mu,\alpha}A_{\alpha,\nu} = A^2_{\mu,\nu}, \end{aligned}$$

i.e., the elements of $A^{(2)}$ are determined by squaring the transfer matrix A. By complete induction it is now proven that the matrix $A^{(\ell)}$, whose elements are the weighted phase differences between two layers separated by $(\ell - 1)$ intermediate layers, is simply given by $A^{(\ell)} = A^\ell$, i.e., as the ℓth power of the transfer matrix A. It is assumed that this relation holds for $\ell = n$: $A^{(n)} = A^n$. We now consider $A^{(n+1)}$, the case where one layer has been added. The weighted phase differences between the reference layer and the $(n+1)$th layer, $A^{(n+1)}_{\mu,\nu}$, can then be calculated by a continuation of the stacking sequence: the weighted phase factors for the n-layer sequence $A^{(n)}_{\mu,\nu}$ are already known and the nth translation was either $\mathbf{r}_1$ or $\mathbf{r}_2$, hence,

$$A^{(n+1)}_{\mu,\nu} = \sum_{\alpha=1}^{2} A_{\mu,\alpha}A^{(n)}_{\alpha,\nu} \sum_{\alpha=1}^{2} A_{\mu,\alpha}A^{n}_{\alpha,\nu}A^{n+1}_{\mu,\nu}$$

which completes the proof.

The average phase factor $\langle e^{i\mathbf{Q}\cdot\Delta\mathbf{R}_\ell}\rangle$ in eq. (3.18) is determined as the sum of all elements of $A^{(\ell)} = A^\ell$, as was just shown for $\ell > 0$:

$$\langle e^{i\mathbf{Q}\cdot\Delta\mathbf{R}_\ell}\rangle = \frac{1}{2}(1\ 1)A^\ell(1\ 1)^T \qquad \text{for} \quad \ell > 0. \tag{B.5}$$

For $\ell < O$, the stacking has to be pursued in the opposite direction, with translation vectors $-\mathbf{r}_1$ and $-\mathbf{r}_2$. The corresponding transfer matrix, defined in analogy with eq. (B.3) as

$$B_{\mu,\nu} := \mathscr{P}(-\mathbf{r}_\mu \to -\mathbf{r}_\nu)\,\mathrm{e}^{-i\mathbf{Q}\cdot\mathbf{r}_\nu}, \tag{B.6}$$

can be related to A. The probability of the occurrence of a given stacking pair does not depend on the direction of the stacking sequence:

$$\mathscr{P}(\mathbf{r}_\mu \to \mathbf{r}_\nu) = \mathscr{P}(-\mathbf{r}_\nu \to -\mathbf{r}_\mu) \tag{B.7}$$

i.e., the probability of finding an $\mathbf{r}_\nu$ translation following $\mathbf{r}_\mu$ is equal to the probability of finding a $-\mathbf{r}_\mu$ translation following $-\mathbf{r}_\nu$, in the opposite direction. We now assume that the probability of a change in the stacking sequence is independent of the preceding translation, thus implying

$$\mathscr{P}(\mathbf{r}_1 \to \mathbf{r}_2) = \mathscr{P}(\mathbf{r}_2 \to \mathbf{r}_1) \quad \text{and} \quad \mathscr{P}(\mathbf{r}_1 \to \mathbf{r}_1) = \mathscr{P}(\mathbf{r}_2 \to \mathbf{r}_2) \tag{B.8}$$

Consequently,

$$B_{\mu,\nu} = \mathscr{P}(\mathbf{r}_\mu \to \mathbf{r}_\nu)\,\mathrm{e}^{-i\mathbf{Q}\cdot\mathbf{r}_\nu} = A^*_{\mu,\nu}. \tag{B.9}$$

In analogy to the treatment of the $\ell > 0$ case, one obtains for $\ell < 0$:

$$\langle e^{i\mathbf{Q}\cdot\Delta\mathbf{R}_\ell}\rangle = \frac{1}{2}(1\;1)A^{|\ell|}(1\;1)^T. \tag{B.10}$$

If these results, Eqs. (B.5) and (B.10), are inserted, the general formula (3.18) for the static structure factor reads

$$\begin{aligned} S_{ML}(\mathbf{Q}) &= \left\langle|\mathcal{L}(\mathbf{Q})|^2\right\rangle \left[1 + \frac{1}{2}\sum_{\ell=1}^{L-1}\left(1-\frac{\ell}{L}\right)(1\;1)\left(A^\ell + A^{*\ell}\right)\begin{pmatrix}1\\1\end{pmatrix}\right] \\ &= \left\langle|\mathcal{L}(\mathbf{Q})|^2\right\rangle \frac{1}{2}(1\;1)\left[I + \sum_{\ell=1}^{L-1}\left(1-\frac{\ell}{L}\right)\left(A^\ell + A^{*\ell}\right)\right]\begin{pmatrix}1\\1\end{pmatrix}, \end{aligned} \tag{B.11}$$

where I denotes the identity matrix. Note that the assumption (B.8) is equivalent to setting $a = d$ and $b = c$ in eq. (B.3) and the matrix A now reads

$$A := \begin{pmatrix} a\,\mathrm{e}^{i\mathbf{Q}\cdot\mathbf{r}_1} & b\,\mathrm{e}^{i\mathbf{Q}\cdot\mathbf{r}_2} \\ b\,\mathrm{e}^{i\mathbf{Q}\cdot\mathbf{r}_1} & a\,\mathrm{e}^{i\mathbf{Q}\cdot\mathbf{r}_2} \end{pmatrix}. \tag{B.12}$$

Equation (B.11) for the static structure factor has to be simplified to be practicable. The auxiliary matrix T is introduced for that purpose,

$$T := I + \sum_{\ell=1}^{L-1}\left(1-\frac{\ell}{L}\right)A^\ell. \tag{B.13}$$

Hence,

$$AT = A + \sum_{\ell=1}^{L-1}\left(1-\frac{\ell}{L}\right)A^{\ell+1} = \sum_{\ell=1}^{L}\left(1-\frac{\ell-1}{L}\right)A^\ell$$

and

$$(I - A)T = I - \frac{1}{L}\sum_{\ell=1}^{L}A^\ell \tag{B.14}$$

The second term on the right-hand side of eq. (B.14) can be neglected for $L \to \infty$ if the sum converges. By virtue of the binomial theorem,

$$(I - A)^{-1} = \sum_{\ell=0}^{\infty} A^{\ell},$$

this condition is intimately related to the existence of the inverse of $(I - A)$. The sum converges if the absolute values of all eigenvalues of A are less than unity. The special structure of the matrix A, cf. eq. (B.12), with the constraints $a + b = 1$ and a, $b > O$, seems to suggest that this restriction should not cause any problem. As a general analysis of the eigenvalues is not conclusive, we take a pragmatic point of view and check the calculated inverse matrix a *posteriori* for possible divergences. For $0 < a < l$ and in the limit $M \to \infty$, eq. (B.14) reads

$$(I - A)T = 1,$$

hence

$$T = (I - A)^{-1}, \tag{B.15}$$

the existence of the inverse $(I - A)^{-1}$ being guaranteed by the same condition. Analogously, $T^* = (I - A^*)^{-1}$ and eq. (B.11) can be written as

$$S_{ML}(\mathbf{Q}) = \left\langle |\mathcal{L}(\mathbf{Q})|^2 \right\rangle \frac{1}{2}(1\ 1)\big[(I - A)^{-1} + (I - A^*)^{-1} - I\big]\begin{pmatrix} 1 \\ 1 \end{pmatrix}. \tag{B.16}$$

The calculation of the inverse matrices is straightforward and if the variable b is substituted by $(1 - a)$ one obtains eq. (3.20) of the text. Equation (3.20) is the key result of the transfer matrix method.

With $\exp(i\mathbf{Q} \cdot \mathbf{r}_1) = \exp(i\mathbf{Q} \cdot \mathbf{r}_2) =: \exp(i2\pi l)$ the matrix A can be written as

$$A = \mathrm{e}^{i2\pi l} \begin{pmatrix} a & b \\ b & a \end{pmatrix} =: \mathrm{e}^{i2\pi l}\, P, \tag{B.17}$$

thus defining a matrix P, which is a *stochastic matrix*, i.e., the sums along its rows and columns all add up to unity and its elements are constrained by $0 \leqslant a, b \leqslant 1$. Stochastic matrices have the property that $\lambda = 1$ is always an eigenvalue with eigenvector $(1\ 1)^T$. This already indicates that the assumption underlying the binomial theorem is violated for .this case. Because $A^{\ell} = \exp(i2\pi l\ell)P^{\ell}$ the recursive matrix multiplication is trivial. For eq. (B.11) one immediately obtains

$$S_{ML}(\mathbf{Q}) = \left\langle |\mathcal{L}(\mathbf{Q})|^2 \right\rangle \left[1 + 2\sum_{\ell=1}^{L-1} \left(1 - \frac{\ell}{L}\right) \cos(2\pi l\ell)\right]. \tag{B.18}$$

Note that this result is independent of the stacking probability a. The means to evaluate sums of the type as occurring in eq. (B.18) are outlined in the Appendix of [143]. Accordingly, one obtains eq. (3.22) of the text.

C Resolution in Reciprocal Space

This appendix explicates how to derive the experimental resolution in order to result with equations (3.44) to (3.48).

Starting from the formula for the scattering vector[1]

$$\mathbf{Q} = \begin{pmatrix} Q_x \\ Q_y \\ Q_z \end{pmatrix} = k \begin{pmatrix} \cos\alpha_f \cos\theta_f - \cos\alpha_i \cos\theta_i \\ \cos\alpha_f \sin\theta_f + \cos\alpha_i \sin\theta_i \\ \sin\alpha_f + \sin\alpha_i \end{pmatrix} \tag{C.1}$$

with $k = 2\pi/\lambda$ one uses the formula for Gaussian error propagation for a function $f(x_1, \ldots, x_n)$ with n variables x_i and corresponding uncertainties Δx_i

$$(\Delta f)^2 = \sum_i \left(\frac{\partial f}{\partial x_i} \Delta x_i \right)^2 \tag{C.2}$$

and finds

$$\begin{aligned} (\Delta Q_x)^2 = {} & \left(\tfrac{Q_x}{k}\right)^2 (\Delta k)^2 \\ & + k^2 \Big[(\sin\alpha_f \cos\theta_f)^2 \cdot (\Delta\alpha_f)^2 + (\cos\alpha_f \sin\theta_f)^2 \cdot (\Delta\theta_f)^2 \\ & + (\sin\alpha_i \cos\theta_i)^2 \cdot (\Delta\alpha_i)^2 + (\cos\alpha_i \sin\theta_i)^2 \cdot (\Delta\theta_i)^2 \Big] \end{aligned} \tag{C.3}$$

$$\begin{aligned} (\Delta Q_y)^2 = {} & \left(\tfrac{Q_y}{k}\right)^2 (\Delta k)^2 \\ & + k^2 \Big[(\sin\alpha_f \sin\theta_f)^2 \cdot (\Delta\alpha_f)^2 + (\cos\alpha_f \cos\theta_f)^2 \cdot (\Delta\theta_f)^2 \\ & + (\sin\alpha_i \sin\theta_i)^2 \cdot (\Delta\alpha_i)^2 + (\cos\alpha_i \cos\theta_i)^2 \cdot (\Delta\theta_i)^2 \Big] \end{aligned} \tag{C.4}$$

$$(\Delta Q_z)^2 = \left(\tfrac{Q_z}{k}\right)^2 (\Delta k)^2 + k^2 \Big[\cos\alpha_f^2 \cdot (\Delta\alpha_f)^2 + \cos\alpha_i^2 \cdot (\Delta\alpha_i)^2 \Big]. \tag{C.5}$$

Using the small angle approximation ($\sin(\alpha_{i,f}, \theta_{i,f}) \backsimeq (\alpha_{i,f}, \theta_{i,f})$ and $\cos(\alpha_{i,f}, \theta_{i,f}) \backsimeq 1$), equations (C.3)-(C.5) can be further simplified to yield

$$\Delta Q_x = \sqrt{\left(\tfrac{Q_x}{k}\right)^2 (\Delta k)^2 + k^2 \left[\alpha_i^2 (\Delta\alpha_i)^2 + \alpha_f^2 (\Delta\alpha_f)^2 + \theta_i^2 (\Delta\theta_i)^2 + \theta_f^2 (\Delta\theta_f)^2 \right]} \tag{C.6}$$

$$\Delta Q_y = \sqrt{\left(\tfrac{Q_y}{k}\right)^2 (\Delta k)^2 + k^2 \left[(\Delta\theta_i)^2 + (\Delta\theta_f)^2 \right]} \tag{C.7}$$

$$\Delta Q_z = \sqrt{\left(\tfrac{Q_z}{k}\right)^2 (\Delta k)^2 + k^2 \left[(\Delta\alpha_i^2 + (\Delta\alpha_f)^2 \right]}. \tag{C.8}$$

---

[1] In the following derivation, the coordinate system is chosen as defined in figure 1.10.

D CAPA Tool

The CAPA Tool has been named and constructed following the example of [156]. Its intention is to have good control over the process parameters important for convective self-assembly as described in chapter 1.1.2. A schematic layout and a general description of the tool is given in the main text in chapter 4.2. This appendix concentrates on the technical implementation of the tool.

The central part of the setup consists of the sample holder on top of a translation stage. The sample holder incorporates several features. It contains different vacuum chucks to hold samples of various sizes in position. An integrated temperature sensor (Pt100) supplies the controller of the Peltier element (Quick-Cool Conrad Elektronik, QC-127-1.4-8.5M) with a measurement of the actual sample stage temperature. This sensor can be applied at different positions. One side of the Peltier element is fixed from below to the sample stage that has been constructed relatively massive in order to result with a stable temperature at the position of the sample. The temperature of the other side of the Peltier element is stabilized by a water cooled copper block. The confinement slide is clamped on a holder that allows the adjustment of the angle and the hight of the slide relative to the surface of the sample stage. The holder itself is mounted at a fixed position on the ground plate beside the body of the motor. A scheme and a photography of the tool can be seen in figure D.1.

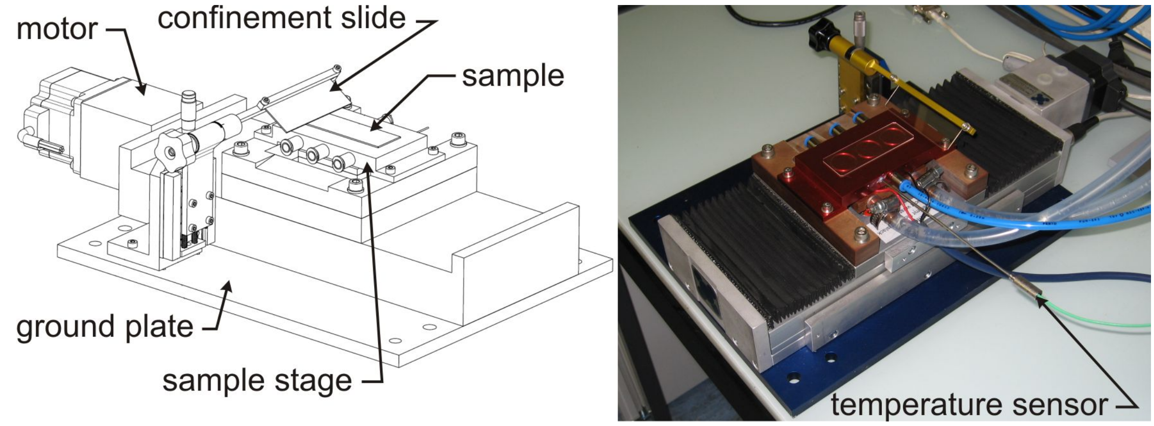

Figure D.1: CAPA Tool

A PID controller (Eurotherm 3504) is used to steady the temperature of the sample stage at a given value. Depending on the input of the temperature sensor located in the sample stage, the PID controller switches the polarity and the pulse durations of the current that drives the Peltier element. The temperature is only stabilized by the variation of the heating or cooling time and not by applying different power levels. A temperature range from 10 to 35 °C was tested during this work. The temperature at the position of the sensor was constant between ±0.04 °C in this range. The PID controller possesses a RS232 interface.

The translation stage (Vögelin) has a maximal drive range of 96 mm. A combined stepping motor/driver-unit (Oriental RK-564-AEC) moves the stage with a minimum step width of 0.1 μm and a maximal velocity of 10 μm/sec. These two values are interdependent and can be adjusted in a certain range. The programmable motor controller (Oriental EMP401) is driven over a RS232 interface.

E GISAXS Data as Collected

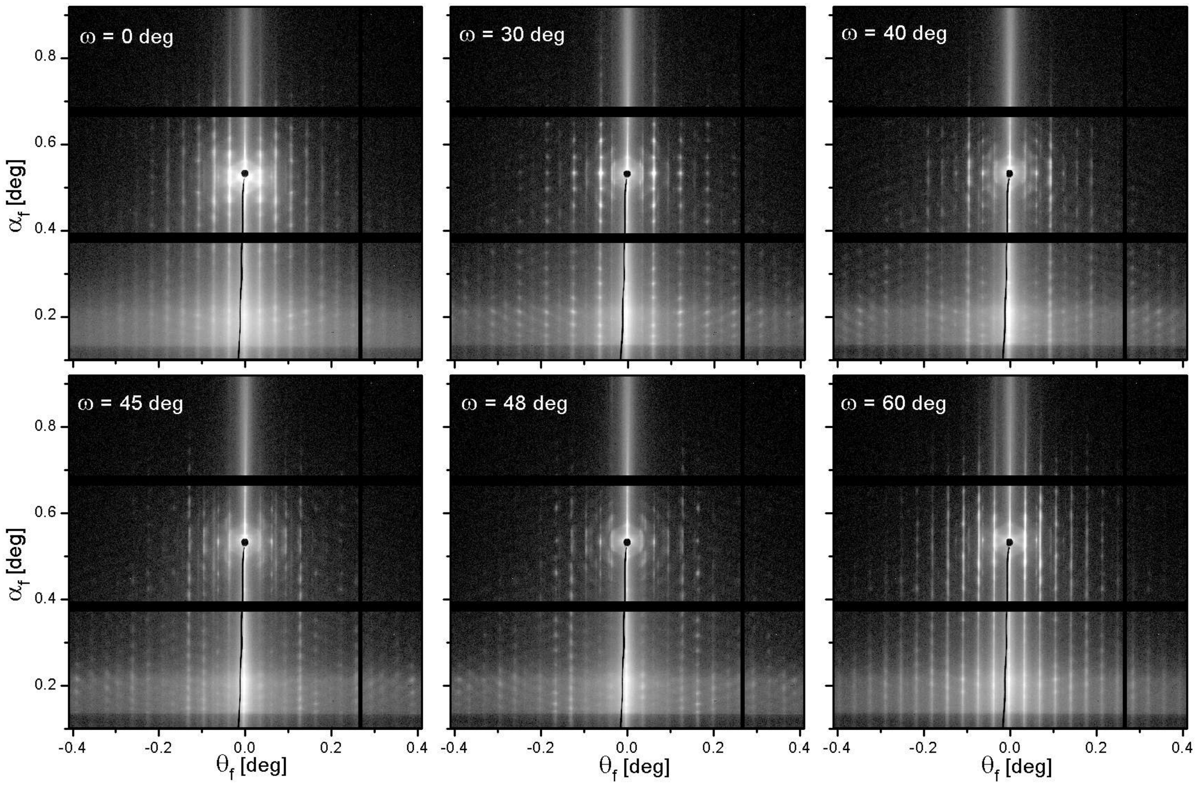

Figure E.1: Scattering patterns collected from sample-277-7. The intensity scale is logarithmic and identical for all scattering patterns.

The scattering data shown in figure E.1 was measured as described in chapter 5.2.2. An incident angle $\alpha_i = 0.53$ deg but different sample orientations ω were used. The displayed scattering intensities correspond exactly to the orientation marked on the individual graphs, i.e., no averaging over different sample orientations was done in this case.

F Fits of in Plane Line Cuts

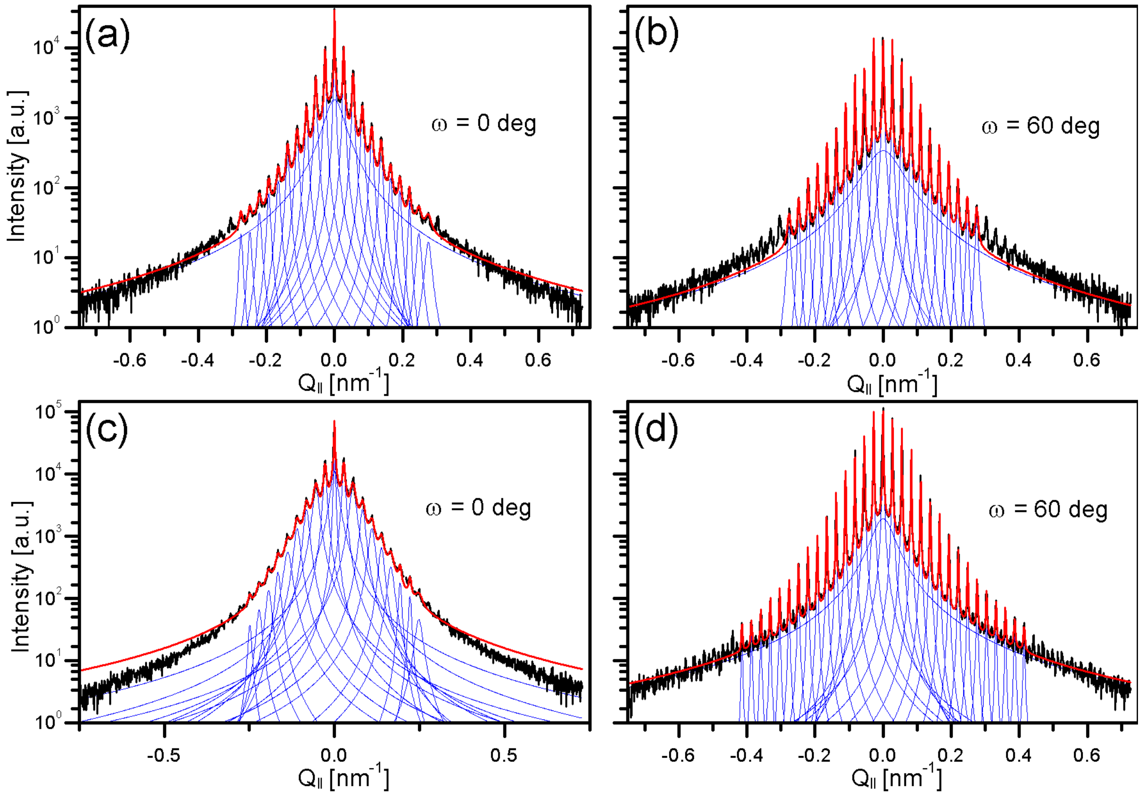

Figure F.1: Elaborated illustration of fits as described in figures 5.13 and 5.14.

The line cuts in figure F.1 (a) and (b) correspond to the fits displayed in figure 5.13 (a). They have been extracted of scattering patterns measured on sample-277-7. The line cuts in figure F.1 (c) and (d) are the fits shown in figure 5.14 (a). They correspond to sample-277-14. See chapter 5.2.2 for the exact description of the data.

The scattering data has been fitted by a sum of Lorentzians peaks. In case of sample-277-7, see figure F.1 (a) and (b), peaks up to the tenth order were included. In case of sample-277-14, peaks up to the ninth order were included along $\omega = 0$ deg, see F.1 (c), and up to the fifteenth along $\omega = 60$ deg, see F.1 (d). An additional Lorentzian peak centered at $\mathbf{Q}_{||} = 0$ was used take account for the broad background. In figure F.1, all fit components are displayed in blue. The final fit corresponds to the red curve.

The sharp dip in the scattering intensity close to $\mathbf{Q}_{||} = 0$ caused by the beam stop in 5.13 (a) and 5.14 (a) is not displayed here because this data has been omitted for the actual fitting process.

G 3Dgisaxs

The theory implemented for the simulation tool 3DGISAXS is discussed in the main part of this work. This appendix explains schematically how the different implemented procedures work together for the simulation and the fitting of scattering data.

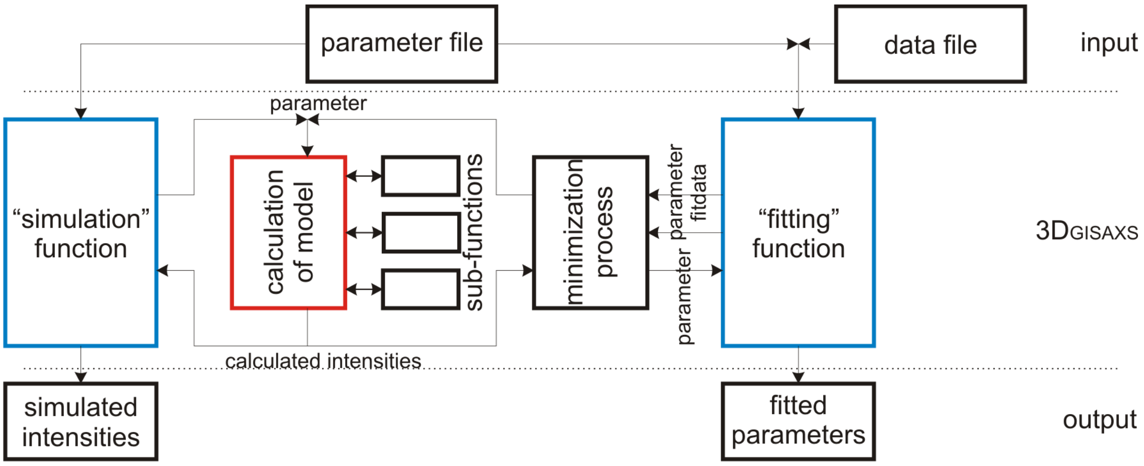

Figure G.1: Flow diagram describing the interplay between the different components of 3DGISAXS

The flow diagram given in figure G.1 demonstrates the interaction of the different parts of 3DGISAXS . The core of the tool is the function marked in red in figure G.1 that does the actual calculation of the model. By invoking different sub-functions, it computes the scattering intensity from the provided parameters that describe the model. Sub-functions calculate for example the scattering from the grating, the Debye-Waller factor or the averaged form factor.

Depending on the use of the program, the parameters are transfered to the "core" function by the "fitting"- or the "simulation"-function marked in blue in figure G.1. The main task of the "simulation" function is to import the parameters from the parameter-file, to call the "core" function and finally to present and save the calculated scattering intensities.

In the case of a fitting process, parameters and measured data are read by the "fitting"-function. The data file contains for each measured intensity the corresponding experimental angles α_f and θ_f and the error. The "fitting"-function calls a dedicated procedure for the minimization process. This procedure was downloaded from the internet [174]. The parameters that optimally describe the experimental data are handed back to the "fitting"-function at the end of the minimization. Saving and displaying of the fitted intensities and the parameters are again done by this function.

H Stacking Sequences of 7 Close Packed Layers

An individual hexagonally ordered layer incorporated in a stack of identical layers is either embedded in a hcp- or a fcc-like surrounding. The surrounding is defined by the relative position of the neighboring layer above and below as illustrated in figure 3.2. In this figure and the accompanying text, the three letters A, B and C have been introduced to denote the possible positions the hexagonally packed layers can take. As these letters specify only *relative* positions, A B C and B A C correspond for example both to fcc ordering whereas sequences such as A B A and C A C correspond to hcp stacking. In general, a triple of letters containing three different letters characterizes a fcc surrounding. If only two letters are included in the triple, it denotes a hcp surrounding. The stacking probability a introduced in chapter 3.2 can accordingly also be defined as the percentage of fcc-like stacked triples in a certain stacking sequence.

In the case of seven hexagonally close packed layers stacked on top of each other, five triples of layers can be established, i.e., one finds $2^5 = 32$ different possible stacking sequences. The corresponding list is given in table H.1 using the notation with the letters A, B, C for the relative positions. The stacking probability associated to each individual combination is shown in the last column. As can be seen, only the values $a = 0.0, 0.2, 0.4, 0.6, 0.8$ and 1.0 appear. These are the possible values in case of a single domain crystal of seven layers. Assuming random stacking and a multi-domain structure, all the 32 stacking variants occur with an equal probability. The overall stacking probability is then the average over all variants resulting in $a = 0.5$.

A	B	A	B	A	B	A	→	$a = 0.0$
A	B	A	B	A	B	C	→	$a = 0.2$
A	B	A	B	A	C	A	→	$a = 0.2$
A	B	A	B	A	C	B	→	$a = 0.4$
A	B	A	B	C	A	B	→	$a = 0.6$
A	B	A	B	C	A	C	→	$a = 0.4$
A	B	A	B	C	B	A	→	$a = 0.4$
A	B	A	B	C	B	C	→	$a = 0.2$
A	B	A	C	A	B	A	→	$a = 0.4$
A	B	A	C	A	B	C	→	$a = 0.6$
A	B	A	C	A	C	A	→	$a = 0.2$
A	B	A	C	A	C	B	→	$a = 0.4$
A	B	A	C	B	A	B	→	$a = 0.6$
A	B	A	C	B	A	C	→	$a = 0.8$
A	B	A	C	B	C	A	→	$a = 0.6$
A	B	A	C	B	C	B	→	$a = 0.4$

Table H.1: The 32 different stacking arrangements of 7 close packed layers and the associated stacking probability, a. Continued on next page.

A	B	C	A	B	A	B	→	$a = 0.6$
A	B	C	A	B	A	C	→	$a = 0.8$
A	B	C	A	B	C	A	→	$a = 1.0$
A	B	C	A	B	C	B	→	$a = 0.8$
A	B	C	A	C	A	B	→	$a = 0.6$
A	B	C	A	C	A	C	→	$a = 0.4$
A	B	C	A	C	B	A	→	$a = 0.8$
A	B	C	A	C	B	C	→	$a = 0.6$
A	B	C	B	A	B	A	→	$a = 0.4$
A	B	C	B	A	B	C	→	$a = 0.6$
A	B	C	B	A	C	A	→	$a = 0.6$
A	B	C	B	A	C	B	→	$a = 0.8$
A	B	C	B	C	A	B	→	$a = 0.6$
A	B	C	B	C	A	C	→	$a = 0.4$
A	B	C	B	C	B	A	→	$a = 0.4$
A	B	C	B	C	B	C	→	$a = 0.2$

Table H.1: (continued)

Bibliography

[1] D.J. Shaw. *Introduction to colloid and surface chemistry.* Butterworth-Heinemann, 4th edition edition, 1992. ISBN 0-7506-1182-0.

[2] Y. N. Xia, B. Gates, Y. D. Yin, and Y. Lu. Monodispersed colloidal spheres: old materials with new applications. *Advanced Materials*, 12(10):693–713, 2000.

[3] U. Gasser, E. R. Weeks, A. Schofield, P. N. Pusey, and D. A. Weitz. Real-space imaging of nucleation and growth in colloidal crystallization. *Science*, 292:258–262, 2001.

[4] A. Yethiraj. Tunable colloids: control of colloidal phase transitions with tunable interactions. *Soft Matter*, 3(9):1099–1115, 2007.

[5] J. D. Joannopoulos, S. G. Johnson, and J. N. Winn. *Photonic crystals: molding the flow of light.* Princeton university press, 2^{nd} edition edition, 2008. ISBN 978-0-691-12456-8.

[6] J. V. Sanders. Colour of precious opal. *Nature*, 204(4964):1151, 1964.

[7] B. Gralak, G. Tayeb, and S. Enoch. Morpho butterflies wings color modeled with lamellar grating theory. *Optics express*, 9(11):567–578, 2001.

[8] L. P. Biró, Z. Bálint, K. Kertész, Z. Vértesy, G. I. Márk, Z. E. Horváth, J. Balázs, D. Méhn, I. Kiricsi, and V. Lousse. Role of photonic-crystal-type structures in the thermal regulation of a lycaenid butterfly sister species pair. *Physical Review E*, 67(2):21907, 2003.

[9] A. R. Parker, V. L. Welch, D. Driver, and N. Martini. Structural colour: opal analogue discovered in a weevil. *Nature*, 426(6968):786–787, 2003.

[10] S. H. Park and Y. N. Xia. Assembly of mesoscale particles over large areas and its application in fabricating tunable optical filters. *Langmuir*, 15(1):266–273, 1999.

[11] C. Lopez. Three-dimensional photonic bandgap materials: semiconductors for light. *Journal of Optics A: Pure and Applied Optics*, 8(5):R1, 2006.

[12] A. P. Hynninen, J. H. J. Thijssen, E. C. M. Vermolen, M. Dijkstra, and A. van Blaaderen. Self-assembly route for photonic crystals with a bandgap in the visible region. *Nature Materials*, 6(3):202–205, 2007.

[13] S. Y. Lin, J. G. Fleming, D. L. Hetherington, B. K. Smith, R. Biswas, K. M. Ho, M. M. Sigalas, W. Zubrzycki, S. R. Kurtz, and J. Bur. Athree-dimensional photonic crystal operating at infrared wavelengths. *Nature*, 394:251, 1998.

[14] J. G. Fleming and S.-Y. Lin. Three-dimensional photonic crystal with a stop band from 1.35 to 1.95 μm. *Optical Letters*, 24:24–51, 1999.

[15] M. H. Qi, E. Lidorikis, P. T. Rakich, S. G. Johnson, J. D. Joannopoulos, E. P. Ippen, and H. I. Smith. A three-dimensional optical photonic crystal with designed point defects. *Nature*, 429(6991):538–542, 2004.

[16] S. Noda, K. Tomoda, N. Yamamoto, and A. Chutinan. Full three-dimensional photonic bandgap crystals at near-infrared wavelengths. *Science*, 289(5479):604-606, 2000.

[17] M. Campbell, D. N. Sharp, M. T. Harrison, R. G. Denning, and A. J. Turberfield. Fabrication of photonic crystals for the visible spectrum by holographic lithography. *Nature*, 404(6773):53–56, 2000.

[18] A. C. Edrington, A. M. Urbas, P. DeRege, C. X. Chen, T. M. Swager, N. Hadjichristidis, M. Xenidou, L. J. Fetters, J. D. Joannopoulos, Y. Fink, and E. L. Thomas. Polymer-based photonic crystals. *Advanced Materials*, 13(6):421–425, 2001.

[19] A. Blanco, E. Chomski, S. Grabtchak, M. Ibisate, S. John, S. W. Leonard, C. Lopez, F. Meseguer, H. Miguez, J. P. Mondia, G. A. Ozin, O. Toader, and H. M. van Driel. Large-scale synthesis of a silicon photonic crystal with a complete three-dimensional bandgap near 1.5 micrometres. *Nature*, 405(6785):437, 2000.

[20] Y. A. Vlasov, X. Z. Bo, J. C. Sturm, and D. J. Norris. On-chip natural assembly of silicon photonic bandgap crystals. *Nature*, 414(6861):289–293, 2001.

[21] B. H. Cumpston, S. P. Ananthavel, S. Barlow, D. L. Dyer, J. E. Ehrlich, L. L. Erskine, A. A. Heikal, S. M. Kuebler, I. Y. Sandy Lee, D. McCord-Maughon,

J. Qin, H. Rockel, M. Rumi, X.-L. Wu, S. R. Marder, and J. W. Perry. Two-photon polymerization initiators for three-dimensional optical data storage and microfabrication. *Nature*, 398(6722):51–54, 1999.

[22] J. Scrimgeour, D. N. Sharp, C. F. Blanford, O. M. Roche, R. G. Denning, and A. J. Turberfield. Three-dimensional optical lithography for photonic microstructures. *Advanced Materials*, 18(12):1557–1560, 2006.

[23] J. S. King, E. Graugnard, O. M. Roche, D. N. Sharp, J. Scrimgeour, R. G. Denning, A. J. Turberfield, and C. J. Summers. Infiltration and inversion of holographically defined polymer photonic crystal templates by atomic layer deposition. *Advanced Materials*, 18(12):1561–1565, 2006.

[24] M. Li and C. K. Ober. Block copolymer patterns and templates. *Materials Today*, 9(9):30, 2006.

[25] I. W. Hamley. Nanostructure fabrication using block copolymers. *Nanotechnology*, 14(10):39–39, 2003.

[26] M. B. Runge and N. B. Bowden. Synthesis of high molecular weight comb block copolymers and their assembly into ordered morphologies in the solid state. *Journal of the American Chemical Society*, 129(34):10551, 2007.

[27] K. Busch and S. John. Photonic band gap formation in certain self-organizing systems. *Physical Review E*, 58(3):3896–3908, 1998.

[28] D. J. Norris and Yu. A. Vlasov. Chemical approaches to three-dimensional semiconductor photonic crystals. *Advanced Materials*, 13(6):371–376, 2001.

[29] H. S. Sözüer, J. W. Haus, and R. Inguva. Photonic bands: convergence problems with the plane-wave method. *Physical Review B*, 45(24):13962, 1992.

[30] C. Paquet and E. Kumacheva. Nanostructured polymers for photonics. *Materials Today*, 11(4):48, 2008.

[31] J. D. Joannopoulos, P. R. Villeneuve, and S. Fan. Photonic crystals: putting a new twist on light. *Nature*, 386(6621):143–149, 1997.

[32] Webpage of the Joannopoulos research group at mit. `http://ab-initio.mit.edu/photons/micropolis.html`. [Online; accessed 14-July-2009].

[33] J. M. Weissman, H. B. Sunkara, A. S. Tse, and S. A. Asher. Thermally switchable periodicities and diffraction from mesoscopically ordered materials. *Science*, 274:959, 1996.

[34] J. H. Holtz and S. A. Asher. Polymerized colloidal crystal hydrogel films as intelligent chemical sensing materials. *Nature*, 389:829, 1997.

[35] J. H. Holtz, J. S. W. Holtz, C. H. Munro, and S. A. Asher. Intelligent polymerized crystalline colloidal arrays: novel chemical sensor materials. *Analytical Chemistry*, 70(4):780–791, 1998.

[36] B. Viel, T. Ruhl, and G. P. Hellmann. Reversible deformation of opal elastomers. *Chem. Mater*, 19(23):5673–5679, 2007.

[37] J. P. Walker, K. W. Kimble, and S. A. Asher. Photonic crystal sensor for organophosphate nerve agents utilizing the organophosphorus hydrolase enzyme. *Analytical and Bioanalytical Chemistry*, 389(7):2115–2124, 2007.

[38] X. Xu, A. V. Goponenko, and S. A. Asher. Polymerized polyhema photonic crystals: ph and ethanol sensor materials. *Journal of the American Chemical Society*, 130(10):3113–3119, 2008.

[39] A. C. Arsenault, H. Míguez, V. Kitaev, G. A. Ozin, and I. Manners. A polychromic, fast response metallopolymer gel photonic crystal with solvent and redox tunability: a step towards photonic ink (p-ink). *Advanced Materials*, 15(6):503–507, 2003.

[40] A. C. Arsenault, D. P. Puzzo, I. Manners, and G. A. Ozin. Photonic-crystal full-colour displays. *Nature Photonics*, 1(8):468–472, 2007.

[41] A. Arsenault, S. Fournier-Bidoz, B. Hatton, H. Míguez, N. Tétreault, E. Vekris, S. Wong, S. M. Yang, V. Kitaev, and G. A. Ozin. Towards the synthetic all-optical computer: science fiction or reality? *Journal of Materials Chemistry*, 14(5):781–794, 2004.

[42] S. Nishimura, N. Abrams, B. A. Lewis, L. I. Halaoui, T. E. Mallouk, K. D. Benkstein, J. van de Lagemaat, and A. J. Frank. Standing wave enhancement of red absorbance and photocurrent in dye-sensitized titanium dioxide photoelectrodes coupled to photonic crystals. *Journal of the American Chemical Society*, 125(20):6306, 2003.

[43] R. C. Schroden, M. Al-Daous, C. F. Blanford, and A. Stein. Optical properties of inverse opal photonic crystals. *Chemistry of Materials*, 14(8):3305, 2002.

[44] N. Kobayashi and C. Egami. High-resolution optical storage by use of minute spheres. *Optics Letters*, 30(3):299–301, 2005.

[45] H. H. Pham, I. Gourevich, J. K. Oh, J. E. N. Jonkman, and E. Kumacheva. A multidye nanostructured material for optical data storage and security data encryption. *Advanced Materials*, 16(6):516–520, 2004.

[46] H. H. Pham, I. Gourevich, J. E. N. Jonkman, and E. Kumacheva. Polymer nanostructured material for the recording of biometric features. *Journal of Materials Chemistry*, 17(6):523–526, 2007.

[47] J. P. Hoogenboom, D. Derks, P. Vergeer, and A. van Blaaderen. Stacking faults in colloidal crystals grown by sedimentation. *Journal of Chemical Physics*, 117(24):11320–11328, 2002.

[48] A. van Blaaderen, R. Ruel, and P. Wiltzius. Template-directed colloidal crystallization. *Nature*, 385(6614):321–324, 1997.

[49] J. P. Hoogenboom, A. Yethiraj, A. K. van Langen-Suurling, J. Romijn, and A. van Blaaderen. Epitaxial crystal growth of charged colloids. *Physical Review Letters*, 89(25), 2002.

[50] M. Holgado, F. Garcia-Santamaria, A. Blanco, M. Ibisate, A. Cintas, H. Miguez, C. J. Serna, C. Molpeceres, J. Requena, A. Mifsud, F. Meseguer, and C. Lopez. Electrophoretic deposition to control artificial opal growth. *Langmuir*, 15(14):4701–4704, 1999.

[51] A. L. Rogach, N. A. Kotov, D. S. Koktysh, J. W. Ostrander, and G. A. Ragoisha. Electrophoretic deposition of latex-based 3D colloidal photonic crystals: a technique for rapid production of high-quality opals. *Chemistry of Materials*, 12(9):2721–2726, 2000.

[52] M. Allard, E. H. Sargent, P. C. Lewis, and E. Kumacheva. Colloidal crystals grown on patterned surfaces. *Advanced Materials*, 16(15):1360-1364, 2004.

[53] P. C. Lewis, E. Kumacheva, M. Allard, and E. H. Sargent. Colloidal crystallization accomplished by electrodeposition on patterned substrates. *Journal of Dispersion Science and Technology*, 26(3):259–265, 2005.

[54] N. V. Dziomkina, M. A. Hempenius, and G. J. Vancso. Symmetry control of polymer colloidal monolayers and crystals by electrophoretic deposition on patterned surfaces. *Advanced Materials*, 17(2):237–240, 2005.

[55] S. Reculusa, P. Masse, and S. Ravaine. Three-dimensional colloidal crystals with a well-defined architecture. *Journal of Colloid and Interface Science*, 279(2):471–478, 2004.

[56] S. Reculusa and S. Ravaine. Synthesis of colloidal crystals of controllable thickness through the langmuir-blodgett technique. *Chemistry of Materials*, 15(2):598–605, 2003.

[57] L. B. Chen, M. K. Chow, B. J. Ackerson, and C. F. Zukoski. Rheological and microstructural transitions in colloidal crystals. *Langmuir*, 10(8):2817, 1994.

[58] S. H. Park, D. Qin, and Y. Xia. Crystallization of mesoscale particles over large areas. *Advanced Materials*, 10(13):1028, 1998.

[59] S. H. Park, B. Gates, and Y. N. Xia. A three-dimensional photonic crystal operating in the visible region. *Advanced Materials*, 11(6):462+, 1999.

[60] Y. D. Yin, Y. Lu, B. Gates, and Y. N. Xia. Template-assisted self-assembly: A practical route to complex aggregates of monodispersed colloids with well-defined sizes, shapes, and structures. *Journal of the American Chemical Society*, 123(36):8718–8729, 2001.

[61] Y. D. Yin and Y. N. Xia. Growth of large colloidal crystals with their (100) planes orientated parallel to the surfaces of supporting substrates. *Advanced Materials*, 14(8):605–608, 2002.

[62] T. Kanai, T. Sawada, A. Toyotama, and K. Kitamura. Air-pulse-drive fabrication of photonic crystal films of colloids with high spectral quality. *Advanced Functional Materials*, 15(1):25–29, 2005.

[63] O. Vickreva, O. Kalinina, and E. Kumacheva. Colloid crystal growth under oscillatory shear. *Advanced Materials*, 12(2):110–112, 2000.

[64] R. M. Amos, J. G. Rarity, P. R. Tapster, T. J. Shepherd, and S. C. Kitson. Fabrication of large-area face-centered-cubic hard-sphere colloidal crystals by shear alignment. *Physical Review E*, 61(3):2929, 2000.

[65] R. M. Amos, T. J. Shepherd, J. G. Rarity, and P. Tapster. Shear-ordered face-centred cubic photonic crystals. *Electronics Letters*, 36(16):1411, 2000.

[66] P. Jiang and M. J. McFarland. Large-scale fabrication of wafer-size colloidal crystals, macroporous polymers and nanocomposites by spin-coating. *Journal of the American Chemical Society*, 126(42):13778, 2004.

[67] A. Mihi, M. Ocaña, and H. Míguez. Oriented colloidal-crystal thin films by spin-coating microspheres dispersed in volatile media. *Advanced Materials*, 18(17):2244–2249, 2006.

[68] B. Gates and Y. N. Xia. Fabrication and characterization of chirped 3D photonic crystals. *Advanced Materials*, 12(18):1329–1332, 2000.

[69] N. D. Denkov, O. D. Velev, P. A. Kralchevsky, I. B. Ivanov, H. Yoshimura, and K. Nagayama. Mechanism of formation of 2-dimensional crystals from latex-particles on substrates. *Langmuir*, 8(12):3183–3190, 1992.

[70] N. D. Denkov, O. D. Velev, P. A. Kralchevsky, I. B. Ivanov, H. Yoshimura, and K. Nagayama. 2-dimensional crystallization. *Nature*, 361(6407):26–26, 1993.

[71] P. A. Kralchevsky, V. N. Paunov, I. B. Ivanov, and K. Nagayama. Capillary meniscus interaction between colloidal particles attached to a liquid-fluid interface. *Journal of Colloid and Interface Science*, 151(1):79–94, 1992.

[72] P. A. Kralchevsky and K. Nagayama. Capillary forces between colloidal particles. *Langmuir*, 10(1):23–36, 1994.

[73] D. J. Norris, E. G. Arlinghaus, L. Meng, R. Heiny, and L. E. Scriven. Opaline photonic crystals: how does self-assembly work? *Advanced Materials*, 16(16):1393–1399, 2004.

[74] A. S. Dimitrov and K. Nagayama. Steady-state unidirectional convective assembling of fine particles into 2-dimensional arrays. *Chemical Physics Letters*, 243(5-6):462–468, 1995.

[75] A. S. Dimitrov and K. Nagayama. Continuous convective assembling of fine particles into two-dimensional arrays on solid surfaces. *Langmuir*, 12(5):1303–1311, 1996.

[76] P. Jiang, J. F. Bertone, K. S. Hwang, and V. L. Colvin. Single-crystal colloidal multilayers of controlled thickness. *Chemistry of Materials*, 11(8):2132–2140, 1999.

[77] Z. Z. Gu, A. Fujishima, and O. Sato. Fabrication of high-quality opal films with controllable thickness. *Chemistry of Materials*, 14(2):760–765, 2002.

[78] Z. Zhou and X. S. Zhao. Flow-controlled vertical deposition method for the fabrication of photonic crystals. *Langmuir*, 20(4):1524–1526, 2004.

[79] B. G. Prevo and O. D. Velev. Controlled, rapid deposition of structured coatings from micro-and nanoparticle suspensions. *Langmuir*, 20(6):2099–2107, 2004.

[80] L. Malaquin, T. Kraus, H. Schmid, E. Delamarche, and H. Wolf. Controlled particle placement through convective and capillary assembly. *Langmuir*, 23(23):11513–11521, 2007.

[81] J. F. Bertone, P. Jiang, K. S. Hwang, D. M. Mittleman, and V. L. Colvin. Thickness dependence of the optical properties of ordered silica-air and air-polymer photonic crystals. *Physical Review Letters*, 83(2):300–303, 1999.

[82] Y. H. Ye, S. Badilescu, V. V. Truong, P. Rochon, and A. Natansohn. Self-assembly of colloidal spheres on patterned substrates. *Applied Physics Letters*, 79(6):872–874, 2001.

[83] J. Zhang, A. Alsayed, K. H. Lin, S. Sanyal, F. Zhang, W. J. Pao, V. S. K. Balagurusamy, P. A. Heiney, and A. G. Yodh. Template-directed convective assembly of three-dimensional face-centered-cubic colloidal crystals. *Applied Physics Letters*, 81(17):3176–3178, 2002.

[84] L. M. Goldenberg, J. Wagner, J. Stumpe, B. R. Paulke, and E. Gornitz. Ordered arrays of large latex particles organized by vertical deposition. *Langmuir*, 18(8):3319–3323, 2002.

[85] J. P. Hoogenboom, C. Retif, E. de Bres, M. V. de Boer, A. K. van Langen-Suurling, J. Romijn, and A. van Blaaderen. Template-induced growth of close-packed and non-close-packed colloidal crystals during solvent evaporation. *Nano Letters*, 4(2):205–208, 2004.

[86] L. K. Teh, N. K. Tan, C. C. Wong, and S. Li. Growth imperfections in three-dimensional colloidal self-assembly. *Applied Physics A: Materials Science and Processing*, 81(7):1399–1404, 2005.

[87] G. Lozano and H. Miguez. Growth dynamics of self-assembled colloidal crystal thin films. *Langmuir*, 23(20):9933–9938, 2007.

[88] D. K. Yi, M. J. Kim, and D. Y. Kim. Surface relief grating induced colloidal crystal structures. *Langmuir*, 18(6):2019–2023, 2002.

[89] D. K. Yi, E. M. Seo, and D. Y. Kim. Surface-modulation-controlled three-dimensional colloidal crystals. *Applied Physics Letters*, 80(2):225–227, 2002.

[90] Y. Yin, Z. Y. Li, and Y. Xia. Template-directed growth of (100)-oriented colloidal crystals. *Langmuir*, 19(3):622–631, 2003.

[91] W. Lee, A. Chan, M. A. Bevan, J. A. Lewis, and P. V. Braun. Nanoparticle-mediated epitaxial assembly of colloidal crystals on patterned substrates. *Langmuir*, 20(13):5262–5270, 2004.

[92] P. Rochon, E. Batalla, and A. Natansohn. Optically induced surface gratings on azoaromatic polymer-films. *Applied Physics Letters*, 66(2):136–138, 1995.

[93] X. Checoury, S. Enoch, C. López, and A. Blanco. Stacking patterns in self-assembly opal photonic crystals. *Applied Physics Letters*, 90:161131, 2007.

[94] T. Kanai, T. Sawada, I. Maki, and K. Kitamura. Kossel line analysis of flow-aligned textures of colloidal crystals. *Japanese journal of applied physics*, 42(6 B):655–657, 2003.

[95] H. Miguez, C. Lopez, F. Meseguer, A. Blanco, L. Vazquez, R. Mayoral, M. Ocana, V. Fornes, and A. Mifsud. Photonic crystal properties of packed submicrometric SiO_2 spheres. *Applied Physics Letters*, 71(9):1148, 1997.

[96] J. F. Galisteo-López, E. Palacios-Lidón, E. Castillo-Martínez, and C. López. Optical study of the pseudogap in thickness and orientation controlled artificial opals. *Physical Review B*, 68(11):115109, 2003.

[97] R. Mayoral, J. Requena, J. S. Moya, C. Lopez, A. Cintas, H. Miguez, F. Meseguer, L. Vazquez, M. Holgado, and A. Blanco. 3D long-range ordering in an SiO_2 submicrometer-sphere sintered superstructure. *Advanced Materials*, 9(3):257–260, 1997.

[98] W. L. Vos, M. Megens, C. M. van Kats, and P. Bosecke. X-ray diffraction of photonic colloidal single crystals. *Langmuir*, 13(23):6004–6008, 1997.

[99] A. V. Petukhov, D. Aarts, I. P. Dolbnya, E. H. A. de Hoog, K. Kassapidou, G. J. Vroege, W. Bras, and H. N. W. Lekkerkerker. High-resolution small-angle X-ray diffraction study of long-range order in hard-sphere colloidal crystals. *Physical Review Letters*, 88(20), 2002.

[100] A. V. Petukhov, I. P. Dolbnya, D. Aarts, G. J. Vroege, and H. N. W. Lekkerkerker. Bragg rods and multiple X-ray scattering in random-stacking colloidal crystals. *Physical Review Letters*, 90(2), 2003.

[101] A. V. Petukhov, I. P. Dolbnya, D. Aarts, and G. J. Vroege. Destruction of long-range order recorded with in situ small-angle X-ray diffraction in drying colloidal crystals. *Physical Review E*, 69(3), 2004.

[102] A. V. Petukhov, J. H. J. Thijssen, D. C. t Hart, A. Imhof, A. van Blaaderen, I. P. Dolbnya, A. Snigirev, A. Moussaid, and I. Snigireva. Microradian X-ray diffraction in colloidal photonic crystals. *Journal Of Applied Crystallography*, 39:137–144, 2006.

[103] J. H. J. Thijssen, A. V. Petukhov, D. C. t Hart, A. Imhof, C. H. M. van der Werf, R. E. I. Schropp, and A. van Blaaderen. Characterization of photonic colloidal single crystals by microradian X-ray diffraction. *Advanced Materials*, 18(13):1662+, 2006.

[104] J. Als-Nielsen and D. McMorrow. *Elements of Modern X-ray Physics*. Wiley, 2000. ISBN 0-471-49858-0.

[105] O. Yefanov. Accessible reciprocal-space region for non-coplanar Bragg and Laue geometries. *Journal of Applied Crystallography*, 41(1):110–114, 2008.

[106] O. Yefanov, V. Kladko, M. Slobodyan, and Y. Polischuk. Xvis: an educational open-source program for demonstration of reciprocal-space construction and diffraction principles. *Journal of Applied Crystallography*, 41(3):647–652, 2008.

[107] M. Sanchez del Rio and R. J. Dejus. Webpage of the european synchrotron radiation facility (ESRF). `http://www.esrf.eu/UsersAndScience/Experiments/TBS/SciSoft/xop2.3`. [Online; accessed 23-July-2009].

[108] M. S. del Rio and R. J. Dejus. Status of xop: an X-ray optics software toolkit. In *Advances in Computational Methods for X-ray and Neutron Optics*, volume 5536, page 171, Denver, CO, USA, 2004. SPIE.

[109] K. Orita, T. Morimura, T. Horiuchi, and K. Matsushige. In situ energy-dispersive X-ray reflectivity measurements of structural changes in thin films for organic electroluminescent devices. *Synthetic Metals*, 91(1-3):155, 1997.

[110] U. Pietsch, J. Grenzer, T. Geue, F. Neissendorfer, G. Brezsesinski, C. Symietz, H. Mohwald, and W. Gudat. The energy-dispersive reflectometer at BESSY II: a challenge for thin film analysis. *Nuclear Instruments & Methods in Physics Research Section a-Accelerators Spectrometers Detectors and Associated Equipment*, 467:1077–1080, 2001.

[111] A. Plech, U. Klemradt, H. Metzger, and J. Peisl. In situ X-ray reflectivity study of the oxidation kinetics of liquid gallium and the liquid alloy. *Journal of Physics: Condensed Matter*, 10:971–982, 1998.

[112] M. Mukherjee, M. Bhattacharya, M. K. Sanyal, T. Geue, J. Grenzer, and U. Pietsch. Reversible negative thermal expansion of polymer films. *Physical Review E*, 66(6):61801, 2002.

[113] S. Kowarik, A. Gerlach, W. Leitenberger, J. Hu, G. Witte, C. Wöll, U. Pietsch, and F. Schreiber. Energy-dispersive X-ray reflectivity and gid for real-time growth studies of pentacene thin films. *Thin Solid Films*, 515(14):5606–5610, 2007.

[114] W. Leitenberger, R. Hartmann, U. Pietsch, R. Andritschke, I. Starke, and L. Struder. Application of a pnCCD in X-ray diffraction: a three-dimensional X-ray detector. *Journal of Synchrotron Radiation*, 15(5):449–457, 2008.

[115] J. R. Levine, J. B. Cohen, Y. W. Chung, and P. Georgopoulos. Grazing-incidence small-angle X-ray scattering: new tool for studying thin film growth. *Journal of Applied Crystallography*, 22(6):528–532, 1989.

[116] M. Schmidbauer, Th. Wiebach, H. Raidt, M. Hanke, R. Köhler, and H. Wawra. Ordering of self-assembled Si1-xGex islands studied by grazing incidence small-angle X-ray scattering and atomic force microscopy. *Physical Review B*, 58(16):10523, 1998.

[117] J. Stangl, V. Holý, P. Mikulik, G. Bauer, I. Kegel, T. H. Metzger, O. G. Schmidt, C. Lange, and K. Eberl. Self-assembled carbon-induced germanium quantum dots studied by grazing-incidence small-angle X-ray scattering. *Applied Physics Letters*, 74:3785, 1999.

[118] M. Rauscher, R. Paniago, H. Metzger, Z. Kovats, J. Domke, J. Peisl, H. D. Pfannes, J. Schulze, and I. Eisele. Grazing incidence small angle X-ray scattering from free-standing nanostructures. *Journal of Applied Physics*, 86:6763, 1999.

[119] K. Zhang, Ch. Heyn, W. Hansen, Th. Schmidt, and J. Falta. Ordering and shape of self-assembled InAs quantum dots on GaAs(001). *Applied Physics Letters*, 76(16):2229, 2000.

[120] G. Renaud, R. Lazzari, C. Revenant, A. Barbier, M. Noblet, O. Ulrich, F. Leroy, J. Jupille, Y. Borensztein, C. R. Henry, J.-P. Deville, F. Scheurer, J. Mane-Mane, and O. Fruchart. Real-time monitoring of growing nanoparticles. *Science*, 300(5624):1416–1419, 2003.

[121] C. Revenant, F. Leroy, R. Lazzari, G. Renaud, and C. R. Henry. Quantitative analysis of grazing incidence small-angle X-ray scattering: Pd/MgO (001) growth. *Phys. Rev. B*, 69:035411, 2004.

[122] P. Müller-Buschbaum. Grazing incidence small-angle X-ray scattering: an advanced scattering technique for the investigation of nanostructured polymer films. *Analytical and Bioanalytical Chemistry*, 376(1):3–10, 2003.

[123] P. Müller-Buschbaum, N. Hermsdorf, S. V. Roth, J. Wiedersich, S. Cunis, and R. Gehrke. Comparative analysis of nanostructured diblock copolymer films. *Spectrochimica Acta Part B: Atomic Spectroscopy*, 59(10-11):1789–1797, 2004.

[124] P. Du, M. Li, K. Douki, X. Li, C. B. W. Garcia, A. Jain, D. M. Smilgies, L. J. Fetters, S. M. Gruner, and U. Wiesner. Additive-driven phase-selective chemistry in block copolymer thin films: the convergence of top-down and bottom-up approaches. *Advanced Materials*, 16(12):953–957, 2004.

[125] B. Lee, I. Park, J. Yoon, S. Park, J. Kim, K. W. Kim, T. Chang, and M. Ree. Structural analysis of block copolymer thin films with grazing incidence small-angle X-ray scattering. *Macromolecules*, 38(10):4311–4323, 2005.

[126] B. Lee, J. Yoon, W. Oh, Y. Hwang, K. Heo, K. S. Jin, J. Kim, K. W. Kim, and M. Ree. In-situ grazing incidence small-angle X-ray scattering studies on nanopore evolution in low-k organosilicate dielectric thin films. *Macromolecules*, 38(8):3395–3405, 2005.

[127] M. P. Tate, B. W. Eggiman, J. D. Kowalski, and H. W. Hillhouse. Order and orientation control of mesoporous silica films on conducting gold substrates formed by dip-coating and self-assembly: a grazing angle of incidence small-angle X-ray scattering and field emmision scanning electron microscopy study. *Langmuir*, 21(22):10112–10118, 2005.

[128] B. W. Eggiman, M. P. Tate, and H. W. Hillhouse. Rhombohedral structure of highly ordered and oriented self-assembled nanoporous silica thin films. *Chem. Mater.*, 18(3):723–730, 2006.

[129] G. E. Stein, E. J. Kramer, X. Li, and J. Wang. Layering transitions in thin films of spherical-domain block copolymers. *Macromolecules*, 40(7):2453–2460, 2007.

[130] V. N. Urade, T.-C. Wei, M. P. Tate, J. D. Kowalski, and H. W. Hillhouse. Nanofabrication of double-gyroid thin films. *Chemistry of Materials*, 19(4):768, 2007.

[131] O. Henneberg, T. Panzner, U. Pietsch, T. Geue, M. Saphiannikova, P. Rochon, and K. Finkelstein. X-ray and vis light scattering from light-induced polymer gratings. *Zeitschrift Fur Kristallographie*, 219(4):218–223, 2004.

[132] M. Yan and A. Gibaud. On the intersection of grating truncation rods with the Ewald sphere studied by grazing-incidence small-angle X-ray scattering. *Journal of Applied Crystallography*, 40(6):1050–1055, 2007.

[133] S. V. Roth, M. Burghammer, C. Riekel, P. Müller-Buschbaum, A. Diethert, P. Panagiotou, and H. Walter. Self-assembled gradient nanoparticle-polymer multilayers investigated by an advanced characterization method: microbeam grazing incidence X-ray scattering. *Applied Physics Letters*, 82:1935, 2003.

[134] S. V. Roth, T. Autenrieth, G. Grubel, C. Riekel, M. Burghammer, R. Hengstler, L. Schulz, and P. Müller-Buschbaum. In situ observation of nanoparticle ordering at the air-water-substrate boundary in colloidal solutions using X-ray nanobeams. *Applied Physics Letters*, 91(9):091915, 2007.

[135] J. I. Flege, Th. Schmidt, V. Aleksandrovic, G. Alexe, T. Clausen, B. Gehl, A. Kornowski, S. Bernstorff, H. Weller, and J. Falta. Grazing-incidence small-angle X-ray scattering investigation of spin-coated $CoPt_3$ nanoparticle films. *Nuclear Instruments and Methods in Physics Research Section B: Beam Interactions with Materials and Atoms*, 246(1):25, 2006.

[136] Y. Chushkin, L. Chitu, Y. Halahovets, S. Luby, E. Majkova, A. Satka, G. Leo, M. Giersig, M. Hilgendorff, V. Holy, and O. Konovalov. GISAXS studies of self-assembling of colloidal Co nanoparticles. *Materials Science and Engineering: C*, 26(5-7):1136, 2006.

[137] P. Siffalovic, E. Majkova, L. Chitu, M. Jergel, S. Luby, A. Satka, and S. V. Roth. Self-assembly of iron oxide nanoparticles studied by time-resolved grazing-incidence small-angle X-ray scattering. *Physical Review B*, 76(19):195432, 2007.

[138] E. Majkova, P. Siffalovic, L. Chitu, M. Jergel, S. Luby, A. Timmann, S. V. Roth, A. Satka, J. Keckes, and G. A. Maier. Real-time tracking of nanoparticle self-assembling using GISAXS. *Superlattices and Microstructures*, 46(1-2):286–290, 2009.

[139] A. Gibaud, D. Grosso, B. Smarsly, A. Baptiste, J. F. Bardeau, F. Babonneau, D. A. Doshi, Z. Chen, C. J. Brinker, and C. Sanchez. Evaporation-controlled self-assembly of silica surfactant mesophases. *Journal of Physical Chemistry B*, 107(25):6114–6118, 2003.

[140] D. K. Smith, B. Goodfellow, D.-M. Smilgies, and B. A. Korgel. Self-assembled simple hexagonal AB_2 binary nanocrystal superlattices: SEM, GISAXS, and defects. *Journal of the American Chemical Society*, 131(9):3281, 2009.

[141] A. Frömsdorf, M. Nagel, A. Kornowski, and S. S. Funari. Structural investigations on 3-D colloidal PbS crystals by means of GISAXS. Technical report, Deutsches Elektronen-Synchrotron (DESY), 2006.

[142] A. Frömsdorf, R. Capek, and S. Roth. μ-GISAXS experiment and simulation by using a simple model of a highly ordered monolayer of PMMA-beads. *Journal of Physical Chemistry B*, 110:15166–15171, 2006.

[143] A. Guinier. *X-ray diffraction: in crystals, imperfect crystals, and amorphous bodies.* Freeman San Francisco, 1963.

[144] W. Loose and B. J. Ackerson. Model calculations for the analysis of scattering data from layered structures. *The Journal of Chemical Physics*, 101(9):7211–7220, 1994.

[145] U. Pietsch, V. Holý, and T. Baumbach. *High-resolution X-ray scattering.* Springer, 2nd edition, 2004. ISBN 0-387-40092-3.

[146] M. P. Tate, V. N. Urade, J. D. Kowalski, T. C. Wei, B. D. Hamilton, B. W. Eggiman, and H. W. Hillhouse. Simulation and interpretation of 2D diffraction patterns from self-assembled nanostructured films at arbitrary angles of incidence: from grazing incidence (above the critical angle) to transmission perpendicular to the substrate. *Journal of Physical Chemistry B*, 110(20):9882–9892, 2006.

[147] P. Mikulík. *X-ray reflectivity from planar and structured multilayers.* PhD thesis, Université Joseph Fourier - Grenoble I, 1997.

[148] L. G. Parratt. Surface studies of solids by total reflection of X-rays. *Physical Review*, 95(2):359, 1954.

[149] M. Rauscher, T. Salditt, and H. Spohn. Small-angle X-ray scattering under grazing incidence: the cross section in the distorted-wave Born approximation. *Physical Review B*, 52(23):16855–16863, 1995.

[150] F. van der Veen and F. Pfeiffer. Coherent X-ray scattering. *Journal of Physics Condensed Matter*, 16:5003–5030, 2004.

[151] D. Y. Kim, S. K. Tripathy, L. Li, and J. Kumar. Laser-induced holographic surface-relief gratings on nonlinear-optical polymer-films. *Applied Physics Letters*, 66(10):1166–1168, 1995.

[152] Surface-relief gratings on azobenzene-containing films. In Z. Sekkat and W. Knoll, editors, *Photoreactive organic thin films*, chapter 14, pages 429–486. San Diego: Academic Press, 2002.

[153] O. Henneberg. *In-situ Untersuchungen zur Entstehung von Oberflächengittern in Polymeren.* PhD thesis, Universität Potsdam, 2004.

[154] G. S. Kumar and D. C. Neckers. Photochemistry of azobenzene-containing polymers. *Chemical Reviews*, 89(8):1915–1925, 1989.

[155] U. Wiesner, M. Antonietti, C. Boeffel, and H. W. Spiess. Dynamics of photoinduced isomerization of azobenzene moieties in liquid-crystalline polymers. *Die Makromolekulare Chemie*, 191(9), 1990.

[156] T. Kraus. *Assembly and printing of micro and nano objects.* PhD thesis, ETH Zürich, 2007. pages 271-276.

[157] R. Vavrin. *Time-resolved investigation of aggregation and sol-gel transition in colloidal suspensions.* PhD thesis, Universität Freiburg, Switzerland, 2005.

[158] Manufacturer's webpage. `http://www.dectris.com/sites/dectris.html`. [Online; accessed 29-November-2009].

[159] cSAXS notes v0.29 (september 23rd, 2008). `http://sls.web.psi.ch/view.php/beamlines/cs/manuals/csaxs_notes.pdf`. [Online; accessed 24-September-2009].

[160] Webpage of cSAXS beam line. `http://sls.web.psi.ch/view.php/beamlines/cs/index.html`. [Online; accessed 24-September-2009].

[161] F. Neissendorfer, U. Pietsch, G. Brezesinski, and H. Mohwald. The energy-dispersive reflectometer diffractometer at BESSY-I. *Measurement Science & Technology*, 10(5):354–361, 1999.

[162] T. Panzner. *Kohärente Reflexion mit weisser Synchrotronstrahlung im harten Röntgenbereich*. PhD thesis, Universität Siegen, 2007.

[163] B. Reinhold. In-situ Untersuchungen zur Abscheidung kolloidaler Schichten auf vorstrukturierten Substraten. Master's thesis, Universität Potsdam, 2006.

[164] T. C. Huang, H. Toraya, T. N. Blanton, and Y. Wu. X-ray powder diffraction analysis of silver behenate, a possible low-angle diffraction standard. *Journal of Applied Crystallography*, 26(2):180–184, 1993.

[165] Kohlbrecher J. Webpage of software package SASfit. `http://kur.web.psi.ch/sans1/SANSSoft/sasfit.html`. [Online; accessed 13-November-2009].

[166] T. M. Blättler. *Particle self-assembly for the creation of biomolecular patterns*. PhD thesis, ETH Zurich, 2007.

[167] C. D. Dushkin, G. S. Lazarov, S. N. Kotsev, H. Yoshimura, and K. Nagayama. Effect of growth conditions on the structure of two-dimensional latex crystals: experiment. *Colloid and Polymer Science*, 277(10):914–930, 1999.

[168] U. Pietsch. X-ray and visible light scattering from light-induced polymer gratings. *Physical Review B*, 66(15), 2002.

[169] Jr T. Alfrey, E. B. Bradford, J. W. Vanderhoff, and G. Oster. Optical properties of uniform particle-size latexes. *Journal of the Optical Society of America*, 44(8):603–607, 1954.

[170] B. Reinhold, T. Geue, P. Huber, T. Sant, U. Pietsch, and M. Sztucki. In situ and ex situ SAXS investigation of colloidal sedimentation onto laterally patterned support. *Langmuir*, 25(2):814–819, 2009.

[171] R. Lazzari. IsGISAXS: a program for grazing-incidence small-angle X-ray scattering analysis of supported islands. *Journal of Applied Crystallography*, 35(Part 4):406–421, 2002.

[172] M. P. Tate and H. W. Hillhouse. General method for simulation of 2D GISAXS intensities for any nanostructured film using discrete Fourier transforms. *Journal of physical chemistry. C*, 111(21):7645–7654, 2007.

[173] Webpage of beam line BW4. `http://hasylab.desy.de/facilities/doris_iii/beamlines/bw4/index_eng.html`. [Online; accessed 06-Dezember-2009].

[174] Markwardt C. Webpage of C. Markwardt. `http://cow.physics.wisc.edu/~craigm/idl/idl.html`. [Online; accessed 09-12-2009].

Acknowledgments

For the last four years, numerous people contributed in various ways to this work. I greatly appreciate this support and dedicate this chapter to the expression of my gratitude.

The first person to thank is my supervisor *Dr. Thomas Geue.* He initiated the PhD project I worked on, gave me through this the opportunity to explore the world of X-ray scattering and colloids and never questioned the realization of this work. These intensive years as a PhD student are very important to me!

Prof. Dr. Marcus Textor accepted me as his PhD student. I appreciated in particular, how he let me always feel that he cares about my success and trusts in my abilities. As his doctoral student, I was also part of the Laboratory for Surface Science and Technology. I experienced the whole group as very welcoming and supportive whenever I had any kind of question or needed an introduction on an instrument in the laboratories at the Hönggerberg. Namely *Christian Zink*, *Christoph Mayer*, *Doris Spori*, *Dr. Ganna Gorodyska*, *Dr. Jarred Clasohm*, *Mirjam Ochsner*, *Thomas Blättler*, *Tobias Künzler* and *Tobias Kraus* dedicated some of their time to introduce me to a wide variety of techniques. The "LSST off-site group meetings" stay of course as a good memory!

The main part of my work was done in the Laboratory for Neutron Scattering at the Paul Scherrer Institute. It provided me with a very agreeable working ambiance - my office colleges *Dr. Antonio Cervellino*, *Dr. Agnieszka Wilk*, *Dr. Murat Ay* and *Dr. Ronny Vavrin* being the most crucial part of it. I also enjoyed the company for lunch both when quietly reading the "Tagesanzeiger" or lively discussing about soccer.

Crucial contributions for my work were done by members of the Laboratory for Developments and Methods - specifically by *Christian Kägi*, *Dieter Graf*, *Marcel Schild*,

Thomas Gahl and *Thomas Mühlebach*. I was amazed several times how they created a perfectly functioning instrument from a simple sketch of my idea. This ability was invaluable for my work!

A big thank does also go to *Prof. Dr. Ullrich Pietsch*, head of the Solid State Physics group of the university of Siegen, Germany. His inputs concerning the data fitting and interpretation were very helpful for the further advancement of my project. Additionally, all structured surface relief gratings used in this work were fabricated with a setup in his laboratories with the friendly help of *Padmanabh Veer*. During my excursions to Siegen, I had the luck to be guest of *Dr. Tobias Panzner* and his lovely wive *Cheerapa Panzner*. I loved the tasty Thai food and the discussions about physics while drinking German beer! The quality of this work was also significantly improved thanks to the critical eye of *Tobias*.

Prof. Dr. Walter Steurer took on different occasions time to look over my project. I am thankful for his discerning questions that helped me to advanced my work significantly.

Different scientists supported me during the X-ray scattering experiments. Thanks to *Dr. Andreas Timmann*, *Dr. Oliver Bunk*, *Dr. Stefan Roth* and *Dr. Wolfram Leitenberger*, these experiments could be successfully completed.

AFM and SEM measurements performed in this work, originate mainly from the Laboratory for Micro and Nanotechnology at PSI. These investigations have proceeded smoothly at perfectly supported equipment. I appreciated the supportive attitude and the help of *Rolf Schelldorfer* concerning the operation of the AFM. *Anja Weber* helped me with the SEM measurements. It was a pleasure to probe my samples with such a skillful operator.

I thank my family and friends for being there when needed; for discussions on everything under the sun - for many, many hours with ball and stick in the gym draining my brain of physics - for good company - for making my live happy! An exceptional thank goes to my parents, *Elisabeth* and *Marc Huber-Nievergelt*. To be honest, I could not wish better ones! A very special thank goes also to *Martina Mittler*. She listened to my concerns, had patience and valued me irrespective of my PhD work. Most importantly, she motivated me time and again to believe in myself!

I appreciate the financial support of my project by the Swiss National Funds Grant No. 200021-107796, the Paul Scherrer Institute and ETH Zurich.